INTERFACE CONTRACTILITY BETWEEN DIFFERENTLY FATED CELLS DRIVES CELL ELIMINATION AND CYST FORMATION

Christina Bielmeier
Ludwig-Maximilians-Universität München

München 2015

INTERFACE CONTRACTILITY BETWEEN DIFFERENTLY FATED CELLS DRIVES CELL ELIMINATION AND CYST FORMATION

Dissertation
der Fakultät für Biologie
der Ludwig-Maximilians-Universität München

vorgelegt von
Christina Bielmeier

München, den 17. Dezember 2015

Erstgutacher: Dr. Anne-Kathrin Classen
Zweitgutachter: Prof. Dr. Nicolas Gompel

Tag der Abgabe: 17. Dezember 2015
Tag der mündlichen Prüfung: 17. Mai 2016

Declaration

Eidesstattliche Versicherung

Hiermit erkläre ich an Eides statt, dass ich die vorliegende Arbeit selbstständig und ohne unerlaubte Hilfe von Dritten angefertigt habe.

München, den 17.12.2015

……
Christina Bielmeier

Erklärung

Hiermit erkläre ich, dass die Dissertation weder als Ganzes, noch in Teilen an einem anderen Ort einer Prüfungskommission vorgelegt wurde. Ich habe weder an einem anderen Ort eine Promotion angestrebt, noch angemeldet oder versucht eine Doktorprüfung abzulegen.

München, den 17.12.2015

……
Christina Bielmeier

Veröffentlichung / Publication

Teile dieser Arbeit wurden zur Erstellung eines Manuskripts verwendet, welches am 08.12.2015 für die Veröffentlichung im Journal Current Biology akzeptiert wurde (siehe unten). / Parts of this work were used for a manuscript that was accepted for publication on 08.12.2015 by the Journal Current Biology (see below).

Interface contractility between differently fated cells drives cell elimination and cyst formation

Christina Bielmeier *[1], Silvanus Alt *[2,3], Vanessa Weichselberger [1], Marco La Fortezza [1], Hartmann Harz [1], Frank Jülicher [2], Guillaume Salbreux [§2,3], Anne-Kathrin Classen [§1]

** shared first co-authors*
[§] corresponding authors

1 Ludwig-Maximilians University Munich, Germany
2 The Max-Planck-Institute for Physics of Complex Systems, Dresden, Germany
3 The Francis Crick Institute, London, UK

Mitwirkungen / Contributions

Teile dieser Arbeit entstanden in Kooperation mit Silvanus Alt und Guillaume Salbreux (The Max-Planck-Institute for Physics of Complex Systems, Dresden). Ihre Arbeit beinhaltet die mathematisch-physikalische Simulierung des Gewebes und wird an gegebener Stelle im Text oder Bildunterschriften gekennzeichnet. / This work was done in collaboration with Silvanus Alt und Guillaume Salbreux (The Max- Planck-Institute for Physics of Complex Systems, Dresden). Their work includes the mathematical-physical modeling of the tissue and their contributions will be stated in the text or figure legends.

Marco La Fortezza hat an der Datenauswertung, statistischen Analyse, sowie der damit verbundenen Datenvisualisierung mitgewirkt. Ebenso waren Anne-Kathrin Classen und Hartmann Harz in Teilen an der experimentellen Analyse involviert. Vanessa Weichselberger und Hanne Hartmann haben im Zuge eines Praktikums teilweise an dieser Arbeit mitgewirkt. Auf ihre Mitwirkungen wird an gegebener Stelle im Text oder Bildunterschriften hingewiesen. Carolin Bleese hat bei Illustrationen der Abbildungen 1, 8 und 44 geholfen. / Aspects of the data analysis including statistical calculations and data representation were supported by Marco La Fortezza. Anne-Kathrin Classen and Hartmann Harz contributed to experiments described in this thesis, as well as Vanessa Weichselberger and Hannelore Hartmann during research practical courses. Their contributions are indicated in the text or figure legends. Carolin Bleese helped with illustrations in Figure 1, 8 and 44.

Contents

List of Figures

Abbreviations

General abbreviations

AEL	After egg lay
AP	Anterior posterior
B/DH	Blade/distal hinge
DAH	Differential adhesion hypothesis
DAPI	4`, 6-diamidino-2-phenylindole
DH/PH	Distal hinge/proximal hinge
DITH	Differential interfacial tension hypothesis
DP	Disc proper
DV	Dorsal ventral
EC	Egg collection
ECM	Extracellular matrix
EL	Egg lay
GFP/RFP	Green/red fluorescent protein
HS	Heat-shock
MWI	Misspecified wild-type interface
NGS	Normal goat serum
PD	Proximal distal
PH/N	Proximal hinge/notum
PM	Peripodial membrane
px	Pixel
ROI	Region of interest
RT	Room temperature
SAR	Subapical regions
SEM	Standard error of the mean
SJ	Septate junctions
TA	Transit amplifying cells
TP	Time point
TS	Temperature shift
Wt	Wild-type
ZA	Zonula adherens

Gene abbreviations

Abd-B	*Abdominal-B*
ap	*apterous*
APC	*Adenomatous Polyposis Coli*
aPKC	*atypical protein kinase C*
arm	*armadillo*
baz	*bazooka*
caps	*capricious*
ci	*cubitus interruptus*
cora	*coracle*
crb	*crumbs*
Dcp-1	*Death caspase-1*
dIAP	*death-associated inhibitor of apoptosis 1*
Dl	*Delta*
dlg	*disc large*
Dll	*Distal-less*
Doc	*Dorsocross*
Dpp	*Decapentaplegic*
E-cad	*E-cadherin*
ed	*echinoid*
en	*engrailed*
Eph	*Eph receptor tyrosine kinase*
ey	*eyeless*
FasIII	*Fasciclin 3*
fkh	*fork head*
fln	*flightin*
flw	*flower*
hep	*hemipterous*
hh	*hedgehog*
hth	*homothorax*
iro-C	*iroquois complex*
JAK/hop	*hopscotch*
JNK	*c-Jun N-terminal Kinase*
lgl	*lethal giant larvae*
lz	*lozenge*
MLCK	*Myosin light chain kinase*
Mmp2	*Matrix metalloproteinase 2*
Moe	*Moesin*
Nrg	*Neuroglian*
Nrx-IV	*Neurexin-IV*
nub	*nubbin*
Omb	*Optomotor-blind*
p120	*p120 catenin*
pnr	*pannier*
Psc	*Posterior sex combs*
ptc	*patched*
puc	*puckered*
Rho1	*Rho Kinase*
RTK	*Receptor tyrosine kinase*
sal	*spalt*
salm	*spalt major*
salr	*spalt related*
scrib	*scribble*
Ser	*Serrate*
sna	*snail*
sqh	*spaghetti squash*
sdt	*stardust*
Su(z)2	*Suppressor of zeste 2*
TGFβ	*Transforming growth factor β*
tkv	*thickveins*
trn	*tartan*
tsh	*teashirt*
twi	*twist*
Ubx	*Ultrabithorax*
vg	*vestigial*
vkg	*viking*
vn	*vein*
Wnt/Wg	*Wnt/Wingless*
yki	*yorkie*
yrt	*yurt*
zip	*zipper*
α-cat	*α-catenin*
β-cat	*β-catenin*

Summary

90 % of human cancers develop from epithelial tissues, emphasizing the importance of studying the regulation of epithelial integrity to identify effective cancer treatments. Whereas mutations in cell polarity and adhesion pathways are known to disrupt epithelial integrity in tumors, little is known about the potential contribution of aberrant cell fate specification that may change aspects of epithelial architecture.

We find that ectopic expression of transcription factors specifying cell fates causes epithelial cysts in *Drosophila* imaginal discs. Cyst formation is driven by cell non-autonomous enrichment of actomyosin at lateral interfaces between wild-type and misspecified cells. By confirming predictions of 3D vertex model simulations with experiments *in vivo*, we demonstrate that interface contractility is necessary and sufficient to drive cyst formation. However, the exact consequences of interface contractility to tissue morphology depend on the size of the cell cluster that experiences increased tension. These consequences range from apoptotic elimination of single misspecified cells to cyst formation in intermediate-sized clones and cell segregation observed in large cell populations. Therefore, interface contractility might exert several distinct functions in development and disease including tissue surveillance through removal of single misspecified cells, promotion of disease-relevant cysts or tissue separation important during development (Figure 1).

Our results show that transcriptional heterogeneities that arise within tissues - either naturally during development or in the context of cell fate misspecification - may underlie several distinct morphogenetic responses by activation of interface contractility. Thus, interface contractility provides a novel and surprisingly general perspective on developmental processes, as well as the etiology of precancerous lesions in the mammalian system.

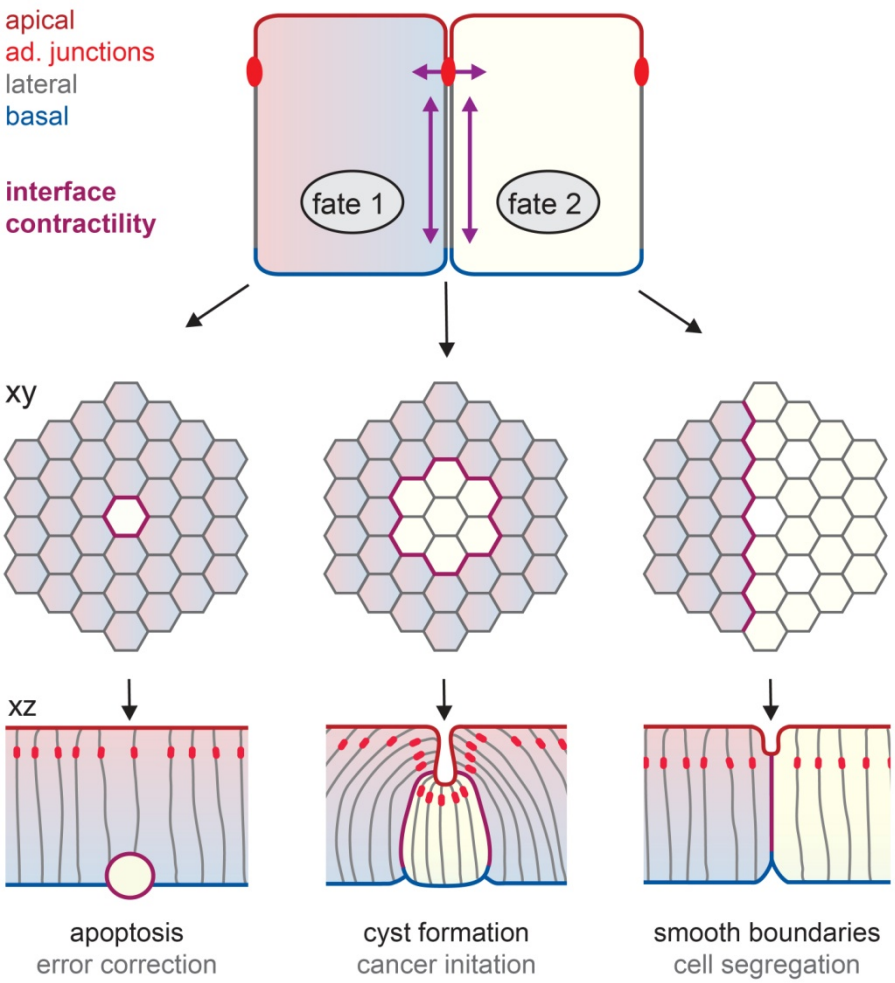

Figure 1: Graphical summary; Actomyosin contractility (magenta) increases at interfaces between differently fated epithelial cells (purple and yellow) at the level of adherens junctions (red) and laterally (grey). This drives apoptotic elimination (left), cyst formation (middle) or cell segregation (right) depending on cell cluster size. Thereby, interface contractility acts as an error correction mechanism on single misspecified cells, but may cause disease-promoting cysts in intermediate-sized cell clusters. Cell segregation of large clusters subjected to interface contractility could drive tissue separation during development.

Zusammenfassung

90 % aller menschlichen Krebserkrankungen haben ihren Ursprung in Epithelgeweben. Dies führt vor Augen, wie wichtig es ist, ein besseres Verständnis über die Aufrechterhaltung von epithelialen Gewebestrukturen zu erlangen. Während der Zusammenhang zwischen Polaritätsdefekten und dessen schädliche Auswirkung auf die Struktur von Epithelien weitestgehend bekannt ist, bleibt der Einfluss von Zellen, die falsche Spezifizierungsprozesse durchlaufen, größtenteils unerforscht.

In dieser Arbeit zeigen wir, dass die ektopische Expression von Transkriptionsfaktoren, die Zellidentitäten vermitteln, epitheliale Zysten in Imaginalscheiben von *Drosophila* verursacht. Die Zysten entstehen nicht durch veränderte, intrinsische Eigenschaften der falsch-spezifizierten Zellen, sondern durch erhöhte Anlagerung von Aktin und Myosin an den lateralen Grenzflächen, an denen normale Zellen und falsch-spezifizierte Zellen aufeinander treffen. Wir konnten mit *in vivo* Experimenten die Prognosen eines neu entwickelten 3D Vertex Models bestätigen, welches aufzeigte, dass erhöhte Kontraktilität an den Grenzflächen sowohl ausreichend, also auch notwendig ist, um Zysten zu induzieren. Weitere Untersuchungen zeigten darüber hinaus, dass die exakten Auswirkungen erhöhter Grenzflächenkontraktilität auf das Gewebe stark mit der Größe der falsch-spezifizierten Zellgruppe zusammen hängen. Dem zu Grunde liegend reichen gewebespezifische Konsequenzen von apoptotischer Eliminierung einzelner, falsch-spezifizierten Zellen, über Zystenbildung mittelgroßer Zellgruppen bis hin zur geradlinigen Trennung großer Zellpopulationen. Dies deutet darauf hin, dass erhöhte Kontraktilität zwischen unterschiedlich spezifizierten Zellgruppen verschiedene Funktionen im Zuge von entwicklungsbiologischen Vorgängen und der Entstehung von Krankheiten einnehmen kann. Erhöhte Grenzflächenkontraktilität spielt also nicht nur eine Rolle bei der Überwachung der Epithelintegrität und der Einführung von Gewebegrenzen, welche wichtig während der Musterbildung sind, sondern auch bei der Entstehung von krankheitsfördernden Zysten.

Unsere Ergebnisse legen dar, dass mehrere, unterschiedliche Ausprägungen der Gewebemorphogenese auf dem gleichem Prinzip beruhen können. Dieses ist - in unserem Fall - der transkriptionelle Unterschied zwischen angrenzenden Zellpopulationen, welcher entweder

natürlicherweise durch Musterbildung in der Entwicklung entstehen kann oder im Zuge von krankhafter, falscher Zellspezifizierung. Dies eröffnet eine neue und sehr generelle Sichtweise auf morphogenetische Prozesse und der Bildung von Zysten, auch als mögliche Ursache für die Entstehung von krebsartigen Veränderungen in Säugetier-Epithelien.

1 Introduction

1.1 Epithelial structure and morphogenesis

Epithelial tissues belong to the four basic tissue types of multicellular organisms. Their development is a fundamental prerequisite for the evolution of metazoans as shown by high functional conservation. The importance of epithelial sheets lies in their barrier function separating distinct body compartments from each other as well as the animal interior from the surrounding environment. Moreover, simple epithelial sheets act as starting points for the formation of various organs through remodeling processes occurring in the course of development (Rodriguez-Boulan and Macara, 2014; Tepass, 2012)

In addition to the prominent role in morphogenesis and development, epithelial tissues also harbor the basis for disease initiation and progression. As an example, about 90 % of human cancers arise in epithelial tissues through transformation of single epithelial cells (McCaffrey and Macara, 2011; Nowell, 2002).

1.1.1 Prerequisites for epithelial function

Epithelial sheets are arrangements of adhesive cells that are uniformly polarized along their apical-basal axis. The cellular polarization leads to the separation of the plasma membrane into apical, lateral, and basal membrane regions with distinct protein and lipid compositions (Figure 2 a). Whereas the apical side faces the exterior or an internal lumen, the lateral and basal regions are engaged in cell-cell and cell-matrix adhesion, respectively. Adhesion, apical-basal polarity, and the possibility to change cell shapes due to polarized cytoskeleton components are indispensable prerequisites for proper epithelial function (Rodriguez-Boulan and Macara, 2014; Schock and Perrimon, 2002).

a. Cell-cell and cell-matrix adhesion

In *Drosophila,* the adhesion of individual epithelial cells is orchestrated in the apical region called Zonula adherens (ZA), which separates the subapical region (SAR) from the more basally located domain of septate junctions (SJ) and, therefore, plays a crucial role in membrane

domain separation (Figure 2 a). The ZA is comprised of a circumfential adhesive belt that connects the actin cytoskeleton of neighboring cells through force-bearing adherens junctions. The main component of adherens junctions is the transmembrane protein E-cadherin (E-cad), whose extracellular cadherin domain binds cadherins from neighboring cells in a Ca^{2+}-dependent manner. Intracellularly, E-cad forms a complex with p120 catenin (p120) and β-catenin (β-cat), which eventually connects E-cad to α-catenin (α-cat) and the actin cytoskeleton (Figure 2 a, b). However, the exact composition of this intracellular assembly is still not fully understood and functional as well as compositional differences depending on cell type or developmental contexts may exist (Bulgakova et al., 2012; Schock and Perrimon, 2002; Tepass et al., 2001).

The region just basally to ZA is marked by another group of intercellular junctions, called septate junctions (SJ). They fulfill similar functions to tight junctions in vertebrates by establishing a paracellular barrier restricting the flow and exchange of molecules between apical and basolateral regions. Structurally, SJ are organized circumferentially around the cell cortex, generating ladder-like structures that bridge the intercellular space of two neighboring cells (Figure 2 a). So far, more than 20 different proteins have been identified to be components of SJ in *Drosophila*. These include, for example, ion channels, FERM-domain proteins, homophilic adhesion molecules, and other transmembrane proteins (Izumi and Furuse, 2014; Tepass et al., 2001).

Interaction with the extracellular matrix (ECM) is the third type of adhesion occurring in epithelial cells. Conceptually, cell-matrix adhesion shares some similarities to the force-bearing aspects of cadherin-based cell-cell contacts. Integrins, another class of transmembrane receptors, connect the intracellular actin cytoskeleton to the basement membrane at basally located hemiadherens junctions (Figure 2 a). The basement membrane is comprised of a layer of ECM material, which covers all epithelial sheets basally, as well as muscles and nerves. It mainly includes the four components laminin, nidogen, proteoglycans and collagen IV and has fundamental implications in protection, stabilization, signaling and polarization of epithelial tissue architecture. Structurally, integrins form a heterodimer composed of one α and one β subunit that recognize and bind specific components of the ECM (Gumbiner, 1996; Schock and Perrimon, 2002; Yurchenco, 2011).

Similar to cadherins, the composition and assembly of the intracellular integrin complex is not yet completely resolved, but Talin has been identified as a crucial interactor mediating the linkage to the actin cytoskeleton (Brown et al., 2002). Over the last few years, it has become clear that the regulation and function of both cadherin and integrin receptors are highly complex and involve, for example, differential expression of receptor subtypes, different synthesis and turnover rates, differential complex composition, phosphorylation and alternative splicing (Bulgakova et al., 2012).

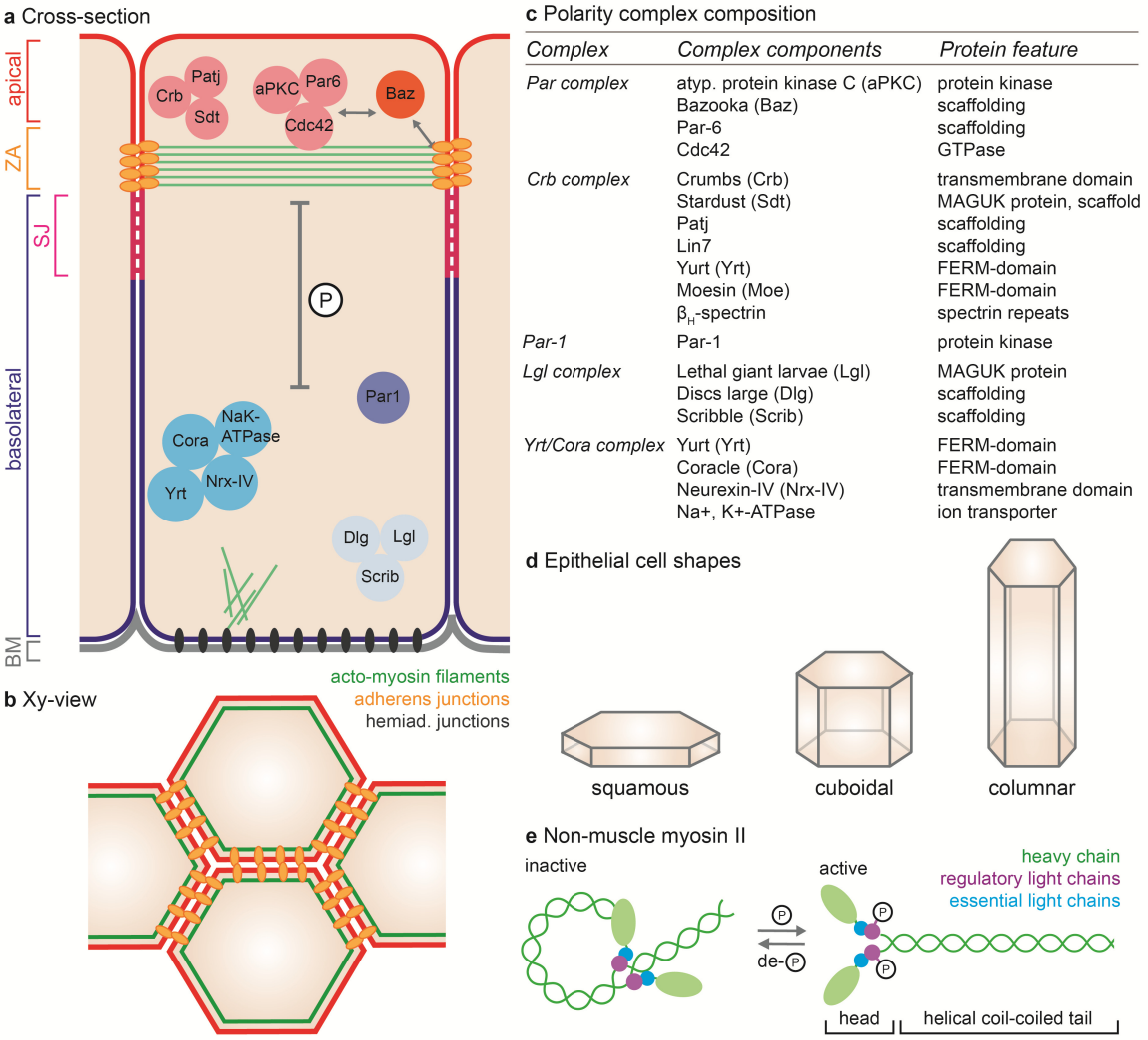

Figure 2: Epithelial architecture and polarity; (a) Schematic cross-section of epithelial cells depicting major membrane domains and polarity complexes. Apical regions and complexes are red, basolateral ones are blue. Adherens junctions within the zonula adherens (ZA) are orange, septate junctions (SJ) pink. Actomyosin structures are green. At the level of adherens junctions an actomyosin belt is formed. Basally, hemiadherens junctions (dark grey) connect the basement membrane (BM) to the cytoskeleton (green, only shown for one interaction). For simplicity, the actin cortex and linker proteins at cell junctions are not represented. Apical and basolateral complexes exclude each other mainly through phosphorylation events (P) **(b)** Xy-view of epithelial cells at the level of adherens junctions (orange) illustrates the actomyosin belt (green) underneath the cells` plasma membrane (red) **(c)** Polarity complexes and their individual components as well as their corresponding protein features are listed. Par complex and Crb complex are apical determinants, Par-1, Lgl complex and Yrt/Cora complex define the basolateral domain. FERM = four-point-one, ezrin, radixin, moesin domain; MAGUK = membrane-associated guanylate kinase protein. **(d)** The different epithelial cell shapes, squamous, cuboidal and columnar are depicted. Note an increase in lateral membrane domain with increasing cell height. **(e)** Structure and activation of non-muscle myosin II is shown. Hexameric non-muscle myosin II consists of two heavy (green), two essential (blue) and two regulatory light (purple) chains, which form a globular head domain and a coil-coiled tail domain. Upon phosphorylation (P) of the regulatory light chains, the hexamer adopts an open and assembly competent configuration.

b. Apical-basal polarity

In addition to adhesion, polarity is another essential characteristic of epithelia, arising from asymmetric protein compositions along the apical-basal axis. In *Drosophila*, the primary epithelium is formed during cellularization at embryonic blastoderm stages. At this time, apical-basal polarity is initially established and relies on two fundamental processes. Firstly, the apical domain becomes delimited from the junctional region of ZA. Secondly, the apical domains and basolateral membranes get clearly separated, and this state has to be maintained throughout later developmental stages (Tepass, 2012; Tepass et al., 2001).

The establishment and maintenance of apical-basal polarity depends on several protein complexes that localize to different subcellular membrane domains, thereby conferring apical or basolateral identity. Whereas the Par complex and the Crb complex set up apical identity, Par-1, the Lgl complex and the Yrt/Cora complex are important for the establishment of basolateral membrane domains (Figure 2 a, c). Although this complex classification is generally accepted, recent studies imply a more complicated and dynamic picture, where components of different complexes interact or proteins act independently of their complex. This is the case for Bazooka (Baz), which is, in addition to its function within the Par complex, crucial for the positioning of adherens junctions (Laprise and Tepass, 2011; Rodriguez-Boulan and Macara, 2014; Tepass, 2012; Tepass et al., 2001).

The molecular mechanism by which polarity proteins get localized within the apical-basal axis depends largely on negative feedback loops between the different complexes. This antagonism is mainly executed through phosphorylation events. Par-1, for example, phosphorylates Baz, thereby restricting Par complex formation to the apical membrane. aPKC in return phosphorylates Lgl and Par-1, which impedes apical membrane association (Figure 2 a). Besides this, differential mRNA location and the phospholipids PtdIns(4,5)P2 and PtdIns(3,4,5)P3 seem to have crucial contributions to polarity set-up and maintenance. To add to the complexity, it has been shown that some of the polarity complexes are required only during specific developmental stages or in specific cell types and that particular cellular conditions, like metabolic stress, recruit additional factors to maintain proper polarity (Laprise and Tepass, 2011; Rodriguez-Boulan and Macara, 2014; Tepass, 2012).

The importance of apical-basal polarity lies in the directionality that it confers to the tissue, which is important for epithelial integrity on several functional levels. This includes, for example, directed vesicle trafficking and cytoskeleton organization. How the polarity regulators discussed above directly account for the asymmetric functional organization in cells is not fully understood and needs further investigation (Tepass, 2012).

c. *Shape and mechanics of epithelial cells*

Epithelial cells can adopt different cell shapes ranging from columnar and cuboidal to very flat through dynamic reorganization of their cytoskeleton (Figure 2 d). The ability to change cell shapes, not only locally but also on a tissue-level, is needed for epithelial morphogenesis (1.1.2) and necessitates a two-step process. Initially, cellular forces are generated, which have to be transmitted to neighboring cells in a second step. On a molecular level, this is achieved by the force-generating actin cortex and cadherin or integrin-based adhesion complexes, respectively. Mechanistically, this means that cellular shape is determined by the balanced actions of cell surface tensions and cell adhesion. Whereas cell adhesion strength positively defines the amount and area of cell contacts, surface tension, largely generated by the actin cortex, aims to reduce the expansion of contacting area (Heisenberg and Bellaiche, 2013; Lecuit et al., 2011).

The actin cortex is a meshwork of cross-linked actin filaments lying directly underneath the plasma membrane of epithelial cells (Figure 24 b). The cortex exhibits a highly dynamic composition of actin filaments, myosin motors and several additional proteins including, for example, cross-linkers and FERM-domain proteins, which are crucial for anchoring the cortex to the plasma membrane. The actin cortex counteracts external forces as well as osmotic pressure, and its properties determine the cell`s stiffness. In epithelial cells, non-muscle myosin II is the crucial component for the generation of contractile forces within the actomyosin cytoskeleton and is therefore required to generate cortical surface tension. Myosin II is composed of two heavy chains, two essential chains and two regulatory chains, whose structure is shown in Figure 2 e. Phosphorylation of the regulatory light chains leads to the active state where assembling into bipolar filaments is possible. These minifilaments are capable of sliding actin filaments passed each other, thereby creating contractions within the cortex. Since phosphorylation of the regulatory light chain is such a crucial event for myosin activity, it can be regulated by several kinases including, for example, Myosin light chain kinase (MLCK) and Rho kinase (Rho1), which are activated through distinct pathways (Lecuit et al., 2011; Salbreux et al., 2012; Tan et al., 1992).

Due to FERM-domain protein dependent anchoring of the cortex to the plasma membrane, the contractility generated within the actin cortex exerts tensions to cell surfaces. Adhesion complexes are capable of transmitting these tensile forces locally through the tissue by connecting the actin cytoskeleton to neighboring cells or the ECM. The molecular details of force transmission remain largely elusive, especially in the case of adherens junctions and at lateral membrane domains, where no adherens junctions are located (Lecuit et al., 2011; Salbreux et al., 2012).

1.1.2 Epithelial morphogenesis

Equipped with all these molecular properties, epithelial tissues carry all prerequisites needed for epithelial morphogenesis. Coordinated cell shape changes and the remodeling of cell-cell junctions or cell-matrix adhesion, for example, contribute to determine the final shape and function of epithelial organs.

The shrinking and expansion of lateral membranes along the apical-basal axis causes cell shape changes that underlie tissue flattening and columnarization, respectively. The latter event is seen during oogenesis in *Drosophila,* where follicle cells surrounding the oocyte become more columnar with time. Invagination is another prominent example of cell shape changes during morphogenesis and causes tissue bending and the creation of a furrow. This is a crucial event during gastrulation in the majority of organisms, but is also important for the development of organs, such as salivary glands in *Drosophila*. During invagination, cells constrict their apical apices through apical localization and activation of myosin. This subcellular increase in surface tension deforms the cell, which becomes wedge-shaped. Together with shortening of the apical-basal axis, this leads to invagination and fold formation within the tissue (Lecuit and Lenne, 2007; Lecuit et al., 2011; Schock and Perrimon, 2002).

Remodeling of cell-cell junctions during tissue morphogenesis can lead to cell intercalation events, where cells change their neighbors and thereby move within the tissue. Concerted cell intercalations orientated along one axis can generate tissue elongation, as seen in the germ band of *Drosophila*. However, removal of cell junctions can also induce cell extrusion and the reduction of cell numbers, an event that has been called ingression (Guillot and Lecuit, 2013; Schock and Perrimon, 2002). Not only cell-cell junctions are remodeled during morphogenesis but also cell-matrix adhesion, where existing integrin-ECM contacts are resolved and new contacts are made. This is important, for example, for cell migration during tubule formation in the trachea of *Drosophila* or during wound closure (Schock and Perrimon, 2002).

1.2 *Drosophila* imaginal discs

Drosophila imaginal discs have been studied for almost a century now. They are an established and well-defined model system for studying epithelial architecture and tissue patterning (Aldaz and Escudero, 2010). Various genetic methods (4.1) make it easy to genetically modify and tract cells within the tissue to answer manifold questions regarding development and disease.

1.2.1 *Drosophila* life cycle

The life cycle of *Drosophila* covers four different developmental stages: adult, embryonic, larval and pupal stages (Figure 3). One complete cycle usually takes 10 days at 25 °C, but can vary significantly depending on environmental conditions. At the beginning of the cycle, fertilized female flies lay eggs, which undergo a 24 h period of embryonic development. Subsequently, larvae hatch and immediately begin to feed for four days, growing from 1st and 2nd instar stages to 3rd instar larvae. The larva enters then the wandering stage, where it leaves the food source to search for appropriate pupariation sites. Once pupariated, the larva undergoes metamorphosis developing into the adult fly within 4 days. After hatching and additional 12-14 h, young flies are sexually mature and start to mate again (Ashburner et al., 2005).

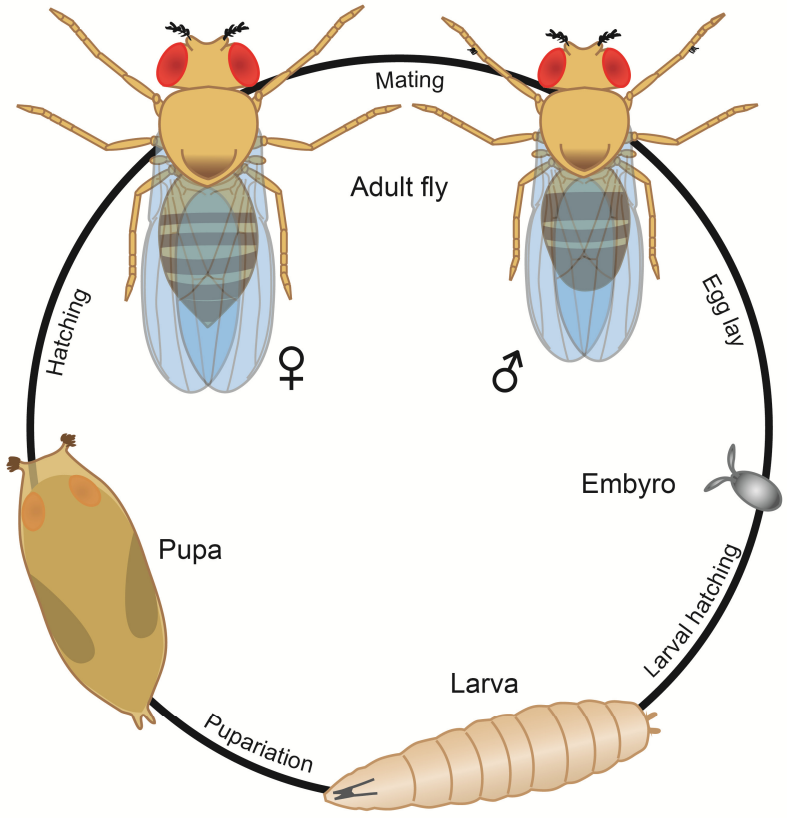

Figure 3: Life cycle of *Drosophila*; The life cycle usually takes 10 days at 25 °C, but can vary depending on environmental circumstances. After mating, fertilized female flies lay eggs. The embryonic development lasts for 24 h followed by larval hatching and a 4-day larval stage. Subsequently, larvae pupariate and undergo metamorphosis, which takes approximately 4 days and ends with the hatching of adult flies.

1.2.2 Imaginal discs are epithelial tissues that give rise to adult fly structures

Imaginal discs are hollow sacs of epithelial sheets found in the larva of *Drosophila*. All larval tissues disintegrate during pupal stages, with the exception of imaginal discs, which will give rise to adult body structures of the head, thorax, limbs and genitalia (Figure 4). The name imaginal disc arose from the Latin word `imago´, which refers to the adult stage of insects. In total, there are 19 discs, 9 pairs of bilateral imaginal discs and one medial genitalia disc (Figure 4). They are specified during embryonic stages, when roughly 10-50 cells invaginate and locate to the inner part of the embryo. They remain located internally during larval stages, when they grow approximately 1000-fold to reach their final size. With the onset of metamorphosis, imaginal discs undergo profound morphological changes by everting to the larval surface and elongating simultaneously. Eventually, imaginal discs fuse with each other to form the continuous epidermal structure of the adult fly (Aldaz and Escudero, 2010; Auerbach, 1936; Cohen, 1993; Held, 2002).

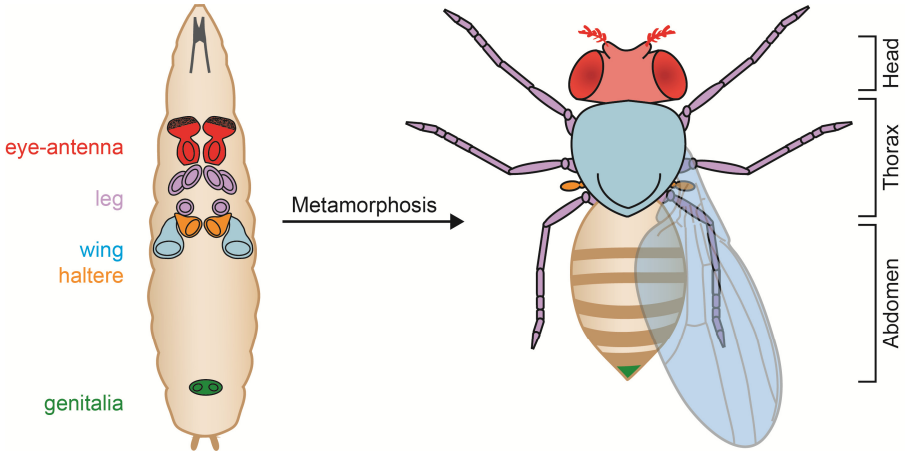

Figure 4: Imaginal discs give rise to adult body structures; Left side shows *Drosophila* larvae with 6 bilateral imaginal disc pairs and one medial genitalia imaginal disc colored individually. The labial, clypeolabral and humeral imaginal disc are not depicted. Right side shows an adult *Drosophila* fly, which can be divided in head, thorax and abdomen. For sake of clearness, only one wing is shown. Colors of body parts refer to the imaginal disc from which they derive. Abdominal parts (brown) are formed by larval histoblasts, which are not depicted.

Looking in more detail at the architecture of imaginal discs reveals a complex 3-dimensional, sac-like structure consisting of a continuous epithelial layer. The apical side of the epithelial sheet sac faces an inner lumen and the basal, ECM-connected side points outwards (Figure 6 e). At early larval stages (1st and 2nd instar), the imaginal sac consists of a cuboidal epithelial sheet, but its morphology dramatically changes during the 3rd instar larval stage. One side of the imaginal sac becomes squamous and gives rise to the so-called peripodial membrane (PM), whereas cells on the other side elongate and form a highly columnar epithelium, the disc proper (DP) (Figure 6 e). Cells at the transition zone connecting the PM and the DP exhibit an intermediate, more cuboidal cell shape (Aldaz and Escudero, 2010; McClure and Schubiger,

2005; Ursprung, 1972). Although the PM has only a minor contribution to epidermal structures, its functions are required for proper disc development. It regulates imaginal disc patterning and the generation of contractile forces important for disc eversion during pupal metamorphosis (Gibson and Schubiger, 2000; Milner et al., 1984).

1.3 Pattern formation and compartmentalization

Cell division, pattern formation, morphogenesis, cell differentiation and growth are the five prerequisites of tissue development and only their coordinated spatial and temporal interplay can generate the complex structure of multicellular organisms. Pattern formation refers to the process in which cells receive information about their location within the tissue, leading eventually to the establishment of differently fated cell populations. The positional information is conveyed by the combinatorial action of different transcription factors belonging either to the class of selector genes or selector-like genes. Eventually, their spatial and temporal pattern is translated by each cell into a specific gene expression pattern giving the cells its particular identity (Weihe et al., 2009; Wolpert et al., 2007).

During early development, pattern formation plays a crucial role by establishing the early body axis of the embryo and specifying the different germ layers. During later stages, patterning remains indispensable to further subdivide appendages, such as legs or wings, into their individual components (Weihe et al., 2009; Wolpert et al., 2007).

1.3.1 Selector genes, compartment boundaries and morphogens

Early clonal experiments in imaginal discs showed that cells do not intermingle freely, but their random intercalation is restricted by the existence of borders (Garcia-Bellido et al., 1973). This was one of the first proofs that tissues are subdivided in compartments that do not mix but stay clearly separated. By definition, compartments are tissue subdomains that are comprised of cells with an identical fate, which is different from those of other compartments. In other words, compartments divide the tissue according to cell identities. Importantly, compartments arise from one cell lineage, where a small group of founder cells inherit its assigned fate to the progeny. The individual fate of compartments is set by transcription factors belonging to the group of so-called selector genes, which pattern the compartment in a cell-autonomous manner (Figure 5 a-b, top panel) (Mann and Morata, 2000; Weihe et al., 2009). Compartments have been extensively studied in *Drosophila*, where they were discovered in the abdomen and in imaginal discs (Garcia-Bellido et al., 1973; Struhl et al., 1997). The establishment of both AP and DV axis through compartmentalization in the wing imaginal disc will be covered in more detail in 1.3.4.

Importantly, compartments are also found in vertebrates, for example in the embryonic hindbrain and limbs (Altabef et al., 1997; Fraser et al., 1990), suggesting compartmentalization to be a common, important theme throughout the animal kingdom.

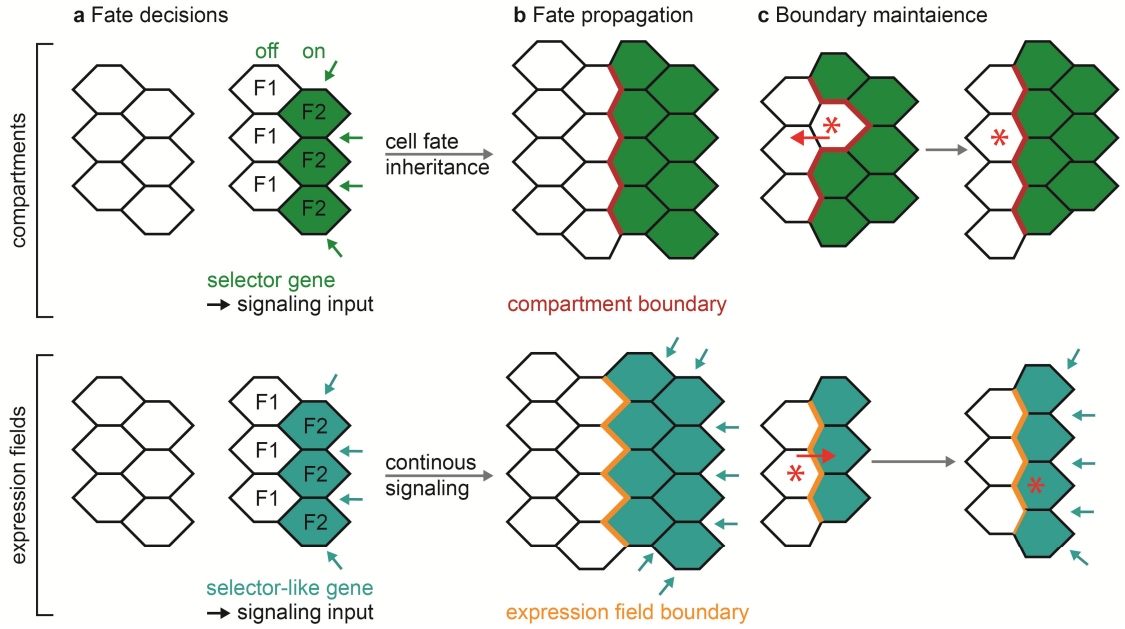

Figure 5: Differences between compartments and expression fields; Compartments are depicted in the top panel, expression fields in the bottom panel **(a)** Selector genes (green) and selector-like genes (turquoise) pattern the tissue leading to two distinct cell fates (F1 and F2). **(b)** In the case of compartments, fate decisions are inherited to daughter cells, whereas in the case of expression fields continuous signaling input is required for fate propagation. **(c)** The boundary between compartments and expression fields is maintained differently. In the case of compartments, a cell of F1 fate that intermingles with cells of F2 fate (red star) is pushed back in their respective compartment. Cells of one expression field (F1) that intermingle with cells of the other expression field (F2) (red star) can adopt a F2 fate due to continuous signaling inputs. Compartment boundary is shown in red, boundary between expression fields in orange. Arrows represent signaling inputs.

Compartments are delimited by compartment boundaries, the region at which two adjacent compartments are in contact and face each other. Compartment boundaries are essential in separating adjacent cell populations and maintaining proper compartmentalization. They play a crucial role as organizing centers of morphogen production. Morphogens are diffusible signaling molecules that give positional information as long-range gradients, which are directly interpreted by cells in a concentration-dependent manner. The organizing centers of compartment boundaries usually translate asymmetric signals of two opposing compartments into symmetric morphogen gradients that originate at the boundary. Since individual cells can translate incoming signals differently depending on their response sensitivity as a function of morphogen concentration, multiple cell types can arise by generating a single, spatially positioned signaling source (Mann and Morata, 2000; Weihe et al., 2009).

Morphologically, compartment boundaries are characterized by increased straightness compared to a line drawn along intra-compartment cell contacts. This minimizes the contact area between the two different cell populations and thereby prevents intermingling. Indeed, conversion of cells to adjacent compartments across the border has only been observed in the context of regeneration (Herrera and Morata, 2014) and stresses the necessity of strict compartment separation for proper development (Figure 5 c, top panel). Several molecular mechanisms ensuring proper tissue separation have been proposed and are discussed below (1.3.3).

1.3.2 Selector-like genes and expression fields

The subdivision of tissues by classical compartments and their boundaries is a rare biological event and does not apply to all subdivisions that occur during animal development. In addition to classical cell-lineage compartments, non-heritable subdivisions also occur quite frequently, for example, during the establishment of the proximal-distal axis in limb morphogenesis (1.3.4). These so-called expression fields are established by continuous signaling inputs and are based on the location of cells and not their cell lineage. In contrast to compartments, non-lineage borders between expression fields have not been studied in great detail. Expression field boundaries are usually not delimited by classical compartment boundaries or morphogen organizing centers and appear to be less strict. Therefore, it is more likely for cells to cross these borders and adopt new cell identities through the continuous signaling input within expression fields. Because of these differences to compartments, genes that convey the identity of an expression field were called selector-like genes and include, for example, v*estigial (vg)* or *homothorax (hth)* (Figure 5 a-c, bottom panel and 1.3.4) (Mann and Morata, 2000; Weihe et al., 2009).

1.3.3 Mechanisms of tissue separation

The prevention of cell mixing of two adjacent compartments or expression fields is crucial for proper development and morphogenesis. However, in proliferating tissues, the maintenance of the straight border separating two compartments is challenged by cell rearrangement and cell mixing that take place as a result of cell division. Therefore, mechanisms must exist that ensure a continuous separation by the formation of sharp boundaries between adjacent compartments (Dahmann and Basler, 1999). In the last century, several attempts to explain mechanistically how tissue borders are established and maintained have raised different hypotheses with ongoing debates and controversies.

a. Differential adhesion (DAH) and differential interfacial tension hypothesis (DITH)

For a long time, the differential adhesion hypothesis (DAH) was generally accepted in the field of boundary formation and was initiated by the early discovery of cell affinity. By definition, cell affinity describes the cellular tendency to preferably cluster together with the same cell type, which was observed during re-sorting of previously dissociated embryonic tissues (Moscona and Moscona, 1952; Townes and Holtfreter, 1955). This was the basis for the early work of Steinberg, who described similarities between sorting of cells and the partition of non-mixable liquids (Steinberg, 1963). Tissues, similar to liquid droplets, tend to minimize their surface area due to increased tissue surface tensions generated at the interface between the tissue and the surrounding environment. Overall tissue surface tension, in contrast to cell surface tension (1.1.1 c), is positively regulated by adhesion. Therefore, according to the DAH, cell sorting is driven only by differences in adhesion strength and the resulting tissue surface tension. Correspondingly, tissues with stronger adhesion will cluster together and will be surrounded by tissues with less adhesion. On a molecular level, differential strength in cell-cell adhesion forces could be achieved through differential expression or deviating quantities of adhesion molecules between two populations. However, this has remained partially controversial, since expression quantities might not directly translate into stronger adhesion forces due to additional levels of adhesion regulation (Fagotto, 2014; Foty and Steinberg, 2013; Lecuit and Lenne, 2007).

Additional critique has been stated by Harris, who proposed a model that considered the actin cortex and its contractile properties as the source of tissue surface tension rather than adhesion (Harris, 1976). This idea was included in the differential interfacial tension hypothesis (DITH) developed in 2002, which suggests that surface tension is not solely regulated by adhesion, but also to a great extent by contractile forces of the actin cortex (Brodland, 2002) (1.1.1 c). As a consequence, interfacial tension is generated by the antagonistic forces of adhesion and cortex contractility, thereby specifying tissue surface tension and sorting behavior (Fagotto, 2014; Foty and Steinberg, 2013).

b. Local increase in tension

A variation of the DITH considers only tension increase at the boundary, rather than global tension differences between two cell populations. This idea is based on the observation that F-actin and Myosin II specifically enrich along the DV and AP compartment boundaries in the wing imaginal disc. Laser ablation experiments could prove that this local enrichment is accompanied by a 2.5-3 fold higher mechanical tension and that this increase is both necessary and sufficient to generate straight boundaries (Aliee et al., 2012; Fagotto, 2014; Landsberg et al., 2009; Major and Irvine, 2005, 2006; Monier et al., 2010). Mechanistically, it was suggested that an actomyosin cable running through cells at the boundary pushes cells back into their

compartment after cell division (Monier et al., 2010). In addition, more recent work showed that in the course of cell intercalations at the AP boundary, new junctions are not positioned in an unbiased manner, but become located closer along the boundary, thereby maintaining the straightness of the AP boundary (Umetsu et al., 2014).

c. Repulsion and retraction

The repulsion and retraction model is based on the action of specific transmembrane proteins including the Ephrin (Eph) receptor tyrosine kinase and its ligand, Ephrin, which have been extensively studied in vertebrates. Upon heterotypic binding and clustering of the two binding partners, activation of Rho family GTPases triggers local actomyosin activity. This leads to active repulsion and retraction of cell contacts, thereby inhibiting adhesion and cell mixing. Since both Eph receptors and Ephrin ligands are capable of intracellular signal propagation, their binding elicits bidirectional signal transduction. In addition to active cell repulsion, Eph signaling events have been linked to roles in cell adhesion and tension generation and open the possibility that Eph and Ephrin ligands play a role in regulating both differential adhesion and local tension increase. However, the exact conditions under which Eph signaling elicits these distinct functions remain very complex and might depend on specific expression patterns, binding strengths, and tissue properties. In summary, the contributions of the different models discussed above to tissue separation and their possible combinatorial actions in imaginal discs and vertebrate systems await further investigations (Cayuso et al., 2015; Fagotto, 2014).

1.3.4 Patterning of the wing imaginal disc

The wing imaginal disc gives rise to the wing itself, but also to the hinge and parts of the thorax (Figure 6 d-g). To accomplish this, the wing disc is subdivided in several domains through combinatorial developmental patterning defining three different axes: the anterior-posterior (AP), the dorsal-ventral (DV) and the proximal-distal axis (PD). Whereas AP and DV orientations are established through compartments in classical terms, expression fields are involved in PD axis formation (Weihe et al., 2009; Wolpert et al., 2007).

The AP axis is first established during embryonic development by the expression of the posterior selector gene *engrailed (en)*. Its expression separates the tissue in two distinct regions: *en*-expressing cells with posterior fate and non-expressing cells with anterior fate. Therefore, early imaginal disc cells already inherit AP information, which initiates a sequence of signaling events that lead to the establishment of long-range AP patterning signal. *en* expression in the posterior compartment induces the expression of the signaling molecule Hedgehog (Hh). Due to its short-range diffusion and the unresponsiveness of the posterior compartment to Hh, only a narrow strip of anterior cells adjacent to the posterior compartment activates the downstream

transcription factor Cubitus interruptus (Ci). This in turn induces the establishment of a symmetric gradient of the long-range morphogen Decapentaplegic (Dpp) along the AP boundary, which is important for patterning and growth of the anterior and posterior compartment (Figure 6 a, c) (Weihe et al., 2009; Wolpert et al., 2007).

As a second step after AP axis formation, the DV axis is defined during 2nd instar larval stages. At this time, the homeotic selector gene *apterous (ap)* becomes expressed exclusively in the dorsal compartment, whereas the ventral fate is determined by its absence. Due to the opposite expression of the two short-range ligands Delta (Dl) and Serrate (Ser), Notch signaling is activated only at the DV border. Eventually, this leads to a symmetric expression gradient of the long-range morphogen Wingless (Wg), important factor for DV patterning, wing blade determination and proliferation (Figure 6 b, c) (Mann and Morata, 2000; Weihe et al., 2009; Wolpert et al., 2007).

The proximal-distal axis distinguishes the morphological units of the distal blade, the hinge and the proximal notum (Figure 6 d, e). Its establishment is not as well characterized as for compartment boundaries and depends on the formation of defined expression fields by various selector-like genes. This process starts during 2nd instar larval stages, when the secreted signaling molecule Vein (Vn) activates EGFR signaling only dorsally, thereby defining the notum region. Through the mutually exclusive activation of EGFR signaling proximally and Wg signaling distally, proper separation of proximal notum and distal blade structures is achieved (Wang et al., 2000). Further subdivisions of distal regions into hinge and blade are regulated by complex transcription factor networks and are not fully understood. Wg and Dpp signaling appear to repress *homothorax (hth)* and *teashirt (tsh)*, two important factors for hinge development (Azpiazu and Morata, 2000; Casares and Mann, 2000; Wu and Cohen, 2002) and activate at the same time genes important for wing blade development, including *vestigial (vg)* and *nubbin (nub)* (Kim et al., 1996; Ng et al., 1995; Wu and Cohen, 2002). In case of the proximal notum, genes of the *iroquois complex (iro-C)* and *pannier (pnr)* are involved in subdividing the notum in lateral and medial regions, respectively (Calleja et al., 2000; Diez del Corral et al., 1999).

Equipped with all the positional information obtained by patterning in larval stages, wing imaginal discs undergo pronounced morphogenetic changes during metamorphosis, where the disc proper turns from a monolayer of columnar cells into two basally apposed layers of extremely flat cells. Coordinated cell shape changes and rearrangements drive pouch evagination along the margin accompanied by dramatic tissue elongation. Eventually, basal sides of the ventral and dorsal blade and hinge regions come into apposition, giving rise to the two-layered epidermis of the adult wing (Figure 6 f, g) (Taylor and Adler, 2008; Wolpert et al., 2007).

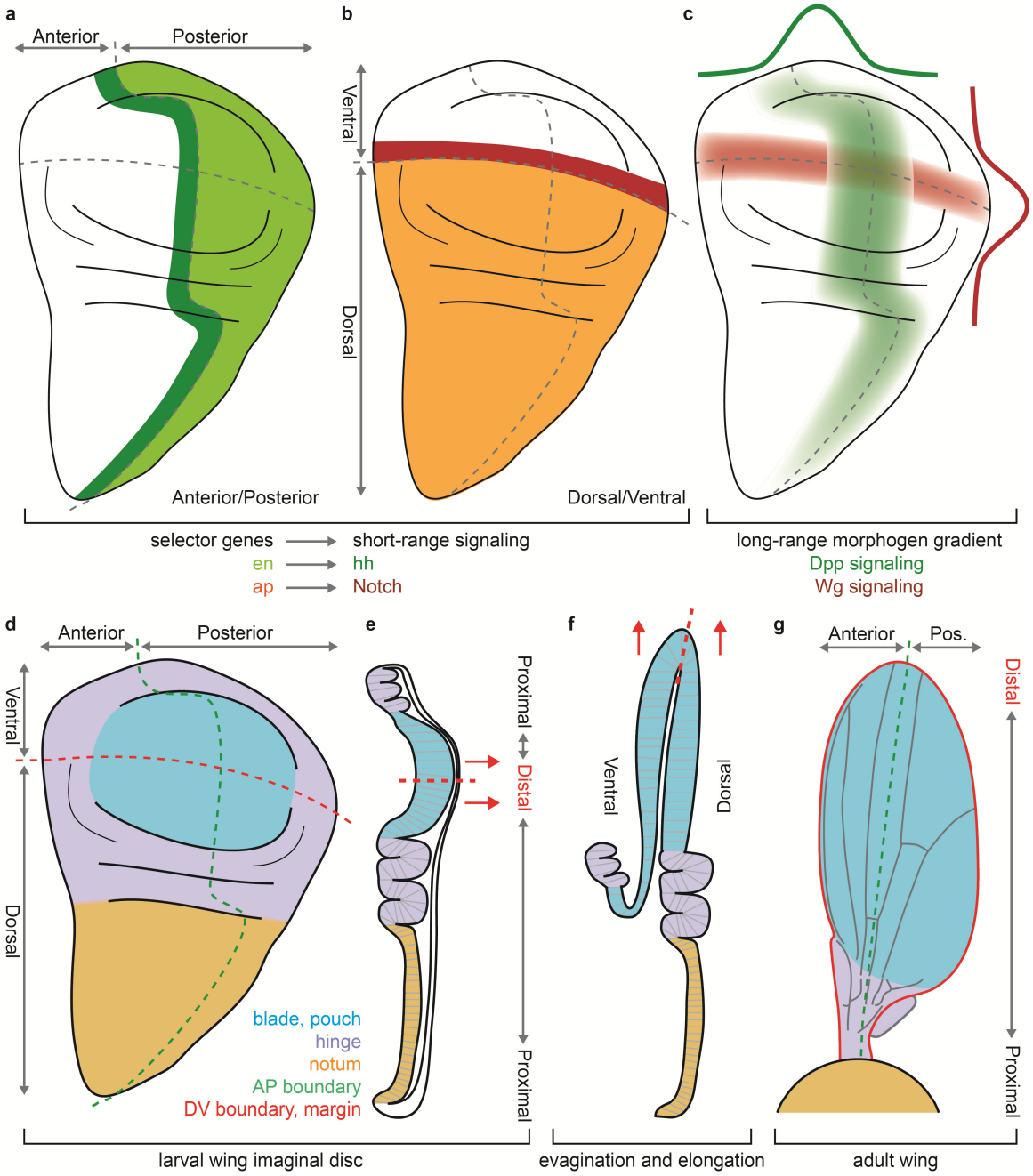

Figure 6: Wing imaginal disc patterning; **(a-c)** (a) AP patterning is established by expression of *engrailed (en)* posteriorly (light green) leading to activation of Hh signaling (dark green) anteriorly to the AP border (b) DV patterning is established by dorsal *apterous (ap)* expression (orange) leading to activation of Notch signaling (red) along the DV boundary (c) Hh and Notch signaling induce long-range gradients of Dpp (green) and Wg (red), which pattern the disc along the AP and DV axis, respectively **(d-g)** PD patterning (d) Xy-view of wing imaginal disc showing the blade (blue), hinge (purple) and notum (orange), the AP (green), DV boundary (red) and PD axis. DV boundary gives rise to margin of the adult wing (red). (e) xz cross-section of the wing imaginal disc. Color codes the same as in (d). Peripodial membrane is white. (f) Evagination and elongation occurring during pupal development. The ventral and dorsal sides come into apposition. (g) Adult wing with pouch, hinge, notum, AP boundary and PD orientation is shown. Color code as in (d).

1.4 Cell fate specification and epithelial structure

Epithelial morphogenesis relies on the coordinated interplay between cell fate specification and the architectural remodeling of cells and tissues. During pattern formation, information regarding epithelial structure and shape are conveyed and executed. One prominent example illustrating this, is mesoderm invagination during gastrulation in *Drosophila*. The transcription factors Twist (Twi) and Snail (Sna) are specifically expressed in ventral cells that invaginate and adopt mesodermal fate (Leptin, 1995). As already mentioned before (1.1.2), a highly polarized cytoskeleton is necessary for the invagination process to occur, as well as for subsequent interior localization of mesodermal cells. Loss of *twi* and *sna* completely abolishes apical myosin II location, ventral furrow formation and mesoderm specification (Simpson, 1983). Due to such tightly connected processes of patterning and epithelial morphogenesis, epithelial defects caused by misregulation of cell fate specification have been observed, but have not been studied as extensively as the interplay of polarity and epithelial structure.

1.4.1 Cell fate misspecification and disruption of epithelial integrity in *Drosophila*

Cell fate misspecification has been previously associated with pronounced disruption of epithelial integrity in the case of epithelial cyst formation by cells mutant for Dpp or Wg signaling pathways. As discussed above (1.3.4), both pathways are required for cell fate specification in wing imaginal discs. Cell clusters (clones) mutant for components of either pathway form cysts by invaginating towards the basal side of the epithelium, thereby creating an apical lumen. Basal invagination can cause clones to become partially extruded and lost from the epithelium (Gibson and Perrimon, 2005; Shen and Dahmann, 2005; Widmann and Dahmann, 2009b).

a. Cell autonomous cell shape changes

As an explanation for these observations, it was suggested that Dpp as well as Wg pathways, promote differentiation of columnar epithelial shapes cell-autonomously. Indeed, their gene expression patterns follow the gradient of columnar cell shapes normally occurring within imaginal discs. Thus, cell-autonomous height reduction from a columnar to cuboidal shape in Dpp or Wg signaling mutant cells has been implicated as the cause of cyst formation in imaginal discs. In the case of Dpp signaling, this function was suggested to be directly mediated by subcellular localization of Rho1 and Myosin II, whereas Vg was identified as an indirect mediator of columnar cell shape regulated by Wg signaling (Widmann and Dahmann, 2009a, b).

b. Cell affinity differences

Clones mutant for *Optomotor-blind (Omb)* or *spalt major (salm)* and *spalt related (salr)* also undergo epithelial retraction of the apical side and exhibit a cystic phenotype (Milan et al., 2002; Organista and De Celis, 2013; Shen et al., 2010). In these contexts, it was suggested that epithelial cyst formation might depend on disruption of cell affinity gradients (1.3.3 a), which might be regulated by these genes. The hypothesis derived from the observation that cystic clones are extremely round and form smooth borders. According to the differential adhesion hypothesis (1.3.3 a), differences in adhesion properties could drive spatial segregation of the mutant cell population and surrounding wild-type cells. In accordance with that, increase or decrease in E-cad levels, the main component of adherens junctions, causes clone smoothening (Zimmerman et al., 2010) (Figure 42). However, the same study also showed that E-cad misregulation is neither sufficient nor necessary for the cystic invagination phenotype observed in Wg signaling mutant clones. In the case of *spalt (sal)* mutant clones, the transmembrane proteins Capricious (Cap) and Tartan (Trn) have been suggested to cause clone smoothening and sorting behavior. But similarly to E-cad, Cap and Trn themselves can only induce clone smoothening, but are not sufficient to induce cystic invagination (Milan et al., 2002; Organista and De Celis, 2013). In summary, it still has to be investigated if cell affinity changes and cell segregation are capable of inducing the dramatic cell shape changes occurring during apical invagination events. Additionally, the possibility that cell affinity differences act in a combinatorial way with other mechanisms during cyst formation cannot be excluded and needs further study.

c. Apical constriction and cell proliferation

The invagination phenotype of epithelial cyst formation resembles invagination events occurring in the course of development, for example, during mesoderm invagination and salivary gland formation (Schock and Perrimon, 2002) (1.1.2 and 1.4). Models trying to explain these endogenous invagination events implicate coordinated apical constriction of multiple cells (Sawyer et al., 2010) or proliferation of cells within a confined space, causing the tissue to bend (Hannezo et al., 2011; Shyer et al., 2013). Further investigation is needed to determine if coordinated apical constriction can also account for cyst initiation and if aberrant proliferation of misspecified cells within a confined space can promote the development of cystic structures.

1.4.2 Cell fate misspecification and disruption of epithelial integrity in mammals

Interestingly, disruption of Wnt/Wg and TGFβ/Dpp signaling has also been connected to the occurrence of cyst-like structures in the mammalian system, specifically in the intestinal epithelium.

Mutations activating the Wnt/Wg signaling pathway, such as those in *Adenomatous Polyposis Coli (APC)*, belong to the most frequent transformations that drive colorectal cancer initiation. In an APC mouse model, adenomatous polyps are characterized by *APC* mutant cell clusters that outpocket into neighboring tissues (Pinto and Clevers, 2005). Interestingly, these morphological changes exhibit phenotypical similarities to epithelial cyst formation described in *Drosophila* imaginal discs. In addition, it was suggested that cyst formation is involved in promoting progressive loss of epithelial integrity occurring during the transition from benign adenoma to more severe forms of adenocarcinomas and carcinomas (Bell and Thompson, 2014). Despite the frequent incidence of invagination events in the context of intestinal cancer, the importance and morphological relevance of cyst formation in both cancer initiation and progression remains poorly understood. Strikingly, some effects that hold true for cell segregation during epithelial morphogenesis have also been implicated in colorectal cancer progression in the mouse model. Eph signaling can inhibit the spreading of cancer cells by inducing cell sorting of transformed cells and promoting the formation of borders. In agreement with this observation, decreased levels of Eph signaling have been linked in some cases to strong invasive cell behaviors (Batlle and Wilkinson, 2012; Cortina et al., 2007).

Secondly, heritable juvenile polyposis is a disease in which patients are predisposed to the development of gastrointestinal polyps and cancer formation. Mutations causing this disease have been located within genes encoding receptors or signal transducers of TGFβ/Dpp signaling (Howe et al., 2001; Howe et al., 1998). It will be interesting to investigate in the future how these protruding structures and cyst formation in *Drosophila* imaginal disc underlie similar mechanisms.

1.4.3 Mechanisms ensuring epithelial integrity

As explained, misspecification of epithelial cells can have dramatic consequences for the integrity and function of tissues (1.4.1 and 1.4.2). To ensure robust epithelial function, several mechanisms have evolved that detect and remove aberrant cells from the tissue, thereby restoring proper patterning and epithelial integrity. In the following sections, homeostatic mechanisms identified in *Drosophila* will be explained in more detail.

a. Morphogenetic apoptosis and short range cell-cell communication

In the wing imaginal disc, it was demonstrated that discontinuities of Dpp or Wg signaling gradients lead to the non-autonomous induction of apoptosis at regions where high and low levels of signaling meet. Due to this, cell with aberrant signaling activities are removed from the tissue and a smooth signaling gradient is restored. Since manipulating several downstream transcription factors of these pathways exerts the same response, it was suggested that the

appearance of differently fated cells is required for morphogenetic apoptosis. The induction of apoptosis depends on the activation of JNK, which belongs to the conserved family of MAP kinases and is responsible for inducing apoptosis in many different biological contexts. Based on round clone shapes observed in these studies, the author speculated that the downstream transcription factors regulate cell affinity and changes therein could trigger JNK activation. However, final proof for this concept is still missing (Adachi-Yamada and O'Connor, 2002, 2004; Igaki, 2009).

More concretely, it has been shown that clones overexpressing the Dpp target genes *sal* are removed by apoptosis from the wing disc in lateral regions, where they are confronted with surrounding cells of low *sal* expression. Interestingly, this removal can be blocked by co-expression of *caps* and *trn,* which encode transmembrane proteins (see also 1.4.1 b). Normally, they are expressed in the lateral wing disc regions and are negatively regulated by Sal. The authors suggest that Caps and Trn might act as ligands for receptors on neighboring cells, thereby ensuring cell survival. However, this mechanism seems to be restricted to regions of endogenous Caps and Trn expression and cannot rescue morphogenetic apoptosis, suggesting that other mechanisms or molecules must be involved (Adachi-Yamada and O'Connor, 2004; Milan et al., 2002).

b. Classical cell competition

The classical definition of cell competition describes the process of removing slower growing or unfit cells (loser cells) from the tissue, but only in conditions where they are surrounded by faster-growing or fitter cells (winner cells). Therefore, cell competition depends on fitness comparison of adjacent cell populations, which leads to the JNK-dependent induction of apoptosis in loser cells induced by surrounding winner cells. Cell competition was described for the first time in the context of *Minute* mutations affecting ribosomal proteins. Mutant cells grow slower and are viable under heterozygous conditions, but are eliminated from the tissue when surrounded by wild-type cells. Later, several other regulators of cell growth, additionally to *Minute* genes, have been shown to induce cell competition, including *dMyc* or components of the Hippo pathway. Based on studies of *dMyc*, the term supercompetitors was defined since high expression of *dMyc* confers increased cellular fitness, leading to the removal of wild-type cells with normal level of *dMyc* expression (de Beco et al., 2012; Levayer and Moreno, 2013).

A central question in cell competition is what defines winner or loser fate downstream of different growth rates. One scenario describes that loser cells, due to their decreased growth and fitness, receive less Dpp ligand compared to surrounding winner cells. This competition for Dpp uptake could lead to discontinuities in the Dpp gradient at the interface of winner and loser cell contacts, similar to morphogenetic apoptosis. Secondly, it was suggested that mechanical

compression from faster growing cells acting on slower growing ones could lead to apoptosis (Levayer and Moreno, 2013; Vincent et al., 2013). Regardless of the upstream signal, the molecular signature of loser cells has been identified and is established by the transmembrane protein Flower (Flw). The *flw* gene encodes three different isoforms, one that is expressed ubiquitously and two that are exclusively expressed by loser cells. The Flw code is necessary and sufficient for apoptosis of loser cells and provides a molecular mechanism for cells to compare their fitness with each other (Rhiner et al., 2010).

c. Intrinsic tumor suppression

Epithelial cells that lose apical-basal polarity because of mutations in *lgl*, *dlg* or *scrib* genes (Figure 2) overproliferate and develop into neoplastic tumors. However, if wild-type cells surround these mutant cells, polarity-deficient cells are removed through JNK-dependent activation of apoptosis. Therefore, direct cell-cell interaction and communication between mutant and wild-type cells are a crucial prerequisite for tissue-intrinsic mechanisms of tumor suppression. Despite several similarities to cell competition, intrinsic tumor suppression only happens after the beginning of morphological cell changes and does not rely on differences in growth rates (Igaki, 2009; Levayer and Moreno, 2013; Vincent et al., 2013).

d. Apoptotic and live cell extrusion

Cells activate the apoptotic cascade in order to shape organs or restore epithelial patterning. To maintain the barrier function of the epithelium, apoptotic cells have to be removed from the tissue layer and the resulting gaps have to be closed. This task is fulfilled by apoptotic cells themselves, who instruct their surrounding cells to create an actomyosin cable that squeezes the apoptotic cell out of the epithelial plane and subsequently prevents the formation of a gap (Rosenblatt et al., 2001).

This important mechanism of apoptotic cell clearance is distinct from live cell extrusion, where cells first leave the epithelium and then activate apoptosis due to loss of cell contacts. Live cell extrusion is triggered by cell crowding, which makes it a powerful mechanism for regulating cell density and epithelial homeostasis. In the pupal notum of *Drosophil*a, live cell extrusion is a stochastic event occurring in regions of high cellular densities. Cells undergoing live cell extrusion experience a step-wise loss of cell junctions leading to their delamination and basal removal from the epithelium. In contrast, apical extrusion has been observed in vertebrates and depends on the cell density-dependent activation of a stretch-induced ion channel called Piezo1. Two questions that need to be further explored are whether this channel also plays a role in live cell extrusion in *Drosophila* and what the molecular pathway downstream of its activation is (Eisenhoffer et al., 2012; Katoh and Fujita, 2012; Marinari et al., 2012).

2 Aim of this study

Although much is known about how cell polarity and adhesion defects harm epithelial integrity (e. g. Halaoui and McCaffrey, 2015; McCaffrey and Macara, 2011), the precise influence of tissue patterning on epithelial integrity remains elusive. Therefore, we aimed to understand the interplay between cell fate patterning and epithelial architecture in more detail. We approach this problem by analysis of epithelial cysts induced upon cell fate misspecification in *Drosophila* imaginal discs, a well-established epithelial model system.

While cyst formation has severe consequences for epithelial function, little is known about the underlying cellular mechanisms and if cysts can be associated with a specific biological function. We wanted to identify under which conditions cyst formation occurs to describe the detailed molecular and cell-biological signature of cystic clone shapes and to decode the biological function driving the formation of this aberrant structure. In addition, we aimed to gain knowledge about the physical forces responsible for the dramatic cell shape changes driving cyst formation. We wanted to test if cell-autonomous shape changes, coordinated apical constriction, or proliferation within a confined space drive cyst formation, since these processes have been linked to cysts and morphogenesis before.

To approach these questions, we conducted a detailed cell-biological and genetic analysis in combination with physical modeling of forces in epithelial sheets. Our interdisciplinary work sheds light on mechanisms of cyst formation operating in *Drosophila* and outlines possible similarities to normal developmental or disease-promoting shape changes.

3 Results

3.1 Ectopic expression of cell-fate specifying transcription factors leads to cyst formation

3.1.1 *Psc-Su(z)2* mutant cells form cysts independent of proliferation and JNK

We performed a mosaic analysis of a precise deletion of the tumor suppressor genes and functional paralogues *Posterior sex combs (Psc)* and *Suppressor of zeste 2 (Su(z)2)* in wing imaginal discs. *Psc* and *Su(z)2* encode Polycomb group proteins, which have important roles in epigenetically maintaining gene expression patterns during development (Beh et al., 2012; Li et al., 2010; Simon and Kingston, 2013). Interestingly, *Psc-Su(z)2* mutant cells have been previously observed to form epithelial cysts (Classen et al., 2009).

We used the FLP/FRT mitotic recombination system (4.1) to induce homozygous mutant cell clusters (clones), which are labeled by loss of GFP expression. We found that early (30 h) after induction of mitotic recombination, *Psc-Su(z)2* mutant clones were rounder when compared to wild-type clones. Phalloidin staining revealed changes to actin localization and cell rearrangements. (Figure 7 a-c, f-h). At later stages (54 h), smoothening of clone shape proceeded leading to large round and confined structures, where mutant cells arranged radially around the clone center (Figure 7 d-e, i-j). To better understand how these structures disrupted normal tissue architecture, we analyzed xz cross-section of *Psc-Su(z)2* mutant clones (Figure 8). Mutant cells started to constrict their apical surfaces (Figure 8 a-c, compare red and blue arrows in c` and h) around 30 h after clone induction followed by an apical invagination. As a consequence, we observed that apical surfaces of mutant cells were shifted more basally when compared to surrounding wild-type cells. This suggested that mutant cells were shortened along their apical-basal axis (Figure 8 a-c). At later time points (54 h), clone invagination had become more pronounced generating basally located spherical structures with deep lumina, which we will term cysts from now on. At this time point, the apical surface of mutant cells was no longer constricted, but appeared to be expanded again (Figure 8 d-f). Nevertheless, mutant cells exhibited a dramatic decrease in cell height indicating further shrinkage of apical-basal axis length. At very late stages

(102 h), some mutant clones completely lost contact to the surrounding wild-type tissue and fully extruded basally as self-contained cystic structures (Figure 8 g). Due to larval lethality, we were not able to investigate the survival and morphology of mutant clones into adult stages. However, a previous study observed *Su(z)12* mutant clones as round vesicles in the adult fly wing that had been sorted out, suggesting that cystic clones can survive until adult stages (Zirin and Mann, 2004). Similarly, it have been reported previously that Dpp mutant cyst survive metamorphosis and remain as cuticular vesicles between dorsal and ventral adult wing layers (Gibson and Perrimon, 2005; Shen and Dahmann, 2005).

We wanted to test if higher rates of cell proliferation within the confined space of the wing imaginal disc are responsible for cyst formation by *Psc-Su(z)2* mutant cells . To this end, we reduced proliferation in *Psc-Su(z)2* mutant clones by introducing the *yorkie* allele yki^{B5} (Huang et al., 2005) into the *Psc-Su(z)2* mutant background. 24 h after clone induction, *Psc-Su(z)2* mutant clones and *Psc-Su(z)2*, *yki* double mutant clones both invaginated. At a later time point (72 h) many double mutant clones had died and the remaining clones were much smaller suggesting that proliferation was indeed restrained. Nevertheless, *Psc-Su(z)2*, *yki* double mutant clones invaginated and formed cysts (Figure 9 a-f), demonstrating that proliferation is not necessary for cyst occurrence.

JNK signaling is known to play a role in cell shape morphogenesis and stress signaling (Rios-Barrera and Riesgo-Escovar, 2013). Since we observed activation of JNK signaling in *Psc-Su(z)2* mutant cells as well as in wild-type cells surrounding the clone (Figure 9 g, h), we wanted to test if JNK signaling could be involved in the process of cyst formation. We generated *Psc-Su(z)2* mutant clones in wing imaginal discs hemizygous for a mutation in the JNK kinase gene *hemipterous* (hep^{R75}) (Glise et al., 1995). The absence of JNK signaling did not interfere with cyst formation (Figure 9 i, j), thereby excluding JNK signaling as the driving force of this process.

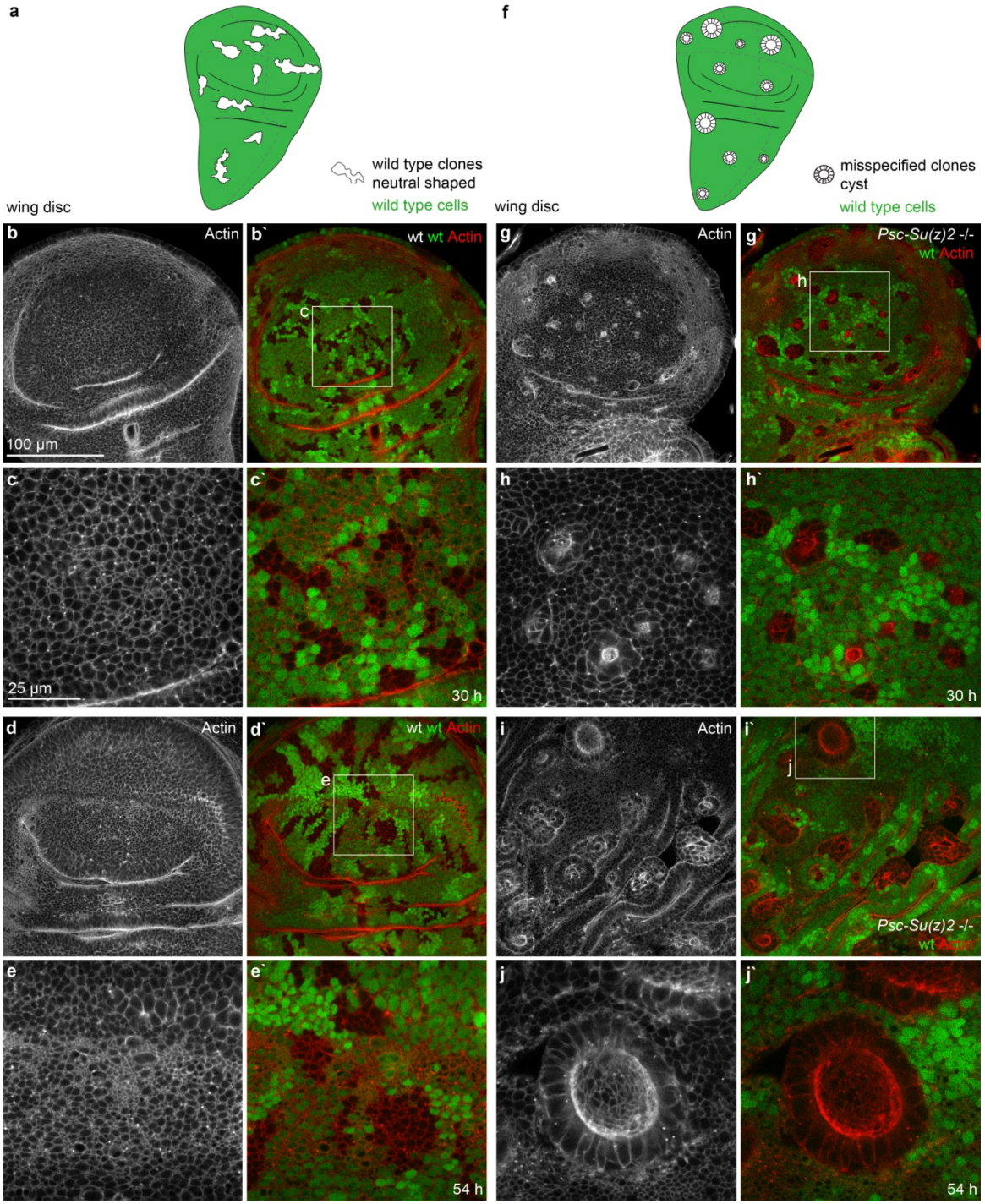

Figure 7: *Psc-Su(z)2* mutant clones invaginate and form cysts; (a, f) Schematic representation of wing imaginal discs containing wild-type clones (a, white) and *Psc-Su(z)2* mutant clones (f, white). Wild-type cells are marked by GFP (green), clones by absence of GFP. Wild-type clones retain a neutral shape (a), whereas clones which are misspecified by a Polycomb mutation invaginate and form round cysts (f). **(b-e and g-j)** Xy sections of wing imaginal discs containing wild-type clones (b-e) or *Psc-Su(z)2*^{XL26} clones (g-j) induced by the FLP/FRT system. Wild-type cells are marked by GFP (green in b`-j`), mutant clones by the absence of GFP: Actin is shown in grey (b-e, g-e) or red (b`-j`). Time points 30 h (b, c and g, h) and 54 h (d, e and i, j) after clone induction are shown. Boxes in (c, d, h, j) frame regions shown at higher magnification in (c, e, h, j). Scale bar as indicated.

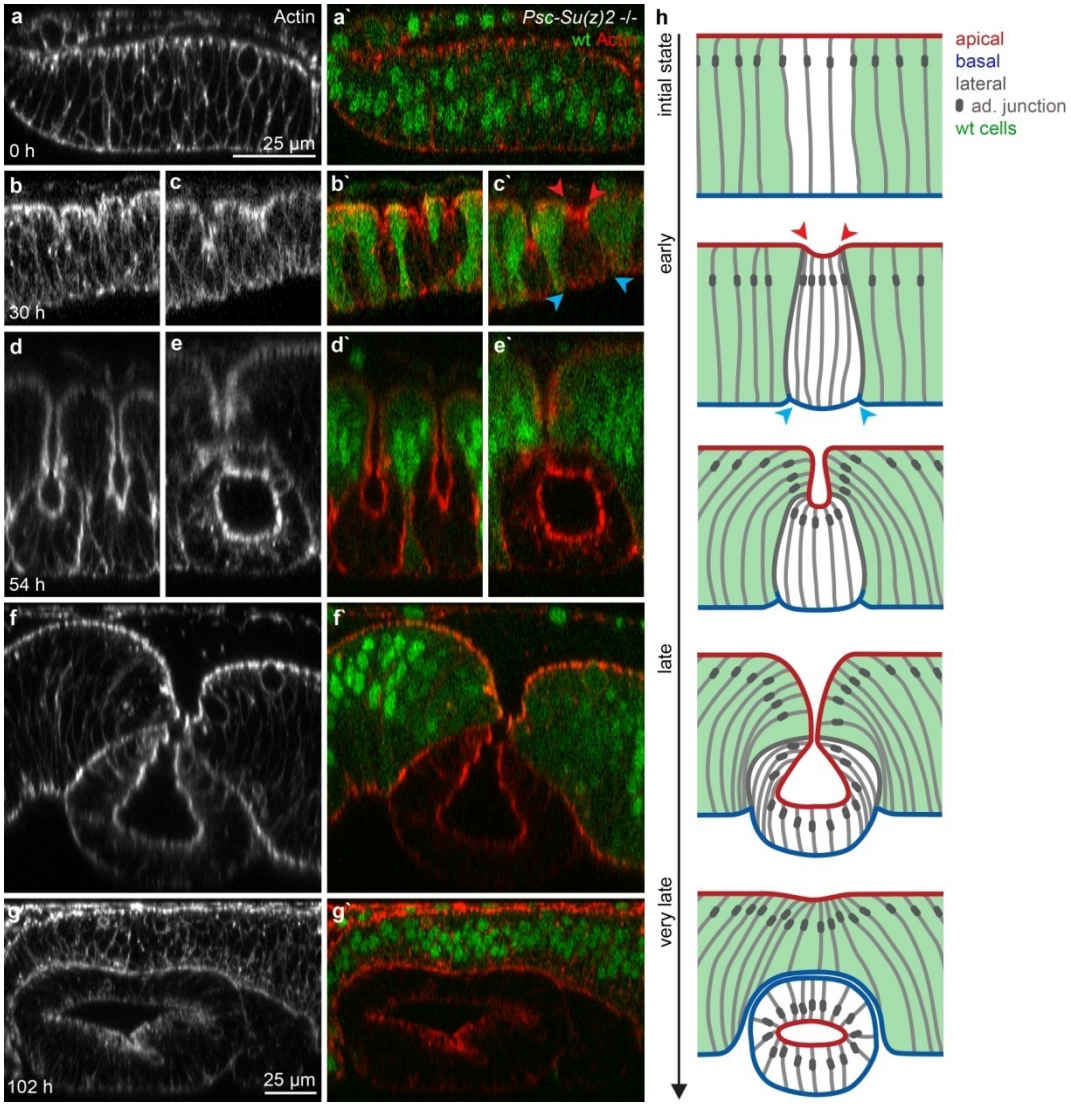

Figure 8: Time course of cyst formation in *Psc-Su(z)2* mutant clones; (a-g) Xz cross-section of *Psc-Su(z)2*^{XL26} clones in wing imaginal discs induced by the FLP/FRT system. Wild-type cells are marked by GFP (green in a`-g`), mutant clones by the absence of GFP: Actin is shown in grey (a-g) or red (a`-g`). Time points 0 h (a), 30 h (b, c), 54 h (d-f) and 102 h (g) after clone induction are shown. Scale bar as indicated. See (h) for explanation of blue and red arrows **(h)** Schematic representation of cyst formation time course. Initially, cells exhibit a columnar shape. Comparing the width of apical (red arrows) and basal (blue arrows) surfaces shows that cells start to constrict apically (compare to c`) during early cyst formation followed by apical invagination. Progressive invagination leads to cysts with deep hollow lumina in the center (late). At very late stages, segregation of mutant cells cumulates in total loss of contact to wild-type tissue leading to enclosed ball-like structures sitting basally.

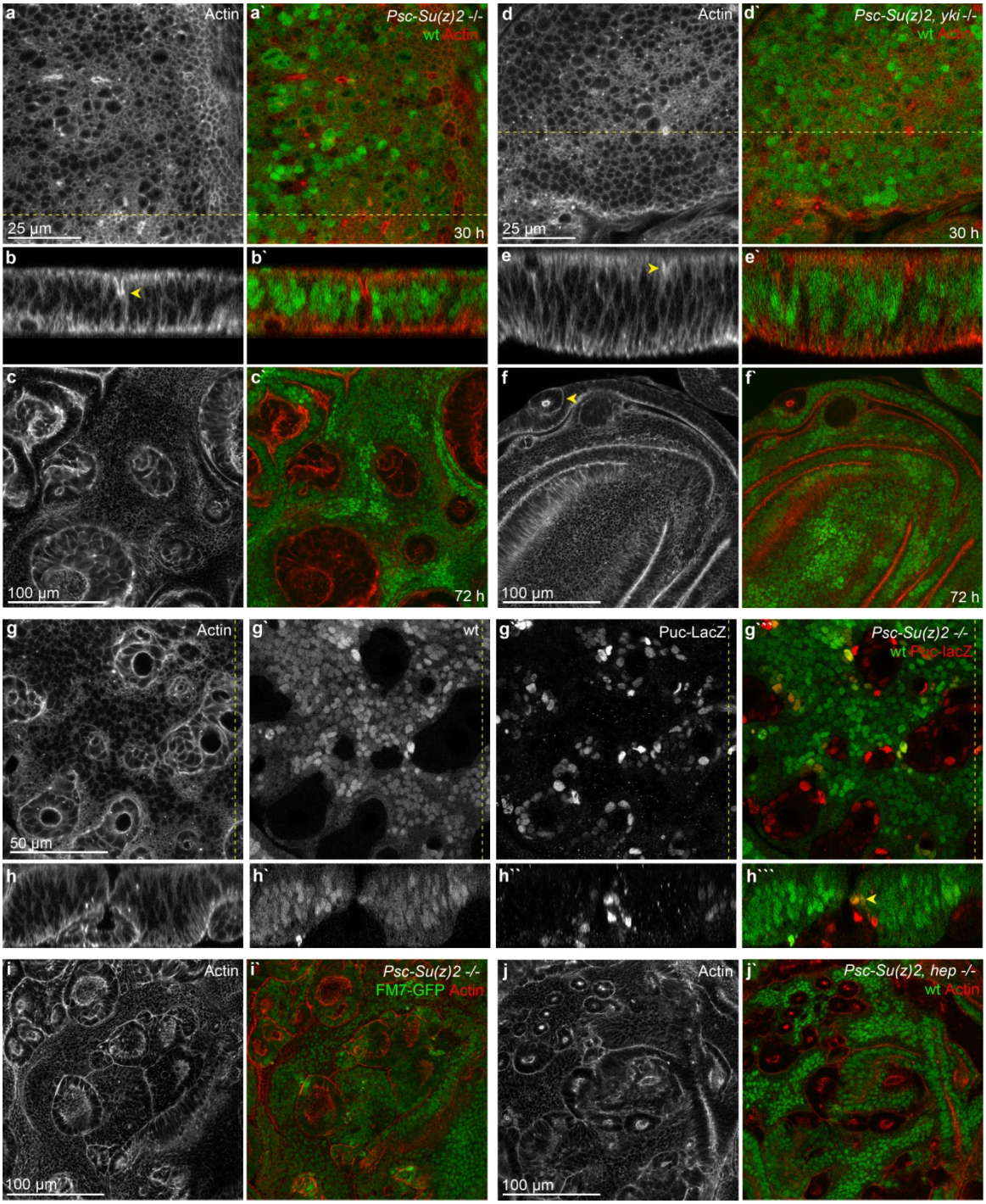

Figure 9: Cyst formation is independent of proliferation and JNK signaling; (a-f) Xy (a, c, d, f) and xz sections (b, e) of wing imaginal disc containing *Psc-Su(z)2*^{1b8} clones (a-c) or *Psc-Su(z)2*^{1b8}, *yki*^{B5} clones (d-f) induced by the FLP/FRT system. Wild-type cells (wt) are marked by GFP (green in a'-f'), mutant clones by absence of GFP. Actin is shown in grey (a-f) or red (a'-f'). Time points 30 h (a, b, d, e) and 72 h (c, f) after clone induction are shown. Arrowheads point to invaginating clones. Dashed yellow lines in (a, e) indicate positions of xz cross-sections shown in (b, e). The *yki*^{B5} allele prevents proliferation and survival of *Psc-Su(z)2*^{1b8} cells, but not invagination and cyst formation (arrowheads in e, f). **(g, h)** Xy (g) and xz (h) section of wing imaginal disc containing *Psc-Su(z)2*^{XL26} clones and Puc-LacZ, a reporter for active JNK signaling (grey in g`, h`, red in g```, h```), which was stained 54 h after clone induction for β-galactosidase expression. Wild-type cells (wt) are marked by GFP (grey in g`, h`, green in g```, h```), clones by absence of GFP. Actin is shown in grey (g). Arrowhead in (h```) is pointing to wt cells with Puc-LacZ staining. Dashed yellow lines in (g) indicate position of xz cross-sections shown in (h). Note the activation of JNK in both mutant and wild-type cells. **(i, j)** Xy sections of wing imaginal disc

containing *Psc -Su(z)2*^{XL26} clones in a FM7-GFP background (i) and *Psc -Su(z)2*^{XL26} clones in a hemizygous *hep*^{R75} background (j) induced by the FLP/FRT system. 3rd instar sibling larvae were dissected. Actin is shown in grey (I, j) or red (i`, j`). Wild-type cells are marked by GFP (green in i`, j`), in (j) mutant clones are marked by absence of GFP. In (i), clonal marker cannot be distinguished from FM7-GFP signal. *hep*^{R75} prevents activation of JNK signaling in imaginal discs, but does not interfere with cyst formation. Scale bars as indicated.

3.1.2 Ectopic expression of unrelated transcription factors leads to position-independent cyst formation

Polycomb proteins execute growth regulatory function through silencing of JAK/STAT or Notch signaling pathways (Classen et al., 2009; Martinez et al., 2009), but Polycomb activity is also important for the regulation of numerous transcription factors involved in cell differentiation (Schuettengruber and Cavalli, 2009). To test whether cell fate misspecification in *Psc-Su(z)2* mutant clones underlies cyst formation, we individually overexpressed cell fate specifying transcription factors silenced by the Polycomb system in wing discs. We used the heat-shock inducible Gal4/UAS flip out system to express transcription factors in small cell patches (clones) (4.1). First, we ectopically expressed the fork head box transcription factor *fork head* (*fkh),* which normally drives salivary gland morphogenesis (Myat et al., 2000). qPCR analysis and RNAseq data (Bunker et al., 2015) revealed a strong upregulation in *Psc-Su(z)2* mutant imaginal discs, supporting the silencing of this transcription factor by the Polycomb system (Table 1). 30 h after induction, *fkh*-expressing clones started to round up and invaginated in contrast to control clones expressing only GFP (Figure 10 a-c, f-h). Similarly to *Psc-Su(z)2* mutant clones, the invagination became more severe at later time points and led to pronounced cysts 54 h after clone induction (Figure 10 d-e, i-j). We continued with the overexpression of two additional genes that were Polycomb regulated (Table 1): the homeobox transcription factor *Abdominal-B* (*Abd-B),* which is involved in segment identity specification (Pearson et al., 2005) and the Runt-domain transcription factor *lozenge (lz)*, required for proper eye development and hemocyte differentiation (Canon and Banerjee, 2000). Both transcription factors were each sufficient to give rise to cysts throughout the entire wing imaginal disc upon overexpression in small patches of cells (Figure 11 a-f).

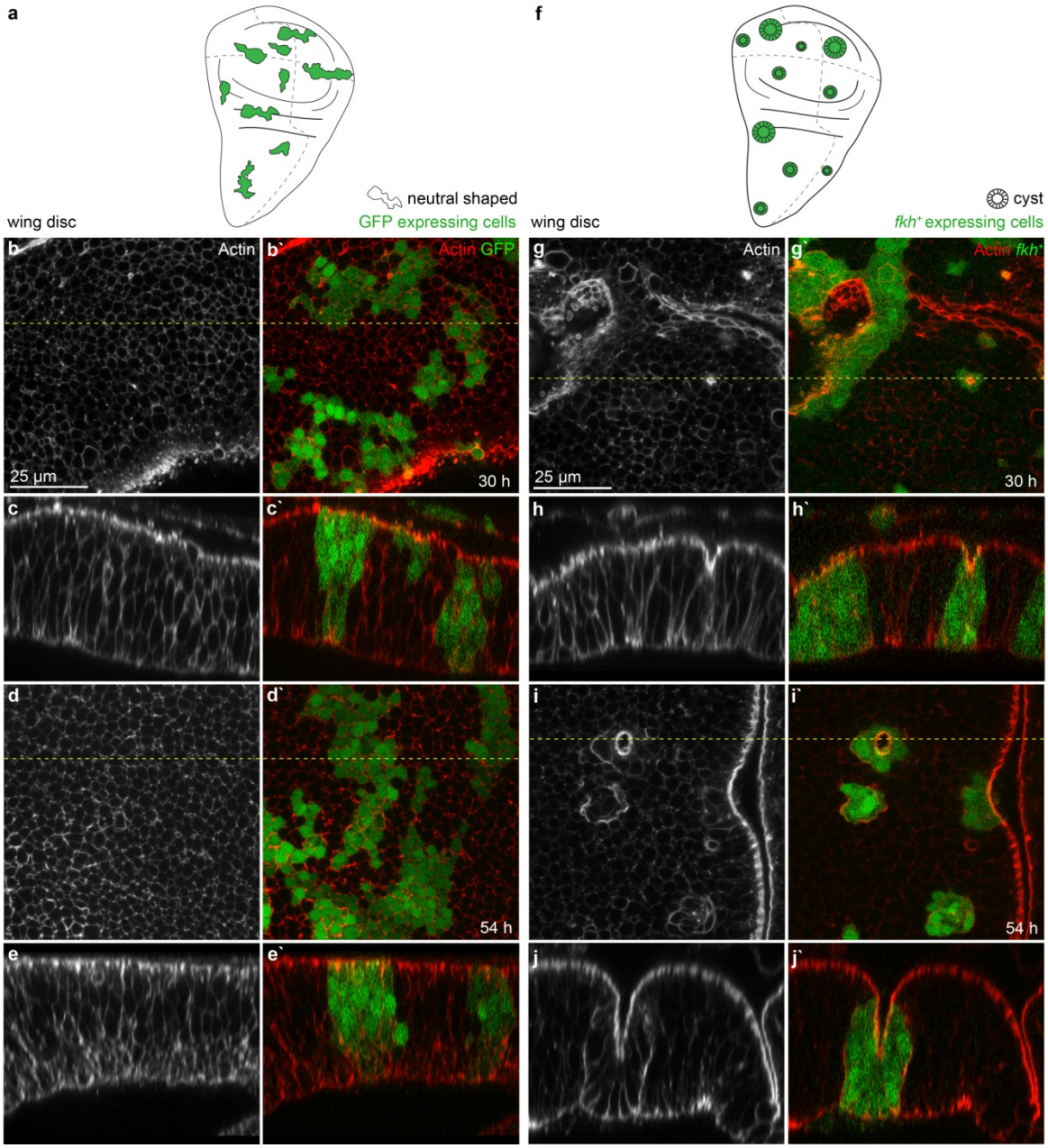

Figure 10: Ectopic expression of *fkh* leads to cyst formation; (a, f) Schematic representation of wing imaginal discs expressing GFP (a) and *fkh* (f) in flip out clones (green). GFP-expressing clones have a neutral shape, whereas *fkh*-expressing clones round up and form cysts at any position within the disc. **(b-e and g-j)** Xy (b, d and g, i) and xz sections (c, e and h, j) of wing pouches expressing GFP (b-e) or *fkh* (g-j) in flip out clones (green in b`-j`) 30 h (b, c and g, h) and 54 h (d, e and i, j) after clone induction using a short heat-shock. Actin is shown in grey (b-j) or red (b`-j`). Dashed yellow lines in (b, d and g, i) indicate positions of xz cross-sections shown in (c, e and h, j). Scale bar as indicated.

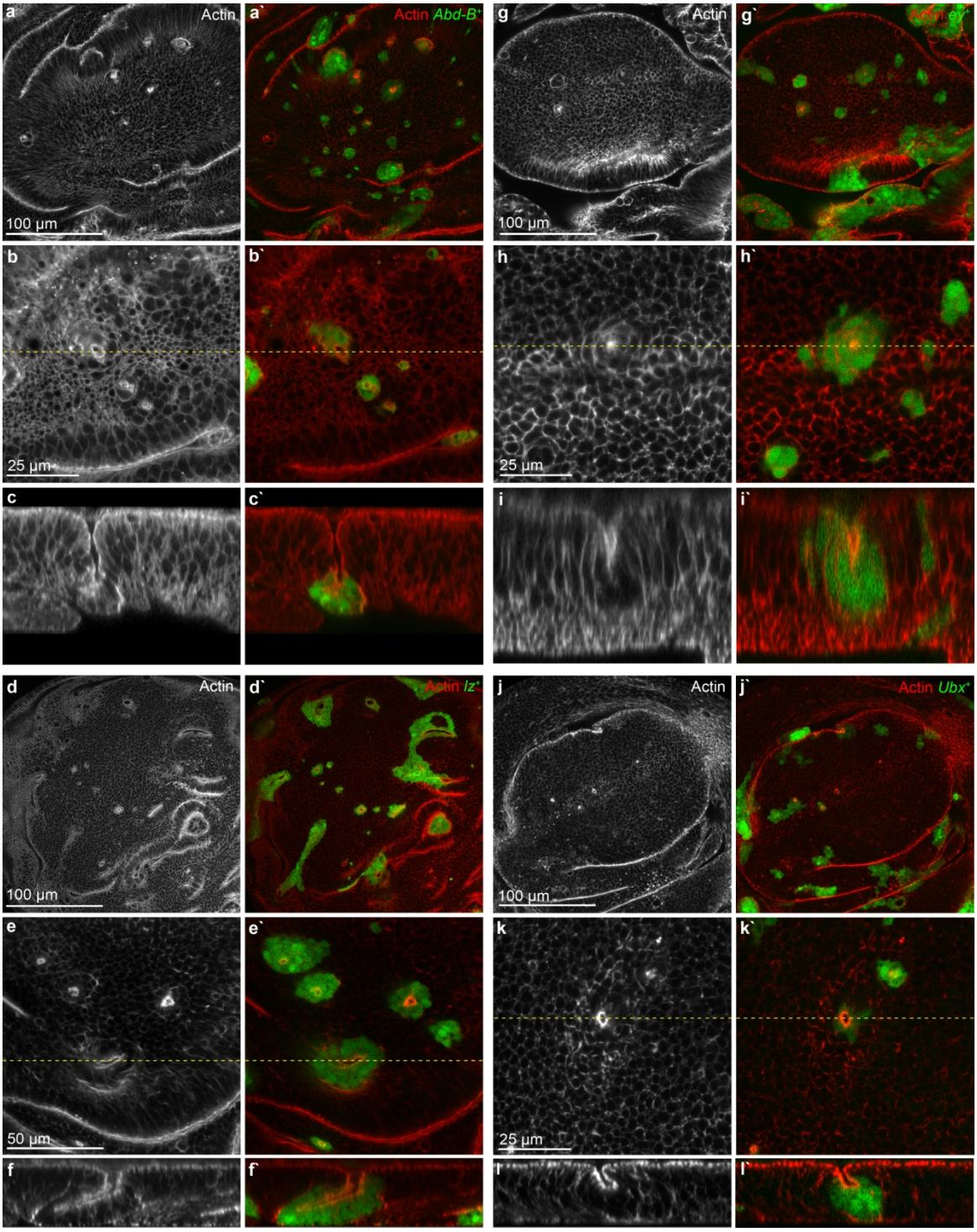

Figure 11: Ectopic expression of unrelated, cell fate specifying transcription factors causes cyst formation; Wing imaginal discs ectopically expressing cell fate specifying transcription factors regulated by Polycomb (a-f) and not regulated by Polycomb (g-l). **(a-l)** Xy sections (a, b, d, e, g, h, j, k) and xz cross-section (c, f, i, l) of wing imaginal discs expressing *Abd-B* (a-c), *lz* (d-f), *ey* (g-i) or *Ubx* (j-l) in flip out clones (green in a`-k`) 54 h after clone induction using a short heat-shock. Actin is shown in grey (a-k) or red in (a`-k`). Xy overviews (a, d, g, j) and higher magnification pictures (b, h, e, k) shown below were not derived from the same disc. Dashed yellow lines in (b, e, h, k) indicate positions of xz cross-sections shown in (c, e, i, l). Scale bars as indicated.

To test if cyst formation is specific to transcription factors silenced by Polycomb, we analyzed additional transcription factors involved in cell fate specification. We ectopically expressed randomly selected transcription factors not de-repressed in *Psc-Su(z)2* mutant wing discs (Table 1). Small clones expressing cell fate specifying transcription factors, such as the Pax6 homologue *eyeless (ey)*, the homeobox transcription factor *Ultrabithorax (Ubx)* (Figure 11 g-l) and the homebox transcription factor *homothorax (hth)* (discussed below, Figure 16 e-h) caused cysts in wing discs as well.

Table 1: RNAseq and qPCR analysis of transcript expression in *Psc-Su(z)2* mutant imaginal discs; **(a)** Fold changes and adjusted p-values (padj) of individual genes analyzed by RNAseq (Bunker et al., 2015) are shown. *Abd-B*, *fkh* and *lz* are transcriptionally upregulated in *Psc-Su(z)2*^{XL26} cells. *ey* shows a slight upregulation. *arm*, *ci*, *hop, Ubx* and *tkv* are not elevated. **(b)** qPCR analysis confirming strong upregulation of *Abd-B* and *fkh* in *Psc-Su(z)2*^{XL26} discs in contrast to *hth*. Fold change and standard deviation (stdv) is shown. Refer to Appendix, Table 12 for more extended data.

a *RNAseq analysis*			**b *qPCR data***		
	Fold change	*padj*		*Fold change*	*stdv*
Abd-B	444.96	1.4E-19	*Abd-B*	1281.55	651.41
fkh	69.60	1.5E-11	*fkh*	5514.40	2289.51
lz	123.74	1.1E-21	*hth*	0.66	0.32
ey	2.46	3.7E-01			
arm	0.80	3.2E-01			
ci	1.68	1.7E-03			
hop	0.78	2.0E-01			
tkv	0.27	1.1E-16			
Ubx	0.85	9.9E-01			

To exclude that cyst formation is only specific to the wing imaginal disc, we also expressed *fkh*, *Abd-B*, *lz*, *ey* and *Ubx* in eye imaginal discs. In the case of *fkh*, *Abd-B*, *lz* and *Ubx* overexpression, we also observed smoothening of clones shapes and cyst formation (Figure 12 a-d, f). Expression of *ey*, a selector gene of eye formation, caused cyst extrusion in wings (Figure 11 g-i), but not in eye imaginal discs (Figure 12 e), where *ey* is endogenously expressed (Quiring et al., 1994). Similarly, rounding and sorting of *hth*. and *Distal-less (Dll)* were previously shown to occur in the leg imaginal disc (Wu and Cohen, 1999). In summary, these results suggest that cyst formation is not restricted to the wing imaginal epithelia.

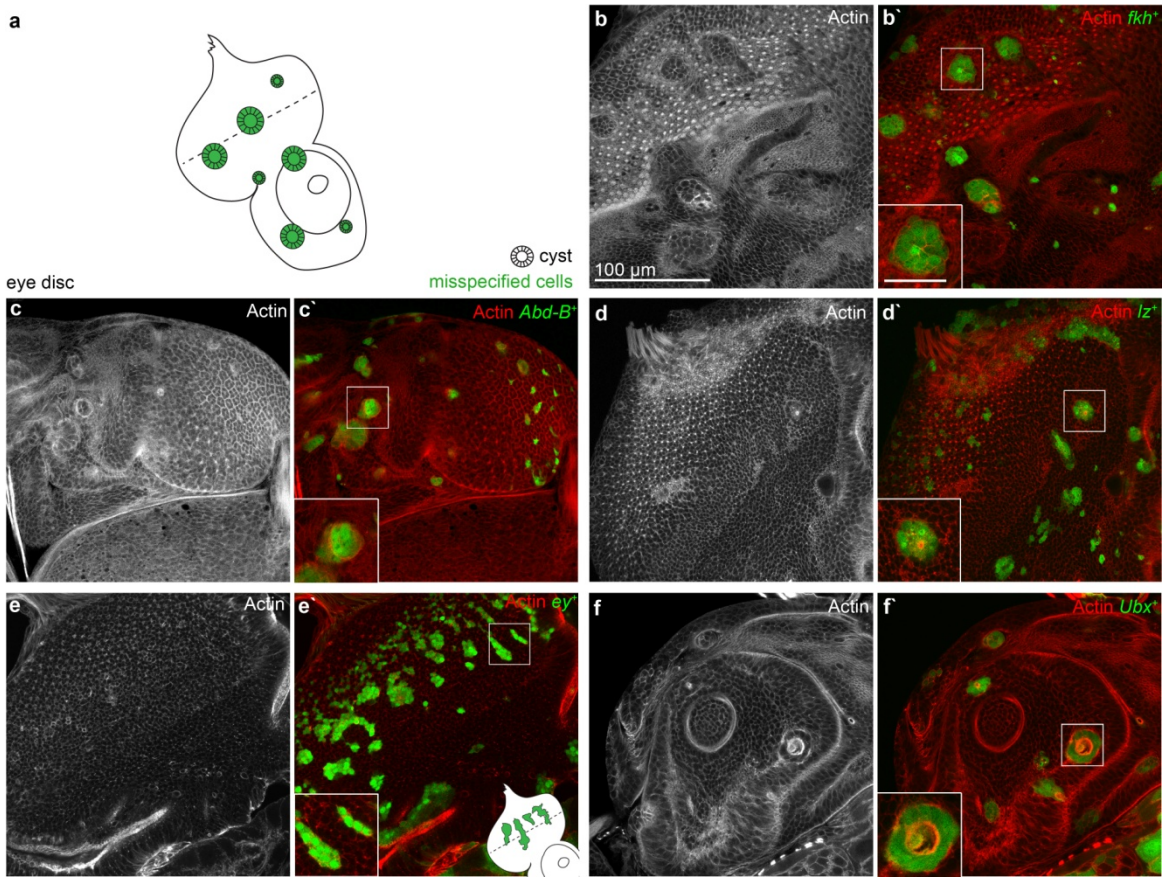

Figure 12: Ectopic expression of cell fate specifying transcription factors causes cysts in the eye disc; (a) Schematic representation of eye imaginal discs expressing a cell fate specifying transcription factor (green, misspecified cells) using a short heat-shock. The misspecified cells invaginate and form cysts. **(b-f)** Xy sections of eye imaginal discs expressing *fkh* (b), *Abd-B* (c), *lz* (d), *ey* (e) and *Ubx* (f) in flip out clones (green in b`-f`) 54 h after clone induction using a short heat-shock. Actin is shown in grey (b-f) or red (b`-f`). Note that *ey*-expressing clones (e`) have a wiggly clone shape resembling wild-type clones represented by little schematic inset in e`. Lower left insets are higher magnifications of framed regions. Scale bar as indicated, scale bar in inset: 25 µm.

3.1.3 Ectopic expression of cytoplasmic proteins or activation of apoptosis is not driving cyst formation

To test if transcription factors not involved in cell fate specification also induce cyst formation, we overexpressed the transcription factor *dMyc*, which is involved in cellular growth but not in cell fate specification (Johnston et al., 1999). Clonal overexpression did not lead to cyst formation, instead clones retained a normal columnar cell shape (Figure 13 a, b). Additionally, ectopic expression of proteins that have a cytoplasmic instead of nuclear functions, like the muscle-specific sarcomer protein *flightin (fln)* (Vigoreaux et al., 1993), did not give rise to cysts (Figure 13 c, d). These results highlight the necessity for ectopic activity of cell fate specifying transcription factors to induce cysts.

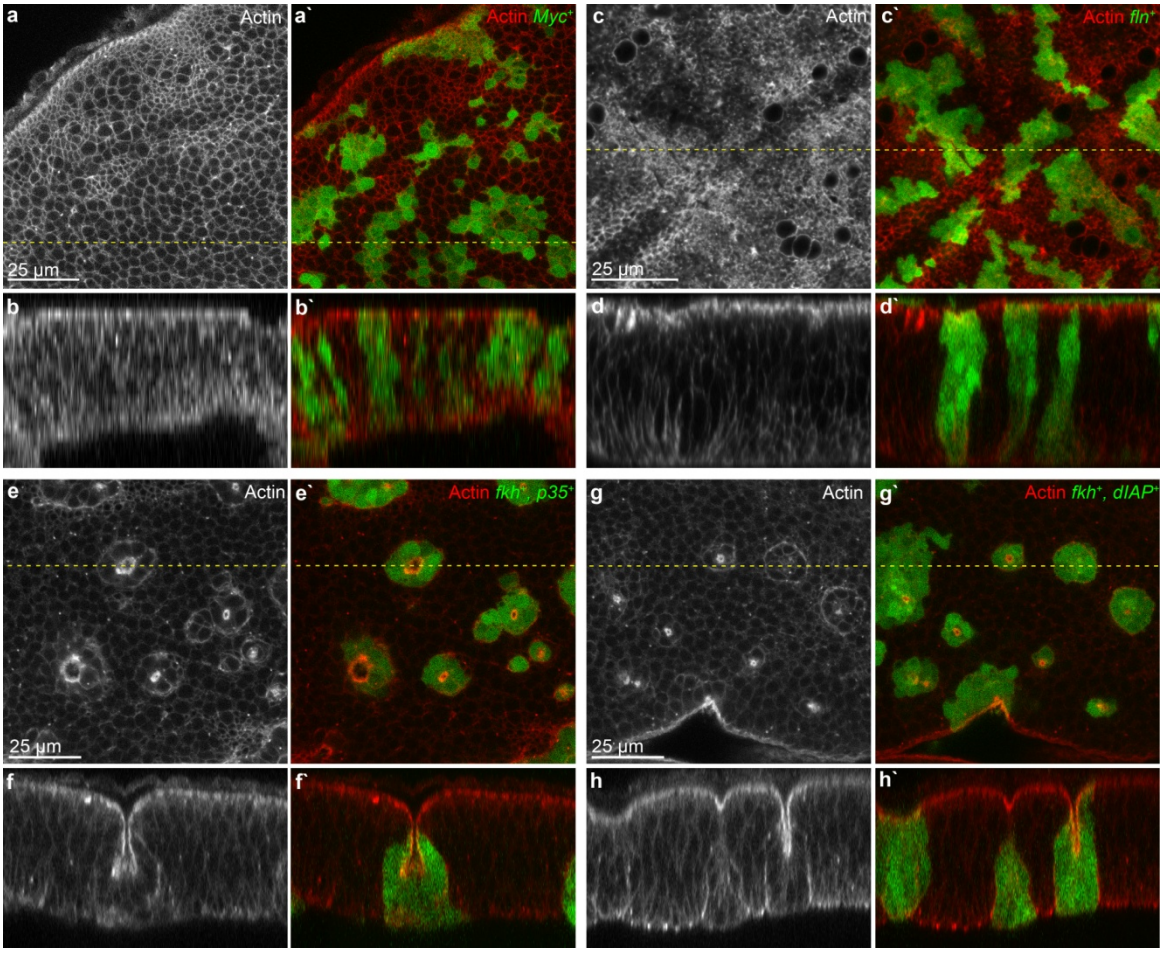

Figure 13: Ectopic expression of cytoplasmic proteins or activation of apoptosis does not cause cysts; Xy (a, c, e, g) and xz sections (b, d, f, h) of wing imaginal disc pouches expressing *Myc* (a, b), *fln* (c, d), *fkh, p35* (e, f) and *fkh, dIAP* (g, h) in flip out clones (green in a`-h`) 54 h after clone induction using a short heat-shock. Actin is shown in grey (a-h) or red (a`-h`). Dashed yellow lines in (a, c, e, g) indicate positions of xz cross-sections shown in (b, d, f, h). Scale bar as indicated. Overexpression of a growth promoting factor (Myc) or cytoplasmic protein (Fln) do not induce cyst formation, whereas blocking apoptosis is not sufficient to prevent cyst formation.

Previously, apoptosis has been reported to cause apical constriction and basal extrusion (Marinari et al., 2012), as well as fold formation in imaginal discs (Manjon et al., 2007). We therefore wanted to understand a possible role for apoptosis in the upstream regulation of cyst formation and tested whether inhibiting apoptosis could interfere with cyst formation. However, neither overexpression of viral anti-apoptotic *p35* nor *death-associated inhibitor of apoptosis 1 (dIAP)* (Figure 13 e-h) prevented cyst formation in *fkh*-expressing clones, suggesting that apoptosis is not the driving force of the observed cell shape changes.

In summary, these observations suggest that activation of ectopic transcription factors associated with cell fate specification underlies cyst formation in imaginal discs independent of Polycomb regulation or induction of apoptosis. Since we could show that the overexpression of several unrelated transcription factors leads to an identical phenotype, we suggest that the underlying cellular mechanism inducing cyst formation must be of very general nature.

3.1.4 Ectopic activation of several signaling pathways leads to position-dependent cyst formation

Psc-Su(z)2 mutant clones, or clones expressing the transcription factors investigated above, formed cysts independent of position within the wing disc (Figure 10 f). Importantly, none of these transcription factors are endogenously expressed in wing imaginal discs at the stage analyzed. We, therefore, wanted to analyze transcription factors that are expressed endogenously in the wing imaginal disc, but in a spatially defined manner. To this end, we analyze the conserved developmental patterning pathways Hh or JAK/STAT (Arbouzova and Zeidler, 2006; Tabata and Takei, 2004), which both show a very specific and highly regulated spatial pattern within the wing imaginal disc (Ayala-Camargo et al., 2013) (1.3.4) (Figure 14 a, g). We introduced clones in wing imaginal disc, that expressed the downstream transcription factor *cubitus interruptus (ci)* of Hh signaling and a dominant-active JAK ($hop^{tum\text{-}L}$), which is rate-limiting for the activation of the transcription factor STAT (Zoranovic et al., 2013). We found that *ci*-expressing clones maintained normal epithelial shapes in the anterior compartment, where Hh signaling is normally high. However, *ci*-expressing clones formed cysts in the posterior compartment, where repression of *ci* normally prevents Hh signaling (Figure 14 a-f) (Morata, 2001). Likewise, activation of STAT induced invagination of clones only in pouch and notum regions of the wing disc, where JAK/STAT signaling is normally low (Figure 14 g-l).

It had been reported previously that Wg or Dpp mutant clones or clones ectopically activating these signaling pathways give rise to cysts dependent on their position within endogenous Wg or Dpp signaling gradients (Gibson and Perrimon, 2005; Shen and Dahmann, 2005; Widmann and Dahmann, 2009a, b; Zimmerman et al., 2010). We were able to recapitulate these results by the clonal expression of a constitutive active version of the Wg transcription factor *armadillo (arm)* (Pai et al., 1997). Cyst formation was observed in the periphery of the wing pouch, but not along the DV boundary, where the endogenous Wg signaling is very high (1.3.4) (Figure 15 a-f). In order to ectopically activate Dpp signaling, we expressed a constitutively active construct of the receptor *thickveins (tkv)* (Nellen et al., 1996). Similarly, we detected cysts only in regions of low Dpp signaling activity in the periphery of the wing imaginal disc, but not in close proximity to the AP boundary (1.3.4) (Figure 15 g-k). Previous reports showed activation of downstream transcription factors of these pathways is responsible for manifestation of the phenotype (Shen et al., 2010; Widmann and Dahmann, 2009a, b). This is in accordance with our findings that only cell fate specifying transcription factors induced cyst formation when ectopically expressed.

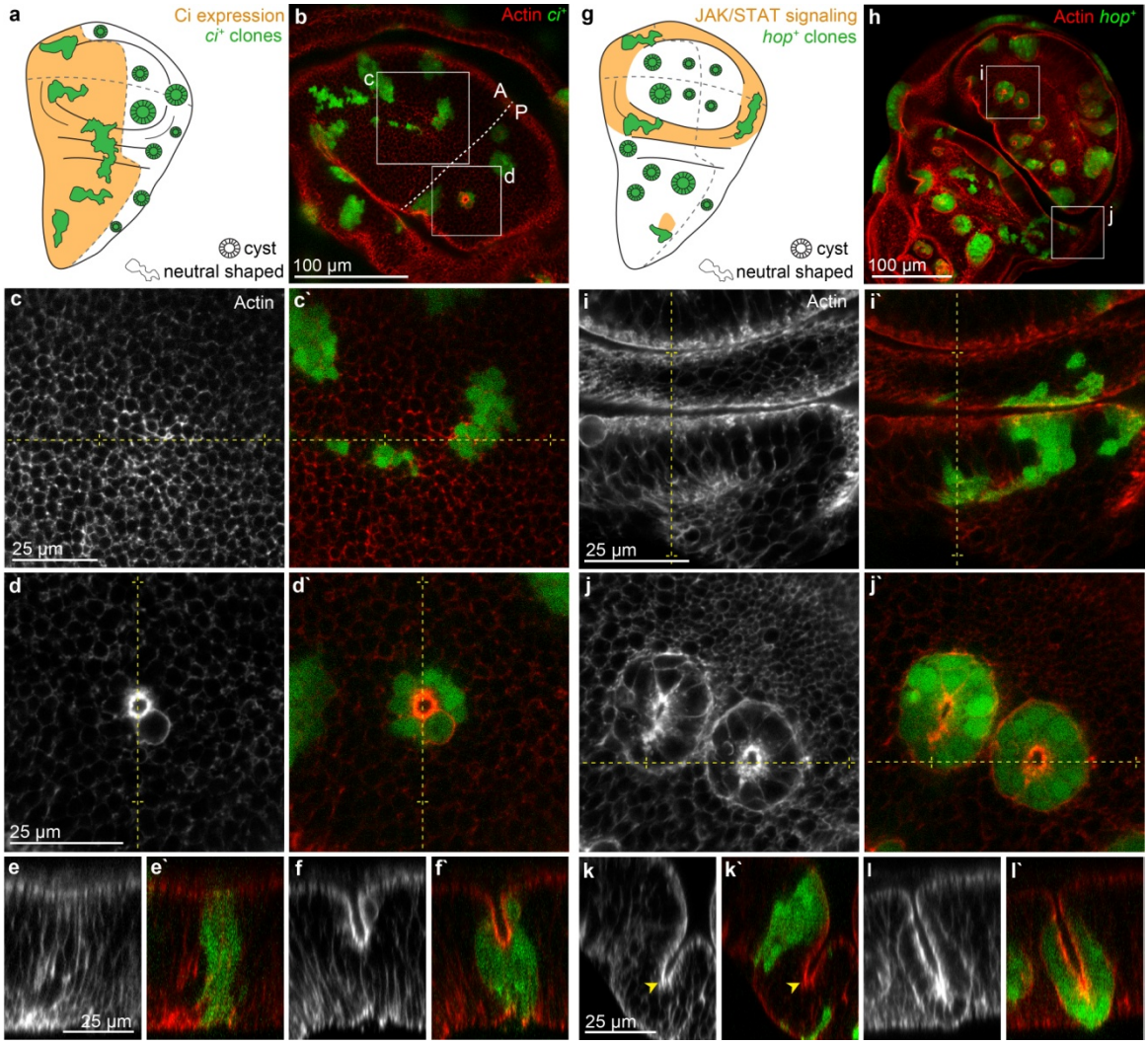

Figure 14: Position-dependent cyst formation within Hh/Ci and JAK/STAT patterning fields; (a, g) Schematic representation of wing imaginal discs with endogenous Hh/Ci (a) and JAK/STAT (g) signaling (orange). *ci* and *hop*-expressing flip out clones are indicated in green. Cysts are only formed in regions where the respective endogenous signaling is low. **(b-f and h-k)** Xy (b-d and h-j) and xz sections (e, f and k, l) of wing imaginal discs expressing *ci* (a-f) *or hop (*g-l) in flip out clones (green in b, c`-f` and h, i`-l`) 54 h after clone induction using a short heat-shock. Actin is shown in grey (c-l) or red in (b, c`-f` and h, i`-l`). Boxes in (b and h) frame regions shown at higher magnification in (c, d and i, j). Dashed yellow lines in (c, d and l, j) indicate positions of xz cross-sections shown in (e, f and k, l). Scale bar as indicated. *Contributions: Experiment and image generation: Vanessa Weichselberger.*

Previous studies suggested that Dpp or Wg signaling directly regulates cell shape and, specifically, columnar cell height. Following this interpretation, signaling-compromised cell clusters would form cysts because of cell-autonomous shape changes that depend on Dpp or Wg signaling. Because of our observations, we want to put forward a much more general interpretation, where misregulation of cell fate specification in general is a driving force for cell shape changes, rather than a specific role for individual signaling pathways in regulating cell height.

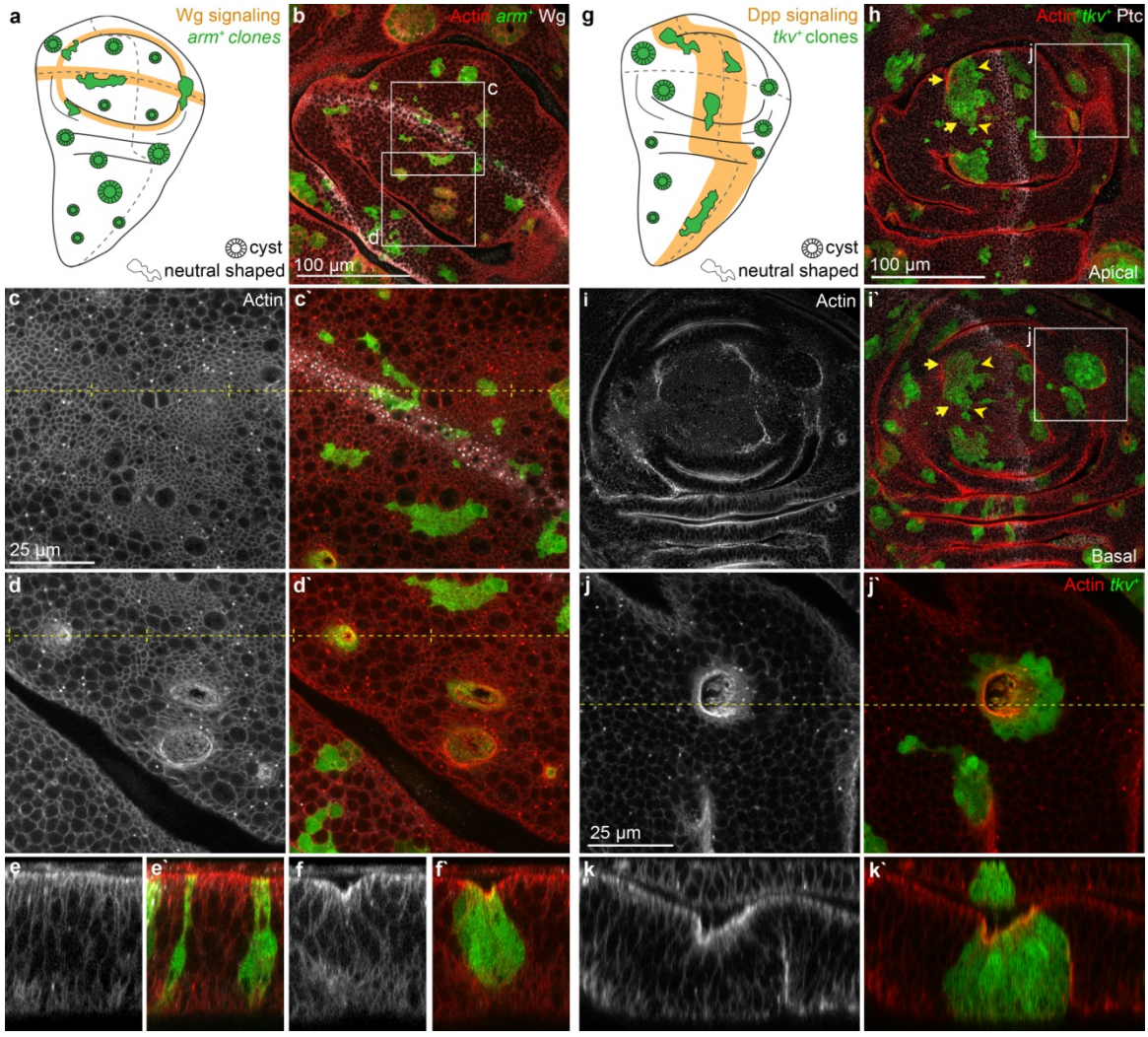

Figure 15: Position-dependent cyst formation within Wg and Dpp signaling patterning fields; (a, g) Schematic representation of wing imaginal discs with endogenous Wg (a) and Dpp (g) signaling (orange). *arm* and *tkv*-expressing flip out clones are indicated in green. Cysts only form in regions where the respective endogenous signaling is low. **(b-f and h-k)** Xy (b-d and h-j) and xz cross-sections (e, f and k) of wing imaginal discs expressing *arm* (a-f) or *tkv (*g-l) in flip out clones (green in b, c`-f` and h, i`-k`) 54 h after clone induction using a short heat-shock. Actin is shown in grey (c-l) or red in (b, c`-f` and h, i`-k`). Boxes in (b and h) frame regions shown at higher magnification in (c, d and j). Dashed yellow lines in (c, d and j) indicate positions of xz cross-sections shown in (e, f and k). For wing disc with *tkv*-clones, an apical (h) and basal (i) section is shown. Yellow arrows indicate smoothening of clone borders outside of the Dpp signaling area (orange in a). The same clone shows wiggly borders on side facing the Dpp signaling area (yellow arrowheads). Scale bar as indicated. *Contributions: Experiment and image generation: Vanessa Weichselberger.*

Our hypothesis of generality was supported by additional experiments where misspecification within other developmentally patterned tissue domains caused position-dependent cyst formation. *vestigial (vg)*-expressing clones gave rise to cysts in the hinge and notum region, where *vg* expression driving wing blade specification is normally low (Figure 16 a-d) (Liu et al., 2000; Widmann and Dahmann, 2009b). Expression of *ey*, a selector gene of eye formation caused cyst extrusion in wings but not in eye imaginal discs (compare Figure 11 g-i and

Figure 12 e). Expression of *hth* generated smoothening and invagination only in the pouch, but not in the hinge that normally expresses *hth* (Figure 16 e-h) (Azpiazu and Morata, 2000).

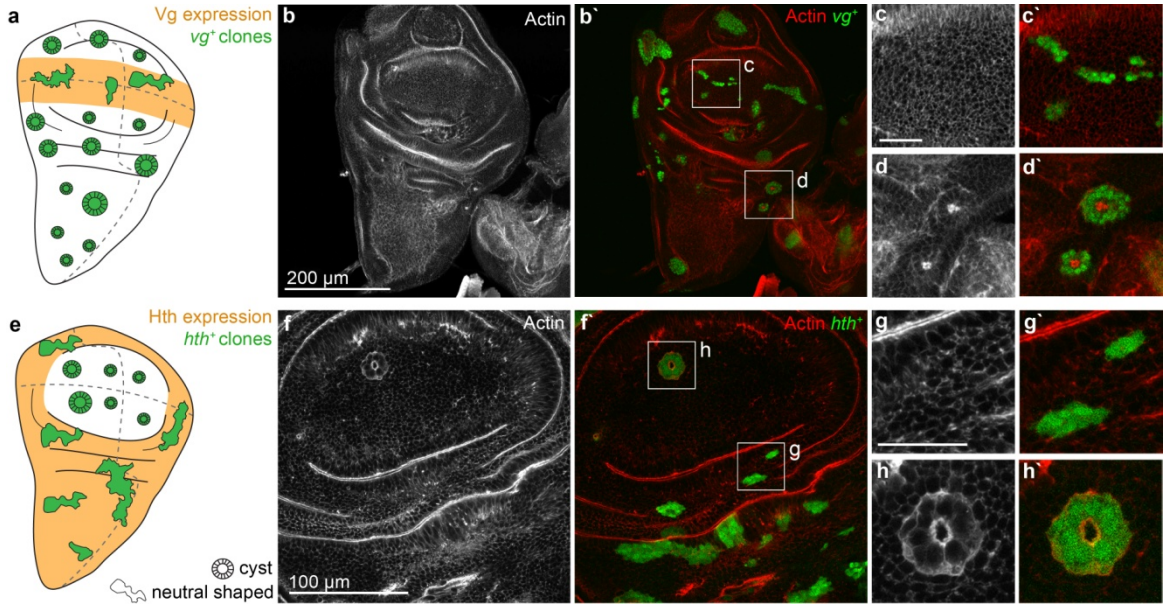

Figure 16: Position-dependent cyst formation in the context of Vg and Hth expression; (a, e) Schematic representation of wing imaginal discs with endogenous Vg (a) and Hth (e) expression (orange). *vg* and *hth*-expressing flip out clones are indicated in green. Cysts are only formed in regions where the respective endogenous expression is low **(b-e and f-h)** Xy section of wing imaginal disc expressing *vg* (b-d) or *hth* (f-h) in flip out clones (green in b`-h`) 54 h after clone induction using a short heat-shock. Actin is shown in grey (b-h) or red (b`-h`). Boxes in (b` and f`) frame regions shown at higher magnification in (c, d and g, h). Scale bar as indicated, scale bar in insets represents 25 µm.

In addition, ectopic expression or mutation of other endogenously patterned transcription factors, such as *Iro-C*, *salm* and *omb* in the wing imaginal disc, have been previously described to cause round invagination phenotypes dependent on location within the endogenous expression domain. In the case of mutations, cysts have been observed in high endogenous expression domains, whereas clonal overexpression leads to cyst formation in domains of low expression (Organista and De Celis, 2013; Shen et al., 2010; Villa-Cuesta et al., 2007). While a detailed cellular description of clone invagination is missing in these studies, several hallmarks of cyst formation, including rounding, clone sorting, and extrusion were often observed. An overview of transcription factors analyzed by us or studies observing similar position-dependent and independent phenotypes is shown in Table 2 and emphasizes the generality of cyst formation as an epithelial response to the presence of aberrantly patterned cells.

Collectively, these observations emphasize that initiation of cyst formation in imaginal discs represents a very general response to cell fate misspecification and seems to be driven by relative fate differences between misspecified and surrounding wild-type tissue in the respective patterning field.

Table 2: Overview of transcription factors or signaling pathways analyzed in this or other studies showing cysts or cyst-related phenotypes upon clonal misregulation; Transcription factors (TF) or signaling pathways as well as the TF-family, the respective study, the analyzed tissue and the phenotypical description of clone appearance within this study are listed. Table also includes studies, in which clone shape was not described, but cystic hallmarks can be identified in published figures (stated in italic). Note that table might not be complete and includes only studies to our knowledge. WID = wing imaginal disc, EID = eye imaginal disc, LID=leg imaginal disc, NE = neuroepithelium

TF /signaling pathway	***TF-family***	***tested in***	***tissue***	***Clonal phenotype***
Abdominal-B	Homeobox domain	this study	WID, EID	Cysts
Wg signaling *armadillo*	β-catenin	this study	WID	Cysts
		(Widmann and Dahmann, 2009b; Zimmerman et al., 2010)	WID	Cysts, round, smooth, apical constricted, invagination
Hh signaling *cubitus interruptus*	Zinc finger	this study	WID	Cysts
		(Worley et al., 2013)	WID	Round, smooth
defective proventriculus	Homeobox domain	(Terriente et al., 2008)	WID	Round, smooth
Distal-less	Homeobox domain	(Wu and Cohen, 1999)	LID	Sorting out, vesicles
Dorsocross	T-box	(Sui et al., 2012)	WID	Basal retraction, actin ring, fold
Dpp signaling		this study (*tkv*)	WID	Cysts
		(Gibson and Perrimon, 2005; Shen and Dahmann, 2005; Widmann and Dahmann, 2009a)	WID	Apical retracted, basal extrusion, cyst-like structure, constriction, invagination
engrailed	Homeobox domain	(Herrera and Morata, 2014)	WID	*Round*
eyegone	paired domain and homedomain	(Aldaz et al., 2005)	WID	*Round*
eyeless	paired domain and homedomain	this study	WID, EID	Cysts in WID
fork head	forkhead box	this study	WID, EID	Cysts
homothorax	Meis homeobox	this study	WID	Cysts
		(Azpiazu and Morata, 2000; Wu and Cohen, 2000)	WID, LID	Sorting out
iroquois complex	Homeobox domain	(Villa-Cuesta et al., 2007)	WID	Invagination, apical-basal shortening
JAK-STAT signaling		this study (*hop*)	WID	Cysts
lozenge	Runt domain	this study	WID	Cysts
Notch, Mef2	MADS-box	(Pallavi et al., 2012)		Protrusion, round
Optomotor-blind	T-box	(Shen et al., 2010)	WID	Rounding, apical indentation, basal clone retraction
Optix	Homeobox domain	(Gold and Brand, 2014)	NE	Round, rosette, apical constriction
Polycomb		this study (*Psc-Su(z)2*)	WID	cysts

		(Beuchle et al., 2001; Gandille et al., 2010)	WID	Smooth, cyst-like, round
RTK signaling		this study (*Ras*)	WID	Cysts
		(Bell and Thompson, 2014; Prober and Edgar, 2000; Worley et al., 2013)	WID	Cysts, round, smooth
spalt	Zinc finger	(Organista and De Celis, 2013)	WID	Folds, clone extrusion
teashirt	Zinc finger	(Azpiazu and Morata, 2000; Wu and Cohen, 2000)	WID, LID	Round, sorting out
tiptop	Zinc finger	(Bessa et al., 2009)	ID	*Round*
Ultrabithorax	Homeobox domain	this study	WID, EID	Cysts
vestigial	TDU repeat	this study	WID	Cysts
		(Azpiazu and Morata, 2000; Liu et al., 2000; Widmann and Dahmann, 2009b)	WID	Round, smooth, invagination
Hippo signaling				
yorkie	Cofactor	(Worley et al., 2013)	WID	Round, smooth
Zinc finger homedomain-2	Zinc finger Homeobox domain	(Perea et al., 2013)	WID	*Round*

3.2 Cyst formation is a cell non-autonomous process

We wanted to investigate how cysts form and why they appear as a general response upon induction of misspecified cells. Therefore, we asked if cyst formation is a cell-autonomous process, where misspecified cells themselves induce the observed cell shape changes due to downstream effects of transcription factors on epithelial architecture. This was suggested in previous reports, where Dpp or Wg signaling mutant cells adopt a columnar cell shape in a cell-autonomous manner (Widmann and Dahmann, 2009a, b).

To easily examine autonomous cell shape changes, we aimed to increase the area occupied by misspecified cells. By extending the length of heat shock that induces the Gal4/UAS flip out system, we generated imaginal discs where the majority of cells overexpressed *fkh* and where only small clones of wild-type cells remained. Strikingly, wild-type clones exhibited smoothening and they retracted from the apical epithelial surface early on after clone induction when compared to control discs only expressing GFP in response to long heat-shock conditions (Figure 17 a-h). At later time points, wild-type cell clusters gave rise to prominent cysts in contrast to surrounding *fkh*-expressing cells, where epithelial architecture was not perturbed (Figure 17 i).

For convenience, cysts that formed from wild-type cells surrounded by misspecified ones will be referred to as inverse cysts in the following text. Inverse cyst formation of small wild-type clones in the wing imaginal disc could also be induced by overexpression of other transcription

factor, such as *AbdB, Ubx* and *ey* (Figure 17 k-l). Furthermore, the effect was not restricted to wing imaginal discs, since inverse cysts could also be observed in the eye imaginal discs when *fkh*, *Abd-B* and *Ubx* were overexpressed in large domains (Figure 18 b, c, e). Similar to our previous results, where clonal *ey* overexpression in the eye disc did not lead to cysts (Figure 12 e), broad overexpression of *ey* neither induced strong smoothening nor invagination of wild-type clones, likely due to endogenous *ey* expression (Figure 18 d). We were also interested in examining transcription factors, where we had observed position-dependent cyst formation in short heat-shock experiments (Figure 14, Figure 15, Figure 16). To do so, we broadly overexpressed *ci* and, importantly, observed inverse cysts, too. However, in accordance with our previous observations (Figure 14 a-f), inverse cysts only formed in the posterior wing compartment, where Hh signaling is normally low, whereas wild-type clones retained their normal shaped in the anterior compartment (Figure 18 f-k). In addition to our results, similar observations have been reported for *Omb* and *Iro-C* previously (Shen et al., 2010; Villa-Cuesta et al., 2007), thereby supporting the generality of our observations.

In summary, our results strongly indicate that cyst formation is not driven cell-autonomously by misspecified cells, since wild-type cells can also undergo the same process. Instead, cyst formation must depend on a cell non-autonomous process, where the apposition of differently fated cell populations acts as the signal to induce cyst formation. (Compare Figure 10 f to Figure 17 e, Figure 12 a to Figure 18 a and Figure 14 a to Figure 18 f).

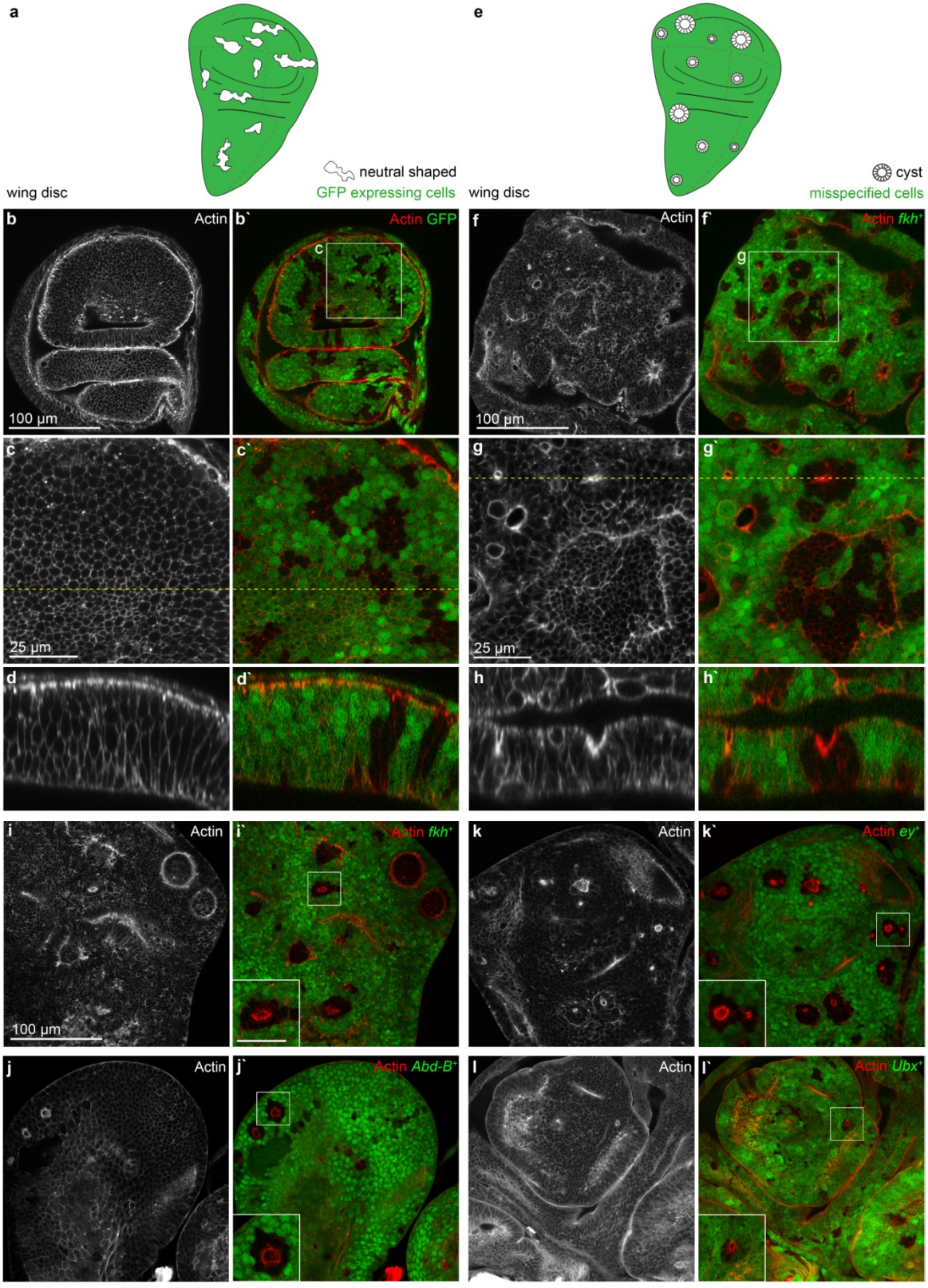

Figure 17: Cyst formation is cell non-autonomous; (a, e) Schematic representation of wing imaginal discs broadly expressing GFP (a, green) and a cell fate specifying transcription factor (e, green, misspecified cells) in flip out clones using a long heat-shock leading to few interspersed wild-type cell clusters (white). Whereas wild-type cell clusters retain a neutral shape if surrounded by GFP-expressing wild-type cells, they invaginate and form cysts if surrounded by *fkh*-expressing cells. **(b-d and f-h)** Xy section (a,c and f, g) and xz cross-section (d, h) of wing imaginal discs expressing GFP (b-d) or *fkh* (f-h) in flip out clones (green in b`-h`) 30 h after clone

induction using a long heat-shock. Actin is shown in grey (b-h) or red in (b`-h`). Boxes in (b, f) frame regions shown at higher magnification in (c, g). Dashed yellow lines in (c, g) indicate positions of xz cross-sections shown in (d, h). **(i-l)** Xy sections of wing imaginal discs expressing *fkh* (i), *Abd-B* (j), *ey* (k) or *Ubx* (l) in flip out clones (green in i`-l`) 54 h after clone induction using a long heat-shock. Actin is shown in grey (i-l) or red in (i`-l`). Lower left insets are higher magnifications of framed regions. **(b-l)** Scale bar as indicated, scale bar in insets represents 25 µm.

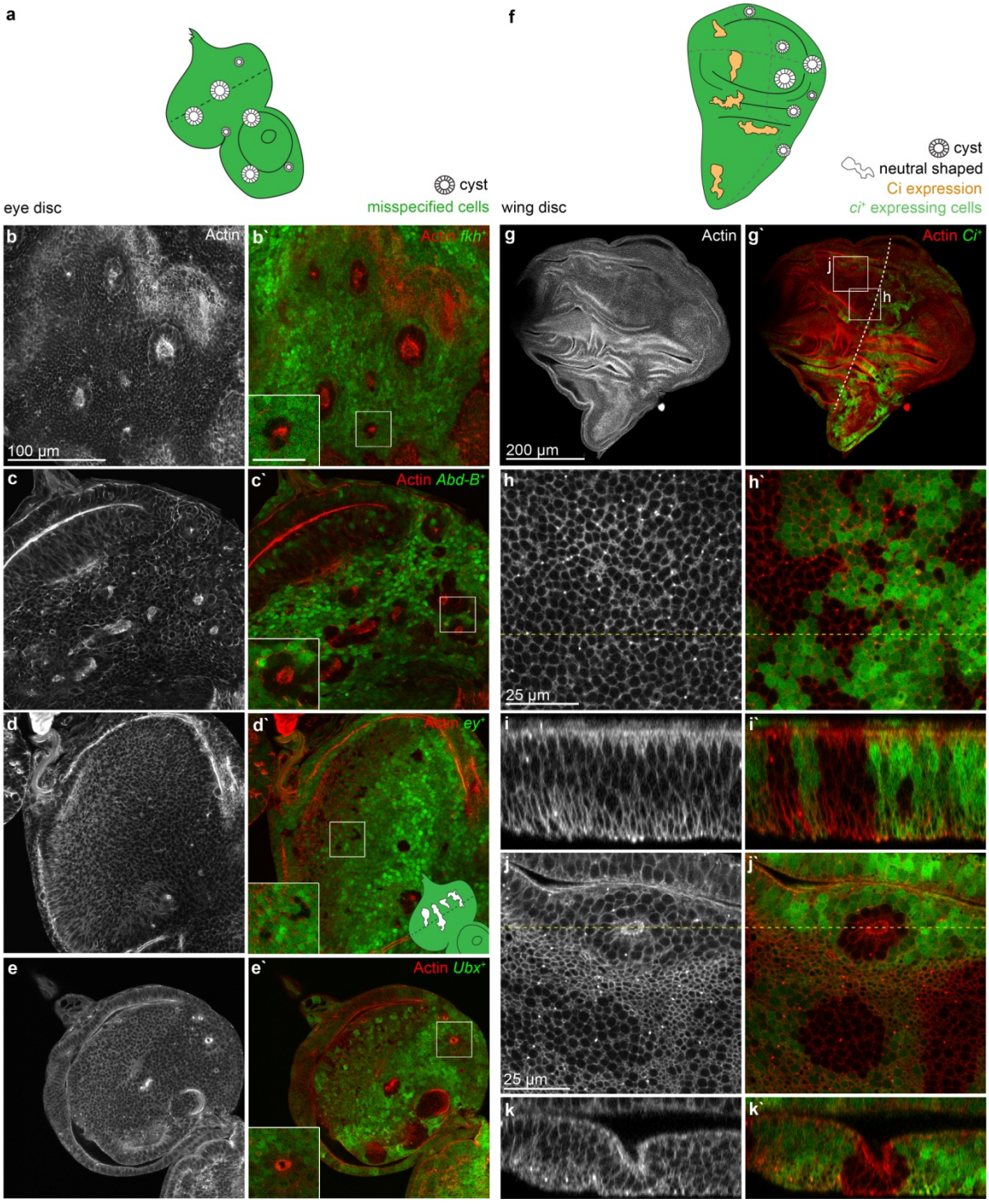

Figure 18: Inverse cysts also form in the eye disc and depend on position within a patterning field; (a) Schematic representation of eye imaginal discs broadly expressing a cell fate specifying transcription factor (green, misspecified cells) in flip out clones using a long heat-shock leading to few interspersed wild-type cell clusters (white). The wild-type clusters invaginate and form cysts. **(b-e)** Xy section of eye imaginal discs expressing *fkh* (b), *Abd-B* (c), *ey* (d) or *Ubx*

(e) in flip out clones (green in b`-e`) 54 h after clone induction using a long heat-shock. Actin is shown in grey (b-e) or red in (b`-e`). Lower left insets are higher magnifications of framed regions. Note that *ey*-expressing clones have a wiggly clone shape resembling wild-type clones represented by little schematic inset in c. **(f)** Schematic representation of wing imaginal discs broadly expressing *ci* (green) in flip out clones using a long heat-shock leading to few interspersed wild-type cell clusters. Cysts are only formed in the posterior compartment, where the endogenous Ci signaling (orange) is low. **(g-k)** Xy (g, h, j) and xz cross-sections (i, k) of wing imaginal discs expressing *ci* in flip out clones (green in g`-k`) 54 h after clone induction using a long heat-shock. Actin is shown in grey (g-k) or red in (g`-k`). Boxes in (g`) frame regions shown in higher magnification in (h, j). Dashed yellow lines in (h, j) indicate positions of xz cross-sections shown in (i, k). **(b-k)** Scale bar as indicated, scale bar in insets represents 25 µm. *Contributions: Experiment and image generation g-k: Vanessa Weichselberger.*

3.3 Cyst formation correlates with accumulation of contractility markers at the MWI

3.3.1 Cell polarity is not altered in cysts and at the MWI

From our previous experiments, we reasoned that cysts must form by mechanisms acting at the interface between misspecified and wild-type cells (MWI). We first aimed to understand the molecular signature of the MWI and, therefore, analyzed the localization of different cell polarity and adhesion markers at apical, adherens junctions or basolateral cell surfaces. We stained wing imaginal discs containing *Psc-Su(z)2* mutant cysts for the apical marker aPKC, the adherens junction protein E-cad and the basolateral component Cora (Figure 19). We were not able to detect any changes neither at the MWI nor in the invaginating *Psc-Su(z)2* mutant clone itself, when compared to marker localization and intensities in surrounding wild-type tissue. This result was reproducible for earlier or later time points after clone induction, additional adhesion and cell polarity markers (e.g. Sdt, Arm and α-cat), as well as upon analysis in *fkh*-expressing rather than *Psc-Su(z)2* mutant cysts (data not shown).

In summary, this suggests that cell polarity or adhesion is not obviously altered at the MWI or within cyst forming cells and, therefore, cell adhesion and polarity changes may not account for observed cell shape changes occurring during cyst formation.

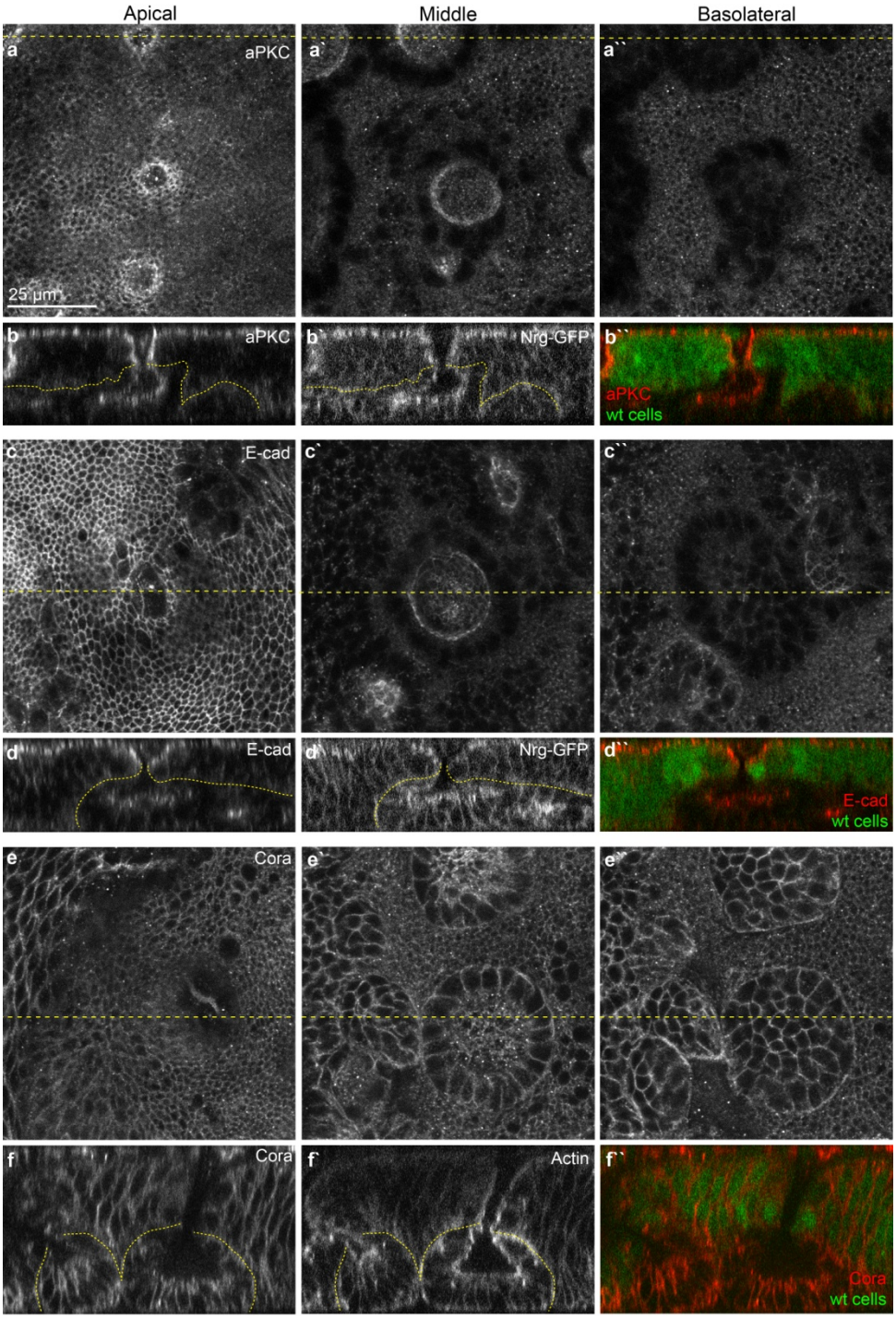

Figure 19: Cell polarity and adhesion markers are not changed in *Psc-Su(z)2* mutant cysts; Pouch regions of wing imaginal discs mosaic for *Psc-Su(z)2*^{XL26} after 54 h of clone induction stained for the apical marker aPKC (a,b), the adherens junction protein E-cad (c, d) and the lateral marker Cora (e-f) are shown. An apical (a, c, e), middle (a`, c`, e`) and basolateral xy section (a``, c``, e``) are displayed. Xz cross-section of polarity or adhesion marker, (b, d, f), a cell outline marker (b`, d`, f`) and the merge of adhesion and polarity marker (red) and clonal marker (wt cells, green) are shown. Dashed yellow lines in xy sections indicate positions of xz cross-section. Dashed yellow lines b, d, f indicate clone borders. Scale bar as indicated. *Contributions: Experiment and image generation e-f: Hannelore Hartmann.*

3.3.2 Actin is enriched at the MWI

In addition to cell polarity and adhesion markers, we had a closer look at the organization of the cellular cytoskeleton during cyst formation. We first focused on describing actin localization and intensities within cysts, at the MWI and the surrounding tissue. First of all, we observed prominent actin enrichment at apical surfaces in misspecified as well as inverse cysts, specifically in the invaginating cells at the center of the clone early after clone induction (Figure 20, compare blue and yellow arrows). We did not observe this accumulation before the onset of invagination and at later stages when the apical surface had expanded again into an apical cyst lumen (data not shown, Figure 8 d-f). Because of these observations, we interpreted the changes in apical actin in invaginating cells as consequences of apical surface constriction that happens early during cyst formation (Figure 8 c`, h). The decrease of apical surface area during this process could lead to increased local actin concentration. We therefore suggest that the actin accumulation observed in invaginating cells is likely to be a secondary effect of invagination.

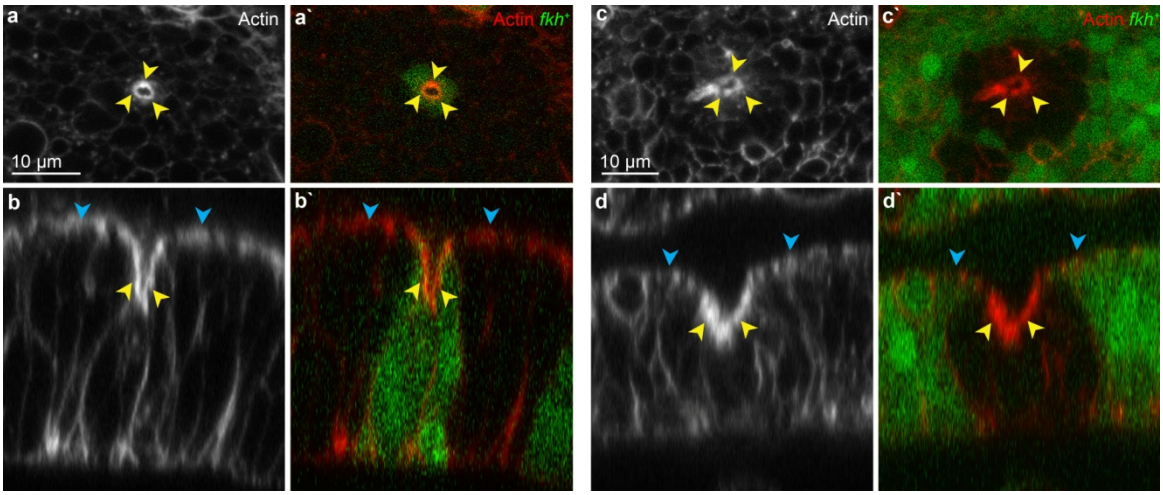

Figure 20: Apical actin accumulation at cyst center during invagination; Xy (a, c) and xz sections (b, d) of wing imaginal discs expressing *fkh* in flip out clones 30 h after clone induction using a short (a, b) and long (c, d) heat-shock. Apical actin enriches in invaginating clones (yellow arrows) when compared to surrounding columnar cells (blue arrows). Scale bar as indicated.

Interestingly, previous studies have described apical actin enrichments along compartment boundaries, locating between two differently specified cell lineages (Landsberg et al., 2009; Major and Irvine, 2005). We, therefore, focused next on the experimentally induced interface between the two differently fated cell populations of wild type and cell fate transcription factor misexpressing cells. Similar to observations at compartment boundaries, we detected increased apical actin intensities around *fkh*-expressing clones (Figure 21 a, b, e). Quantifications revealed that actin intensities at MWI adherens junctions of misspecified clones were increased by at least 30 % compared to actin intensities at interfaces between wild-type or misspecified cells. This was the case at early stages 30 h after clone induction, when even a subpopulation of

clones had not yet undergone invagination. At later stages, actin intensities at the MWI increased even further, but correlated with increased actin intensities at interfaces between misspecified cells (Figure 21 f). This observation can be explained by a late onset of cell-autonomous changes in misspecified cells and will be discussed later (3.4.6).

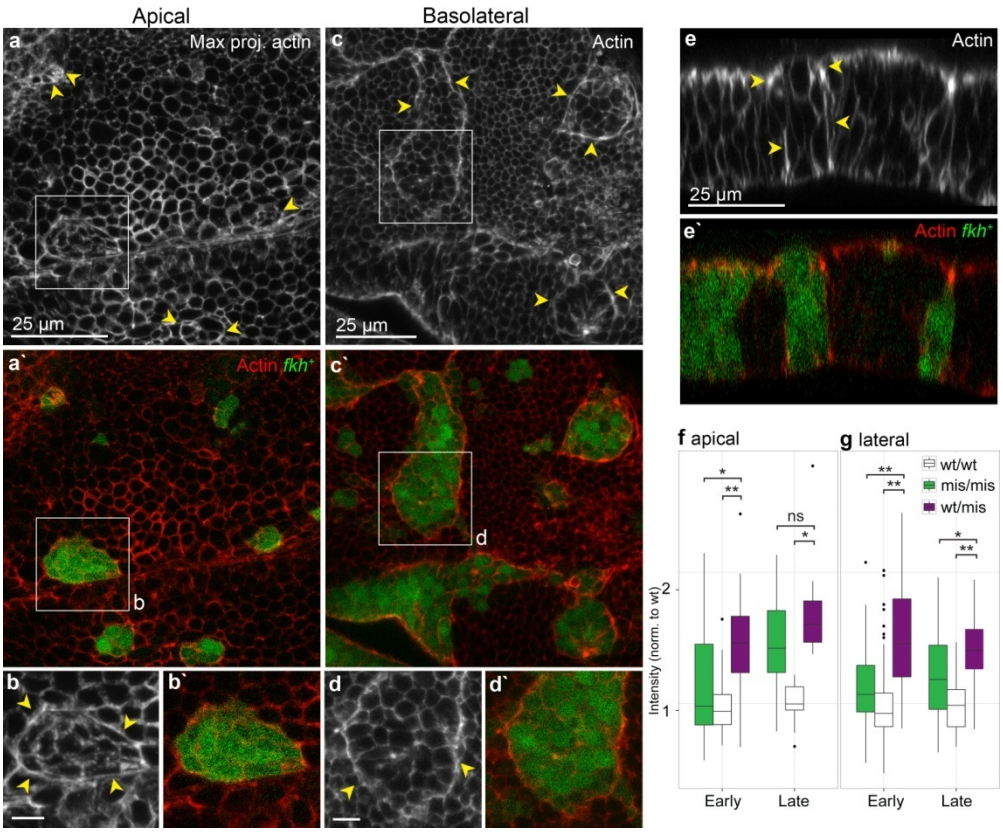

Figure 21: Actin is enriched at the MWI; (a-e) Xy sections (a-d) and xz cross-section (e) of pouch regions expressing *fkh* in flip out clones (green in a`-e`) 30 h after induction using a short heat-shock. Actin is shown in grey (a-e) or red (a`-e`). Apical xy section are shown in (a, b), basolateral sections in (c, d). Yellow arrowheads point to accumulation of actin at the MWI. Boxes in (a, c) frame regions shown at higher magnification in (b, d). Scale bars as indicated, in (b, d) 5 µm. **(f-g)** Box plots of normalized actin intensity at apical adherens junction (f) and basolateral interfaces (g) between wild-type cells (wt/wt), misspecified *fkh*-expressing cells (mis/mis) and between wild-type and misspecified *fkh*-expressing cells (wt/mis) 30 h (early) and 54 h (late) after clone induction. * = p-val < 0.01, ** = p-val < 0.001, ns= not significant. Refer to Appendix, Table 13 for statistical analysis and data. *Contributions: Actin quantification f, g: Anne Classen, Data analysis and representation f, g: Marco La Fortezza.*

Importantly, in addition to early apical actin accumulation, we found that filamentous actin was enriched also along the entire basolateral MWI (Figure 21 c, d, e). Early after clone induction, actin intensities were increased about 40 % at the basolateral MWI compared to basolateral interfaces between wild-type or between misspecified cells. At late stages of cyst formation, when cysts were fully invaginated, actin enrichment at the MWI persisted (Figure 21 g). Both lateral and apical quantifications revealed that actin intensities at interfaces between misspecified cells were not significantly different from intensities observed between wild-type

cells. Importantly, actin also enriched at MWI interfaces of inverse cysts included in the quantifications. Unfortunately, the resolution of a confocal microscope did not allow us to distinguish actin enrichment between interfaces, making it difficult to speculate if both interfaces at the MWI contribute to the observed actin accumulation or only one.

In conclusion, this analysis again supports our interpretation of a cell non-autonomous mechanism being responsible for the induction of cyst formation. We found that actin enrichment at the MWI, rather than cell-autonomous changes in misspecified or wild-type cells is a defining feature of early and late stages of cyst formation.

3.3.3 The contractile machinery is enriched at the MWI

Actin accumulation at the apical and basolateral MWI could indicate the possibility of higher tension and contractility generated at this specific subcellular location. To get further insights, we continued with a more detailed analysis of contractility regulators at early stages of cyst formation. We looked at myosin II regulatory light chain in the context of *fkh*-overexpressing cysts, using a GFP reporter of Spaghetti squash (Sqh) and also stained for the activated phosphorylated form of Sqh (Sqh 1P). Strikingly, we detected in both cases increased intensities basolaterally only at the MWI, but not within the *fkh*-expressing clone (Figure 22 a-f). The same result was observed when we analyzed the GFP-fusion protein of myosin II heavy chain, Zipper (Zip) (Figure 22 g-i). We also observed increased levels of the FERM domain protein Moesin (Moe) at the MWI upon examination of a GFP-fusion construct and antibody stainings for the phosphorylated, active Moe (Figure 22 j-n). Interestingly however, the upstream myosin II regulator Rho1 was not enriched at basolateral MWI locations (Figure 22 o, p).

Our results showed that misspecified cells themselves were not affected by changes to the localization and levels of contractility regulators. Again, this observation makes it unlikely that cell-autonomous mechanisms are causing cyst formation. Surprisingly, we observed changes in components of contractile machinery more prominently at the basolateral surface of the MWI, when compared to changes at apical adherens junction for which previous models implied a strong function contribution to cell segregation mechanisms (Landsberg et al., 2009; Major and Irvine, 2006).

In summary, these observations demonstrate that, similar to actin, activated Myosin and Moesin are specifically recruited to the MWI and suggest that the MWI may be under increased actomyosin-mediated contractile tension, specifically laterally.

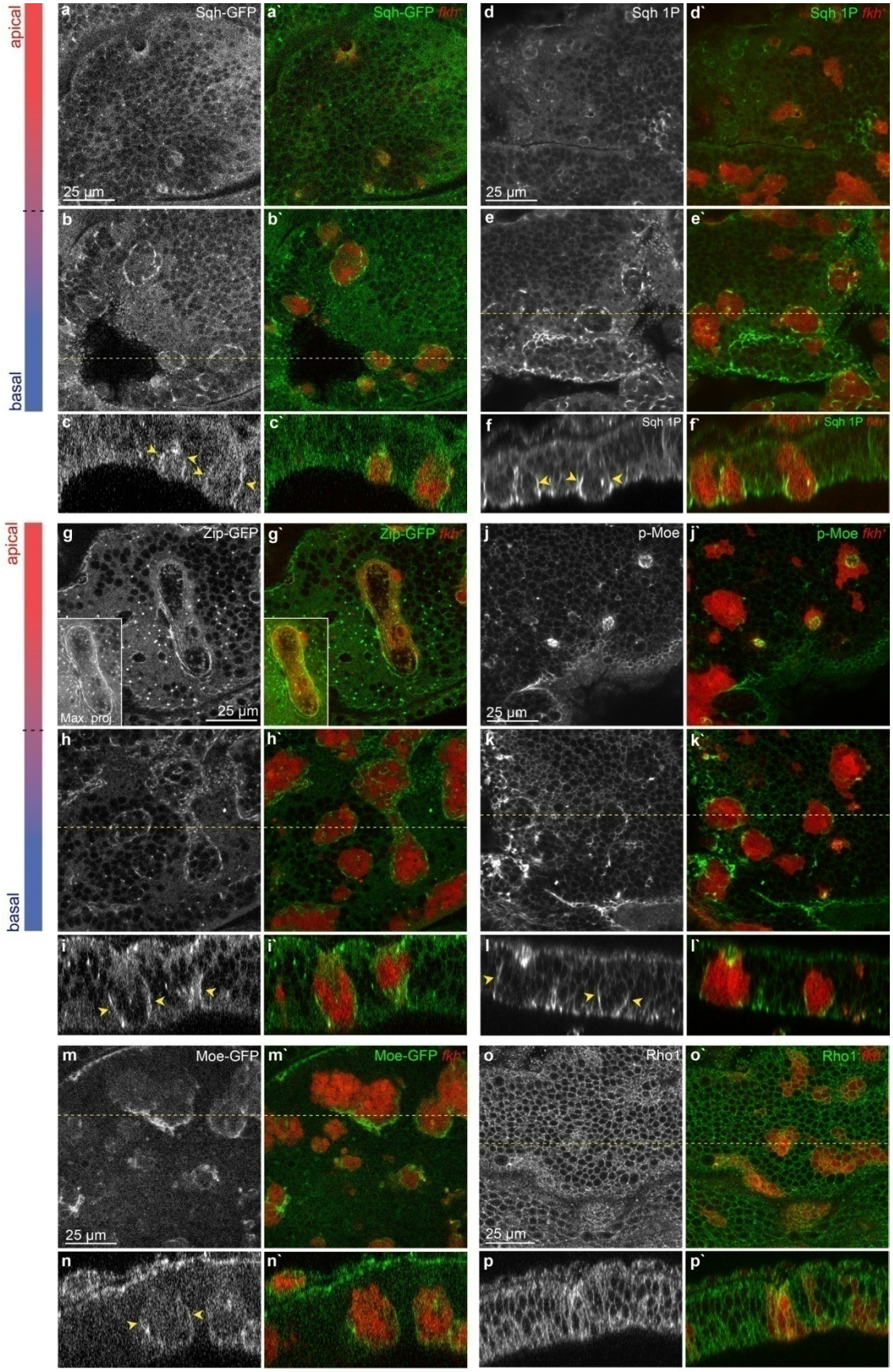

Figure 22: The contractile actomyosin machinery is enriched at the MWI; Xy sections (a, b, d, e, g, h, j, k, m, o) and xz cross-section (c, f, i, l, n, p) of pouch region expressing *fkh* in flip out clones (red in merges) 30 h after induction using a short heat-shock. Expression of Sqh-GFP (a-

c), Zip-GFP (g-i), Moe-GFP (m, n), staining for Sqh 1P (d-f), p.Moe (j-l) and Rho1 (o, p) are shown in grey or green in merged images. For (a-k) apical (a, d, g, j) and basolateral (b, e, h, k) sections are shown. Lower left inset in (g) shows a maximum projection of apical sections. Dashed yellow lines indicate positions of xz cross-sections. Yellow arrowheads point to increased intensities at the MWI. Scale bar as indicated.

3.3.4 MWIs are characterized by ECM deformations and increase in clone circularity

Concurrent with enrichment in contractile components, we observed dramatic changes to the shape of the interface between misspecified and wild-type cells. Detailed interface analysis revealed an upward deformation of the basement membrane at the MWI using a GFP fusion construct of Viking (Vkg), the Collagen IV homologue in *Drosophila*. The deformation was accompanied by a focused increase of actin and the βPS subunit of integrin (Figure 23 a, b). These changes may reflect actin polymerization and integrin engagement at the basal ECM (Lecuit et al., 2011) as cells respond to deformation of a shared contractile MWI away from the basement membrane.

Previously, it had been reported that integrin-ECM interactions regulate cell shape of imaginal disc cells and that degradation of ECM components induces tissue folding (Dominguez-Gimenez et al., 2007; Sui et al., 2012). We did not detect global changes to Vkg-GFP expression or to integrin localization in misspecified clones compared to wild-type cells 54 h (Figure 23 a, b) or 72 h after clone induction (Figure 23 c, d). This analysis eliminates ECM degradation as a possible driving force for the observed cell shape changes occurring during cyst formation.

At the apical side of the tissue, we often observed minimization of contacts at adherens junction between misspecified cells and wild-type cells. While smoothening of interfaces at the level of adherens junction between differently fated cells has been previously described (i.e. Dahmann and Basler, 2000; Roper, 2012; Zimmerman et al., 2010) and quantified (i.e. Shen et al., 2010), we observed that misspecified clones exhibited prominent smoothening and minimization of interface contact area especially basolateral (Figure 23 f-i). Quantification of basolateral clone circularity revealed an increase from 0.32 in wild-type clones to 0.76 in *fkh*-expressing clones early after clone induction (30 h). We detected a similar increase in basolateral circularity for inverse cysts formed by wild-type cells (0.37 and 0.74 for clones surrounded by *GFP* and *fkh* expressing tissue, respectively). At later time points (54 h), the difference in circularity between wild-type and misspecified clones became even more pronounced (Figure 23 j).

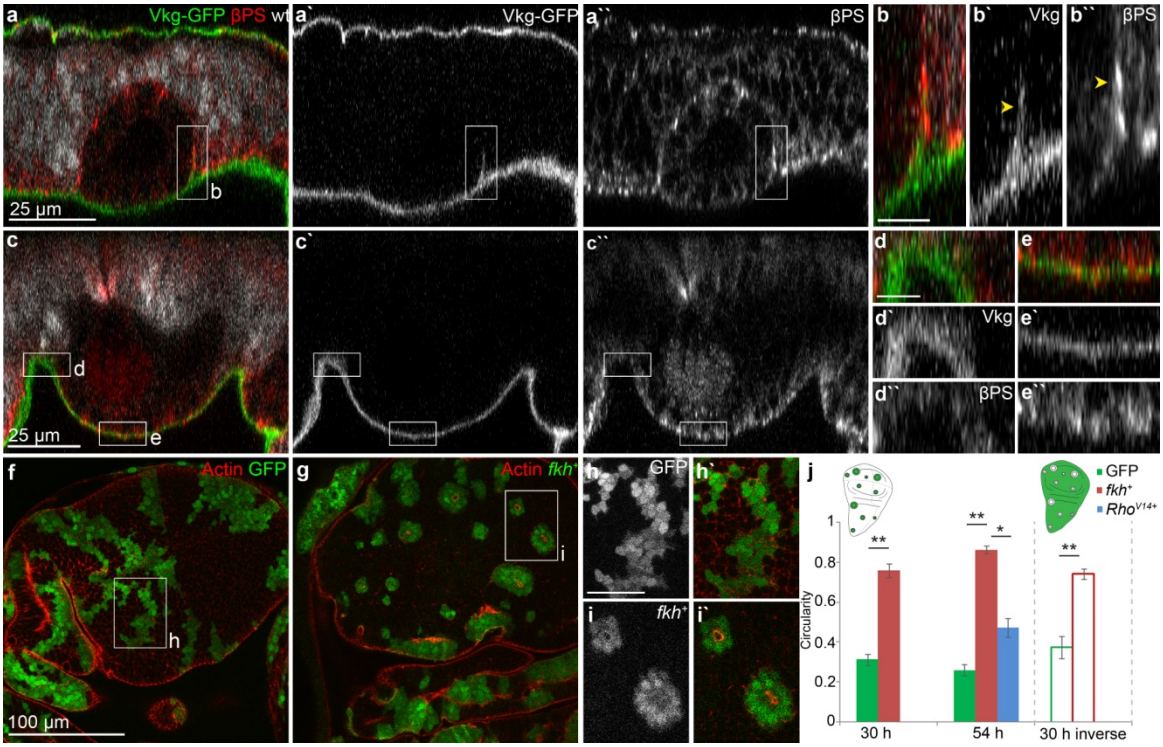

Figure 23: Higher MWI contractility causes ECM deformations and increase in clone circularity; (a-e) Xz cross-sections of wing imaginal discs mosaic for *Psc-Su(z)2*^{XL26} 54 h (a, b) and 72 h (c-e) after clone induction expressing a Collagen IV GFP-fusion protein (Vkg-GFP, grey in a`-e`, green in a-e). Additionally, discs were stained for the βPS subunit of integrin (βPS, grey in a``-e``, red in a-e). Wild-type cells are displayed in grey and boxes frames regions shown at higher magnification. Yellow arrowheads in (b) point to deformation of the basement membrane at the MWI. **(f-i)** Xy sections of wing discs expressing GFP (f, h) and *fkh* (g, i) in flip out clones (green in f, g, h`, i`; grey in h, i) 54 h after induction using a short heat-shock. Actin is shown in red (f, g, h`, i`). Basolateral sections are shown. Boxes in (f, g) frame regions shown at higher magnification in (h, i). Note differences in clone shape. **(a-i)** Scale bar as indicated, scale bar in inset represents 5 µm (b) and 25 µm (h). **(j)** Bar plot of clone circularities. Solid colored bars represent circularity of clones expressing GFP (green), *fkh* (red) or *Rho*^{V14}*, p35* (blue) surrounded by wild-type cells early (30 h) and late (54 h) after clone induction. White bars represent circularity for wild-type clones if surrounded by GFP (green outline) or *fkh* (red) expressing cells (red outline) at early stages after induction (30 h).* = p-val < 0.01, ** = p-val < 0.001. Refer to Appendix, Table 15 for data and statistical analysis, *Contributions: Statistical analysis j: Marco La Fortezza. Experiment and image generation a, b: Vanessa Weichselberger.*

These results suggest that contractile changes to both apical and basolateral MWI surfaces result in dramatic minimization of the entire lateral contact area between wild-type and misspecified cells. This likely causes clones to acquire the characteristic smooth ball-like shape as they invaginate towards the basal side of the epithelium. Ultimately, minimization of basolateral and apical MWIs culminate in complete resolution of MWI contacts and eventually release *Psc-Su(z)2* cysts from the surrounding wild-type epithelium, as described before (Figure 8 g).

3.4 Interface contractility is sufficient and necessary for cyst formation

3.4.1 3D vertex model

The complex three-dimensional deformations that occur during cyst formation depend on changes of mechanical properties of cells and forces generated by the cytoskeleton. Different approaches have been published that engaged in modeling the mechanical forces in epithelial sheets (Fletcher et al., 2014). To understand how changes in the distribution of cytoskeletal forces could specifically drive cyst formation, our collaborators Silvanus Alt and Guillaume Salbreux developed a novel physical model for the mechanics of epithelial tissues (Figure 24). The model is based on a vertex representation of the epithelium with the novelty of not being restricted to two dimensions, but covering the epithelium in all three dimensions. Every individual cell is defined by a set of vertices that are connected in the tissue plane and between apical and basal vertex points. The internal force component of the model takes into account the cellular pressure, surface tensions generated on cell surfaces between multiple vertices and line tensions generated along cell edges between neighbouring vertices. The model also considers external forces arising from the extracellular matrix connections and the overall tissue compression. In addition to 3D vertex simulations, the model procedures were supported by calculations using continuum theories, which will be not covered here in more detail. For details about the 3D vertex model, the continuum theory and the parameter definition, please refer to a more detailed description provided by Silvanus Alt and Guillaume Salbreux in our manuscript.

To simulate cyst formation using the 3D vertex model, we aimed to identify a parameter set that would represent force conditions found in normal imaginal discs and during cyst formation. Measurements of the height-width aspect ratio of wild-type cells allowed us to establish first estimations on the sum of apical and basal forces that must act in imaginal disc epithelia. Secondly, we defined a parameter for ECM-induced tissue compression, inspired by previous studies, which indicate that imaginal discs are under ECM-induced tissue compression enabling the cells to adopt a columnar cell shape (Aegerter-Wilmsen et al., 2007; Aegerter-Wilmsen et al., 2012; Pastor-Pareja and Xu, 2011). We thus experimentally removed the ECM by collagenase treatment and indeed observed tissue flattening (Appendix, Figure 45, Table 16). By measuring the cell aspect ratio change induced by collagenase treatment, we were able to specify the parameter for ECM-induced external compression. As a third step, exact parameters for apical and basal line and surface tension, as well as ECM stiffness, were extracted from clone shape quantifications discussed in 3.4.4.

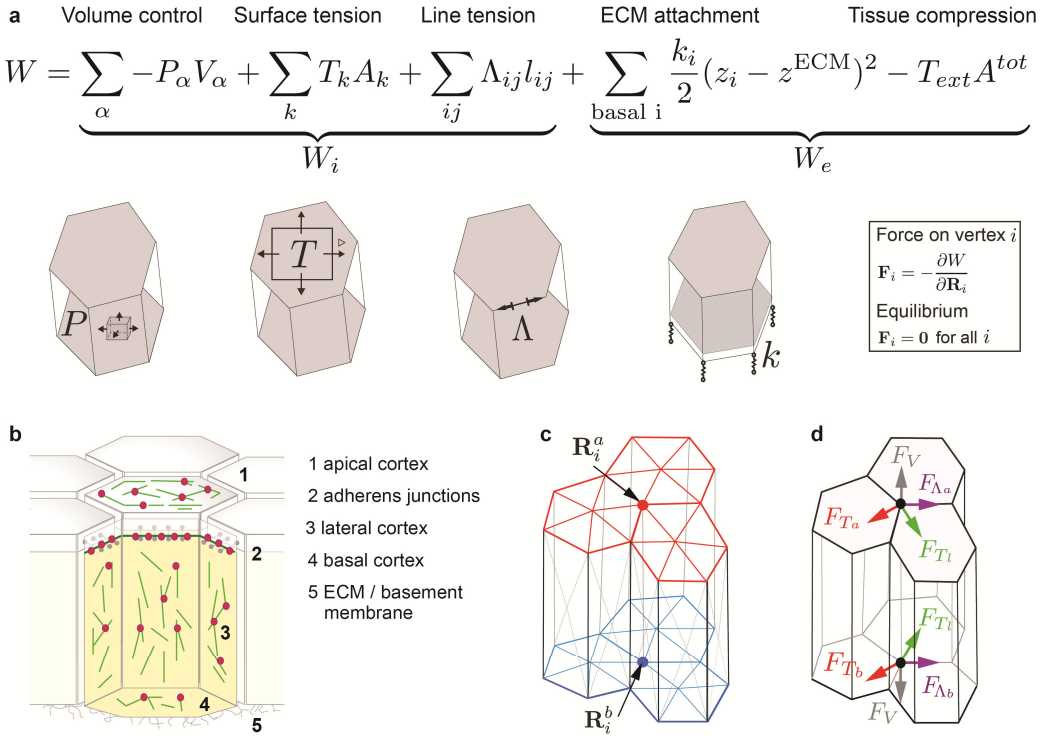

Figure 24: Physical description of epithelial tissues in a 3D vertex model; **(a)** Forces acting in the vertex model epithelium are obtained from an effective mechanical work function W that is the sum of an internal work functions W_i and an external work function W_e. The internal work function includes (1) an intracellular pressure P_α constraining the volume of cell α, (2) surface tensions T_k acting on cell surfaces k, (3) line tensions Λ_{ij} acting on apical and basal edges connecting neighboring vertices i and j. The external work function includes (1) basal springs counteracting basal deformations out of the reference plane representing the ECM, (2) external forces establishing the overall tissue compressive stress T_e **(b)** In epithelial tissues, surface tensions arise from the actomyosin cortex (actin in green, myosin in red) which is associated with the apical, lateral and basal membranes. Line tensions are generated by mechanical coupling of neighboring cell through adherens junctions. The basement membrane composed of ECM proteins covers the basal side. **(c)** In the 3D vertex model, the tissue geometry is characterized by a set of vertices R_i. For each cell surface, an additional central vertex is introduced at the barycenter of the surface contour. Planar triangles connecting the central and contour vertices define cell boundaries. **(d)** Forces acting on a vertex R_i are obtained by minimizing the virtual mechanical work with respect to vertex position. Forces have contributions from the surface tensions F_t, line tensions F_Λ and cellular pressures F_v. *This figure was generated by Silvanus Alt.*

3.4.2 Interface contractility is sufficient and necessary for cyst formation

Having defined a parameter set reflecting experimental observed tissue properties, we aimed to gain more insights into the mechanism responsible for cyst formation. Within the model, we simulated the presence of a clone by placing a number of misspecified cells N_c among a wild-type cell population (Figure 25 a) and then applied two different types of mechanical changes. Firstly, we modified line or surface tensions in misspecified cells (bulk contractility, Figure 25 b) and secondly, we modified line and surface tensions only at the interface between misspecified and wild-type cells (interface contractility, Figure 25 c).

Because reduction of columnar height in mutant cells has been previously linked to cyst formation (Gibson and Perrimon, 2005; Shen and Dahmann, 2005; Widmann and Dahmann, 2009a, b), we first performed bulk contractility simulations in which all misspecified cells experienced an increase in lateral surface tensions. Over a range of different parameters (Figure 25 b, top row, parameter choice discussed in 3.4.4), this perturbation changed the preferred aspect ratio towards a cuboidal shape and, indeed, caused cyst formation in simulations. However, inverse cyst formation by wild-type cells could not be recapitulated: wild-type cells did not invaginate, but instead exhibited increased heights compared to surrounding misspecified cells (Figure 25 b, bottom row). We wanted to confirm this simulation prediction experimentally. It had been previously shown that ectopic expression of an activated form of *Rho1 (Rho^{V14})* leads to reduced cell heights (Widmann and Dahmann, 2009a). Since a lot of apoptosis in overexpressing Rho^{V14}-clones made it difficult to analyze cell shape changes, we blocked apoptosis by co-expression of *p35*. Expression of Rho^{V14}*, p35* in clones caused actin to accumulate predominantly at the lateral cell cortex and strongly reduced the height of cells. This is in consistency with an increase in lateral surface tension. As predicted by simulations, small Rho^{V14}-expressing clones caused deep indentations in imaginal discs (Figure 25 d-f). In contrast, overexpression of Rho^{V14} in larger areas did not cause inverse cyst formation, where wild-type cells undergo invagination. Instead, Rho^{V14}-expressing cells and wild-type cells exhibited different heights and failed to perform MWI smoothening, as predicted by simulations (Figure 25 g, h). These results confirmed that altering mechanical properties of individual cells can cause cysts, but not inverse cysts.

This suggests again that cyst formation observed after cell misspecification does not solely arise from cell-autonomous changes to the mechanical properties of misspecified cells. Instead, cellular apposition of different fates must induce a tissue response upstream of potential cell-autonomous shape changes in differently-fated cells to drive cyst formation.

After excluding bulk changes as the driving force for cyst formation, we simulated interface contractility at the MWI to see if this is sufficient to explain cyst formation by misspecified and by wild-type cells. At the interface, we increased apical line tension and lateral surface tension by 3-fold (parameter choice discussed in 3.4.4) and found that clones invaginated and formed cysts (Figure 25 c, top row). Since these simulations only changed forces along the interface between misspecified and wild-type cells, inverse cyst formation by wild-type cell clones could also be recapitulated by these conditions (Figure 25 c, bottom row). Of note, bulk contractility changes were not able to recapitulate clone smoothening neither in experiments (Figure 23 j, blue bar) nor in simulations (Figure 25 b), whereas interface contractility caused pronounced interface smoothening in simulated as well as experimental clones (Figure 25 c, Figure 23 j).

From these observations, we conclude that only higher contractility at the MWI is sufficient and necessary to account for misspecified and inverse cyst formation observed in our experiments.

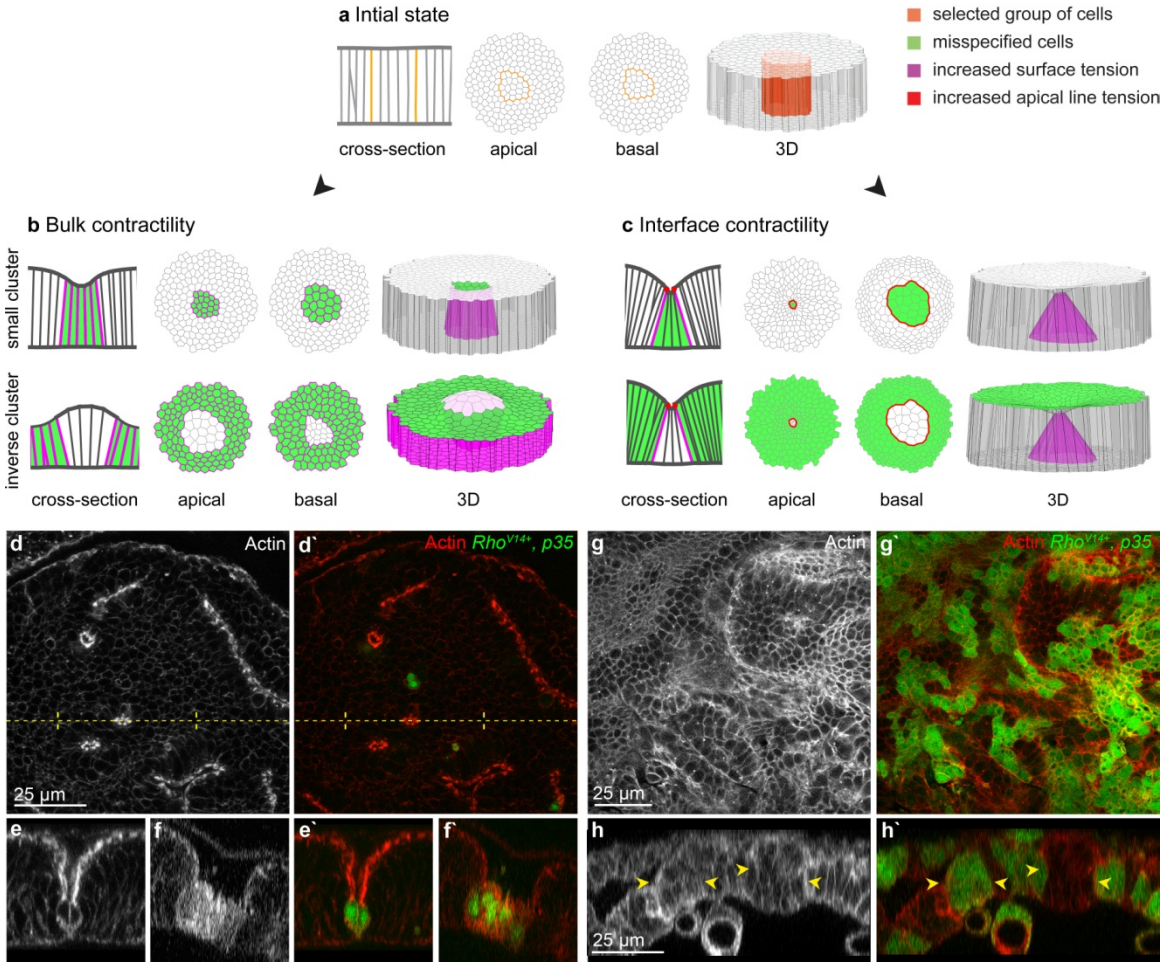

Figure 25: Increased interface contractility is sufficient and necessary for cyst formation by misspecified and wild-type cells; (a-c) 3D vertex model simulations visualize epithelial cell shapes in cross-section views, apical and basal views, as well as in 3D representations of the tissue. A tissue containing a clone of 20 misspecified cells is shown before (a, initial stage) and after changes to the mechanical properties of misspecified cells (b, bulk contractility') or to the MWI (c, interface contractility). Simulations of misspecified cells (green) being surrounded by wild-type cells (white) (small cluster) and vice versa (inverse cluster) are shown. Magenta lines represent a 3-fold surface tension increase. Red lines in (c) represent a 3-fold increase to apical line tension. Note the absence of interface smoothening between cell populations in bulk contractility simulations. **(d-h)** xy sections (d, g) and reconstructed xz cross-sections (e, f, h) of wing discs containing Gal4/UAS flip out clones expressing *Rho^{V14}, p35* (green in d`-h') at 54 h after clone induction using a short (d-f) and long (g-h) heat-shock. Actin is shown in grey (d-h) or red (d'-h'). Interspersed *Rho^{V14}, p35*-expressing clones (d-f) give rise to cysts, whereas interspersed wild-type clones (g, h) fail to do so (yellow arrowheads). Dashed yellow line in (d) indicates positions of xz cross-section in (e). Note the absence of interface smoothening between wild-type and *Rho^{V14}, p35*-expressing cells. Scale bar as indicated. *Contributions: Simulations a-c: Silvanus Alt.*

3.4.3 Cyst formation depends on cell cluster size

We noticed that interface contractility simulations predicted a strong dependency of the final clone shape on the size of the clone. To better analyze this dependency, we turned to a continuum theory of tissue mechanics, which allowed us to draw generic conclusions on tissue shape stability. On large spatial scales, the epithelium described by our 3D vertex model effectively behaved as a continuous elastic sheet. Continuous elastic sheets tend to buckle if compressed. We postulated that cyst formation in our 3D vertex model simulations is driven by this buckling instability. The threshold level of compression at which elastic sheets undergo buckling is determined by two considerations. First, for a circular contractile boundary, the compression felt by the enclosed elastic sheet depends on the radius and the contractile boundary tension, as described by the law of Laplace. As a consequence, large clones feel less pressure from a contractile circular boundary than small ones and are therefore less likely to buckle and to invaginate (Figure 26 a). Secondly, the resistance of an elastic sheet to bending is higher for small-scale deformations. That means that small clones have a higher resistance to buckling than larger clones preventing them from invaginating (Figure 26 b). The combination of these two aspects, predicted that very small and very large clones do not invaginate and do not form cysts. Indeed, simulations using a continuum model of elastic sheets confirmed these predictions (data not shown).

To corroborate the results of these simulations experimentally, we performed a quantitative analysis, where we measured clone shapes as a function of clone size. We analyzed 79 *fkh*-expressing clones from 2 to 120 cells early after clone induction (30 h) using intermediate heat-shocks lengths. For each clone, we determined the number of cells N_c and characterized the clone shape, when possible, in two perpendicular cross-sections. We specifically measured apical and basal clone width w_a and w_b, as well as apical and basal deformation, away from the apical and basal plane of the surrounding tissue, u_a and u_b (Figure 26 e). This analysis showed clearly that apical indentation u_a and basal deformation u_b were maximal for intermediate clone sizes (N_c ~70 cells) and minimal for either small or very large clones (Figure 26 c, dotted line). In addition, the difference in apical and basal widths w_a and w_b was maximal for intermediate clone sizes and represented strongly wedge-shaped cysts. Very large clones showed a reduction in apical and basal width differences, but still exhibited smoothening at the MWI (Figure 26 d, dotted line, Figure 33).

In summary, the experimental quantifications, indeed, recapitulated predictions of the continuum model of a circular contractile boundary dependent on the Law of Laplace and the buckling resistance.

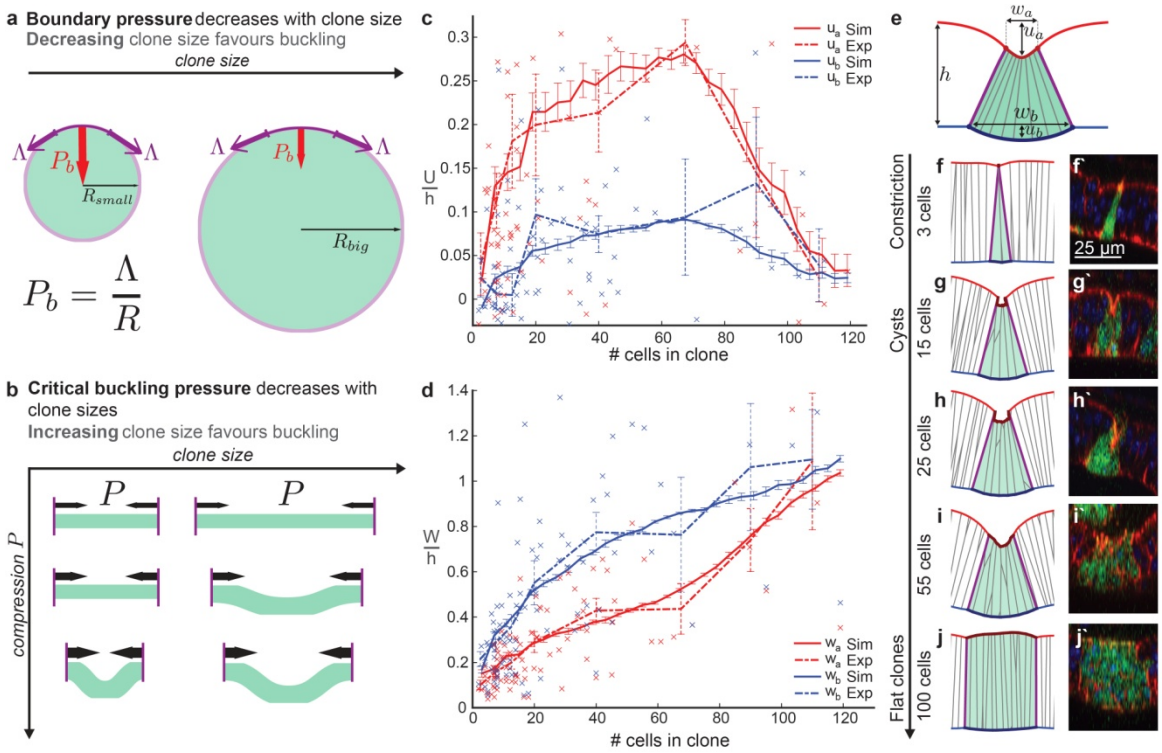

Figure 26: Clone size dependency of cyst formation; (a) Laplace's Law predicts that the pressure P_b coming from a contractile boundary with the force Λ declines with increasing diameter R of the encircled area. Therefore, large clones encounter less pressure and are less likely to buckle. **(b)** The resistance for bending a flat elastic sheet depends on the radius of the material. Consequently, smaller clones display a higher resistance to buckling than bigger clones. **(c, d)** Experimental (dotted line) and simulated (continuous line, 3-fold increase in apical line and lateral surface tension) deformations of apical (red) or basal (blue) cyst surfaces are shown. Absolute apical and basal deformation (U_a, and U_b) and absolute apical and basal widths (W_a and W_b) were normalized to tissue height h to obtain u_a, u_b, w_a, w_b and are plotted with respect to cyst size (see also e). Intermediate-sized clones show highest apical and basal deformations whereas small and large clones have minimal deformations. Mean values and SEM of 79 *fkh*-expressing clones 30 h after clone induction and of 5 3D vertex model simulations per data point are shown.**(e)** Illustration of experimentally measured parameters which were fitted by simulations. w_a :apical clone width, w_b: basal clone width, u_a: apical surface indentation, u_b: basal surface deformation **(f-j)** Simulated (f-j) (3-fold increase in apical line and lateral surface tension) and *fkh*-expressing (f'-j') cross-sections of clones containing 3 (f), 15 (g), 25 (h), 55 (i) and 100 (j) cells. Small clones exhibit pronounced apical constriction, intermediate clones form to cysts, whereas large clones only show interface smoothening. *Contributions: a, b: Silvanus Alt, Experimental data analysis, simulations and graphs c-j: Silvanus Alt.*

3.4.4 3-fold increase in interface contractility recapitulates early shape changes

After we established experimentally the range of clone sizes in which maximal deformations occur, we asked what range of physical forces could explain the dependency of clone shape on this defined clone size range. We, therefore, performed 3D vertex model simulations of cyst formation for varying clone sizes. In doing so, we searched for the smallest increase in apical line and lateral surface tension at the MWI that could account for experimental measurements. We found that with a 3-fold increase in apical line and lateral surface tensions at

the MWI, all features of the 4 measured experimental curves for w_a, w_b, u_a and u_b could be accurately reproduced by simulations (Figure 26 c, d, f-j). In addition to the mechanical changes occurring at the interface, the quantifications also allowed us to adjust initial parameters for (1) apical, lateral and basal surface tension of the tissue, (2) apical and basal line tension and (3) stiffness of tissue-ECM attachment (Appendix, Table 17).

3.4.5 Simulation requirements for potent interface contractility

After having identified the optimal parameter set that recapitulated experimental tissue properties required for cyst formation in the 3-D vertex model, we were interested to see how deviations of individual parameters influence the simulation outcome. As described before, a 3-fold increase of apical line and surface tension at the MWI reflected experimental measurements the best. Interestingly, when apical line and lateral surface tensions were only increased by a factor of 2, the clonal deformations were weaker than observed experimentally. This suggested that a stronger boundary effect is required to achieve the measured deformations (Figure 27 a). On the contrary, when apical line and lateral surface tensions at the interface were increased 4-fold, the deformations were stronger compared to experimentally observed shape behaviors. Especially simulated clones bigger than 80 cells, displayed a strong apical and basal deformation, which did not appear in experimental quantifications (Figure 27 b). This again supports the importance of an increase in interface tension in the order of 3-fold.

Furthermore, we tested if both increase in apical line tension, as well as surface tension, were necessary to mirror the observed shape quantifications. Importantly, a 3-fold increase in only apical line tension was insufficient to induce buckling, neither apically nor basally (Figure 27 c). Increasing the apical line tension even 10-fold did not simulate the strong deformations observed experimentally neither (Figure 27 d). This strongly suggests that contribution of basolateral contractility is indispensable in describing the observed clone shapes. Vice versa, if only the lateral surface tension at the interface was increased 3-fold, simulated clones did not display a constant basal deformation, but remained mainly flat. In addition, the apical deformation was not as strong as observed experimentally (Figure 27 e). This indicates that the increase in apical line tension is required to explain the observed deformations.

In summary, the simulations strongly suggest that at the interface an increase in apical line tension together with an increase in lateral surface tension is necessary to mimic the observed clone shapes for a range of different clone sizes, as an increase in apical line or lateral surface tensions alone did not recapitulate experimental observations.

We also increased the ECM attachment stiffness by 2-fold and observed that especially the basal surfaces remained flat. This suggests that the stiffness of the ECM attachment influences the strength of the basal deformations and thus final cyst shape (Figure 27 f).

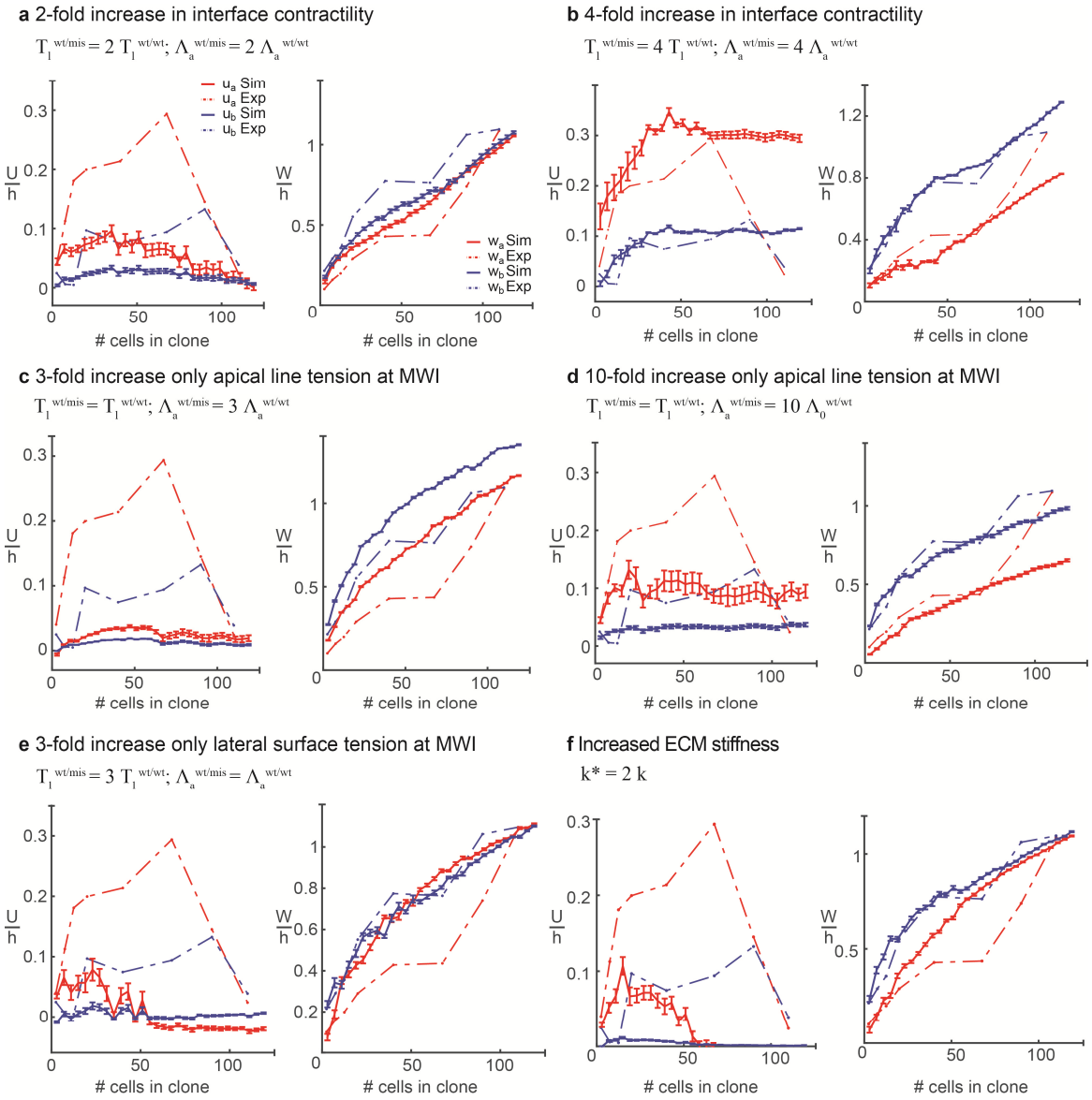

Figure 27: 3D vertex model simulations deviating from optimal parameter set; Deviations of mechanical parameters from the optimal parameter set ($T_l^{wt/mis}$ = 3 $T_l^{wt/wt}$; $\Lambda_a^{wt/mis}$ = 3 $\Lambda_a^{wt/wt}$) demonstrate how changes influences equilibrium shapes in comparison to experimental clone quantifications. Experimental (dotted line) and simulated (continuous line) deformations of apical (red) or basal (blue) cyst surfaces are shown by plotting the parameters u_a, u_b (left graphs), w_a, w_b (right graphs) (see Figure 26 e) with respect to cyst size. Simulations parameters are listed for each scenario. Graph shows mean values and SEM of 18 simulations. Experimental data set is the same as in Figure 26, for clarity error bars are excluded. *Simulations and graphs by Silvanus Alt.*

3.4.6 Cell-autonomous shape changes influence clone shapes at late stages

We wanted to understand if increased interface contractility could also explain the clonal shapes of later stages. Therefore, we quantified 30 clones at 54 h after clone induction using a short heat-shock. At this time point, the strongest apical and basal indentation did not occur for intermediate-sized clusters, but for larger clone sizes (Figure 28 a, top graph). In addition, the

strongest wedge-shaped behavior of clones was observed for large cell clusters (Figure 28 a, bottom graph). Interestingly, simulation of bulk effects by increased lateral surface tension in all misspecified cells generated a similar trend. Apical as well as basal indentation and wedge-shaped behavior were the strongest for bigger and not intermediate clones (Figure 28 b).

This suggests that cell-autonomous cell shape changes of misspecified cells have to be considered at later stages as additional mechanical perturbations that influence final clone shape. The occurrence of bulk effects at later stages is supported by the observation that misspecified clones have undergone pronounced cell height decrease at 54 h after clone induction which is accompanied by cell volume reduction (Figure 28 c-d, Appendix, Table 16).

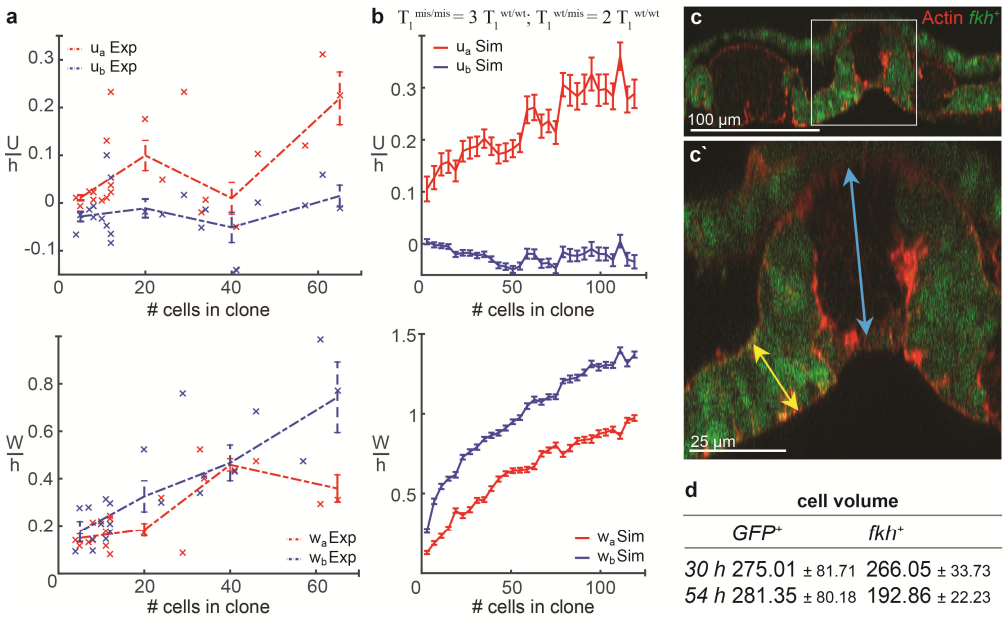

Figure 28: Cell-autonomous shape changes influence clone shapes at late stages; (a) Experimental deformations of apical (red) or basal (blue) cyst surfaces 54 h after clone induction are shown. Parameters u_a, u_b (top graph), w_a, w_b (bottom graph) (see Figure 26 e) are plotted with respect to cyst size. Mean values and SEM of 30 *fkh*-expressing clones 54 h after clone induction are shown **(b)** Bulk simulations by increasing lateral surface tension 3-fold in clone and 2-fold at interfaces are shown. Graph illustrates simulated apical (red) and basal (blue) deformation by plotting the parameters u_a, u_b (top graph), w_a, w_b (bottom graph) (see Figure 26 e) with respect to cyst size. Graphs show mean values and SEM of 18 simulations. **(c)** Xz cross-sections of wing imaginal disc containing Gal4/UAS flip out clones expressing *fkh* (shown in green) 54 h after clone induction using a long heat-shock. Actin is shown in red. Note the difference of tissue height between wild-type cells (blue arrow) and *fkh*-expressing cells (yellow arrow). Scale bar as indicated **(d)** Volume measurements of GFP and *fkh*-expressing Gal4/UAS flip out clones at 30 h and 54 h after clone using a short heat-shock. Note the tendency of volume decrease for *fkh*-expressing clones after 54 h. *Contributions: Simulations a, b: Silvanus Alt.*

3.5 Interface contractility drives apoptotic extrusion of small, misspecified clones

3.5.1 Small, misspecified clones are extruded via apoptosis

In simulations and experiments, single cells or very small clones did not form cysts but display significantly reduced apical cell areas (Figure 26 f). This resembled initial stages of cell extrusion events that occur during clearing of apoptotic cells from epithelial tissues or during live cell extrusion initiated by cell crowding (Eisenhoffer et al., 2012; Eisenhoffer and Rosenblatt, 2013; Marinari et al., 2012; Monier et al., 2015). Our observations, therefore, suggested that interface contractility may specifically drive elimination of single misspecified cells or small misspecified cell clusters by promoting apical surface constriction and, potentially, basal extrusion. To understand if size-dependent elimination of misspecified cell clusters indeed occurred, we quantified the frequencies of misspecified clone sizes and compared them to those of wild-type clones. To control for variability in experimental conditions, we used the Tie-Dye technique to generate misspecified cells marked by RFP and wild-type clones marked by GFP in the same imaginal disc (4.1) (Worley et al., 2013). To normalize for intrinsic differences in frequencies of GFP and RFP clone induction (Worley et al., 2013), clone counts were compared to those for neutral GFP and neutral RFP clones from control discs (Figure 29 a-d). When we analyzed the total amount of GFP and RFP clones in all *fkh*-expressing Tie-Dye discs and control discs, we found that small *fkh*-expressing clones were indeed dramatically underrepresented compared to RFP clones of control discs (Figure 29 e`, light blue and orange line). GFP clones of *fkh*-expressing discs did not show differences to GFP clones of control discs (Figure 29 e, light blue and orange line) suggesting that the underrepresentation of small *fkh* clones is specific to *fkh* expression. We made use of the Tie-Dye technique by normalizing the clone frequency in each disc to its internal GFP control. This analysis revealed that *fkh*-expressing clones are underrepresented up to clonal size of 6 cells (Figure 29 f) when compared to clone frequencies in control discs.

To understand if apoptosis is necessary for elimination of small clones, we inhibited apoptosis in *fkh*-expressing cells by co-expression of *dIAP*, an inhibitor of Caspase activation. Interestingly, we still observed that the amount of small *fkh, dIAP* clones was reduced when compared to RFP control clones (Figure 29 e`, dark blue and red line). Analysis of RFP clone frequencies relative to GFP clone frequencies in each disc, revealed that *dIAP* significantly rescued distribution of large *fkh* clones sizes back to wild-type levels indicating that apoptosis in large clones was strongly reduced. Strikingly, however, *dIAP*-expression was not able to rescue loss of single *fkh*-expressing cells when compared to control *dIAP*-expressing Tie-Dye discs (Figure 29 f`). This was also evident, when relative clone frequencies were analyzed in binned

clone size categories that have been previously determined to be statistically significant (Figure 29 f, f`, Appendix, Table 22). In Figure 29 g, significant clone size categories determined for *dIAP* / *fkh, dIAP* were applied to all genotypes, in Figure 29 h, individually determined clones sizes categories were applied to wt / *fkh* and *dIAP* / *fkh, dIAP* data sets, respectively.

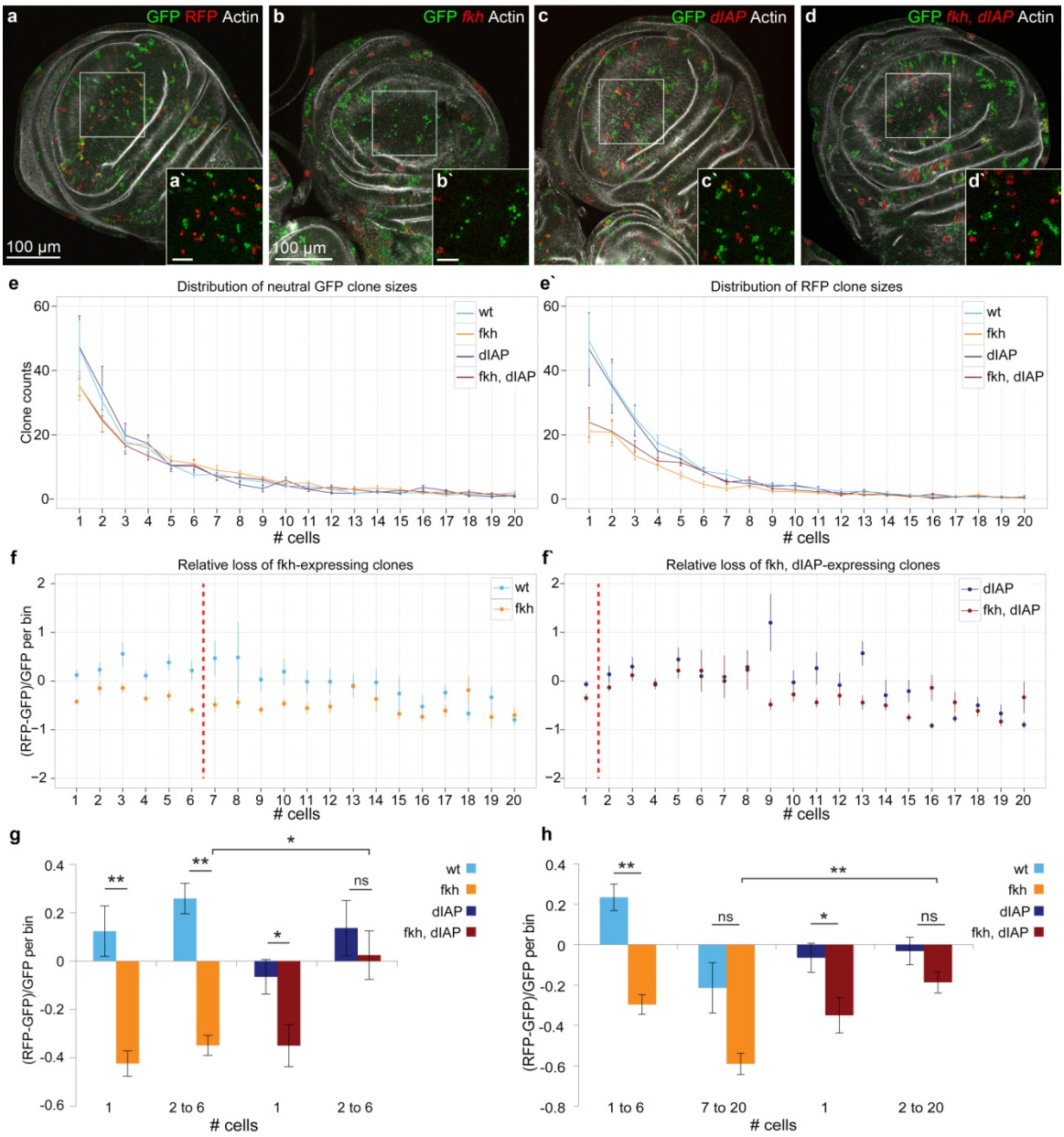

Figure 29: Tie-Dye analysis of clone size-dependent elimination of aberrant cells; (a-d) Tie-Dye imaginal discs 30 h after clone induction using a short heat-shock carrying control GFP-expressing clones (green) and RFP clones expressing RFP alone (a), *fkh* (b), *dIAP* (c) and *fkh, dIAP* (red). Actin is shown in grey. White boxes frame higher magnification insets shown in (a'-d'). Scale bar as indicated, scale bar in inset (a`-d`) represents 25 µm. **(e)** Frequencies of control GFP (e) and RFP (f) clones of a given size in Tie-Dye wing discs at 30 h after clone induction. RFP clones express RFP (light blue), *fkh* (orange), *dIAP* (dark blue) or *fkh, dIAP* (dark red). Mean and SEM of clone counts analyzed for 10 (wt, *fkh* and *fkh, dIAP)* and 8 discs (*dIAP)* are shown. See also Appendix, Table 20 and Table 21. **(f)** Relative RFP clone frequencies of *fkh* (f) and *fkh, dIAP* clones (f`) compared to relevant control RFP clones (RFP alone in f and *dIAP* in f`, respectively) in Tie-Dye wing discs. For each disc, the number of control GFP-expressing clones was

subtracted from the number of RFP-clones and normalized to the number of GFP-clones per bin size. Mean and SEM of 10 (*wt*, *fkh* and *fkh, dIAP)* and 8 discs (*dIAP)* are shown, color code as in (e). Dashed red line indicates threshold for statistical significance (refer to Appendix, Table 22 and Table 23). This analysis utilizes the strength of the Tie-Dye system as the data is normalized to intrinsic control GFP-clones for each clone size bin and genotype. See also Appendix, Table 22 **(g, h)**. Relative RFP clone frequencies of *fkh* (f) and *fkh, dIAP* clones (f`) compared to relevant control RFP clones (RFP alone in f and *dIAP* in f`, respectively) in Tie-Dye wing discs shown for different clone bins. Graphs report mean and SEM of 10 (*wt*, *fkh* and *fkh, dIAP)* and 8 discs (*dIAP)*. Calculations as in (f), color code and data set as in (e). In (g) clones sizes were binned into statistically significant clone size categories determined for *dIAP* (see f). In (h) statistically significant clone size categories of *fkh* and *fkh, dIAP* were used respectively (see f).* = p-val < 0.01, ** = p-val < 0.001, ns= not significant. Refer to Appendix, Table 23 for statistical analysis. *Contributions: Data analysis including statistics and representation e-h: Marco La Fortezza.*

These observations suggest that small *fkh*-expressing clones up to 6 cells are efficiently eliminated from the tissue. Furthermore, apoptosis seems to play a role in this process, since *dIAP* co-expression could rescue clone frequencies with the exception of single cell clones. Therefore, we wanted to understand if single misspecified cells are extruded via a distinct mechanism to apoptosis or if *dIAP* co-expression did not blocked apoptosis efficiently in single cell clones.

3.5.2 Clone size-dependent efficiency of dIAP in blocking apoptosis

We continued to analyze if the efficiency with which *dIAP* suppressed apoptosis depended on clone size. In general, we often observed apoptosis in misspecified cells (Figure 30 a). We now asked whether small *fkh*-expressing clones exhibited higher levels of apoptotic signal than larger clones. We thus quantified the volume occupied by apoptotic cells positive for cleaved Caspase Dcp-1 within *fkh*-expressing clones. While the relative proportion of apoptotic clones did not change between small and larger clone size bins (Figure 30 d), we found that relative apoptotic volumes in clones of up to 6 cells were strongly increased when compared to clones larger than 6 cells (Figure 30 c). This suggested that small *fkh*-expressing clones may be subject to stronger apoptotic stimuli than larger clones.

We were then curious to see if the distribution of apoptosis in *fkh, dIAP* clones is different, and analyzed Dcp-1 volumes with respect to clone size in *fkh, dIAP*-expressing clones. We found that dIAP was only half as efficient in inhibiting apoptosis in single cell clones as in clones of larger sizes (Figure 30 b, d). Similarly, *dIAP*-expression could not reduce the proportion of apoptotic volumes in very small clones as observed for larger clone sizes (Figure 30 c).

This suggests that specifically small *fkh*-expressing cell clusters are subject to strong apoptotic stimuli resistant to limiting dIAP levels. In contrast, apoptosis in large cell clusters, which incidentally do not experience strong apical constriction induced by the MWI, may arise via less potent and MWI-independent signals.

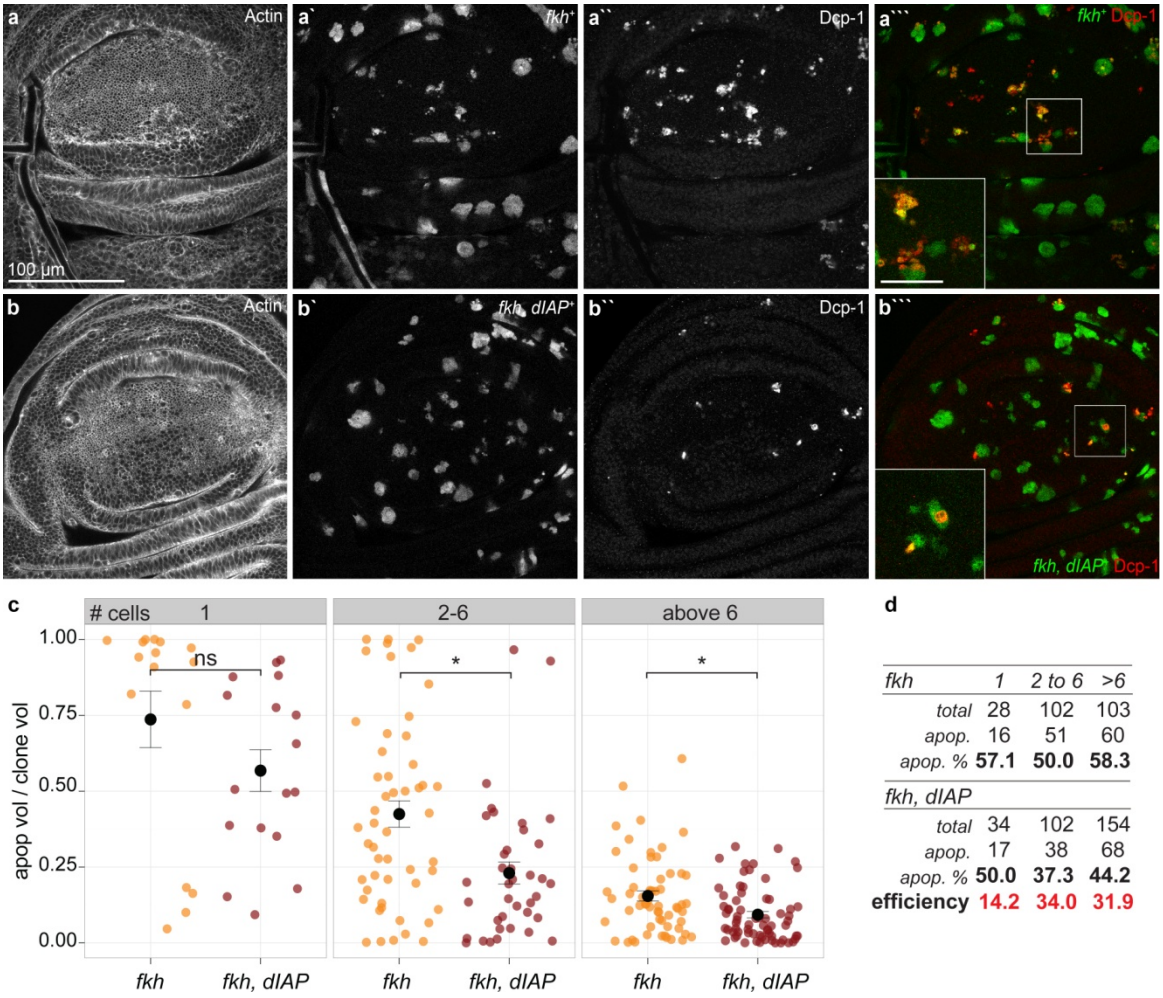

d

fkh	*1*	*2 to 6*	*>6*
total	28	102	103
apop.	16	51	60
apop. %	**57.1**	**50.0**	**58.3**
fkh, dIAP			
total	34	102	154
apop.	17	38	68
apop. %	**50.0**	**37.3**	**44.2**
efficiency	**14.2**	**34.0**	**31.9**

Figure 30: Clone size-dependent efficiency of dIAP in blocking apoptosis; (a-b) Xy sections of wing discs expressing *fkh* (a) and *fkh, dIAP* (b) in flip out clones (green in a```, b```; grey in a`, b`) 30 h after induction using a short heat-shock. Actin is shown in grey (a, b), Dcp-1 is shown in grey (a``, b``) or red (a```, b```). Lower left insets in (a```, b```) are higher magnifications of framed regions. Scale bar as indicated, scale bars in inset represent 25 µm. **(c)** Dot plot of Dcp-1 positive volume fractions for *fkh*- and *fkh, dIAP*-expressing apoptotic clones (light red and dark red, respectively). Data was binned into clone size classes analyzed for Tie-Dye sets (1 cell, 2-6 cells and clones larger than 6 cells). Mean and SEM for each clone size bin is shown. * = p-val < 0.01, ns= not significant. Refer to Appendix, Table 24 for statistical analysis. Single cell clones do not show a significant decrease in proportion of apoptotic volume upon *dIAP*-expression, whereas larger clones do. **(d)** Table listing relative proportions of apoptotic clones for *fkh*-expressing (top) and *fkh, dIAP*-expressing (below) clones binned into the same clone size categories as in (c). Total clone count, apoptotic clone count and percentage of apoptotic clones per bin size are shown. Efficiency of inhibition of apoptosis by *dIAP*-expression was calculated as percentage of apoptosis in *fkh* (n=3 discs, 233 clones) / percentage of apoptosis in *fkh, dIAP* clones (n=3 discs, 290 clones) per bin size. *Contributions: Quantification support c: Hartmann Harz; Data analysis including statistics and representation c, d: Marco La Fortezza.*

3.5.3 Wild-type clones subjected to MWI contractility activate apoptosis

We hypothesized that if apoptosis in small, misspecified cell clusters is specific to MWI contractility, then apoptosis must also be induced in small inverse wild-type cell clusters encircled by misspecified cells. We thus examined inverse clones at early stages after induction of large domains of *fkh*-expressing cells. Strikingly, we indeed observed frequent Dcp-1 activation in small wild-type cell clusters (Figure 31 a-c). Nevertheless, we also detected a lot of apoptosis in the large regions of *fkh*-expressing cells, suggesting that overexpression of *fkh* itself activated the apoptotic pathway independent of MWI contractility. To reduce the amount of ectopic apoptosis and potential non-autonomous effects on interspersed wild-type cells, we analyzed wild-type clones in the context of broad *fkh, dIAP* overexpression. We observed significant suppression of apoptosis in *fkh, dIAP*-expressing tissue, but frequent Dcp-1 positive signals in inverse clones. This suggested that the activation of apoptosis in inverse wild-type clones is due to the MWI contractility and is not caused by unspecific effects from surrounding, dying cells (Figure 31 d-f). To further support our theory, we examined wing disc that ectopically expressed *ey*. Even if apoptosis was observed in *ey*-expressing cells, we found that apoptosis was repeatedly activated in small, inverse wild-type cell clones (Figure 31 g-h).

Our combined results strongly suggest that MWI contractility may drive cell elimination by specifically inducing apoptosis in small clusters of MWI-encircled cells.

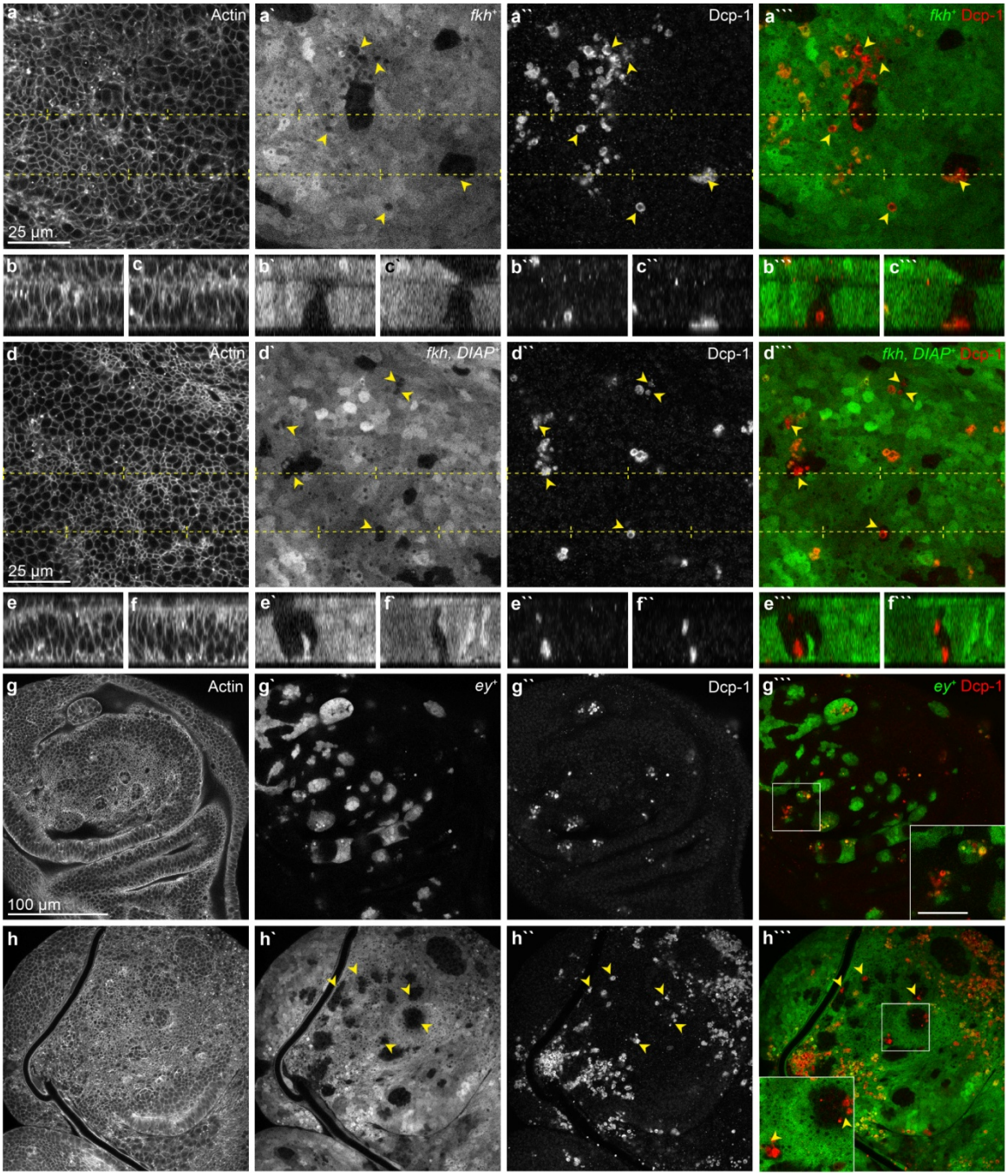

Figure 31: Apoptosis is activated in wild-type cells when surrounded by misspecified cells; (a–c) Xy section (a) and xz cross-section (b, c) of pouch region expressing *fkh* in flip out clones (green in a```-c```; grey in a`-c`) 30 h after induction using a long heat-shock. Actin is shown in grey (a-c), Dcp-1 is shown in grey (a``-c``) or red (a```-c```). Dashed yellow lines in (a) indicate position of cross-section shown in (b, c). **(d-f)** Xy section (d) and xz cross-section (e, f) of pouch region expressing *fkh, dIAP* in flip out clones (green in d```-f``; grey in d`-f`) 30 h after induction using a long heat-shock. Actin is shown in grey (d-f), Dcp-1 is shown in grey (d``-f``) or red (d```-f```). Dashed yellow lines in (d) indicate position of cross-section in (e, f). **(g-h)** Xy sections of wing disc expressing *ey* in flip out clones (green in g```, h```; grey in g`, f`) 30 h after induction using a short (g) and long (h) heat-shock. Actin is shown in grey (g, h), Dcp-1 in grey (g``, h``) or red (g```, h```). **(a-h)** Scale bars are indicated, scale bar in inset (g```, h```) represents 25 µm. Yellow arrows point to regions of apoptosis activation in wild-type cells.

3.5.4 Ectopic expression of *Ras* elicits MWI contractility

We were curious to investigate a potential relevance for our observations to mechanisms that disrupt epithelial integrity in mammalian models of cancer. We wanted to understand specifically, if the occurrence of round clones in imaginal discs upon overexpression of oncogenic *Ras (Ras^{V12})* (Prober and Edgar, 2000) is driven by MWI contractility. Indeed, when we visualized small *Ras^{V12}*-expressing clones, we found that they formed basally extruding cysts in peripheral domains of the wing disc (Figure 32 c, d) (Bell and Thompson, 2014). Excitingly, we found that in these regions, wild-type cell patches surrounded by *Ras^{V12}*-expressing cells underwent interface smoothening and cyst formation (Figure 32 e-g).

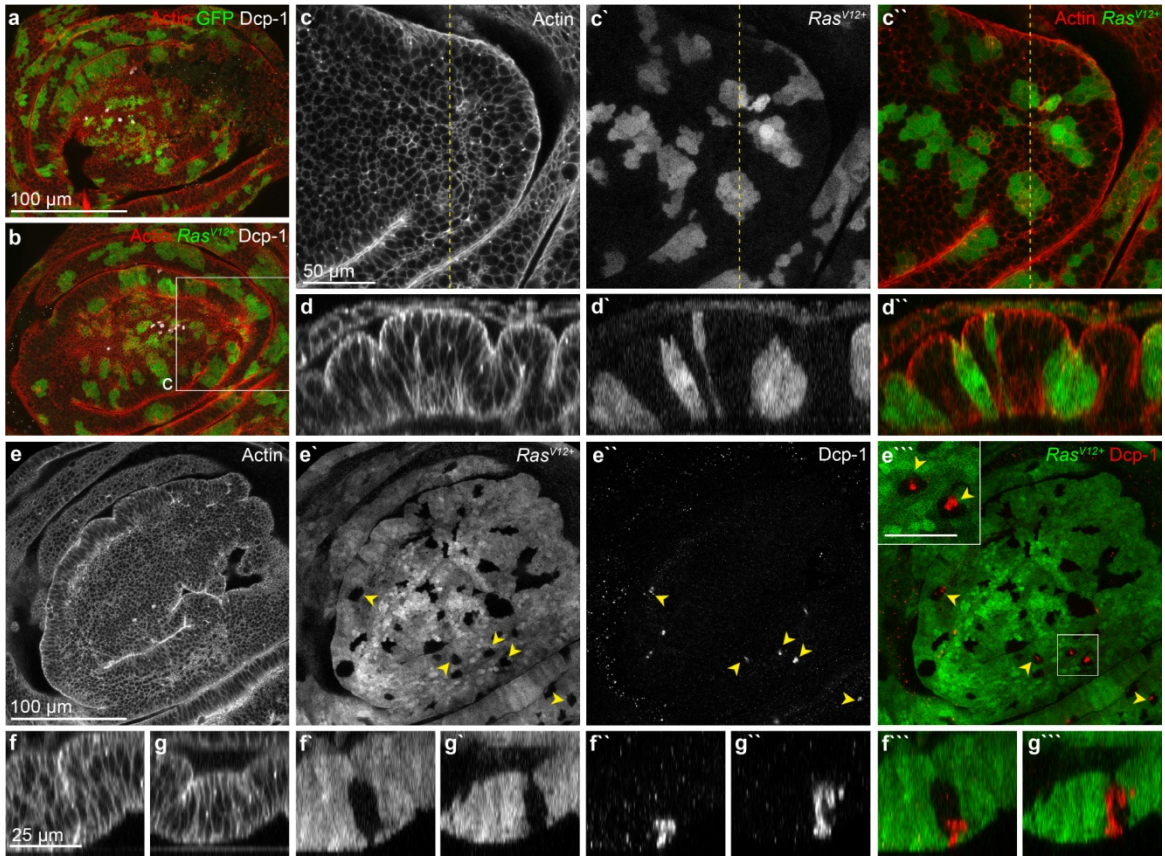

Figure 32: *Ras^{V12}* overexpression leads to cyst formation and activation of apoptosis in wt cells; (a, b) Xy sections of wing discs expressing GFP (a) or *Ras^{V12}* (b) in flip out clones (green) 30 h after induction using a short heat-shock. Actin is shown in red and the apoptosis marker Dcp-1 in grey. Box frames region shown in (c). **(c-d)** Xy section (c) and xz cross-section (d) of pouch region expressing *Ras^{V12}* in flip out clones (green in c``,d``; grey in c`, d`) 30 h after induction. Actin is shown in grey (c, d) or red (c``, d``). Dashed yellow lines in (c) indicate position of cross-section in (d). **(e-g)** Xy section (e) and xz cross-section (f, g) of pouch region expressing *Ras^{V12}* in flip out clones (green in e```-g```; grey in e`-g`) 30 h after induction using a long heat-shock. Actin is shown in grey (e-g), Dcp-1 is shown in grey (e``-g``) or red (e```-g```). Yellow arrows point to regions of apoptotic wild-type cells. Upper left inset in (e```) is higher magnification of framed region. **(a-g)** Scale bars as indicated, scale bar in inset represents 25 µm.

This suggested that oncogenic Ras promotes cyst formation by inducing MWI contractility, likely because Ras signaling also specifies cell fate (Halfar et al., 2001). While we rarely observed apoptosis in wild-type GFP-expressing or Ras^{V12}-transformed cells (Figure 32 a, b), we found that Dcp-1 was frequently activated in small wild-type cell clusters surrounded by Ras^{V12}-expressing cells (Figure 32 e-g). Apoptosis in wild-type cells occurred almost exclusively in the disc periphery where Ras^{V12}-induced MWI-effects are strongest.

Combined, these results reinforce our conclusion that MWI contractility is induced by diverse transcriptional perturbations and that MWI contractility drives cell elimination by activation of apoptosis in small, encircled cell clusters.

3.6 Large misspecified clones smoothen and minimize interface contacts

After analyzing the consequences of small and intermediate-sized misspecified cell clusters on tissue architecture in detail, we concentrated on understanding the effects of larger clones on epithelial structure. Simulations and shape quantifications already showed that large clones were less likely to invaginate, because, according to the Law of Laplace, they experienced less pressure coming from a contractile boundary (Figure 26).

Using an intermediate heat-shock, we wanted to analyze the behavior of larger clones more precisely. Large clones underwent dramatic interface smoothening 30 h after clone induction, accompanied by prominent lateral actin accumulations at the interface (Figure 33 a-c, blue arrows). As predicted by simulations, we did not observe prominent invaginations events, but in some cases only slight apical indentations at the MWI (Figure 33 c, red arrow). Therefore, large misspecified clones did not exhibit dramatic 3-dimensional shape changes, such as apical constriction or invagination seen in small or intermediate clones, respectively. However, big clones minimized their contact area with the neighboring cell populations, thereby ensuring a strict separation between two cell populations invoking similarities to compartment boundaries that separate differently fated cell populations during development (1.3.1).

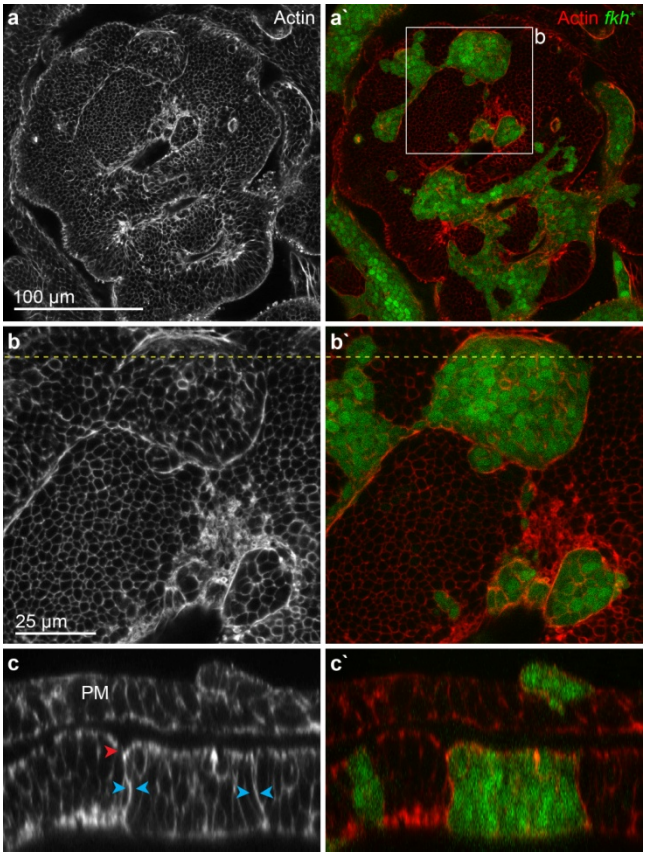

Figure 33: Large misspecified clones minimize interface contacts; Xy (a, b) and xz sections (c) of wing pouch containing *fkh*-expressing clones marked by GFP (green in a`-c`) 30 after clone induction using an intermediate heat-shock. Actin is shown in grey (a-c) or red (a`-c`). Dashed yellow lines in (b) indicate position of cross-section shown in (c). Box in (a`) frames region shown at higher magnification in (b). Scale bars are indicated. Blue arrows point to lateral actin accumulation, red arrow to slight apical indentation at interface.

3.7 Interface contractility may drive fold formation

In the course of our analysis, we observed in xz cross-section a striking phenotypical similarity between endogenous wing disc folds and the invagination of intermediate-sized, misspecified clones. This included the overall shape of the indentation as well as actin localization and cellular arrangements (compare Figure 34 to cysts in e.g. Figure 8, Figure 10 or Figure 13).

The appearance of endogenous folds in the wing imaginal disc is spatially and temporally highly regulated. The most prominent folds separate the blade from the distal hinge (B/DH fold), the distal hinge from the proximal hinge (DH/PH fold) and the proximal hinge from the notum (PH/N fold) (Figure 34, Figure 36). The function of endogenous disc folds is not fully understood, but B/DH folds might have an implication in the bending event during pupariation that forms to the two-layered adult wing (Sui et al., 2012). Because of these phenotypical similarities between

clones subjected to MWI contractility and endogenous folds, we wondered if endogenous folds could arise due to mechanisms involving modulation of lateral contractility.

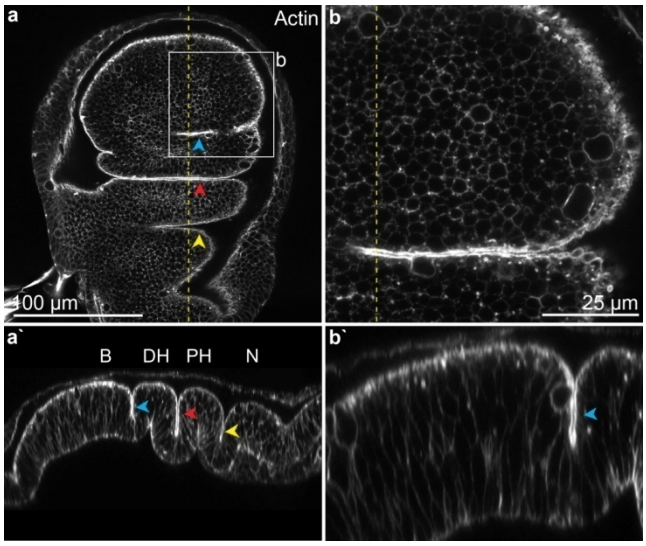

Figure 34: Endogenous folds exhibit similarities to epithelial cysts; Xy (a, b) and xz (a`, b`) sections of wild-type imaginal disc stained for actin. Dashed yellow lines in (a, b) indicate position of cross-section shown in (a`, b`). Box in (a) frames region shown at higher magnification in (b). Scale bars as indicated. Blue arrow marks B/DH fold, red arrow DH/PH fold, yellow arrow PH/N fold.

3.7.1 Stripe-shaped overexpression of *ey* induces ectopic fold formation

Following this idea, we wanted to test if we could induce an ectopic fold by overexpression of transcription factors in a stripe-shaped pattern. To do so, we expressed the eye selector gene *ey* within the *patched (ptc)* expression domain (Figure 35 a).

As described before, expressing *ey* in flip out clones led to cyst formation in the wing imaginal disc, but not in the eye (Figure 11, Figure 12).Visualized by GFP, it can be seen that *ptc* is expressed in a narrow stripe along the AP boundary of the wing imaginal disc. The expression domain is marked by a sharp border on the posterior side, whereas the expression declines gradually on the anterior side (Figure 35 b-d). Indeed, ectopic expression of *ey* using *ptc*-Gal4, led to a strong invagination and fold formation throughout the pouch, hinge and notum region of the wing imaginal disc. Phenotypically, the ectopic fold exhibited high similarity to endogenous folds regarding actin intensities and fold width (Figure 35 b-g).

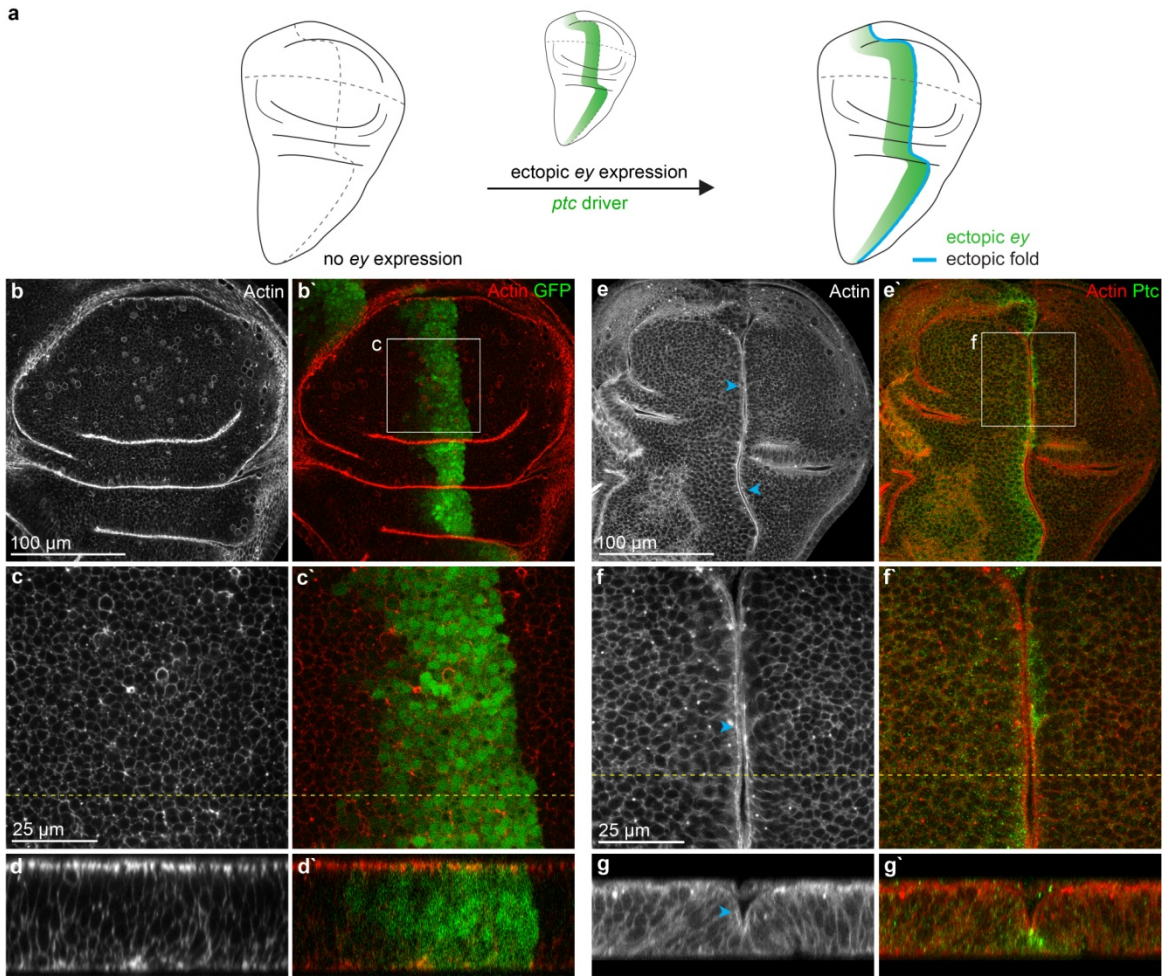

Figure 35: Stripe-shaped overexpression of *ey* induces ectopic fold formation; (a) Schematic representation of wing imaginal disc, where *ey* is usually not expressed (left side). Using the *ptc*-Gal4 driver (middle, green), *ey* is ectopically expressed along the AP boundary (right) leading to an ectopic fold (blue). **(b-g)** Xy (b, c, e, f) and xz sections (d, g) of wing imaginal discs expressing GFP (b-d) and e*y* (e-g) using the *ptc*-Gal4 driver. In (b-d) expression domain is marked by GFP (green in b`-d`), in (e-g) by Ptc staining (green in e`-g`). Actin is shown in grey (b-g) or in red (b`-g`). Dashed yellow lines in (c, f) indicate position of cross-section shown in (d, g). Boxes in (b, e) frame regions shown at higher magnification in (c, f). Scale bars as indicated. Blue arrows point to ectopic fold formation.

3.7.2 Expanding *hth* expression domain alters depths of endogenous folds

Because of these remarkable results, we raised the question whether endogenous expression patterns of transcription factors could induce the same MWI effect that we observed for the clonal expression of ectopic transcription factors. Interestingly, expression domains of several transcription factors established during PD pattering are often delimited by epithelial folds in the wing imaginal disc. In Figure 36, transcription factor expression domains aligning with hinge folds are depicted.

We concentrated on Hth, which is uniformly expressed in the disc at early stages and restricted to the hinge region at later stages (Azpiazu and Morata, 2000). In the 3rd instar larvae,

the Hth expression domain is dorsally bordered by a fold separating the distal hinge from the wing blade (B/DH fold) (Figure 36). We aimed to understand if the apposition of Hth-expressing and non Hth- expressing cells at this location might drive fold formation, which would be in accordance with our interpretation of cyst formation induced by MWI contractility. We have shown before, that clonal expression of *hth* led to cyst formation in the pouch, but not in hinge region coinciding with endogenous Hth expression domain. By driving expression of UAS-*hth* construct using the MS1096-Gal4 driver (Figure 37 a), we expanded the *hth* expression pattern into the pouch region generating a continuous expression pattern over the dorsal B/DH fold.

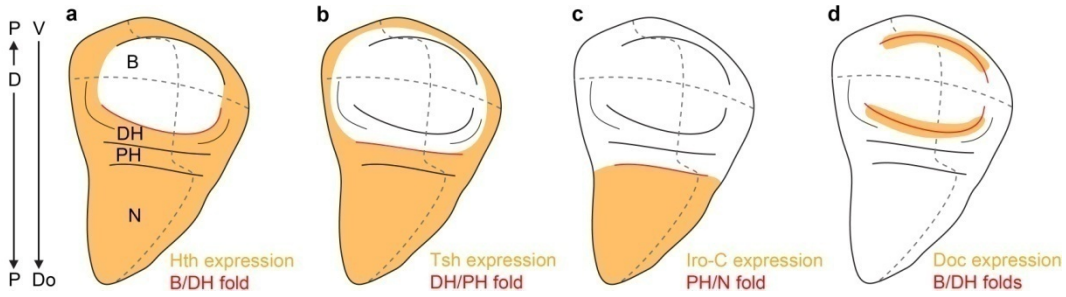

Figure 36: Expression domains of several transcription factors align with epithelial folds; Schematic representation of the expression domains (orange) of Homothorax (Hth) (a), Teashirt (Tsh) (b) (Azpiazu and Morata, 2000; Zirin and Mann, 2004), members of the Iroquois complex (Iro-C) (c) (Cavodeassi et al., 2001; Diez del Corral et al., 1999) and Dorsocross transcription factors (Doc) (d) (Sui et al., 2012). Borders of the expression domains align with endogenous folds (red). P = Proximal, D = Distal, V=Ventral, Do = Dorsal, B= Blade, DH = Distal hinge, PH = Proximal hinge, N= Notum.

Interestingly, this reduced the B/DH fold depth compared to control wild-type folds, whereas the remaining hinge folds were unaffected. In addition, we observed ectopic fold formation along the DV boundary (Figure 37 b-e). Since the MS1096-Gal4 driver is weaker in the ventral compared to the dorsal region of the pouch, this fold might occur due to strong expression differences of *hth*. Both results, the weakening of the B/DH fold and the ectopic fold formation at the DV boundary, support the notion that imaginal disc cells exhibit a quantitative comparison mechanism regarding differently fated cell populations.

These experiments indicated that fold formation in the wing imaginal disc may be based on the apposition of transcriptionally divergent cell populations leading to increased MWI tensions. Due to the extensive patterning of imaginal disc, the apposition of differently patterned cell groups occurs frequently during normal development and might be a prerequisite and cause for endogenous fold formation.

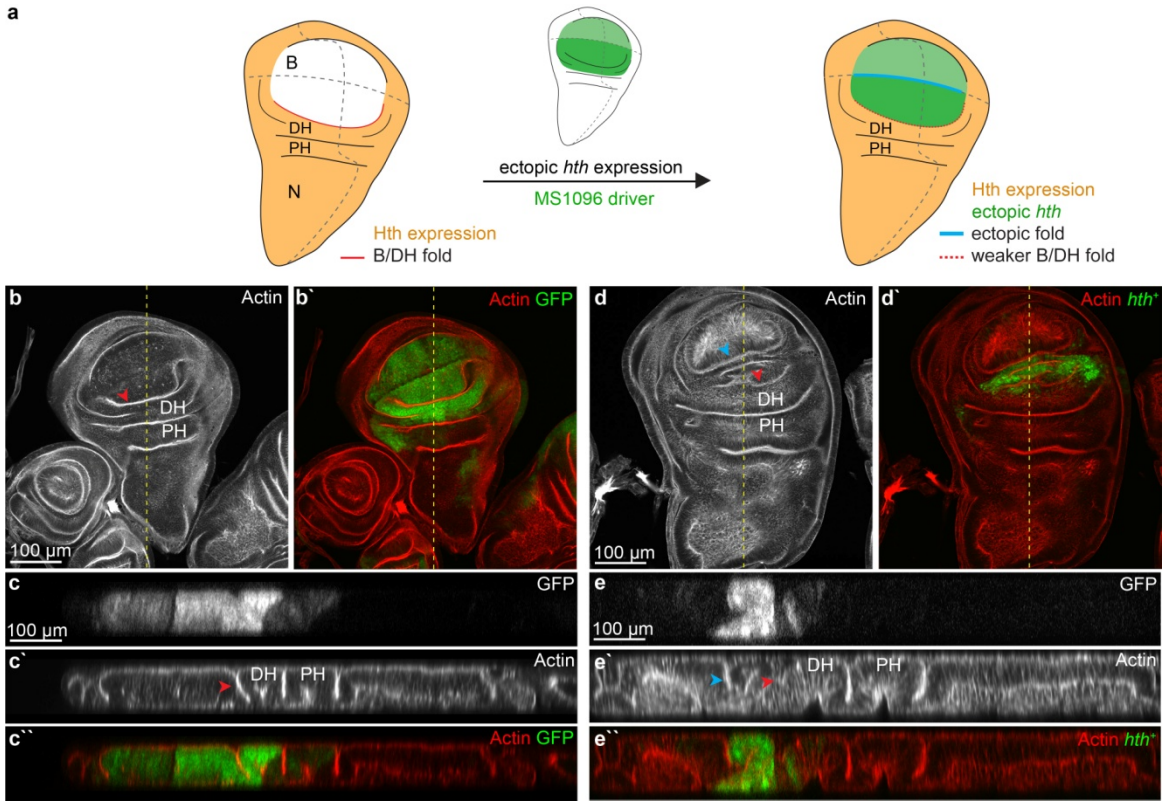

Figure 37: Expanding *hth* expression domain alters depth of endogenous folds; (a) Schematic representation of wing imaginal disc with endogenous Hth expression domain (orange, left side). The expression domain borders the fold between wing blade (B) and distal hinge (DH) (red). Ectopic *hth* expression using the MS1096 driver (green, middle) leads to expression of *hth* also in the pouch (green, right). Expression is ventrally weaker than dorsally (light and dark green). Continuous *hth* expression leads to a weakening of the B/DH fold (dashed red line) and to an ectopic fold along the DV boundary (blue). **(b-e)** Xy (b, d) and xz sections (c, e) of wing imaginal discs expressing GFP (d, c) and *hth* (d, e) using the MS1096-Gal4 driver (grey in c, e or green in b`, d`, c``, e``). Actin is shown in grey (b, d, c`, e`) or red (b`, c``, d`, e``). Dashed yellow lines in (b, d) indicate position of cross-section shown in (c, e). Scale bars are indicated. Red arrows point to fold between blade and distal hinge, blue arrow to ectopic fold formation. PH = proximal hinge, DH = distal hinge, B/DH fold = Blade/Distal hinge fold.

4 Material and Methods

4.1 Mosaic genetic systems

In the course of this study, two powerful *Drosophila* genetic tools and variations of them were used.

(1) FLP/FRT system. This genetic tool can be used to create mosaic tissues with homozygous mutant cells within a wild-type cell population. The technique is based on site-specific recombination events induced by a yeast recombinase (flipase, FLP) binding to its FRT (FLP recognition target) sites. FRT sites are inserted close to the centromere on the chromosome arm where a mutation of interest is located. A fly strain carrying these genetic elements is crossed to a fly carrying a chromosome with a FRT site at exactly the same position and a clonal marker (e.g. GFP) on the corresponding chromosome arm. During mitosis, the homologous chromosomes come into close proximity enabling the FLP to recombine and exchange the chromosome arms in *trans*. The recombinant chromosomes are segregated in course of mitosis, leading to daughter cells that are homozygous for the mutation (GFP negative) or homozygous for the marker (GFP positive). Since the FLP expression can be controlled spatially and temporally by different promoters, this technique makes it possible to study the tissue-specific function of genes, that otherwise would cause lethality if the entire animal carried a mutation in these gene (Golic and Lindquist, 1989; Hafezi and Nystul, 2012; Xu and Rubin, 1993) (Figure 38 a).

(2) *Gal4/UAS flip out system* (Pignoni and Zipursky, 1997). This approach is a combination of the classical GAL4/UAS technique (Brand and Perrimon, 1993) and the flip out technique (Struhl and Basler, 1993) and is widely used for overexpression experiments. The classical Gal4/UAS system is a two-component expression system. It consists of the yeast transcriptional activator protein Gal4 and a transgene under control of the UAS promoter, which is only activated by binding of Gal4. The ability to control Gal4 expression by various cell and tissue-specific enhancers allows highly targeted transgene expression. Separating transcriptional activator and transgene in two individual fly lines makes this technique very powerful and practical in use (del Valle Rodriguez et al., 2012; Hafezi and Nystul, 2012) (Figure 38 b). The flip out technique uses

FLP induced recombination to excise DNA sequences flanked by FRT sites. Since these FRT sites are localized in *cis*, the recombination event is not dependent on chromosome alignments during mitosis. Combining this approach with the Gal4/UAS system increases the level of temporal regulation. The Gal4 sequence is placed downstream of a ubiquitous promoter (act5C), but expression is impeded by insertion of a flip out cassette consisting of transcriptional stop sequences flanked by FRT sites on both ends. Upon expression of the flipase, the flip out cassette is removed and expression of Gal4 is enabled. Consequently, this leads to expression of a UAS-driven clonal marker (e.g. GFP) and the UAS-driven transgene (del Valle Rodriguez et al., 2012; Hafezi and Nystul, 2012) (Figure 38 c).

(3) *Gal80ts system.* This technique is a variation of the classical Gal4/UAS system, which allows not only spatial but also temporal control of gene expression. This is achieved by using a temperature-sensitive version of the yeast Gal4 inhibitor Gal80, called Gal80ts. At low temperatures, Gal80 binds Gal4 thereby blocking its ability to bind to UAS sequences. Increasing the temperature leads to inhibition of Gal80ts repressor activity and allows transcriptional activation by Gal4 (McGuire et al., 2003) (Figure 38 d).

(4) *Tie Dye system*. This system is a variation of the flip out technique using three independent flip out cassettes of which one is Gal4/UAS dependent. Successful excision of the stop cassette sequences can lead to expression of GFP, lacZ or Gal4. Because of the spatially stochastic nature of the recombination events in the tissue, expression of either one, combinations of two or all three marker genes are possible in an individual cell, giving rise to up to 7 genotypically distinct cell populations. This technique makes it possible to trace different cell lineages simultaneously and genetically manipulate a subpopulation at the same time based on Gal4/UAS-transgene expression driven from one cassette. In our case, we made use of the ubi-GFP and act-Gal4, UAS-RFP flip out cassette only to compare frequencies of misspecified clone sizes to wild-type clone sizes in the same disc (Worley et al., 2013) (Figure 38 e).

Note for all cases: Clones are continuous patches of numerous cells with the same genotype that probably originated from one cell. Since the DNA excision of the recombination event is irreversibly inherited to daughter cells, we induced clones in all techniques described above. Therefore, these techniques are suitable for cell lineage tracing and observation of clonal behavior. For all genetic approaches, we used heat-shock driven expression of the flipase. By doing so, we did not only control the time of clone induction but also the amount of genetically altered cells and indirectly the number of cells within one clone by varying the length of heat-shocks.

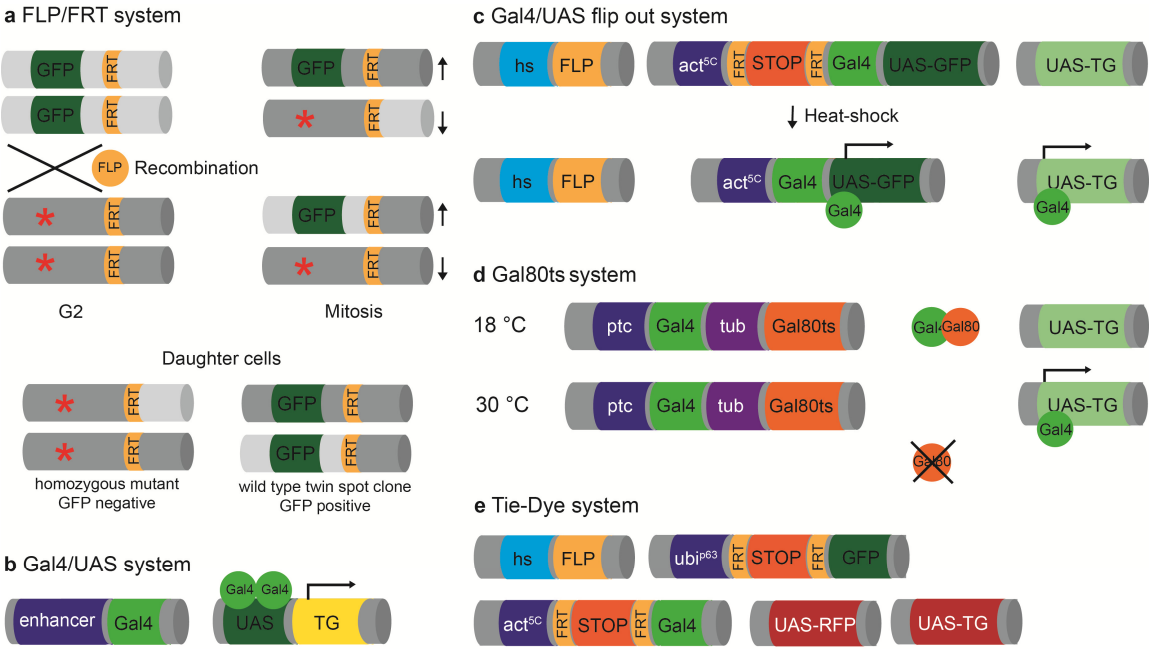

Figure 38: Mosaic genetic systems used in this study; (a) FLP/FRT system. Cell heterozygous for a mutation (asterisk) and a marker gene (GFP) that each lie distal to FRT sites (yellow) undergoes DNA synthesis. After G2, homologous chromosomes align and become located in close proximity. This allows the FLP induced recombination and the exchange of the homologous chromosome arms to occur. Chromosome segregation leads to daughter cells that are either homozygous for the mutation or the marker **(b)** Binary Gal4/UAS system. Expression of Gal4 is controlled by a tissue specific enhancer (blue). Binding of Gal4 (green) to the UAS sequence leads to transcription of the downstream transgene (TG). **(c)** Gal4/UAS flip out system. After heat-shock, the flipase (FLP, yellow) is expressed and excises the transcriptional stop sequence (orange) allowing expression of Gal4 under the act5C promoter (blue) and subsequent transcriptional activation of GFP and transgene (TG) **(d)** Gal80ts system. At 18 °C, transcriptional activation is blocked by binding of Gal80ts (orange) to Gal4 (green). At 30 °C, Gal80ts is inhibited and Gal4 can bind to UAS sequences. In this case, Gal4 and Gal80ts are expressed under the control of ptc and tub promotor (blue and purple), respectively. **(e)** Tie-Dye system. Only two flip out cassettes are shown. Expression of the FLP after heat-shock leads to excision of transcriptional stop sequences (not depicted) allowing expression of downstream genes (GFP and Gal4). Expression of Gal4 leads to subsequent expression of RFP and the transgene (TG). Excision happens randomly either on one cassette or on both cassettes, leading to GFP, RFP or GFP and RFP positive cells.

4.2 Fly husbandry and experimental protocols

For detailed fly genotypes, exact heat-shock lengths and time point of dissection time, refer to Appendix, Table 11. All flies and crosses were kept on standard media and general procedures are described below.

FLP/FRT experiments:

- ► 72 h egg lay at 25 °C
- ► Heat-shock for 40 – 30 min at 37°C
- ► Dissection as indicated (usually 30 h or 54 h after HS)

Gal4/UAS flip out experiments:
► 72 h egg lay at 25 °C
► Heat-shock for 5-30 min at 37°C
► Dissection as indicated (usually 30 h or 54 h after HS)

Staged Gal4/UAS flip out: (Eggcollection, for shape quantifications)
► 7 h egg lay on grape plates
► 24 h AEL, 1st instar larvae are transferred to standard media
► 72 h AEL, vials were heat-shocked for 10, 15 and 25 min
► Dissection 30 h and 54 h after HS

Gal80TS experiments:
► 4-6 days of egg lay at 18 °C
► Temperature shift, 24 h 30 °C
► 1st option: immediate dissection
► 2nd option: dissection after additional 24 h at 18 °C

Tie-Dye experiments:
► 24 h egg lay at 18 °C (to prevent early induction of FLP)
► 8 h at 18 °C
► 32 h AEL, vials are transferred to 25 °C
► Dissection 30 h after HS

4.3 Dissection and immunostaining of imaginal disc

Dissection of imaginal discs was done in a transparent glass dissection dish in 1x PBS using fine forceps and a stereo microscope with flexible swan neck lighting illuminating the samples from the side rather than from above. Using both forceps, the larva was separated in the middle. The front part was inverted by grabbing the mouth parts with the right forceps and pushing the cuticle onto the right forceps using the left one. After that, fat body (non-transparent, white) and parts of the digestive tract (yellow) were removed. Cuticles were transferred to a reaction tube and fixed for 18 min at RT with 4 % paraformaldehyde in PBS. After three times of 10 min washing with PBS + 0.1 % Triton-X-100 (PBT), cuticles were blocked with PBT + 5 % NGS (PBTN) for at least 20 min. Primary antibodies (Table 6) were incubated overnight in PBTN at 4 °C. Secondary antibodies, phalloidin (Table 7) and DAPI (0.25 ng/µl) were incubated for 2-3 h at RT in PBTN followed by three 10 min washing circles. Cuticles were emptied in a glass dissection dish and imaginal discs were separated from the cuticle in PBS. Imaginal discs were transferred onto a microscope slide using a pipette (20 µl). Excessive PBS was removed using the pipette and position of imaginal discs could be carefully adjusted. A drop of antifade medium was added close to the imaginal discs and a coverslip was carefully placed on top. When squeezing of

imaginal disc was not wanted, two strips of double-side tape were attached to the microscope slide and imaginal discs were placed in between.

4.4 qPCR analysis

Expression levels of *fork head (fkh)*, *Abdominal-B (Abd-B)* and *homothrorax (hth)* were analyzed in *Psc-Su(z)2* mutant wing imaginal discs and compared to wild-type conditions. Mutant 3rd instar larvae (*ubxflp/+; FRT42D cell lethal / FRT42D Psc-Su(z)2^{XL26} ; +/+*) and wild-type larvae (*w^{118}*) were dissected in cold Shields&Sang M3 medium using an ice-chilled dissection dish. *w^{118}* discs had been verified as suitable control discs before, since comparison of *ubxflp/+; FRT42D cell lethal / FRT42D; +/+* discs and *w^{118}* discs had showed no significant differences (personal communication with Anne Classen). At least 15 mutant and 30 wild-type discs where collected in RNA*later* and kept on ice. 3 batches of each genotype were dissected and used as biological replicates. RNA was extracted using the RNeasy Mini Kit (Qiagen) and TURBO DNA-free™Kit (Ambion). Sample quality was validated using a Bioanalyzer set-up following standard protocols. For reverse transcription, the Superscript III First strand synthesis Supermix (Invitrogen) was used. Subsequently, samples were treated for 20 min at 37 °C with RNAse H. Transcript detection was performed using the Power SYBR Green PCR Master Mix (Applied Biosystems) with 2-3 technical replicates per sample. Reaction mix composition and PCR protocol are listed in Table 3, primers in Table 4. Ct values of technical replicates were averaged and were normalized to an average of ct values from 3 different cDNA control genes (GAPDH2, CG12703, HP1or CP-1, see also Table 4) using the ΔΔCt method (Livak and Schmittgen, 2001; Winer et al., 1999). Since in wild-type discs, no transcript could be detected for *fkh*, Ct values were set to 40. 3 (for *fkh* and *hth*) or 2 (for *Abd-B*) biological replicates were analyzed. Refer to Appendix, Table 12 for overview of average Ct values.

Table 3: qPCR reaction mix and program; **(a)** Components of qPCR reaction mix and their volumes are listed: Final volume for one reaction was 10 µl. **(b)** PCR program used for qPCR analysis. Time and temperature (Temp) is indicated.

a *Reaction mix*		**b** *PCR program*		
Component	*µl*	*Time*	*Temp*	
2x SYBR Green mix	5	3 min	95 °C	
forward Primer*	0.2			
reverse Primer*	0.2	10 s	95 °C	
cDNA	4	30 s	60 °C	40x
DEPC-water	0.6	30 s	72 °C	
	10			
		10 s	95 °C	
* concentration: 10 µM		Melt curve (0.2 steps)		

Table 4: Primers used for qPCR; Primer number, gene name and primer sequence are listed.

Primer No.	*Gene name*	*Primer sequence*
AC01	GAPDH2 forward	GTGAAGCTGATCTCTTGGTACGAC
AC02	GAPDH2 reverse	CCGCGCCCTAATCTTTAACTTTTAC
AC89	CG12703 forward	ATGGGCATCATCGACAACATTATC
AC90	CG12703 reverse	AGCATGCGTCCGTAGGTGTAGTAG
AC127	Su(var) 205 (HP1) forward	ATCTGTGGTACGTTTTGATTTATTG
AC128	Su(var) 205 (HP1) reverse	AGCAAGCGAAAGTCCGAAGAAC
AC129	Cysteine Proteinase 1 (CP-1) forward	TGGTCATGGAGGAATGGCATACG
AC130	Cysteine Proteinase 1 (CP-1) reverse	ACGCTCCTCGGTTTCATCCTGATAG
AC353	fork head (fkh) forward	GAATCTTTACGAAGCAATCGTTGAA
AC354	fork head (fkh) reverse	ATTCAGAATAACCCCACCAGAATGT
AC394	homothorax (hth) forward	ACTGAACATTGCAATATCCTCGTTG
AC395	homothorax (hth) reverse	ACAAACGTGATAAGGATGCGATTTA
AC461	Abdominal-B (Abd-B) forward	CTGGAACTTCGAGTACGGCTTG
AC462	Abdominal-B (Abd-B) reverse	ATCCCAGCGAGAACTACTCCAG

4.5 Collagenase treatment of imaginal discs

Wing imaginal discs were incubated for 12 min in 200 µl – 400 µl of Collagenase (1000 u/ml + 2 mM $CaCl_2$ and 2 mM $MgCl_2$). Discs were immediately fixed and processed as described above. For better comparison, imaginal discs siblings of one larva were used. One disc was incubated only with PBS as control and the corresponding sibling disc with collagenase. For Quantifications of cell shapes see 4.6.2.

4.6 Image quantification using Fiji

4.6.1 Characterization of clone shape and cell dimensions

We aimed to analyze misspecified clone shapes in order to compare simulations results of the 3D vertex model to experimental outcomes. In addition, we quantified wild-type cell dimensions in order to implement this information in the model.

Extensive analysis of clone shape included measuring of actin intensities (a), clone volume (b), cell numbers (c), clone shape coordinates (d) and clone circularity (e). This analysis was done on staged Gal4/UAS flip out wing imaginal discs expressing *fkh* at different time points (30 h and 54 h) and with different heat-shock conditions (10 min, 15 min and 25 min). Circularity was additionally measured using corresponding GFP-expressing control discs (30 h and 54 h, 10 min and 25 min heat-shocks, staged Gal4/UAS flip out protocol) and Rho^{V14}-expressing discs (54 h, 10

min heat-shock, standard Gal4/UAS flip out protocol). Cell dimensions of wild-type cells were measured in *GFP*-expressing control discs with an additional time point at 0 h after heat-shock (standard Gal4/UAS flip out protocol) and in *fkh*-expressing discs in GFP-negative areas. All measurements were done using Fiji Software (Table 9).

To obtain an overview of the pouch, discs were usually imaged using a 63x objective (zoom 1, xy 0.24 µm, z 1.51 – 2.98 µm). Subsequently, selected regions were imaged at higher magnification (zoom 2.5 or zoom 3, xy 0.08 µm – 0.096 µm, z 0.42 – 1 µm). Refer to Appendix, Table 14 for overview on genotypes, experimental conditions and types of analysis that were applied.

a. Actin intensities

Actin intensities were measured on reconstructed xz-cross-section (reslice tool, 1 µm spacing, top and left) using zoom 1 image stacks of *fkh*-expressing discs. In overlay stacks of phalloidin and clonal marker, the section at a vertical position through the center of radially symmetric clones was identified. Using a 5 px line, apical junctions and lateral surfaces were selected and average fluorescence intensity was measured using the measure tool. For each clone, the two lateral MWI interfaces, up to 8 cell surfaces inside the clone and up to 15 cell surfaces outside the clone near the MWI were measured. Data points were averaged to obtain a single value for wt/wt, wt/mis and mis/mis interfaces for each clone. These values were then normalized to the average mean intensity of actin staining on wt/wt interfaces within the experimental series (done by Anne Classen and Marco La Fortezza) (Figure 39 a) (Appendix, Table 13 for measurements).

b. Clone volumes

To determine volumes of individual *fkh*-expressing clones, the GFP-signal defining the clone volume was used to generate a quantification mask using the Threshold (settings: default, stack histogram, dark background, between 5-30) and Remove outlier (settings: black and white pixel removal with radii 0.5-2 at a threshold of 50, see macro below) functions in Fiji. The resulting binary mask was used to measure clone area in each section using the Analyze particles function (settings: size (micron^2): usually 10-Infinity for images with higher zoom and 5-Infinity for zoom 1 images, Circularity 0.00-1.00). To control if the clone area was well defined, the outlines of the binary mask were merged with the original GFP stack and manually validated. Area measurements in all sections for each clone were summed up and multiplied with z-stack step size to obtain clone volumes (Figure 39 b).

Removing outliers macro – Clone volumes

```
run("Remove Outliers...", "radius=0.5 threshold=50 which=Bright stack");
run("Remove Outliers...", "radius=0.5 threshold=50 which=Bright stack");
run("Remove Outliers...", "radius=0.8 threshold=50 which=Bright stack");
run("Remove Outliers...", "radius=2 threshold=50 which=Dark stack");
```

```
run("Remove Outliers...", "radius=2 threshold=50 which=Dark stack");
run("Remove Outliers...", "radius=5 threshold=50 which=Dark stack");
run("Remove Outliers...", "radius=3 threshold=50 which=Bright stack");
```

c. Cell number and average cell volumes

Nuclei counts were obtained using reslices of zoom 2.5 or zoom 3 image stacks of *fkh*-expressing discs. In an overlay stack between DAPI and clonal marker, nuclei were tracked through each slice and counted with the help of the text tool of Fiji. An average cell volume for each experimental condition was calculated by dividing the clone volume obtained above by nuclear counts for each individual clone. Average cell volumes obtained in higher zoom images were used to extrapolate cell numbers from the GFP-volume measured for additional clones imaged at zoom 1 of the same experimental condition (Figure 39 c) (Appendix, Table 16 for measurements).

d. Experimental clone shape analysis

To quantify experimental clone shapes, we extracted 22 characteristic shape coordinates for individual *fkh*-expressing clones (Figure 39 d). Precision of coordinate selection was verified between higher zoom and zoom 1 image stacks. Zoom 1 image data was then used for further analysis because more clones could be sampled. Coordinates were defined using the Fiji Point picker tool. For clones showing no apical indentation, Points 15-20 were not defined. Following part was performed by Silvanus Alt. From each set of coordinates, 4 characteristic data points were extracted using MATLAB. (1) The apical surface of the wild-type tissue was identified by the least-square fit of a linear function through all apical wild-type coordinates. (2) Tissue height h was defined as the average distance of all basal wild-type coordinates to the apical surface. (3) The absolute apical indentation U_a was defined as the distance of the apical midpoint of the cyst to the apical wild-type surface. (4) The basal deformation U_b was defined as the distance of the basal clone midpoint to a straight line fitted through basal wild-type points. The apical and the basal width W_a and W_b were defined as the distance between the left and right clone interfaces apically and basally, respectively. Finally, the data points were normalized to the wild-type height of the surrounding tissue in order to obtain relative tissue deformations:

$$u_a = \frac{U_a}{h};\quad u_b = \frac{U_b}{h};\quad w_a = \frac{W_a}{h};\quad w_b = \frac{W_b}{h}$$

Each clone was analyzed in two perpendicular cross sections which were averaged. By doing so, we accounted for deviations from a rotationally symmetric clone (Figure 39 d).

e. Clone circularity

A section at exactly a third (for *fkh*-expressing clones and GFP-expressing clones) and a fifth (for Rho^{V14}-expressing clones) of the clone height from the most basal section was identified and used for tracing a clone outline with the help of the polygon tool. Area and perimeter of this region

were measured and circularity was defined using the following equation: $C = 4\pi \frac{Area}{Perimeter^2}$ (Figure 39 e) (Appendix, Table 15 for measurements).

f. Wild-type cell dimensions

Based on phalloidin counterstain, 2 regions within the same stack of GFP-expressing discs were chosen for analysis: 15-25 wild-type cells with (1) small apical cell areas and (2) big apical areas. This approach was chosen to capture the endogenous diversity of cell shapes in wing imaginal discs. The height of cells was defined in reslices at the ROI positions and multiplied by the apical area of all selected cells. An average wild-type cell volume was obtained by dividing the resulting volume through the number of selected cells. Aspect ratios were calculated using the equation $\beta = {height}/{\sqrt{area}}$ (Figure 39 f). In addition, we aimed to analyze volumes of wild-type cells surrounding *fkh*-expressing clones. Therefore we followed the same procedure as described above but chose ROIs in GFP negative regions (Appendix, Table 16 for measurements).

4.6.2 Cell dimensions before and after Collagenase treatments

4 pairs of imaginal discs were quantified. Measurements of cell volumes and calculation of aspect ratios was performed accordingly to 4.6.1 f. See Appendix, Figure 45 for microscopy images and Appendix, Table 16 for measurements.

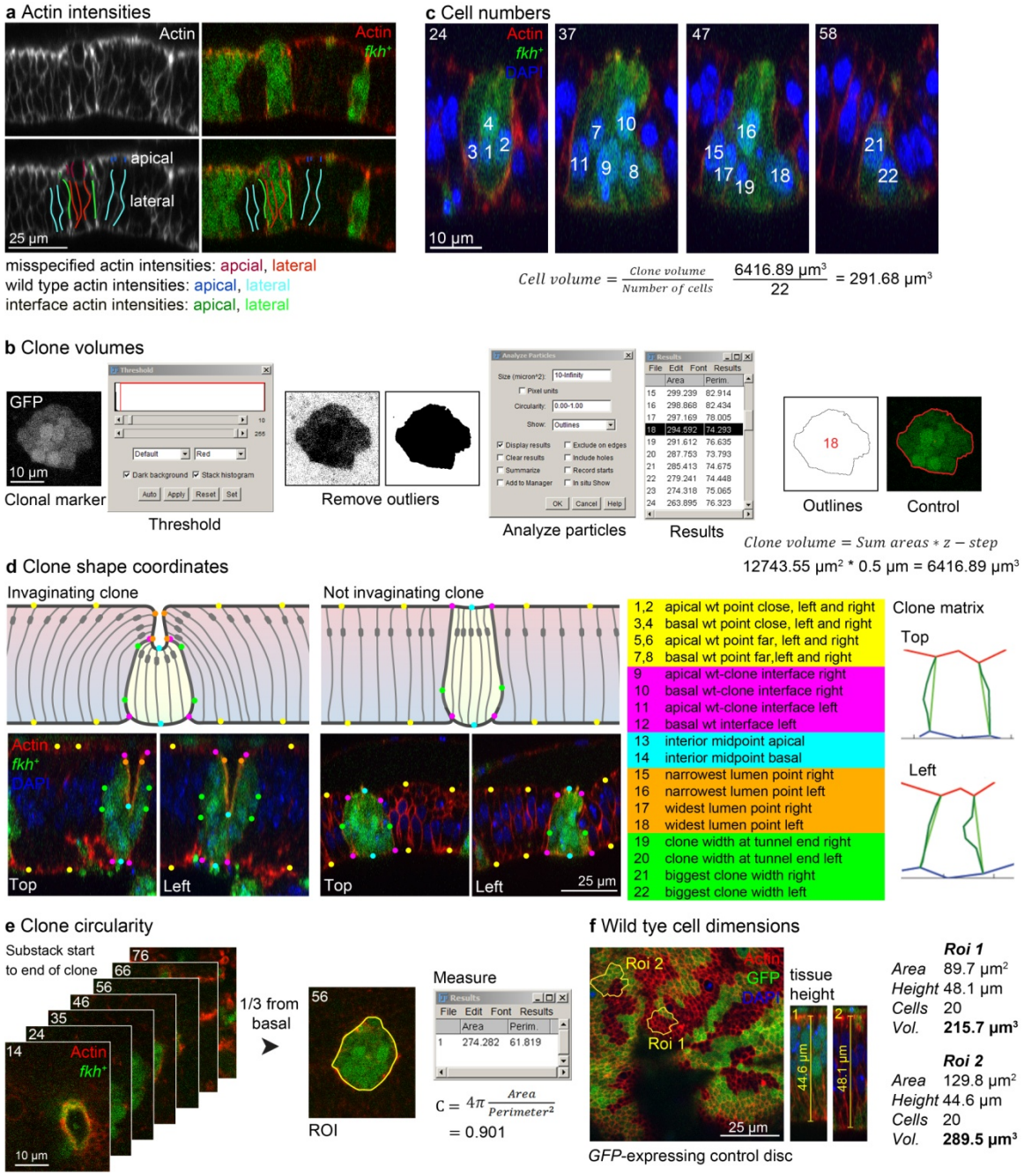

Figure 39: Workflow for analysis of clone shape and cell dimensions; Wing imaginal discs with Gal4/UAS flip out clones expressing *fkh* (green) are shown **(a)** Xz cross-section of wing disc is shown, phalloidin (Actin) staining is presented in grey and red. Actin intensities at cell-cell interfaces were quantified tracing actin staining with a 5 px wide line. The average fluorescence intensities were measured within the misspecified clone (*fkh*$^+$), wild-type cells and at the MWI apically and laterally as indicated by colored lines. **(b)** Single clone marked by GFP is shown in xy. Clone volumes were determined by generating a GFP mask using the Threshold function. Outliers were removed and area of each slice was measured with the Analyzes particle tool. Results were summed up and multiplied with the stack z-step size to obtain clone volumes. Threshold choice was controlled by merging mask outlines with original images (clonal marker is shown in green, mask outline in red) **(c)** Single clone is shown in different xz cross-section. Actin is shown in red, clonal marker in green and DAPI in blue. The number of cells in a clone was defined by counting nuclei in GFP-positive areas using the DAPI staining (blue). Individual nuclei were tracked throughout the clone. Average single cell volume was calculated by dividing the clone volume by the number of cells. **(d)** Scheme of invaginating and non- invaginating clone in xz cross-section is shown. Lighter yellow marks misspecified cells. Experimental images of two

perpendicular cross-sections (Top and Left) are shown below. Clone shape was defined by creating a coordinate matrix of up to 22 points marking characteristic hallmarks of clone shapes (coloured dots in scheme and images, description is shown). These coordinates were used for constructing a vector matrix of clone shape (apical is red, lateral green and basal blue). Compare images of non-invaginating clone to clone matrixes. Not all coordinates could be set in all images. **(e)** Substack of clone in xy is shown. Actin is shown in red, clonal marker in green. Clone circularity was measured by choosing the 1/3 basal section of a clone and tracking the outlines. Clone area and perimeter were measured and circularity was calculated as indicated. **(f)** Wing imaginal disc with Gal4/UAS flip out clones expressing GFP is shown in xy. Wild-type cell dimensions were analyzed by defining 2 ROIs containing 15-20 cells: ROI1 is located in the periphery of the pouch, Roi2 in the center of the disc. Tissue height and areas were measured and cell dimensions were calculated by dividing the area of ROI1 and 2 through the number of cells.

4.6.3 Tie-Dye analysis

Tie-Dye analysis was run on 4 different genotypes: (1) GFP/RFP control discs, n=10 (2) GFP/RFP*, fkh* expressing discs, n=10 (3) GFP/RFP*, fkh*, *dIAP*-expressing discs, n=10 (4) GFP/RFP*, dIAP* expressing discs, n=8. Imaginal discs of all Tie-Dye genotypes were counterstained with DAPI and phalloidin and were imaged using a 20x objective to obtain an overview of the pouch and hinge region (xy 0.45 – 0.54 µm, z=2.01 – 2.18 µm). Image stacks were processed as follows:

► Peripodial membrane clones were excluded from the analysis and deleted in both GFP and RFP channels manually using the polygon and clear function (Figure 40 a).

► Since a majority of the Tie-Dye signal in the notum derived from adepithelial cells, the ROI set for subsequent analysis only considered the pouch and hinge regions (Figure 40 b).

► To identify the optimal fluorescence threshold for RFP and GFP masks, different thresholds were tested. This was done by choosing a threshold, removing outliers (see macro below) and generating outlines of the resulting mask. Mask outlines were merged with original images and checked for visual match with GFP and RFP borders. GFP and RFP thresholds were determined separately for each disc (Figure 40 c), but were validated by optimal fit and similar volume measurements for clones that expressed both GFP and RFP (Figure 40 d).

Removing outlier macro – Tie-Dye

```
run("Remove Outliers...", "radius=0.5 threshold=50 which=Bright stack");
run("Remove Outliers...", "radius=0.5 threshold=50 which=Bright stack");
run("Remove Outliers...", "radius=0.8 threshold=50 which=Bright stack");
run("Remove Outliers...", "radius=2 threshold=50 which=Dark stack");
run("Remove Outliers...", "radius=3 threshold=50 which=Dark stack");
run("Remove Outliers...", "radius=3 threshold=50 which=Bright stack");
```

► We decided to exclude GFP/RFP double-labelled clones from our final analysis because small differences in GFP and RFP masks leads to systematic underestimations of their size. We therefore only selected GFP or RFP positive clones by subtracting the mask of GFP from that of RFP and vice versa using the Image calculator tool. In the resulting masks (GFP only, RFP only) outliers were removed by a series of Remove outlier commands (see above) (Figure 40 e). Mask holes were filled using the Fill holes tool (Figure 40 f).

► The resulting GFP only and RFP only masks were analyzed using the 3D object counter (Version V2.0, Threshold 128, No exclusion of size or edges, Maps to show: Objects, Results table to show: Summary, Statistics). Volume measurements were transferred to Excel (Figure 40 g).

► 3-4 small clones per disc where selected from the object map, identified in original image and nuclei were counted for each clone. The clone volume determined by the 3D analysis was divided by the number of nuclei to obtain an average nuclei volume for each genotype (Figure 40 h) (Appendix, Table 19 for measurements).

► GFP and RFP volumes below an empirically determined minimum cell volume (<60 μm^3) were excluded from the analysis. All remaining data points were binned into multiples of empirically determined average cell volumes for each genotype. Relative RFP clone frequencies were calculated for each chosen bin: (RFP clone count - GFP clone count) / GFP clone count within the analyzed bin. (done by Marco La Fortezza, Appendix, Table 18, Table 19, Table 20, Table 21, Table 22, Table 23 for quantifications).

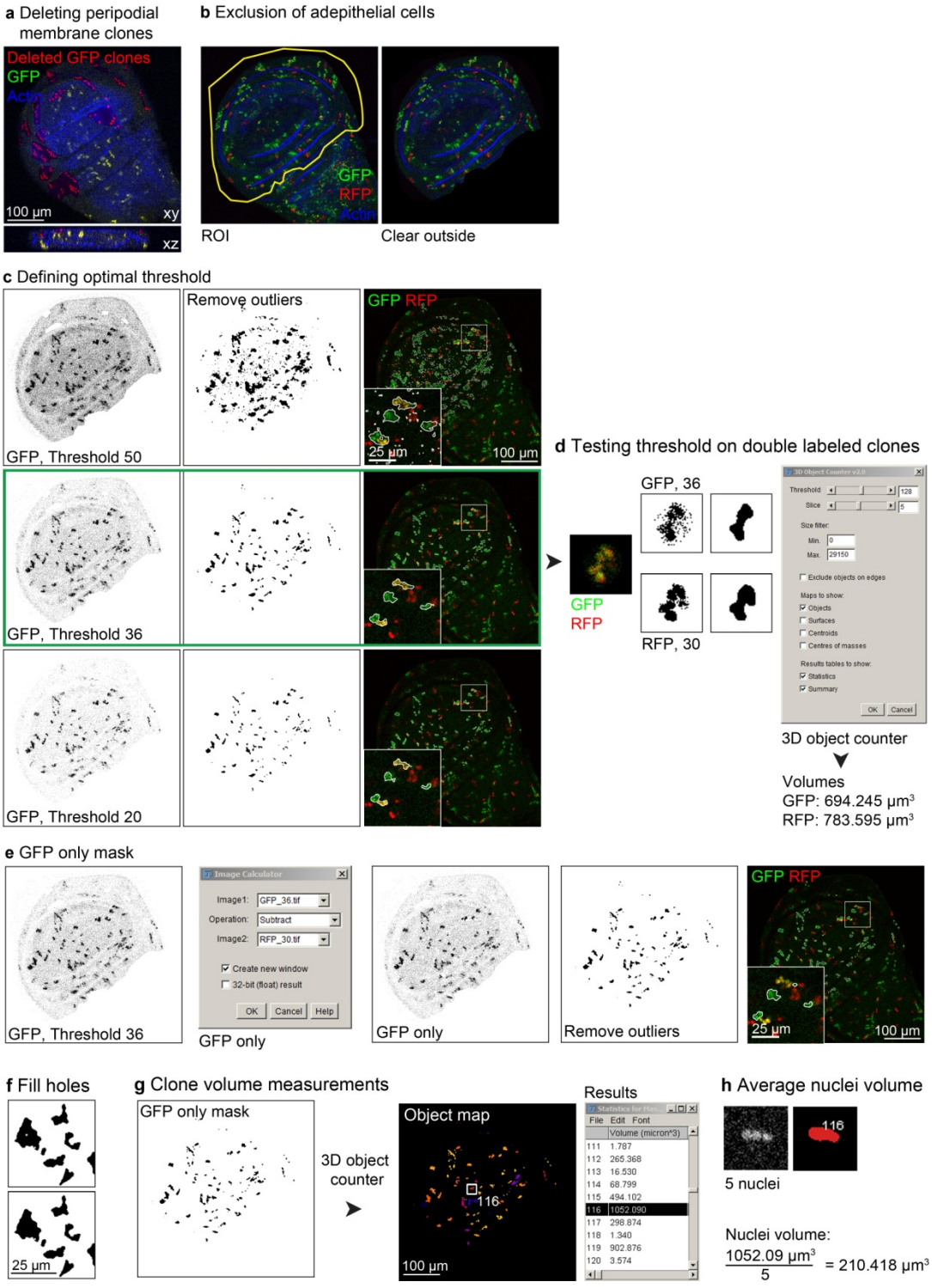

Figure 40: Workflow of Tie-Dye analysis; Figure displays examples for the GFP channel; the same analysis war performed on RFP channels. **(a)** Apical xy section and xz cross-section of wing imaginal disc with neutral GFP clones is shown. DAPI is shown in blue. Peripodial membrane clones were deleted manually and are visualized in red, clones in the columnar epithelium are yellow. **(b)** Wing imaginal disc expressing neutral GFP (green) and RFP (red) clones is shown. DAPI is shown in blue. To exclude adepithelial cells, a ROI (yellow) including only pouch and hinge was set and signal outside was cleared. **(c)** For defining the optimal threshold, different thresholds were applied (first row, threshold 50, 36 and 20), outliers were removed (second row) and mask outlines were merged with original images (third row, GFP clones in green, RFP clones in red, outlines in white). Threshold 36 was determined visually to be most suitable (green box). **(d)** After defining optimal thresholds for GFP and RFP channels of one

disc, thresholds were tested for accordance by measuring volumes in double labeled clones. GFP and RFP volumes were expected to be in a similar range. **(e)** To exclude double labeled clones from the analysis, RFP mask was subtracted from GFP mask using the Image Calculator tool (and vice versa, not shown). **(f)** Holes in masks were filled using the Fill Holes tool. **(g)** Final masks were analyzed using the 3D object counter. Resulting Object map and clone volume results are shown. **(h)** 3-5 different clones were chosen, e.g. Clone 116 in (g). Nuclei were counted using the clonal marker and divided by clone volume to obtain average nuclei volume; (a – h) Scale bar lengths are indicated and refer to related images.

4.6.4 Apoptotic volume analysis

To understand the correlation between clone size and extent of apoptosis, we analyzed the total volume of apoptotic particles within differently sized clones. Gal4/UAS flip out discs expressing *fkh* or *fkh, dIAP* were stained for Dcp-1, DAPI and phalloidin. Discs were imaged using a 63x objective (zoom 1, xy 0.24 µm, z 2.01 – 3.48 µm). 3 wing discs per genotype were analyzed. Images were processed in Fiji as follows:

► Peripodial membrane clones were excluded from the analysis and manually deleted using the polygon and clear function (refer to Figure 40 a).

► Each stack was classified in background, clonal marker (GFP signal) and Dcp-1 signal using the trainable Weka segmentation tool. Mask holes were filled using the Fill Holes function. The quality of the segmentation was verified visually by overlaying mask outlines with original images (Figure 41 a).

► Dcp-1 signal that was not part of a flip out clone was removed by combining Dcp-1 and GFP masks with a logical AND operation of the Image Calculator tool (Figure 41 b).

► Segmented stacks were used to reconstruct 3D objects of clonal marker and Dcp-1 staining. For each clone, the total volume and the volume of all included Dcp-1 sites was determined. All 3D operations were performed with custom macros using the API of the 3D ImageJ Suite (done by Hartmann Harz) (Figure 41 c and d).

► For defining the average cell volume, 3-4 clones were selected per disc, nuclei within the clones were counted and divided by clone volume (refer to Figure 40 h). GFP volumes below an empirically determined minimum cell volume (<50 μm^3) were excluded from the analysis. All remaining data points were binned into multiples of empirically determined average cell volumes for each genotype (done by Marco La Fortezza, Appendix, Table 24 for measurements and statistical test).

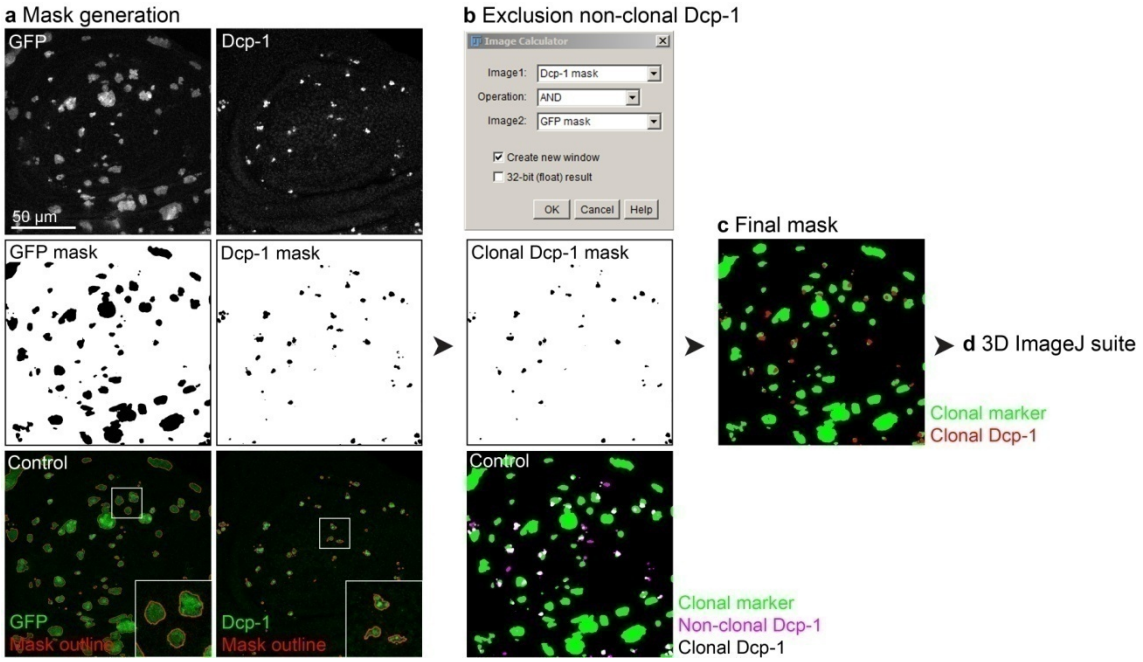

Figure 41: Workflow for analysis of apoptotic volumes; (a) GFP (clonal marker) and Dcp-1 channels (top row) were segmented using the trainable Weka segmentation tool. Binary masks (middle row) where controlled by overlaying mask outlines (red) with original images (green, bottom row). **(b)** Dcp-1 signal that was not part of a flip out clone was excluded from the analysis using the AND operation of the Image calculator tool (top row). The resulting mask only includes Dcp-1 signal inside of a clone (middle row). This step was controlled by merging clonal marker (green), Dcp-1 mask before and after AND operation (bottom row). Clonal marker is shown in green, Dcp-1 staining outside of clones in magenta and clonal Dcp-1 signal in white. **(c)** Final mask only includes clonal Dcp-1 signal (red, clonal marker green) **(d)** Clone volumes in combination with their apoptotic volume was measured using the 3D ImageJ Suite. Scale bar is indicated and refers to all following related images. Insets in (a) represent a 250 % increase in magnification.

4.7 Statistical analysis of imaging data

Every data set was checked for normality of distribution and homogeneity of variances by applying Shapiro's and Bartlett's test, respectively. The α value for each analysis was set to 0.01 (α =0.01). Wilcoxon Signed-Rank test (WSR), Wilcoxon-Mann-Whitney test (WMW) and Welch's t-test were applied to check for statistical significance as indicated in figure legends or Appendix information (done by Marco La Fortezza).

4.8 Fly stocks

Table 5: Fly stocks; Fly stocks are divided in **(a)** wild-type stock, **(b)** drivers (FLP or Gal4), **(c)** UAS constructs, **(d)** mutations, **(e)** GFP-constructs. Source of fly stocks is listed. Bloomington stands for Bloomington *Drosophila* Stock Center at Indiana University.

Fly lines	***Provided by***
a *Wild-type stock*	
w^{118}	Bloomington
b *Drivers*	
$hsflp^{122}$; Sp/CyO GFP; Dr/TM6c	Bloomington
$hsflp^{122}$; FRT42D ubi-eGFP/CyO, GFP	Bloomington
$hsflp^{122}$; FRT42D ubi-mRFP	Bloomington
ubxflp; FRT42D cell-lethal/CTG	Bloomington
$hsflp^{122}$; Sp/CyO GFP; act > y^{+} > GAL4, UAS GFP/TM6b	Bloomington
$hsflp^{122}$; Sp/CyO, ubi-GFP; Act5C.GAL4 (FRT.CD2), UAS-RFP/TM6c	Bloomington
act > CD2 > GAL4, UAS GFP/CyO; MKRS hsflp/TM6b	Bloomington
FRT42D ubi-eGFP/CyO; T155 GAL4, UAS-flp/TM6	Bloomington
MS1096 Gal4/FM7a; UAS-eGFP/CyO	Bloomington
ptc Gal4, $tubGal80^{TS-20}$/ CyO	A. Classen
c *UAS-constructs*	Bloomington
w;UAS-Abd-B	Bloomington
$UAS\text{-}arm^{S10}$	S. Eaton
UAS-ci.HA.wt	Bloomington
UAS-dIAP.HA	Bloomington
UAS-Ecad-GFP	K. Röper
yw; UAS-ey	Bloomington
UAS-hth	N. Azpiazu
UAS-fkh-3xHA	M. Jünger
UAS-fln.HA3	F. Schnorrer
UAS-GFP S56T/CyO	Bloomington
$UAS\text{-}hop^{TumL}$/ CyO	N. Perrimon
UAS-lz	Bloomington
Sp/CyO; UAS-myc/TM6c	I. Hariharan
UAS-p35; Dr/TM6c	Bloomington
Sp/CyO; UAS-p35/TM6c	Bloomington
w; $UAS\text{-}Ras^{V12}$/(CyO); Dr/TM6c	H.Richardson
$UAS\text{-}Rho1^{V14}$	Bloomington
UAS-tkv.CA	Bloomington
w; UAS-Ubx/TM3, Ser	Bloomington
UAS-vg	Bloomington
w; ubi <stop <GFP^{nls}, act5C <stop <$lacZ^{nls}$; Act5C <stop <GAL4, UAS-his2A::RFP/SM5-TM6b	I. Hariharan
d *Mutants*	
w; FRT 42D iso	Bloomington
FRT42D Psc-$Su(z)2^{XL26}$/CyO, ubi-GFP	Bloomington

FRT42D Su(z)2^{1b8}/CyOKG	Bloomington
FRT42D Su(z)2^{1b8}, yki^{B5}/ CTG	Bloomington
hep^{r75}/FM7, ubi-GFP	Bloomington
FRT42D shg^{R69b}/SM6b	U. Tepass
e *GFP or lacZ-constructs*	
sqh:sqh-GFP/CyO; Dr/TM6c	D. Bilder
zip>GFP	Flytrap
Sp/CyO; sqh>MoeGFP/TM6c	D. Kiehart
Nrg-GFP/FM7; Sco/CyO	D. Bilder
vkg>GFP	Flytrap
$puc^{A251.1F3}$ ry^{506}/ TM3Sb	Bloomington
gstD-GFP	D. Bohmann

4.9 Antibodies

4.9.1 Primary antibodies

Table 6: Primary antibodies; Antigen, source, catalogue numbers, manufacturers and working dilutions are listed. DHSB stands for Developmental Studies Hybridoma Bank, Iowa.

Antigen	*Derived from*	*Cat #*	*Provided by*	*Dilution*
aPKC	Rabbit	Sc-216	Santa Cruz Biotechnology	1:1000
Cleaved Dcp-1	Rabbit	9578	Cell signaling Technology	1:250
Coracle (Cora)	Mouse	C566.9	DHSB	1:100
Discs large (Dlg)	Mouse	4F3	DHSB	1:100
E-cadherin (Ecad)	Rat	DCAD2	DHSB	1:100
Patched (Ptc)	Mouse	Apa1	DHSB	1:20
P-Ezrin/radixin/moesin	Rabbit	3149	Cell signaling Technology	1:500
Rho1	Mouse	p1D9	DHSB	1:100
Sqh 1P	Guinea pig	/	Robert Ward	1:400
Wingless (Wg)	Mouse	4D4-s	DHSB	1:100
βPS-integrin	Mouse	CF.6G11	DHSB	1:100

4.9.2 Secondary antibodies and phalloidin

Table 7: Secondary antibodies and phalloidin; Antigen, source, fluorescent label, manufacturer and working dilution are listed.

Antigen	*Derived from*	*Label*	*Provided by*	*Dilution*
Rabbit	Goat	Alexa 488 or 647	Life Technologies GmbH, Darmstadt	1:500
Mouse	Goat			
Guinea pig	Goat	Alexa 647		
Rat	Goat	Alexa 647		
Phalloidin		Alexa 647	Life Technologies GmbH, Darmstadt	1:200
		Alexa 488		1:100
		TRITC	Sigma-Aldrich Chemie GmbH, München	1:400

4.10 Buffer and reagents

Table 8: Buffers and chemicals; Individual manufacturers are listed.

Buffer/ chemicals	*Manufacturer*
Collagenase (CLSPA, Cat # LS005275)	Worthington Biochemical Corporation, Lakewood
DAPI	Sigma-Aldrich Chemie GmbH, München
Normal goat serum	BIOZOL Diagnostica Vertrieb GmbH, München
Paraformaldehyde	Science Services GmbH, München
PBS	Sigma-Aldrich Chemie GmbH, München
Phalloidin Alexa488 and Alexa647	Life Technologies GmbH, Darmstadt
Phalloidin-TRITC	Sigma-Aldrich Chemie GmbH, München
Power SYBR Green Master Mix	Life Technologies GmbH, Darmstadt
RNA*later*	Qiagen GmbH, Hilden
RNase H	Life Technologies GmbH, Darmstadt
RNeasy Mini Kit	Qiagen GmbH, Hilden
Shields&Sang M3 medium	Sigma-Aldrich Chemie GmbH, München
SlowFade® Antifade Kit (Cat # S2828)	Life Technologies GmbH, Darmstadt
SlowFade® Gold Antifade reagent (Cat #S36936)	Life Technologies GmbH, Darmstadt
Superscript III First strand synthesis SuperMix	Life Technologies GmbH, Darmstadt
Triton-X 100	Sigma-Aldrich Chemie GmbH, München
TURBO DNA-free™Kit	Life Technologies GmbH, Darmstadt

4.11 Equipment

Table 9: Technical equipment, consumables and software; **(a)** Technical equipment, **(b)** consumables, **(c)** software; individual manufacturers are listed.

Equipment	*Manufacturer*
a *technical*	
Agilent 2100 Bioanalyzer	Agilent Technologies GmbH, Oberhaching
CFX96 Real-Time PCR Detection System	Bio-Rad Laboratories, Inc; Hercules
Incubator (18 °C), Percival	CLF Plant Climatics GmbH, Wertingen
Incubator (25°C), Mir-154	Panasonic Biomedical Sales, Europe
Nutating Mixer	VWR International GmbH, Darmstadt
Vortex mixer	Scientific Industries, Inc., New York
Water bath	Julabo GmbH, Seelbach
b *Consumables*	
Coverslips	Gerhard Menzel GmbH, Brauschweig
Dissection dish	Science Services GmbH, München
Double sided tape #5338	tesa
Fine forceps	Fine Science Tool, Dumont, Switzerland
Immersion oil 518F	Carl Zeiss, Jena
Microscope slides	Carl Roth GmbH + Co. KG, Karlsruhe

Nail polish (transparent)	p2 cosmetics
Reaction tubes, Rotilabo®	Carl Roth GmbH + Co. KG, Karlsruhe
c *Software*	
Adobe Illustrator CS5.1	Adobe Systems, Inc., San José
Adobe Photoshop CS5.1	Adobe Systems, Inc., San José
Image J1.48 b	Wayne Rasband, National Institues of Health, USA; http://imagej.nih.gov/ij
Office 2007	Microsoft, Redmond

Table 10: Microscopes; Equipment and manufacturers are listed.

Microscope	***Equipment***	***Manufacturer***
Confocal laser scanning microscope Leica TCS Sp5	*Lasers:* Diodenlaser 405 nm, 25 mV Argon Laser 458, 476, 488 and 514 nm DPSS Laser 561 nm, 10 mV HeNe Laser 633 nm, 10 mV *Objectives:* HCX PL APO Lambda Blue 20x 0.7 imm HCX PL APO Lambda Blue 63x 1.4 oil *Software:* Leica Application Suite *Emission filte*rs: detection spectrally adjusted	Leica, Heidelberg
Stereoscopic Zoom Microscope SMZ745	SMZ745 zooming body, C-PS plain focusing stand *Eyepieces:* C-W10XB, 10x/22 *Lightsource:*	Nikon
	KL 1500 LCD with flexible light guides	Schott AG, Mainz
	Halogen lamp 15V/150W, Type 6423FO	Philips, Eindhoven
Fluorescence Stere Stereomicroscope StereoLumar v12	*Optics:* Neolumar S 0.8x FWD 80mm, PI 10x/23 eyepieces *Filters:* 38 HeGFP BP470/40, BP525/50 43 Cy3 BP545/25, BP605/70 *Lightsource:* HXP 120 C	Carl Zeiss, Jena

5 Discussion

With this work, we showed that ectopic expression of transcription factors that specify cell fates causes epithelial cysts of intermediated-sized cell clusters in *Drosophila* imaginal discs. In contrast, small misspecified clones undergo apoptotic extrusion and large clones induce cell segregation by interface minimization. These distinct, clone-size dependent tissue responses are all accompanied by cell non-autonomous enrichment of actomyosin at lateral interfaces between wild-type and misspecified cells. This suggested that the interface might be under higher tension. We aimed provide experimental evidence that higher interface contractility is sufficient and necessary for the observed morphogenetic behaviors, but technical restrictions did not allow us to genetically manipulated specifically only the lateral interfaces between two cell populations. Therefore, we combined experimental approaches and 3D vertex model simulations to demonstrate that interface contractility is the driving force of tissue shape changes that are induced by the apposition of differently fated cell populations. Our work has important implications for understanding the interplay between cell fate patterning and epithelial structure in the course of development and disease, not only in *Drosophila*.

5.1 Mechanics of cyst formation

Using a 3D vertex model of the epithelium combined with a continuum description of the tissue allowed us to identify the mechanical principles driving cyst formation and cell extrusion. In principle, the observed cell shape changes arise from two simple physical effects that drive tissue buckling instability: the law of Laplace and the resistance of the tissue to bending. Furthermore, by confirming predictions of 3D vertex model simulations with experiments *in vivo*, we demonstrated that interface contractility is necessary and sufficient to drive cyst formation.

5.1.1 Introduction of 3rd dimension in epithelial modeling

Previous studies have simulated a tension increase at adherens junctions and described its role in determining interface morphology at compartment boundaries in 2D models (Aliee et al., 2012; Landsberg et al., 2009; Major and Irvine, 2005). However, what had been missing so far, is a physical description of the 3rd dimension along the apical-basal axis and the analysis of morphogenetic behaviors arising from cellular forces acting along this interface dimension. In addition to forces arising from adherens junction, we demonstrated that actomyosin contractility at basolateral interfaces can be extensively increased, which has dramatic consequences for tissue shape. Our novel mechanical description of this 3rd tissue dimension has crucial implications in our understanding of epithelial morphology and force generation during development and disease.

5.1.2 Role of cell-autonomous cell height reductions

As discussed in the introduction, cyst formation in Dpp or Wg signaling compromised cell clusters had been linked to a role for these pathways in regulating columnar cell height. This suggests that cyst formation is caused by cell-autonomous cell height reductions in mutant cells (Widmann and Dahmann, 2009a, b). As shown by our simulations and experiments (Figure 25), changes in the bulk properties of misspecified cell clusters indeed explain cyst formation, but not inverse cyst formation by wild-type cells that are surrounded by misspecified cells. In addition, we observed accumulation of actin and other components of the contractile machinery only at the interface between cyst cells and surrounding cells and not throughout the entire misspecified clone, suggesting that cell-autonomous changes to subcellular actin organization are unlikely to play a role during cyst initiation (Figure 21, Figure 22). Combined, this line of evidences demonstrates clearly that bulk property changes are neither necessary nor sufficient for the initiation of the cyst formation process. Nevertheless, we cannot exclude the possibility that bulk effects are occurring at later stages. As shown in Figure 28, misspecified cells exhibited a significant decrease in cell volume at late stages. Moreover, increased interface contractility could not recapitulate experimental clone shapes at 54 h after clone induction indicated that additional factors influence clone shape at later stages. Late clone shape analysis revealed some similarities to simulations of bulk effects, which suggest that at later stages misspecified cells are changing indeed their clone shape because of cell-autonomous cell aspect ratio changes. It is possible that the bulk effect strength differs between the clonal overexpression of distinct transcription factors as well as the time point of bulk effect initiation. These differences might explain variations in final clone shape behaviors induced by different transcription factors.

5.1.3 A similar change in interface contractility maintains developmental compartment boundaries

Our simulations suggest that higher apical and lateral interface contractility explains all observed size-dependent tissue deformations including cell extrusion and tissue invagination accompanied by interface smoothening. We showed that a simulated 3 fold increase in lateral surface tension and apical line tension accounts for the tissue deformations seen in experiments. Using laser ablation approaches, it was shown previously that apical line tensions at the compartment boundary between anterior and posterior cells fates in the wing imaginal disc is increased by a factor of 2.5 and between the dorsal and ventral compartment by 2.5 to 3 fold. Simulations revealed that this increased tension is necessary and sufficient to generate smooth boundaries and that considering in addition anisotropic tissue stress, oriented cell division and reduced proliferation rates at the boundary could accurately simulated the temporal developmental of the DV boundary (Aliee et al., 2012; Landsberg et al., 2009). Interestingly, the increase in measured tension at compartment boundaries and the increase in simulated interface contractility acting during cell fate misspecification fall into the same range. However, it is important to stress that the experimental and simulation analysis of tension at compartment boundaries is restricted to the 2D plane of adherens junctions. It will be interesting to investigate if enrichment of the actomyosin machinery can be detected basolaterally at compartment boundaries and how addition of a 3-fold increase in basolateral surface tension would influence simulations of compartment boundary functions.

5.1.4 Clone smoothening and cell affinity changes

One prominent feature of clones subjected to MWI contractility is the dramatic smoothening of clone interfaces. This indicates that adjacent, differently fated cell populations minimize their common contact area, a characteristic feature of many developmental processes involving apposition of differently fated cells (Batlle and Wilkinson, 2012; Fagotto, 2014). However, smoothening itself is not sufficient to induce the invaginating phenotype observed during cyst formation. For example, the deregulation of E-cad (Zimmerman et al., 2010) (Figure 42), of the transmembrane proteins Caps and Trn (Milan et al., 2002) or of the homophilic adhesion molecule Echinoid (Ed) (Chang et al., 2011) leads to clone smoothening specifically at adherens junctions, but no invagination is observed. Closer investigation of the degree of lateral smoothening in these different genetic contexts is still outstanding. A lack of lateral smoothening may provide an explanation why genetic manipulation of these adhesion regulators fails to induce a full cystic phenotype. In addition to smoothening, round clones lacking *caps* and *trn* as well as overexpressing clones located in the dorsal compartment do not activate the apoptotic cascade (Milan et al., 2002; Milan et al., 2001).

Taken together, these observations suggests that smoothening induced by altered adhesion functions may be neither sufficient to induce the full range of observed clone shape behavior, nor induce apoptosis as observed for small clones subjected to MWI contractility.

According to the DITH, interfacial tension is regulated by the opposing contributions of adhesion and contractility (1.3.3). Therefore, clone smoothening could be driven either by adhesion or by contractility changes. Since we observed a prominent enrichment of filamentous actin and myosin components apically and especially laterally at the MWI, it is tempting to speculate that contractility is the dominant determinant of clone smoothening. However, the temporal correlation of increased MWI contractility and smoothening, as well as the lack of genetic tools to specifically manipulate interface contractility, makes it challenging to define if MWI contractility is upstream of smoothening. Supporting the idea of predominant contractility, it could be shown that during zebrafish gastrulation, adhesion forces are indeed small compared to those generated by tension and that the function of adhesion mainly lies in the transmission and scaffolding of these forces to neighboring cells (Maitre et al., 2012). However, as adherens junctions are tightly connected to the actin cytoskeleton, we cannot exclude the possibility that cell affinity differences are achieved through the combinatorial action of adhesion and contractility and that this is linked to a cellular comparison mechanism that leads to increased MWI contractility (5.2).

5.2 What is compared between differently fated cells?

5.2.1 Generality of interface contractility

We showed that ectopic expression of several unrelated cell fate specifying transcription factors induces MWI contractility. Misspecification of both selector and selector-like transcription factors led to cyst formation showing that the mechanism of increased MWI contractility does not discriminate between these two major classes of transcription factors. In addition to the transcription factors analyzed by us, several publications have described the occurrence of round or cystic clones in mosaic analysis of fate specification in imaginal discs and neuroepithelia. An overview of these transcription factors is provided in Table 2 and stresses the generality of MWI contractility as tissue-level response to the presence of aberrantly specified cells.

Interestingly, phenotypes similar to cyst formation in *Drosophila* have been shown to occur in the context of the mouse small intestine and colon. The small intestine consists of invaginating crypts and evaginating villi, the colon of crypts and a flat surface epithelium. At the crypt bottom, multipotent stem cells produce transit amplifying cells (TA), which locate to the bottom 2/3 of the crypt. TA cells generate precursor cells that migrate to the upper part of the

crypt, where they finish differentiation as soon as they reach the transition zone from crypt to villus. The villus is completely occupied by differentiated cells, which undergo apoptosis once they reach the tip of the villus. The spatial and temporal coordination of proliferation, differentiation, and apoptosis is essential for homeostasis of the intestinal epithelium and is regulated mainly by Wnt/Wg signaling. Wg/Wnt signaling activity is high at the bottom of the crypt, regulating a stem cell and progenitor cell fate as well as proliferation. Wg/Wnt activity decreases in the direction of cell migration and ongoing differentiation along the crypt-villus axis (Pinto and Clevers, 2005; Reya and Clevers, 2005). Interestingly, cells mutant for *Adenomatous Polyposis Coli (APC)*, a negative regulator of Wnt/Wg signaling, remain within the epithelium at the crypt bottom, but extrude as they migrate into regions of low Wnt/Wg signaling. There, cluster of *APC* mutant cells form outpocketings and polyps, which are clinically staged as adenomas and which develop into carcinomas upon acquisition of additional mutations (Barker et al., 2009; van de Wetering et al., 2002). Adenoma formation exhibits striking similarities to MWI induced cyst formation in *Drosophila.* Both processes are dependent on position of mutant cell within a signaling gradient and lead to aberrant, epithelial structures with phenotypical similarities. These include epithelial outpocketing or invagination and lumen formation, during which epithelial polarity is preserved. Due to these striking similarities, it is tempting to speculate that adenomas are caused by induction of interface contractility at mutant-wild-type cell boundaries. Future studies should analyze the localization of actomyosin components in this context to elucidate potential contributions to the outpocketing of mutant cells located in regions of surrounding cells with different fates. Interestingly, Eph signaling is implicated in compartmentalization along the crypt-villus axis and during colorectal cancer progression and might therefore provide link to actomyosin regulation at cellular interfaces (5.2.4) (Batlle et al., 2002; Clevers and Batlle, 2006; Cortina et al., 2007).

In summary, given the diversity of transcription factors investigated in *Drosophila* and the possibility of interface contractility in the mammalian system, we suggest that a very general mechanism must underlie these observations. However, so far, we do not understand which cues epithelial cells utilize to detect different cell fates and what a common signaling pathway may be, but possible scenarios are discussed below.

5.2.2 Differential adhesion and homophilic bindings

Clones subjected to MWI contractility exhibit dramatic smoothening and clone rounding. This reflects differences in cell affinity, a term describing the cellular tendency to preferably cluster together with the same cell type (1.3.3). In several previous studies, clone rounding of misspecified clones had been linked to a function of the respective transcription factor in regulating cell adhesion (Liu et al., 2000; Organista and De Celis, 2013; Shen et al., 2010; Villa-

Cuesta et al., 2007; Worley et al., 2013). However, specific cell surface molecules or signaling pathways mediating this response have only been proposed for *sal*-expressing clones and include Caps, Trn and FasIII (Milan et al., 2002; Organista and De Celis, 2013). Nevertheless, differential adhesion could be a possible mechanism how differently fated cell populations detect differences and initiate the process of increased MWI contractility.

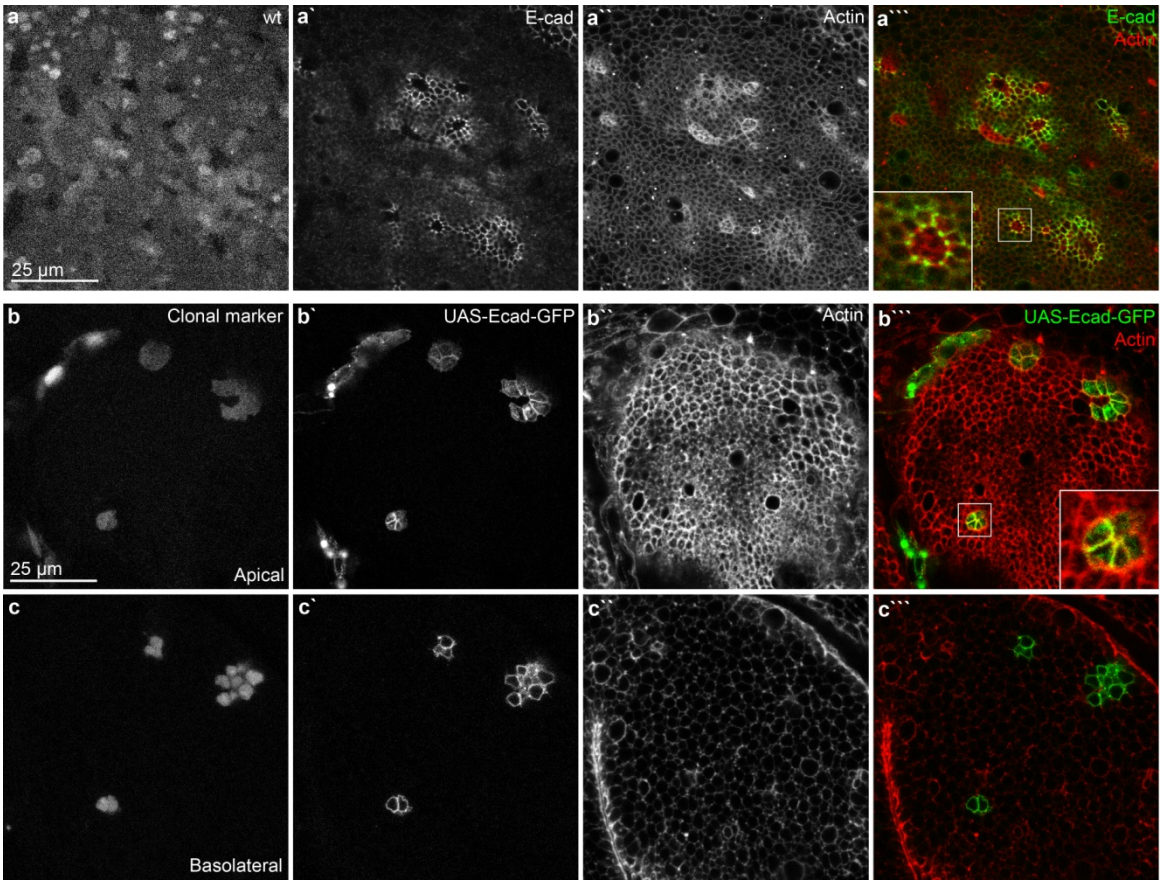

Figure 42: Clones mutant for or overexpressing *E-cad* show smoothening but no invagination; (a) Xy section of wing imaginal discs containing shg^{R69b} (null-allele for *E-cad*) mutant clones 30 h after induction using the FLP/FRT system. Wild-type cells are marked by RFP (a), mutant clones by the absence of RFP: Actin is shown in grey (a``) or red (a```). E-cad staining shows loss of *E-cad* in mutant clones (grey in a`, green in a```). Mutant clones smoothen but do not invaginate. Note the accumulation of actin around *E-cad* mutant clones (a``). **(b, c)** Apical (b) and basolateral (c) xy sections of wing imaginal discs overexpressing *Ecad-GFP* (grey in b`, c`, green in b```, c```) in flip out clones 30 h after a short heat-shock. The clonal marker RFP is shown in (b, c). Actin is shown in grey (b``, c``) or red (b```, c```). Note apical smoothening. Scale bars as indicated.

We therefore analyzed the localization several intercellular junctions and polarity markers during cyst formation (Figure 19 and data not shown). This analysis included markers known to mediate extracellular homophilic interactions, such as E-cad, Crb and Nrg. We found that junctional and polarity markers distributed normally and no consistent changes could be observed between wild type and aberrantly specified cells (Figure 19). However, this analysis is far from complete, since we did not study several adhesion molecules, such Ed or Fas III or did analyze

activation or phosphorylation states. Moreover, we manipulated cellular adhesion properties in clones by mutating or overexpressing *E-cad*. Clones exhibited smoothening at apical adherens junctions, but basolateral smoothening or actin enrichment at the basolateral interface of clones was not observed (Figure 42). Similarly, overexpression or knock-down of a list of other junctional or polarity regulators in clonal assays was not sufficient to induce cyst formation (data not shown).

In summary, this suggests that changes to adhesion or cell affinity may not be the only comparison cue utilized by differently fated cells to elicit the program of MWI contractility. We cannot exclude the possibility that differential adhesion mechanisms induce and regulate MWI contractility more downstream via unknown mechanisms. Many more experiments are clearly needed to explore the contribution of adhesion as a cell fate comparison cue regulating interface contractility.

5.2.3 Metabolic changes as signals mediating cell-cell comparison

According to the concept of DAH, the final comparison cues reside on the extracellular surface. Alternatively, one could consider differences in metabolic states as possible and general read-outs of fate differences between cells, similar to signals that are thought to mediate cell-cell competition (Levayer and Moreno, 2013). Due to the transcriptional diversity implicated in MWI contractility, we imagine that very general cellular pathways might be altered and used as comparison cues. We speculate that such pathways include, for example, Calcium signaling or oxidative stress sensing. Therefore, we made use of the oxidative stress sensor gstD-GFP in the context of *fkh* and *ci*-overexpressing clones (Sykiotis and Bohmann, 2008). Indeed, *fkh*-overexpressing cells showed reporter activity both in the context of short and long heat-shock induced experiments (Figure 43 b, c). This suggested that *fkh*-overexpressing cells are under oxidative stress in contrast to wild type cells, which could provide a comparison cue for the detection of metabolic differences. However, in the case of clonal *ci*-overexpression, we did not observe similar results (Figure 43 d), suggesting that oxidative stress is not a common feature potentially acting upstream of MWI contractility induced cyst formation.

In addition to the identity of a metabolic pathway that could be used for fate comparison, it is completely unclear how differences between two cell populations are detected and translated into increased interface contractility. In the case of calcium signaling, detection of calcium level differences could be directly achieved at gap junctions, which allow for exchange of small signaling molecules between neighboring cells (Bauer et al., 2005). However, a mechanism connecting gap junctions to actin regulation has, to our knowledge, not been identified. Alternatively, metabolic differences could induce expression or alterations in signaling properties of specific cell surface molecules. A mismatch in cell surface molecule activity could signal cell

fate differences between neighboring cells and elicit intracellular signals that increase contractility at the mismatched interfaces. A link between a mismatch in cell surface molecules and actin regulation has already been shown for Eph signaling and Toll-receptors (5.2.4) (Fagotto et al., 2014; Pare et al., 2014).

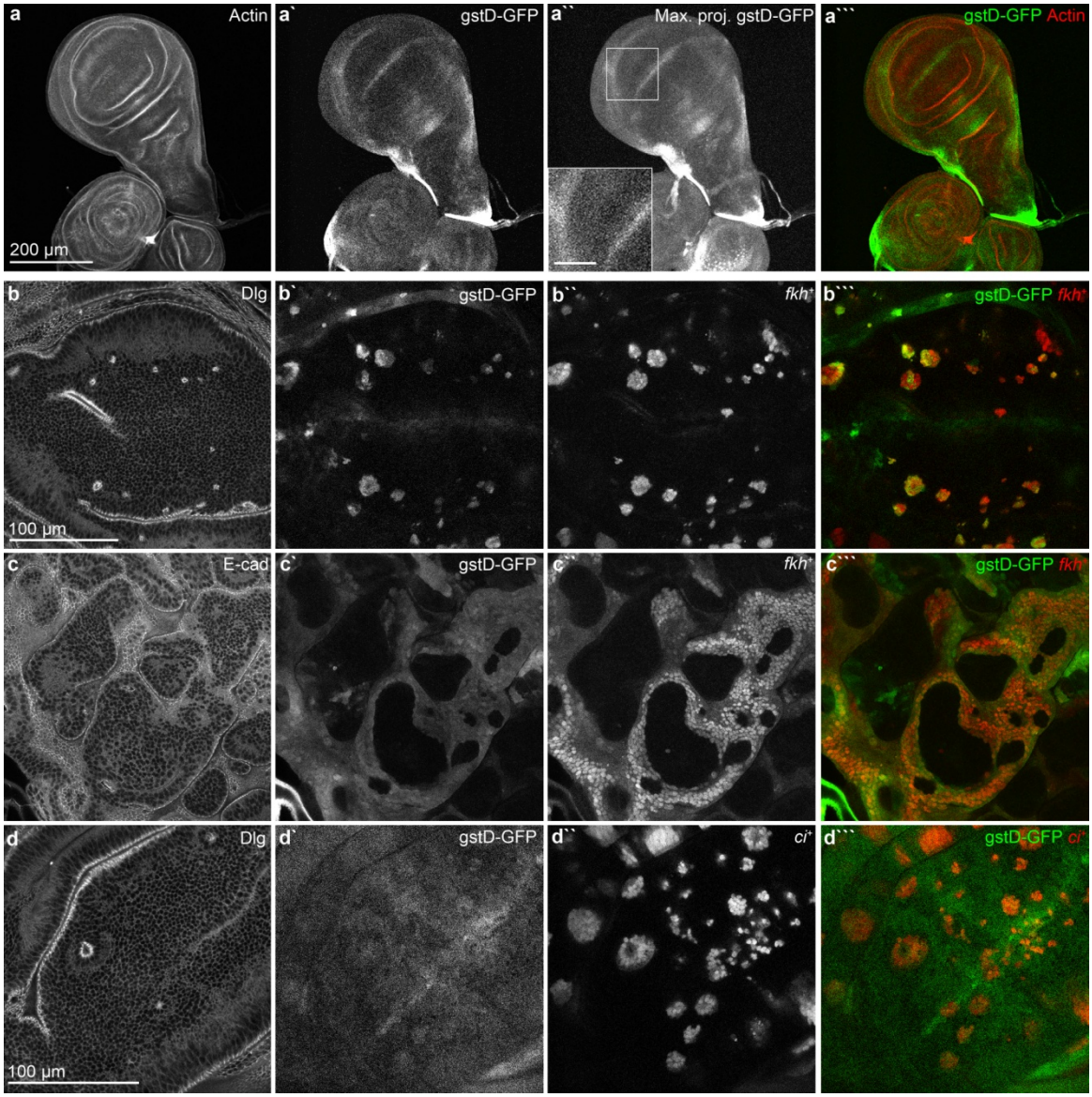

Figure 43: *fkh* but not *ci*-expressing cells are under oxidative stress; (a) Xy section of wing imaginal disc expressing the oxidative stress sensor gstD-GFP (grey in a`, maximum projection in a``, red in a```). Actin is shown in grey (a) or red (a```). Note the specific pattern along the DV boundary around the pouch and at the edges of the imaginal disc. Lower left inset in (a``) is a higher magnification of framed region. Scale bar as indicated, scale bar in inset represents 100 µm. **(b-c)** Xy sections of wing imaginal discs expressing *fkh* (b, c) and *ci* (d) in flip out clones 54 h after heat-shock using a short (b, d) or long (c) heat-shock. gstD-GFP expression pattern is shown in in grey (b`-d`) or red (b```-d```). Actin is shown in grey (b-d), clonal marker in grey (b``) and red (b```-d```). Scale bar as indicated. Note that *fkh*-expressing are under oxidative stress (c d), whereas *ci*-expressing cells are not (d). Wild-type cells that invaginate are do not show gstD-GFP expression (c).

5.2.4 Cell surface proteins and heterophilic binding

Eph signaling has emerged as an attractive candidate connecting cell surface cues to the regulation of cytoskeleton components. Heterotypic binding of Eph receptors to their ligands activates several downstream signaling pathways, including the regulation of actomyosin components. Since both the Eph receptors as well as the ligands are capable of signal transduction, activation of Eph signaling is an interesting model for the detection of differences and the induction of increased actomyosin contractility at both sides of the interface (Cayuso et al., 2015). In fact, Eph signaling components are differentially expressed in specific rhombomere lineages during mouse development and appear to be required to establish sharp, actomyosin rich lineage boundaries (Calzolari et al., 2014). Future experiments could address the questions if Eph signaling is regulated by cyst-inducing transcription factors and if misregulation could have any implications in increased MWI contractility.

During convergent extension, tissues elongate in one specific direction through spatially organized cell intercalations, which are driven by orientated actomyosin contractility. The authors of a recent study showed that transmembrane molecules belonging to the Toll family, establish this positional information through heterophilic receptor interactions (Pare et al., 2014). Although the exact linkage between the toll receptors and the actomyosin contractile network is still missing, this study, similarly to Eph signaling, links cell surface molecules capable of signal transduction, to the regulation of actomyosin contractility.

Further supporting the concept of cell surface cues acting as signal-inducing detectors of cell fate differences, Milan and colleagues showed that the transmembrane proteins Caps and Trn are ligands providing cell identity cues between neighboring cells. They suggest that Caps and Trn binding to cell surface receptors on neighboring cells elicits survival signals. Loss of ligand expression in misspecified cells leads to compromised ligand-receptor binding and might prompt neighboring cells to induce apoptosis in misspecified cells. They specifically observed that *sal*-overexpressing clones, in which *caps* and *trn* expression is lost, undergo apoptosis in lateral wing disc region, where Caps and Trn are endogenously expressed. *caps* and *trn* re-expression was sufficient to rescue clone survival. However, several observations led the authors to the conclusion that Caps and Trn do not serve as common survival factors and that additional cell interactions engaged in presenting cell fate decision and survival cues must exist. For example, the recovery of misspecified clones by *caps* and *trn* re-expression was only observed in their endogenous expression domains, which are restricted to the dorsal compartment early in wing disc development and to lateral regions at later stages (Milan et al., 2002; Milan et al., 2001). So far, the nature of the cell surface receptor involved in Caps and Trn binding remains elusive, as well as the possible contribution of actomyosin contractility to apoptotic elimination and clone rounding. However, it would be interesting to see if *caps* and *trn* are misregulated in cyst-forming

contexts and if actomyosin levels or distributions are changed in clones overexpressing *caps* or *trn*.

In the future, it will be crucial to determine if and which of these cell surface molecules are involved in the increase of MWI contractility. Importantly, the mechanisms of differential adhesion, metabolic cues and cell surface signals might not exclude each other, but could act in combinatorial and interdependent pathways. Eph signaling, for example, was shown to also regulate adhesion, positively in regions of low Eph activation or negatively through cleavage of E-cad molecules (Cayuso et al., 2015; Hansen et al., 2004; Solanas et al., 2011). Therefore, Eph-elicited cell surface signals at MWI interfaces could connect contractility generation to differential adhesion.

5.3 Interface contractility as potent error correction mechanism

We suggest that interface contractility is a potent mechanism to eliminate aberrantly specified clones from the epithelium in order to maintain proper tissue patterning and epithelial integrity. The extrusion of misspecified cell clusters is size-dependent with cell cluster up to 6 cells being removed most efficiently (Figure 29). Since small cell cluster experience more pressure from MWI tensions compared to big clones, we suggest that MWI tensions acting on big clones are not strong enough to elicit an extrusion process. This observation may convey the impression that interface contractility is not a potent error correction mechanism, as size-dependent extrusion of larger clones initiates the formation of aberrant cyst structures. However, we assume that most mutations in nature arise on a single cell level and are therefore subject to MWI mediated cell elimination (5.4, Figure 44 a, b).

5.3.1 Interface contractility does not induce live cell extrusion

As shown in Figure 29, cell elimination of small cell clusters by MWI contractility depends on the activation of the apoptotic pathway. Therefore, MWI contractility causes cell elimination by inducing cell death, rather than by directly driving mechanical live cell extrusion which was observed in the context of cell crowding (Eisenhoffer et al., 2012; Marinari et al., 2012). Our experiments suggest that small *fkh*-expressing clones are subjected to stronger apoptotic stimuli than larger clones, as they contain proportionally more apoptotic cells (Figure 30). The apoptotic stimuli may arise indirectly from strong apical constriction, which was observed in our simulations and experiments. Apical constriction may limit the apical surface area available for survival signals (Fletcher et al., 2015). This is consistent with the survival of large

clones undergoing MWI-induced cyst formation when their apical face expands into a large cyst lumen after initial invagination events causing apical constriction.

Recent studies illustrate the differences between live cell and apoptotic extrusion on a mechanistic level. Whereas progressive loss of apical area is associated with apoptotic extrusion, live cells leaving the epithelium first undergo loss of individual cell junctions and significant neighbor exchanges (Marinari et al., 2012). It will be interesting to distinguish if different localization of cellular forces and mechanical parameters regulate these distinct processes.

5.3.2 Morphogenetic apoptosis and short range interactions

As discussed above (1.4.3 a), morphogenetic apoptosis describes JNK-dependent induction of apoptosis where discontinuities in Wg and Dpp morphogen gradients occur. Similar to interface contractility, morphogenetic apoptosis removes aberrantly specified cells from the tissue to restore a smooth morphogen gradient (Adachi-Yamada and O'Connor, 2002). In the respective study, localization of actomyosin components as well as shapes of clones deregulating Wg or Dpp components were not analyzed in detail. Our own experiments show that clones ectopically activating Dpp and Wg signaling invaginate and form cysts as a result of MWI interface contractility (Figure 15). This suggests that morphogenetic apoptosis might be also driven by an increase in MWI tension. However, it remains elusive if morphogenetic apoptosis displays the same size-dependent clonal extrusion as shown for interface contractility. In addition, we did not specifically address the importance of activated JNK signaling for extrusion of small clones by increased interface contractility (5.3.4). Therefore, we cannot draw a final conclusion regarding the possibility that morphogenetic apoptosis and increased interface contractility are the same or two distinct mechanisms.

In agreement with our results, clones overexpressing the transcription factors *salm* and *salr* undergo cyst formation in regions of low endogenous expression (Organista and De Celis, 2013). The frequency of *sal*-overexpressing clones outside the endogenous expression regions can be increased by blocking apoptosis, suggesting that the majority of clones are normally lost from the epithelium by an apoptosis-dependent mechanism. This mechanism is likely to be the same we observe for misspecified clones experiencing interface contractility. Interestingly, co-expression of the cell surface proteins Capricious (Caps) and Tartan (Trn) leads to the recovery of *sal*-overexpressing clones comparable to blocking apoptosis. The authors suggest that these surface proteins act as ligands for the neighboring cells thereby ensuring survival. Therefore, *sal*-overexpressing clones are lost from the epithelium because they negatively regulate *caps* and *trn* (Milan et al., 2002). We cannot exclude the possibility, that Caps and Trn play also a role in eliminating clones subjected to increased interface contractility. However, several observations speak against a mechanism solely relying on these two transmembrane proteins. Most

prominently, the authors show that *caps* and *trn* co-expression only rescues clone survival in the lateral regions of the wing imaginal disc where Caps and Trn are endogenously expressed (Milan et al., 2002). *fkh*-expressing clones, however, do not exhibit a position-dependent extrusion. Furthermore, morphogenetic apoptosis induced by the overexpression of a dominant-active version of the Dpp receptor *tkv* cannot be blocked by *caps* co-expression (Adachi-Yamada and O'Connor, 2004). Therefore, we conclude that deregulation of *caps* and *trn* alone cannot explain all apoptotic events occurring upon misspecification of cells. However, it supports the exciting idea that several cell surface molecules are employed to signal cellular fate decision between neighboring cells enabling them to compare each other and detect perturbations (5.2.4).

5.3.3 Cell competition is distinct to interface contractility

As discussed in section 1.4.3 b, cell competition is an interface-dependent tissue surveillance mechanism. During this process, metabolically unfit 'loser' cells that touch metabolically fitter 'winner' cells are induced to undergo apoptosis. Several arguments suggest that cell competition is mechanistically distinct from increased interface contractility. Cell competition has not been shown to cause contractile changes at interfaces between winner and loser cells or clone smoothening. In addition, cell competition always acts unidirectional by eliminating loser cells, even if they surround a cluster of winner cells (Levayer and Moreno, 2013). In contrast, interface contractility extrudes the encircled cell clusters regardless of their metabolic state since misspecified as well as wild-type cells extrude via apoptosis (Figure 31). Experiments changing the metabolic fitness status of misspecified cells did not prevent MWI-induced cyst formation (data not shown). This suggests that epithelial tissues likely evolved multiple mechanisms to eliminate homeostatic perturbations, either in metabolic activity (cell competition) or cell fate specification (interface contractility). Future studies should aim to provide insight into which triggers initiate one process or the other.

5.3.4 JNK signaling and interface contractility

Several error correction mechanisms including cell competition, intrinsic tumor suppression or morphogenetic apoptosis (1.4.3) rely on JNK activation for apoptotic clearance of aberrant cells. As shown in Figure 9, JNK signaling is activated in *Psc-Su(z)2* mutant and surrounding wild-type cells. We demonstrated that JNK signaling is not necessary for an increase in interface contractility, since *Psc-Su(z)2* mutant clones still formed cysts in a JNKK mutant background (Figure 9). Similarly, it was suggested that JNK activation is not the cause of clonal extrusion in Dpp-signaling compromised clones, but likely a secondary stress response (Gibson and Perrimon, 2005). This suggests that JNK is not an upstream regulator of interface contractility.

However, the activation of apoptosis in small misspecified cell cluster and their subsequent extrusion might be JNK-dependent. Interestingly, morphogenetic apoptosis induced by discontinuities in morphogen gradients can be blocked by mutations in the JNK pathway (Adachi-Yamada and O'Connor, 2002). Therefore, future experiments need to address if JNK is indeed a downstream effector of interface contractility and if it is necessary for the removal of small misspecified clones subjected to interface contractility. The signal that could promote pro-apoptotic JNK activity in small cluster of misspecified cells remains elusive and awaits further investigations. Alternatively to the idea of reduced uptake of survival signals discussed above (5.3.1), it was shown that mechanical stress activates JNK in the course of wound healing (Galko and Krasnow, 2004; Ramet et al., 2002). In addition, imbalances between Dpp and Hh signaling levels were reported to cause JNK activation, suggesting that perturbed signaling ratios are sensed by cells and initiate the apoptotic program (Adachi-Yamada and O'Connor, 2002). It will be interesting to investigate if these JNK-activating mechanisms are restricted to the specific context in which they were described or if they may also apply to apoptotic processes induced by interface contractility.

5.4 Interface contractility and cancer initiation

Paradoxically, cysts are caused by a failure to eliminate intermediate-sized aberrant cell cluster from the epithelium. For intermediate-sized clones, increased interface contractility is able to induce the observed cell shape changes of cyst formation, but the forces are not strong enough for a complete removal by apoptosis. Although cysts are not eliminated by apoptosis, in several cases full extrusion as self-contained structures from the wing disc epithelium was observed (Figure 44 b). In these cases, cysts can survive metamorphosis and become located within the adult wing structure (Gibson and Perrimon, 2005; Shen and Dahmann, 2005; Shen et al., 2010). We observed full cystic extrusion only in the case of *Psc-Su(z)2* mutant clones (Figure 8), suggesting that the success of complete extrusion might depend on the genetic background or the experimental approach. In agreement with this, Gibson and colleagues found significant differences in clone extrusion and clone death using two different flipping approaches (Gibson and Perrimon, 2005).

In a disease promoting scenario, cysts surviving abscission from the surrounding wild-type tissue may promote displacement of cells into new microenvironments and may precede emergence of invasive cell behaviors (Figure 44 b). Strikingly, cystic deformations have been observed in mouse models of colon cancer upon deregulation of Wnt/Wg and TGFβ/Dpp signaling (Barker et al., 2009; Batlle et al., 2002; Haramis et al., 2004; Pinto and Clevers, 2005).

These observations emphasize that epithelial cysts may be an early hallmark of tissue disruption in cancer driven by mutagenic changes to differentiation state. However, the exact implication and function of cyst formation in cancer initiation and progression is not understood and needs further investigations.

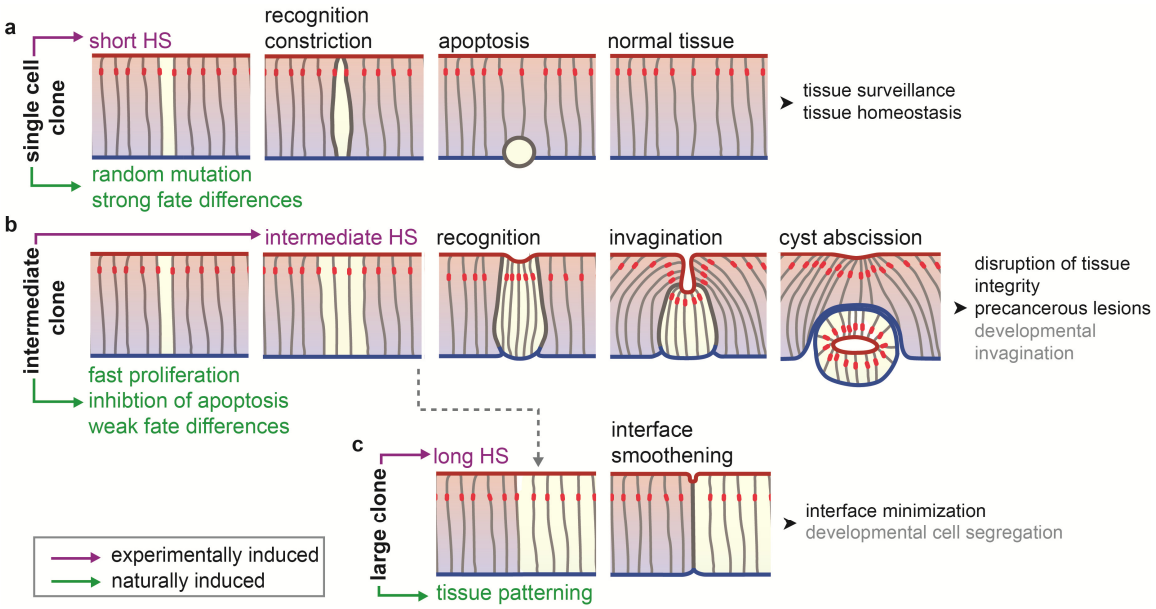

Figure 44: Model of interface contractility acting between differently fated cell populations; Schematic tissue cross-sections with apical surfaces in red, basal surfaces in blue, lateral cell surfaces in grey and adherens junctions as red dots. Magenta writing indicates experimentally used conditions (HS = heat-shock) and green writing indicates possible naturally occurring scenarios creating clusters sizes of differently fated cells. Grey writing indicates speculations on a role of interface contractility in normal development. **(a)** Single misspecified cells are experimentally induced by a short heat-shock (HS). In nature, random mutations may arise leading to strong fate differences compared to surrounding wt tissues. Experimentally or naturally induced differences induce interface contractility, which causes apical constriction, apoptosis and preserve tissue homeostasis. **(b)** Intermediate clone sizes are induced experimentally by intermediate HS. In nature, clusters of misspecified cells could arise from single mutant cells that proliferate before the onset of interface contractility or escape induction of apoptosis. Both scenarios could be mediated by onco- or tumor suppressor gene mutations. Weak fate differences that are not immediately recognized may also allow for proliferation. During development, differently fated intermediate cell clusters arise by means of tissue patterning. Developmental or abnormal fate differences drive cell cluster invagination and cyst abscission. Cyst formation by misspecified cells compromises tissue integrity and might be cause for the development of precancerous lesions. **(c)** Large clone sizes are induced experimentally by a long HS. During development, large domains of cell fates arise by tissue growth and patterning. We speculate that fate differences at cell fate interfaces could be translated into enhanced contractility, leading to a decrease in interface roughness. Large clones also arise from intermediate sizes (indicated by dashed line) due to reasons described in (b).

Experimentally, intermediate-sized cell clusters giving rise to cysts can be generated by a long heat-shock causing an increase in the likelihood of neighboring cells to flip and generate larger misspecified clone patches. For tumor initiation and progression, it is usually anticipated that mutations occur on a single cell level (Nowell, 2002). This raises the question what

mechanism may prevent the extrusion of these single, misspecified cells by increased interface contractility and allows their proliferations to intermediate-sized clusters. One explanation might lie in the strength of differences between misspecified and surrounding cells. Big fate differences are probably sensed immediately enabling a quick tissue response, whereas slight fate differences could allow cells to proliferate before increased tension at the interfaces is generated. Similarly, in the case of *APC* mutations and intestinal polyp formation (5.2.1), mutations constitutively activating Wnt/Wg signaling might not be detected at the crypt base, where all cell are characterized by high Wnt/Wg signaling levels. This circumstance might allow a single, mutant cell to proliferate before it migrates to the crypt/villus junction, an environment of low Wnt/Wg signaling activity. There, mutant cells may be detected by surrounding cells and the, meanwhile, intermediate-sized cluster will form cyst-like outpocketings. Alternatively, intermediate clusters may also arise by continuous proliferation of single misspecified cells resistant to apoptotic signals. This scenario could either arise from two mutations promoting apoptotic resistance and cell fate differences independently, or one mutation fulfilling both of these conditions (Figure 44 b). Prominently, based on our experiments, tumor suppressor gene mutations, such as *Psc-Su(z)2* or Ras^{V12} confer apoptosis resistance shown by apoptotic marker staining, and elicit MWI contractility and cyst formation (Figure 32). Supporting this, several studies describe altered interface actin dynamics of Ras^{V12} transformed cells in MDCK monolayers, suggesting that one of the most potent human oncogenes may indeed induce interface contractility (Hogan, 2012; Hogan et al., 2009; Liu et al., 2012; Wu et al., 2014).

5.5 Role of interface contractility during morphogenesis

Since increased interface contractility is driven by the apposition of differently fated cell populations, it raises the questions if interface contractility could not only play a role as error correction mechanism for cell fate misspecification, but also as a driver of epithelial morphogenesis during development. Interface contractility mechanisms would thereby offer an opportunity to understand similarities and differences between morphogenetic behaviors in development or disease. It has become clear, that spatial regulation of actomyosin at specific cellular interfaces is a crucial concept for several morphogenetic processes (Lecuit et al., 2011; Schock and Perrimon, 2002) and that many developmental invagination processes are driven by cell fate specification of intermediate-sized cell clusters (Bate and Arias, 1991; Cohen et al., 1993; Roper, 2012). As mentioned previously (1.3.3 b), a local increase in actomyosin contractility at the AP compartment boundary in imaginal discs, where two cell lineages meet, is sufficient and necessary for boundary maintenance and straightness (Aliee et al., 2012; Landsberg et al., 2009; Major and Irvine, 2006). Similarly, in the hindbrain of zebrafish, the segmentation of

individual specified rhombomeres is accompanied by Eph signaling-dependent actomyosin enrichment and contractility increase at the borders. The increase in contractility is required to prevent cell mixing and assure border straightness (Calzolari et al., 2014).

Our own experiments suggest that increased interface contractility might also play a role in endogenous fold formation in the wing imaginal disc. The occurrence of these folds is highly regulated and coincides temporally as well as spatially with the apposition of different transcription factor domains (Sui et al., 2012) (Figure 36). We showed that ectopic transcription factor domains, as well as changes to endogenous ones, can induce ectopic folds and weakens endogenous folds, respectively In agreement with that, a previous study connected the expression of *Dorsocross (Doc)* transcription factors to fold formation. Doc is expressed specifically at the B/DH hinge folds ventrally and dorsally (Figure 36) and its expression pattern coincides spatially and temporally with B/DH fold formation. Reduction of *Doc* leads, similar to our results, to weakening of the B/DH fold and *Doc* overexpression is able to induce ectopic folds and cyst formation (Sui et al., 2012). Although this result had been interpreted as a specific cell-autonomous function for Doc in inducing cell shape changes, it would be important to test if specifically the apposition of Doc- positive and Doc-negative cell populations is sufficient to drive fold formation.

Endogenous folds exhibit a distinct cell-biological signature compared to non-fold cells including microtubule redistribution, reduction of collagen and integrin levels as well as Matrix metalloproteinase 2 (Mmp2) expression (Sui et al., 2012). So far, we have not yet tested if ectopic folds exhibit a similar molecular signature compared to normal folds. This is important to understand if ectopic folds resemble endogenous ones not only phenotypically, but also on a molecular level. Future experiments need to analyze if lateral actomyosin accumulates as a hallmark of increased interface contractility, in ectopic or endogenous folds. Details of a molecular signature of ectopic and endogenous folds will provide insights if both fold types arise from similar or distinct mechanisms.

Large misspecified clones smoothen at the contact side to surrounding wild-type cells, and sometimes show slight apical indentations. So far, we do not understand what regulates the occurrence of smoothening or indentations. However, clone shape might influence how much tension is felt. Ectopic expression of cell fate specifying transcription factors in large, elongated clones led to deep invaginations and fold formation. Possibly, 3D-vertex model simulations could give more insights in the mechanical and experimental parameters that distinguish between fold formation and just smoothening of contact surfaces. These simulations have important implications for understanding the distinct mechanisms of cell segregation at compartment boundaries and invagination into cysts (Figure 44 b, c).

Moreover, it will be crucial to investigate if cellular mechanisms that regulate interface contractility at aberrantly specified cells and at developmental compartments are alike. We could show that the change in interface tensions is similar in the context of misspecified clones subjected to MWI contractility and compartment boundaries in imaginal discs (5.1.3). So far, we have not analyzed, if actomyosin at compartment boundaries only enriches at adherens junctions, but if it is also found at lateral surfaces right at the cell lineage interface. Thus, understanding if lateral MWI contractility plays a role in compartment boundary formation requires further experiments.

Strikingly, morphogenetic apoptosis does not only play a role as an error correction mechanism, but also during normal development. The leg of *Drosophila* consists of different segments, which are connected by joints. In the leg imaginal discs, the future joints are represented as folds in the tissue (Manjon et al., 2007). It has been shown, that fold formation depends on the activation of JNK-dependent apoptosis induced by the establishment of sharp Dpp borders distally in each segment. Interestingly, compromising these sharp boundaries lead to loss of fold and joint formation (Manjon et al., 2007). Although the exact correlation of morphogenetic apoptosis and interface contractility is not resolved yet (5.3.2), this example illustrates that sharp interfaces of differently fated cells arise in different developmental processes and induce a mechanism that can translate cell fate patterning into the required shape changes. Interestingly, only the distal joints in the leg imaginal disc are formed by JNK-dependent apoptosis, whereas proximal fold formation arise due to another mechanism (Manjon et al., 2007). It would be interesting to see, if interface contractility at these sharp boundaries could play a role in joint morphogenesis.

6 Conclusion

By combining experimental and modeling approaches, we demonstrated that actomyosin contractility increases at lateral interfaces between normal and aberrantly specified epithelial cells in *Drosophila* imaginal discs. This drives apoptotic cell elimination, cyst formation or cell lineage segregation depending on cell cluster size. Thereby, interface contractility acts as an error correction mechanism on single misspecified cells, but may cause disease-promoting cysts in intermediate-sized cell clusters. Cell segregation of large clusters subjected to increased interface contractility could drive tissue separation during development (Figure 1, Figure 44).

These results provide a novel and very general perspective on morphogenetic mechanisms arising from cell fate heterogeneities within tissues. Our work has important implications for understanding the interplay between cell fate patterning and epithelial structure in the course of development and disease, not only in *Drosophila*, but likely also in the mammalian system.

However, several intriguing questions remain unanswered and have to be addressed in future experiments. First of all, the upstream mechanism that allows detection of many unrelated cell fates and of misspecified cells could, due to the generality of this phenomenon, not be resolved yet. Understanding the contributions of differences in adhesion, metabolic states or cell surface molecules between different fates might shed light on the complex nature of this process. Secondly, the translation of cell fate differences into the molecular regulation and coordination of increased actomyosin contractility at the interface need to be further addressed. Investigating a potential role for Eph signaling may be of particular interest. Apart from unraveling the exact upstream pathway of interface contractility, the implications of this mechanism during normal development and morphogenesis, as well as for cancer initiation and progression in mammalian systems, remain exciting starting points for future studies.

References

Adachi-Yamada, T., and O'Connor, M.B. (2002). Morphogenetic apoptosis: a mechanism for correcting discontinuities in morphogen gradients. Developmental biology *251*, 74-90.

Adachi-Yamada, T., and O'Connor, M.B. (2004). Mechanisms for removal of developmentally abnormal cells: cell competition and morphogenetic apoptosis. J Biochem *136*, 13-17.

Aegerter-Wilmsen, T., Aegerter, C.M., Hafen, E., and Basler, K. (2007). Model for the regulation of size in the wing imaginal disc of Drosophila. Mechanisms of development *124*, 318-326.

Aegerter-Wilmsen, T., Heimlicher, M.B., Smith, A.C., de Reuille, P.B., Smith, R.S., Aegerter, C.M., and Basler, K. (2012). Integrating force-sensing and signaling pathways in a model for the regulation of wing imaginal disc size. Development *139*, 3221-3231.

Aldaz, S., and Escudero, L.M. (2010). Imaginal discs. Current biology : CB *20*, R429-431.

Aldaz, S., Morata, G., and Azpiazu, N. (2005). Patterning function of homothorax/extradenticle in the thorax of Drosophila. Development *132*, 439-446.

Aliee, M., Roper, J.C., Landsberg, K.P., Pentzold, C., Widmann, T.J., Julicher, F., and Dahmann, C. (2012). Physical mechanisms shaping the Drosophila dorsoventral compartment boundary. Current biology : CB *22*, 967-976.

Altabef, M., Clarke, J.D., and Tickle, C. (1997). Dorso-ventral ectodermal compartments and origin of apical ectodermal ridge in developing chick limb. Development *124*, 4547-4556.

Arbouzova, N.I., and Zeidler, M.P. (2006). JAK/STAT signalling in Drosophila: insights into conserved regulatory and cellular functions. Development *133*, 2605-2616.

Ashburner, M., Golic, K.G., and Hawley, R.S. (2005). Life Cycle. In Drosophila: a laboratory handbook (New York, Cold Spring Harbor: Cold Spring Harbor Laboratory Press), pp. 121-184.

Auerbach, C. (1936). The development of of legs, wings, and halteres in wild type and some mutant strains of Drosophila melanogaster. Trans R Soc Edinb *58*, 87-815.

Ayala-Camargo, A., Anderson, A.M., Amoyel, M., Rodrigues, A.B., Flaherty, M.S., and Bach, E.A. (2013). JAK/STAT signaling is required for hinge growth and patterning in the Drosophila wing disc. Developmental biology *382*, 413-426.

Azpiazu, N., and Morata, G. (2000). Function and regulation of homothorax in the wing imaginal disc of Drosophila. Development *127*, 2685-2693.

Barker, N., Ridgway, R.A., van Es, J.H., van de Wetering, M., Begthel, H., van den Born, M., Danenberg, E., Clarke, A.R., Sansom, O.J., and Clevers, H. (2009). Crypt stem cells as the cells-of-origin of intestinal cancer. Nature *457*, 608-611.

Bate, M., and Arias, A.M. (1991). The embryonic origin of imaginal discs in Drosophila. Development *112*, 755-761.

Batlle, E., Henderson, J.T., Beghtel, H., van den Born, M.M., Sancho, E., Huls, G., Meeldijk, J., Robertson, J., van de Wetering, M., Pawson, T.*, et al.* (2002). Beta-catenin and TCF mediate cell positioning in the intestinal epithelium by controlling the expression of EphB/ephrinB. Cell *111*, 251-263.

Batlle, E., and Wilkinson, D.G. (2012). Molecular mechanisms of cell segregation and boundary formation in development and tumorigenesis. Cold Spring Harb Perspect Biol *4*, a008227.

Bauer, R., Loer, B., Ostrowski, K., Martini, J., Weimbs, A., Lechner, H., and Hoch, M. (2005). Intercellular communication: the Drosophila innexin multiprotein family of gap junction proteins. Chem Biol *12*, 515-526.

Beh, L.Y., Colwell, L.J., and Francis, N.J. (2012). A core subunit of Polycomb repressive complex 1 is broadly conserved in function but not primary sequence. Proceedings of the National Academy of Sciences of the United States of America *109*, E1063-1071.

Bell, G.P., and Thompson, B.J. (2014). Colorectal cancer progression: Lessons from Drosophila? Seminars in cell & developmental biology.

Bessa, J., Carmona, L., and Casares, F. (2009). Zinc-finger paralogues tsh and tio are functionally equivalent during imaginal development in Drosophila and maintain their expression levels through auto- and cross-negative feedback loops. Developmental dynamics : an official publication of the American Association of Anatomists *238*, 19-28.

Beuchle, D., Struhl, G., and Muller, J. (2001). Polycomb group proteins and heritable silencing of Drosophila Hox genes. Development *128*, 993-1004.

Brand, A.H., and Perrimon, N. (1993). Targeted gene expression as a means of altering cell fates and generating dominant phenotypes. Development *118*, 401-415.

Brodland, G.W. (2002). The Differential Interfacial Tension Hypothesis (DITH): a comprehensive theory for the self-rearrangement of embryonic cells and tissues. J Biomech Eng *124*, 188-197.

Brown, N.H., Gregory, S.L., Rickoll, W.L., Fessler, L.I., Prout, M., White, R.A., and Fristrom, J.W. (2002). Talin is essential for integrin function in Drosophila. Developmental cell *3*, 569-579.

Bulgakova, N.A., Klapholz, B., and Brown, N.H. (2012). Cell adhesion in Drosophila: versatility of cadherin and integrin complexes during development. Current opinion in cell biology *24*, 702-712.

Bunker, B.D., Nellimoottil, T.T., Boileau, R.M., Classen, A.K., and Bilder, D. (2015). The transcriptional response to tumorigenic polarity loss in Drosophila. Elife *4*.

Calleja, M., Herranz, H., Estella, C., Casal, J., Lawrence, P., Simpson, P., and Morata, G. (2000). Generation of medial and lateral dorsal body domains by the pannier gene of Drosophila. Development *127*, 3971-3980.

Calzolari, S., Terriente, J., and Pujades, C. (2014). Cell segregation in the vertebrate hindbrain relies on actomyosin cables located at the interhombomeric boundaries. The EMBO journal *33*, 686-701.

Canon, J., and Banerjee, U. (2000). Runt and Lozenge function in Drosophila development. Seminars in cell & developmental biology *11*, 327-336.

Casares, F., and Mann, R.S. (2000). A dual role for homothorax in inhibiting wing blade development and specifying proximal wing identities in Drosophila. Development *127*, 1499-1508.

Cavodeassi, F., Modolell, J., and Gomez-Skarmeta, J.L. (2001). The Iroquois family of genes: from body building to neural patterning. Development *128*, 2847-2855.

Cayuso, J., Xu, Q., and Wilkinson, D.G. (2015). Mechanisms of boundary formation by Eph receptor and ephrin signaling. Developmental biology *401*, 122-131.

Chang, L.H., Chen, P., Lien, M.T., Ho, Y.H., Lin, C.M., Pan, Y.T., Wei, S.Y., and Hsu, J.C. (2011). Differential adhesion and actomyosin cable collaborate to drive Echinoid-mediated cell sorting. Development *138*, 3803-3812.

Classen, A.K., Bunker, B.D., Harvey, K.F., Vaccari, T., and Bilder, D. (2009). A tumor suppressor activity of Drosophila Polycomb genes mediated by JAK-STAT signaling. Nature genetics *41*, 1150-1155.

Clevers, H., and Batlle, E. (2006). EphB/EphrinB receptors and Wnt signaling in colorectal cancer. Cancer research *66*, 2-5.

Cohen, B., Simcox, A.A., and Cohen, S.M. (1993). Allocation of the thoracic imaginal primordia in the Drosophila embryo. Development *117*, 597-608.

Cohen, S.M. (1993). Imaginal Disc development. In The Development of Drosophila melanogaster, M.B.a.A.M. Arias, ed. (NY: Cold Spring Harbor Laboratory Press: Cold Spring Harbor), pp. 747-841.

Cortina, C., Palomo-Ponce, S., Iglesias, M., Fernandez-Masip, J.L., Vivancos, A., Whissell, G., Huma, M., Peiro, N., Gallego, L., Jonkheer, S.*, et al.* (2007). EphB-ephrin-B interactions suppress colorectal cancer progression by compartmentalizing tumor cells. Nature genetics *39*, 1376-1383.

Dahmann, C., and Basler, K. (1999). Compartment boundaries: at the edge of development. Trends Genet *15*, 320-326.

Dahmann, C., and Basler, K. (2000). Opposing transcriptional outputs of Hedgehog signaling and engrailed control compartmental cell sorting at the Drosophila A/P boundary. Cell *100*, 411-422.

de Beco, S., Ziosi, M., and Johnston, L.A. (2012). New frontiers in cell competition. Developmental dynamics : an official publication of the American Association of Anatomists *241*, 831-841.

del Valle Rodriguez, A., Didiano, D., and Desplan, C. (2012). Power tools for gene expression and clonal analysis in Drosophila. Nat Methods *9*, 47-55.

Diez del Corral, R., Aroca, P., JL, G.m.-S., Cavodeassi, F., and Modolell, J. (1999). The Iroquois homeodomain proteins are required to specify body wall identity in Drosophila. Genes & development *13*, 1754-1761.

Dominguez-Gimenez, P., Brown, N.H., and Martin-Bermudo, M.D. (2007). Integrin-ECM interactions regulate the changes in cell shape driving the morphogenesis of the Drosophila wing epithelium. Journal of cell science *120*, 1061-1071.

Eisenhoffer, G.T., Loftus, P.D., Yoshigi, M., Otsuna, H., Chien, C.B., Morcos, P.A., and Rosenblatt, J. (2012). Crowding induces live cell extrusion to maintain homeostatic cell numbers in epithelia. Nature *484*, 546-549.

Eisenhoffer, G.T., and Rosenblatt, J. (2013). Bringing balance by force: live cell extrusion controls epithelial cell numbers. Trends Cell Biol *23*, 185-192.

Fagotto, F. (2014). The cellular basis of tissue separation. Development *141*, 3303-3318.

Fagotto, F., Winklbauer, R., and Rohani, N. (2014). Ephrin-Eph signaling in embryonic tissue separation. Cell adhesion & migration *8*, 308-326.

Fletcher, A.G., Osterfield, M., Baker, R.E., and Shvartsman, S.Y. (2014). Vertex models of epithelial morphogenesis. Biophys J *106*, 2291-2304.

Fletcher, G.C., Elbediwy, A., Khanal, I., Ribeiro, P.S., Tapon, N., and Thompson, B.J. (2015). The Spectrin cytoskeleton regulates the Hippo signalling pathway. EMBO J *34*, 940-954.

Foty, R.A., and Steinberg, M.S. (2013). Differential adhesion in model systems. Wiley Interdiscip Rev Dev Biol *2*, 631-645.

Fraser, S., Keynes, R., and Lumsden, A. (1990). Segmentation in the chick embryo hindbrain is defined by cell lineage restrictions. Nature *344*, 431-435.

Galko, M.J., and Krasnow, M.A. (2004). Cellular and genetic analysis of wound healing in Drosophila larvae. PLoS biology *2*, E239.

Gandille, P., Narbonne-Reveau, K., Boissonneau, E., Randsholt, N., Busson, D., and Pret, A.M. (2010). Mutations in the polycomb group gene polyhomeotic lead to epithelial instability in both the ovary and wing imaginal disc in Drosophila. PloS one *5*, e13946.

Garcia-Bellido, A., Ripoll, P., and Morata, G. (1973). Developmental compartmentalisation of the wing disk of Drosophila. Nat New Biol *245*, 251-253.

Gibson, M.C., and Perrimon, N. (2005). Extrusion and death of DPP/BMP-compromised epithelial cells in the developing Drosophila wing. Science *307*, 1785-1789.

Gibson, M.C., and Schubiger, G. (2000). Peripodial cells regulate proliferation and patterning of Drosophila imaginal discs. Cell *103*, 343-350.

Glise, B., Bourbon, H., and Noselli, S. (1995). hemipterous encodes a novel Drosophila MAP kinase kinase, required for epithelial cell sheet movement. Cell *83*, 451-461.

Gold, K.S., and Brand, A.H. (2014). Optix defines a neuroepithelial compartment in the optic lobe of the Drosophila brain. Neural Dev *9*, 18.

Golic, K.G., and Lindquist, S. (1989). The FLP recombinase of yeast catalyzes site-specific recombination in the Drosophila genome. Cell *59*, 499-509.

Guillot, C., and Lecuit, T. (2013). Mechanics of epithelial tissue homeostasis and morphogenesis. Science *340*, 1185-1189.

Gumbiner, B.M. (1996). Cell adhesion: the molecular basis of tissue architecture and morphogenesis. Cell *84*, 345-357.

Hafezi, Y., and Nystul, T.G. (2012). Advanced Techniques for Cell Lineage Labelling in Drosophila. In eLS (John Wiley & Sons, Ltd). DOI: 10.1002/9780470015902.a0022539

Halaoui, R., and McCaffrey, L. (2015). Rewiring cell polarity signaling in cancer. Oncogene *34*, 939-950.

Halfar, K., Rommel, C., Stocker, H., and Hafen, E. (2001). Ras controls growth, survival and differentiation in the Drosophila eye by different thresholds of MAP kinase activity. Development *128*, 1687-1696.

Hannezo, E., Prost, J., and Joanny, J.F. (2011). Instabilities of monolayered epithelia: shape and structure of villi and crypts. Phys Rev Lett *107*, 078104.

Hansen, M.J., Dallal, G.E., and Flanagan, J.G. (2004). Retinal axon response to ephrin-as shows a graded, concentration-dependent transition from growth promotion to inhibition. Neuron *42*, 717-730.

Haramis, A.P., Begthel, H., van den Born, M., van Es, J., Jonkheer, S., Offerhaus, G.J., and Clevers, H. (2004). De novo crypt formation and juvenile polyposis on BMP inhibition in mouse intestine. Science *303*, 1684-1686.

Harris, A.K. (1976). Is Cell sorting caused by differences in the work of intercellular adhesion? A critique of the Steinberg hypothesis. J Theor Biol *61*, 267-285.

Heisenberg, C.P., and Bellaiche, Y. (2013). Forces in tissue morphogenesis and patterning. Cell *153*, 948-962.

Held, L.I. (2002). Imaginal Discs: the Genetic and Cellular Logic of Pattern Formation (Cambridge: Cambridge University Press, ISBN 0-521-01835-8).

Herrera, S.C., and Morata, G. (2014). Transgressions of compartment boundaries and cell reprogramming during regeneration in Drosophila. Elife *3*, e01831.

Hogan, C. (2012). Impact of interactions between normal and transformed epithelial cells and the relevance to cancer. Cell Mol Life Sci *69*, 203-213.

Hogan, C., Dupre-Crochet, S., Norman, M., Kajita, M., Zimmermann, C., Pelling, A.E., Piddini, E., Baena-Lopez, L.A., Vincent, J.P., Itoh, Y.*, et al.* (2009). Characterization of the interface between normal and transformed epithelial cells. Nat Cell Biol *11*, 460-467.

Howe, J.R., Bair, J.L., Sayed, M.G., Anderson, M.E., Mitros, F.A., Petersen, G.M., Velculescu, V.E., Traverso, G., and Vogelstein, B. (2001). Germline mutations of the gene encoding bone morphogenetic protein receptor 1A in juvenile polyposis. Nature genetics *28*, 184-187.

Howe, J.R., Roth, S., Ringold, J.C., Summers, R.W., Jarvinen, H.J., Sistonen, P., Tomlinson, I.P., Houlston, R.S., Bevan, S., Mitros, F.A*., et al.* (1998). Mutations in the SMAD4/DPC4 gene in juvenile polyposis. Science *280*, 1086-1088.

Huang, J., Wu, S., Barrera, J., Matthews, K., and Pan, D. (2005). The Hippo signaling pathway coordinately regulates cell proliferation and apoptosis by inactivating Yorkie, the Drosophila Homolog of YAP. Cell *122*, 421-434.

Igaki, T. (2009). Correcting developmental errors by apoptosis: lessons from Drosophila JNK signaling. Apoptosis : an international journal on programmed cell death *14*, 1021-1028.

Izumi, Y., and Furuse, M. (2014). Molecular organization and function of invertebrate occluding junctions. Seminars in cell & developmental biology *36*, 186-193.

Johnston, L.A., Prober, D.A., Edgar, B.A., Eisenman, R.N., and Gallant, P. (1999). Drosophila myc regulates cellular growth during development. Cell *98*, 779-790.

Katoh, H., and Fujita, Y. (2012). Epithelial homeostasis: elimination by live cell extrusion. Current biology : CB *22*, R453-455.

Kim, J., Sebring, A., Esch, J.J., Kraus, M.E., Vorwerk, K., Magee, J., and Carroll, S.B. (1996). Integration of positional signals and regulation of wing formation and identity by Drosophila vestigial gene. Nature *382*, 133-138.

Landsberg, K.P., Farhadifar, R., Ranft, J., Umetsu, D., Widmann, T.J., Bittig, T., Said, A., Julicher, F., and Dahmann, C. (2009). Increased cell bond tension governs cell sorting at the Drosophila anteroposterior compartment boundary. Current Biology: CB *19*, 1950-1955.

Laprise, P., and Tepass, U. (2011). Novel insights into epithelial polarity proteins in Drosophila. Trends in cell biology *21*, 401-408.

Lecuit, T., and Lenne, P.F. (2007). Cell surface mechanics and the control of cell shape, tissue patterns and morphogenesis. Nature reviews Molecular cell biology *8*, 633-644.

Lecuit, T., Lenne, P.F., and Munro, E. (2011). Force generation, transmission, and integration during cell and tissue morphogenesis. Annual review of cell and developmental biology *27*, 157-184.

Leptin, M. (1995). Drosophila gastrulation: from pattern formation to morphogenesis. Annual review of cell and developmental biology *11*, 189-212.

Levayer, R., and Moreno, E. (2013). Mechanisms of cell competition: themes and variations. The Journal of cell biology *200*, 689-698.

Li, X., Han, Y., and Xi, R. (2010). Polycomb group genes Psc and Su(z)2 restrict follicle stem cell self-renewal and extrusion by controlling canonical and noncanonical Wnt signaling. Genes & development *24*, 933-946.

Liu, J.S., Farlow, J.T., Paulson, A.K., Labarge, M.A., and Gartner, Z.J. (2012). Programmed cell-to-cell variability in Ras activity triggers emergent behaviors during mammary epithelial morphogenesis. Cell reports *2*, 1461-1470.

Liu, X., Grammont, M., and Irvine, K.D. (2000). Roles for scalloped and vestigial in regulating cell affinity and interactions between the wing blade and the wing hinge. Developmental biology *228*, 287-303.

Livak, K.J., and Schmittgen, T.D. (2001). Analysis of relative gene expression data using real-time quantitative PCR and the 2(-Delta Delta C(T)) Method. Methods *25*, 402-408.

Maitre, J.L., Berthoumieux, H., Krens, S.F., Salbreux, G., Julicher, F., Paluch, E., and Heisenberg, C.P. (2012). Adhesion functions in cell sorting by mechanically coupling the cortices of adhering cells. Science *338*, 253-256.

Major, R.J., and Irvine, K.D. (2005). Influence of Notch on dorsoventral compartmentalization and actin organization in the Drosophila wing. Development *132*, 3823-3833.

Major, R.J., and Irvine, K.D. (2006). Localization and requirement for Myosin II at the dorsal-ventral compartment boundary of the Drosophila wing. Developmental dynamics : an official publication of the American Association of Anatomists *235*, 3051-3058.

Manjon, C., Sanchez-Herrero, E., and Suzanne, M. (2007). Sharp boundaries of Dpp signalling trigger local cell death required for Drosophila leg morphogenesis. Nature cell biology *9*, 57-63.

Mann, R.S., and Morata, G. (2000). The developmental and molecular biology of genes that subdivide the body of Drosophila. Annual review of cell and developmental biology *16*, 243-271.

Marinari, E., Mehonic, A., Curran, S., Gale, J., Duke, T., and Baum, B. (2012). Live-cell delamination counterbalances epithelial growth to limit tissue overcrowding. Nature *484*, 542-545.

Martinez, A.M., Schuettengruber, B., Sakr, S., Janic, A., Gonzalez, C., and Cavalli, G. (2009). Polyhomeotic has a tumor suppressor activity mediated by repression of Notch signaling. Nature genetics *41*, 1076-1082.

McCaffrey, L.M., and Macara, I.G. (2011). Epithelial organization, cell polarity and tumorigenesis. Trends in cell biology *21*, 727-735.

McClure, K.D., and Schubiger, G. (2005). Developmental analysis and squamous morphogenesis of the peripodial epithelium in Drosophila imaginal discs. Development *132*, 5033-5042.

McGuire, S.E., Le, P.T., Osborn, A.J., Matsumoto, K., and Davis, R.L. (2003). Spatiotemporal rescue of memory dysfunction in Drosophila. Science *302*, 1765-1768.

Milan, M., Perez, L., and Cohen, S.M. (2002). Short-range cell interactions and cell survival in the Drosophila wing. Developmental cell *2*, 797-805.

Milan, M., Weihe, U., Perez, L., and Cohen, S.M. (2001). The LRR proteins capricious and Tartan mediate cell interactions during DV boundary formation in the Drosophila wing. Cell *106*, 785-794.

Milner, M.J., Bleasby, A.J., and Kelly, S.L. (1984). The role of the peripodial membrane of leg and wing imaginal discs of Drosophila melanogaster during evagination and differentiation in vitro. Wilhelm Roux's Arch Dev Biol *193*, 180–186.

Monier, B., Gettings, M., Gay, G., Mangeat, T., Schott, S., Guarner, A., and Suzanne, M. (2015). Apico-basal forces exerted by apoptotic cells drive epithelium folding. Nature *518*, 245-248.

Monier, B., Pelissier-Monier, A., Brand, A.H., and Sanson, B. (2010). An actomyosin-based barrier inhibits cell mixing at compartmental boundaries in Drosophila embryos. Nature cell biology *12*, 60-65; sup pp 61-69.

Morata, G. (2001). How Drosophila appendages develop. Nat Rev Mol Cell Biol *2*, 89-97.

Moscona, A., and Moscona, H. (1952). The dissociation and aggregation of cells from organ rudiments of the early chick embryo. J Anat *86*, 287-301.

Myat, M.M., Isaac, D.D., and Andrew, D.J. (2000). Early Genes Required for Salivary Gland Fate Determination and Morphogenesis in Drosophila melanogaster. Advances in Dental Research *14*, 89-98.

Nellen, D., Burke, R., Struhl, G., and Basler, K. (1996). Direct and long-range action of a DPP morphogen gradient. Cell *85*, 357-368.

Ng, M., Diaz-Benjumea, F.J., and Cohen, S.M. (1995). Nubbin encodes a POU-domain protein required for proximal-distal patterning in the Drosophila wing. Development *121*, 589-599.

Nowell, P.C. (2002). Tumor progression: a brief historical perspective. Semin Cancer Biol *12*, 261-266.

Organista, M.F., and De Celis, J.F. (2013). The Spalt transcription factors regulate cell proliferation, survival and epithelial integrity downstream of the Decapentaplegic signalling pathway. Biology open *2*, 37-48.

Pai, L.M., Orsulic, S., Bejsovec, A., and Peifer, M. (1997). Negative regulation of Armadillo, a Wingless effector in Drosophila. Development *124*, 2255-2266.

Pallavi, S.K., Ho, D.M., Hicks, C., Miele, L., and Artavanis-Tsakonas, S. (2012). Notch and Mef2 synergize to promote proliferation and metastasis through JNK signal activation in Drosophila. The EMBO journal *31*, 2895-2907.

Pare, A.C., Vichas, A., Fincher, C.T., Mirman, Z., Farrell, D.L., Mainieri, A., and Zallen, J.A. (2014). A positional Toll receptor code directs convergent extension in Drosophila. Nature *515*, 523-527.

Pastor-Pareja, J.C., and Xu, T. (2011). Shaping cells and organs in Drosophila by opposing roles of fat body-secreted Collagen IV and perlecan. Developmental cell *21*, 245-256.

Pearson, J.C., Lemons, D., and McGinnis, W. (2005). Modulating Hox gene functions during animal body patterning. Nat Rev Genet *6*, 893-904.

Perea, D., Molohon, K., Edwards, K., and Diaz-Benjumea, F.J. (2013). Multiple roles of the gene zinc finger homeodomain-2 in the development of the Drosophila wing. Mechanisms of development *130*, 467-481.

Pignoni, F., and Zipursky, S.L. (1997). Induction of Drosophila eye development by decapentaplegic. Development *124*, 271-278.

Pinto, D., and Clevers, H. (2005). Wnt control of stem cells and differentiation in the intestinal epithelium. Experimental cell research *306*, 357-363.

Prober, D.A., and Edgar, B.A. (2000). Ras1 promotes cellular growth in the Drosophila wing. Cell *100*, 435-446.

Quiring, R., Walldorf, U., Kloter, U., and Gehring, W.J. (1994). Homology of the eyeless gene of Drosophila to the Small eye gene in mice and Aniridia in humans. Science *265*, 785-789.

Ramet, M., Lanot, R., Zachary, D., and Manfruelli, P. (2002). JNK signaling pathway is required for efficient wound healing in Drosophila. Developmental biology *241*, 145-156.

Reya, T., and Clevers, H. (2005). Wnt signalling in stem cells and cancer. Nature *434*, 843-850.

Rhiner, C., Lopez-Gay, J.M., Soldini, D., Casas-Tinto, S., Martin, F.A., Lombardia, L., and Moreno, E. (2010). Flower forms an extracellular code that reveals the fitness of a cell to its neighbors in Drosophila. Developmental cell *18*, 985-998.

Rios-Barrera, L.D., and Riesgo-Escovar, J.R. (2013). Regulating cell morphogenesis: the Drosophila Jun N-terminal kinase pathway. Genesis (New York, NY : 2000) *51*, 147-162.

Rodriguez-Boulan, E., and Macara, I.G. (2014). Organization and execution of the epithelial polarity programme. Nature reviews Molecular cell biology *15*, 225-242.

Roper, K. (2012). Anisotropy of Crumbs and aPKC drives myosin cable assembly during tube formation. Developmental cell *23*, 939-953.

Rosenblatt, J., Raff, M.C., and Cramer, L.P. (2001). An epithelial cell destined for apoptosis signals its neighbors to extrude it by an actin- and myosin-dependent mechanism. Current biology : CB *11*, 1847-1857.

Salbreux, G., Charras, G., and Paluch, E. (2012). Actin cortex mechanics and cellular morphogenesis. Trends in cell biology *22*, 536-545.

Sawyer, J.M., Harrell, J.R., Shemer, G., Sullivan-Brown, J., Roh-Johnson, M., and Goldstein, B. (2010). Apical constriction: a cell shape change that can drive morphogenesis. Developmental biology *341*, 5-19.

Schock, F., and Perrimon, N. (2002). Molecular mechanisms of epithelial morphogenesis. Annual review of cell and developmental biology *18*, 463-493.

Schuettengruber, B., and Cavalli, G. (2009). Recruitment of polycomb group complexes and their role in the dynamic regulation of cell fate choice. Development *136*, 3531-3542.

Shen, J., and Dahmann, C. (2005). Extrusion of cells with inappropriate Dpp signaling from Drosophila wing disc epithelia. Science *307*, 1789-1790.

Shen, J., Dahmann, C., and Pflugfelder, G.O. (2010). Spatial discontinuity of optomotor-blind expression in the Drosophila wing imaginal disc disrupts epithelial architecture and promotes cell sorting. BMC Dev Biol *10*, 23.

Shyer, A.E., Tallinen, T., Nerurkar, N.L., Wei, Z., Gil, E.S., Kaplan, D.L., Tabin, C.J., and Mahadevan, L. (2013). Villification: how the gut gets its villi. Science *342*, 212-218.

Simon, J.A., and Kingston, R.E. (2013). Occupying chromatin: Polycomb mechanisms for getting to genomic targets, stopping transcriptional traffic, and staying put. Mol Cell *49*, 808-824.

Simpson, P. (1983). Maternal-Zygotic Gene Interactions during Formation of the Dorsoventral Pattern in Drosophila Embryos. Genetics *105*, 615-632.

Solanas, G., Cortina, C., Sevillano, M., and Batlle, E. (2011). Cleavage of E-cadherin by ADAM10 mediates epithelial cell sorting downstream of EphB signalling. Nature cell biology *13*, 1100-1107.

Steinberg, M.S. (1963). Reconstruction of tissues by dissociated cells. Some morphogenetic tissue movements and the sorting out of embryonic cells may have a common explanation. Science *141*, 401-408.

Struhl, G., Barbash, D.A., and Lawrence, P.A. (1997). Hedgehog organises the pattern and polarity of epidermal cells in the Drosophila abdomen. Development *124*, 2143-2154.

Struhl, G., and Basler, K. (1993). Organizing activity of wingless protein in Drosophila. Cell *72*, 527-540.

Sui, L., Pflugfelder, G.O., and Shen, J. (2012). The Dorsocross T-box transcription factors promote tissue morphogenesis in the Drosophila wing imaginal disc. Development *139*, 2773-2782.

Sykiotis, G.P., and Bohmann, D. (2008). Keap1/Nrf2 signaling regulates oxidative stress tolerance and lifespan in Drosophila. Developmental cell *14*, 76-85.

Tabata, T., and Takei, Y. (2004). Morphogens, their identification and regulation. Development *131*, 703-712.

Tan, J.L., Ravid, S., and Spudich, J.A. (1992). Control of nonmuscle myosins by phosphorylation. Annu Rev Biochem *61*, 721-759.

Taylor, J., and Adler, P.N. (2008). Cell rearrangement and cell division during the tissue level morphogenesis of evaginating Drosophila imaginal discs. Developmental biology *313*, 739-751.

Tepass, U. (2012). The apical polarity protein network in Drosophila epithelial cells: regulation of polarity, junctions, morphogenesis, cell growth, and survival. Annual review of cell and developmental biology *28*, 655-685.

Tepass, U., Tanentzapf, G., Ward, R., and Fehon, R. (2001). Epithelial cell polarity and cell junctions in Drosophila. Annu Rev Genet *35*, 747-784.

Terriente, J., Perea, D., Suzanne, M., and Diaz-Benjumea, F.J. (2008). The Drosophila gene zfh2 is required to establish proximal-distal domains in the wing disc. Developmental biology *320*, 102-112.

Townes, P.L., and Holtfreter, J. (1955). Directed movements and selective adhesion of embryonic amphibian cells. J Exp Zool *128*, 53-120.

Umetsu, D., Aigouy, B., Aliee, M., Sui, L., Eaton, S., Julicher, F., and Dahmann, C. (2014). Local increases in mechanical tension shape compartment boundaries by biasing cell intercalations. Current biology : CB *24*, 1798-1805.

Ursprung, H. (1972). The fine structure of imaginal disks. In The Biology of Imaginal Disks, H.U.a.R. Nöthiger, ed. (Berlin: Springer Verlag), pp. 93-107.

van de Wetering, M., Sancho, E., Verweij, C., de Lau, W., Oving, I., Hurlstone, A., van der Horn, K., Batlle, E., Coudreuse, D., Haramis, A.P.*, et al.* (2002). The beta-catenin/TCF-4 complex imposes a crypt progenitor phenotype on colorectal cancer cells. Cell *111*, 241-250.

Vigoreaux, J.O., Saide, J.D., Valgeirsdottir, K., and Pardue, M.L. (1993). Flightin, a novel myofibrillar protein of Drosophila stretch-activated muscles. The Journal of cell biology *121*, 587-598.

Villa-Cuesta, E., Gonzalez-Perez, E., and Modolell, J. (2007). Apposition of iroquois expressing and non-expressing cells leads to cell sorting and fold formation in the Drosophila imaginal wing disc. BMC developmental biology *7*, 106.

Vincent, J.P., Fletcher, A.G., and Baena-Lopez, L.A. (2013). Mechanisms and mechanics of cell competition in epithelia. Nature reviews Molecular cell biology *14*, 581-591.

Wang, S.H., Simcox, A., and Campbell, G. (2000). Dual role for Drosophila epidermal growth factor receptor signaling in early wing disc development. Genes & development *14*, 2271-2276.

Weihe, U., Milan, M., and Cohen, S.M. (2009). Drosophila Limb Development. In Insect Development: Morphogeneis, Molting and Metamorphosis, G.I. Lawrence, ed. (London: Academic Press, Elsevier BV), pp. 59-97.

Widmann, T.J., and Dahmann, C. (2009a). Dpp signaling promotes the cuboidal-to-columnar shape transition of Drosophila wing disc epithelia by regulating Rho1. J Cell Sci *122*, 1362-1373.

Widmann, T.J., and Dahmann, C. (2009b). Wingless signaling and the control of cell shape in Drosophila wing imaginal discs. Developmental biology *334*, 161-173.

Winer, J., Jung, C.K., Shackel, I., and Williams, P.M. (1999). Development and validation of real-time quantitative reverse transcriptase-polymerase chain reaction for monitoring gene expression in cardiac myocytes in vitro. Analytical biochemistry *270*, 41-49.

Wolpert, L., Jessel, T., Lawrence, P., Meyerowitz, E., Robertson, E., and Smith, J. (2007). Principles of Develoment: Das Original mit Übersetzungshilfen, Third Edition edn (Springer-Verlag Berlin Heidelberg: Spektrum Akademischer Verlag, ISBN 3827418569).

Worley, M.I., Setiawan, L., and Hariharan, I.K. (2013). TIE-DYE: a combinatorial marking system to visualize and genetically manipulate clones during development in Drosophila melanogaster. Development *140*, 3275-3284.

Wu, J., and Cohen, S.M. (1999). Proximodistal axis formation in the Drosophila leg: subdivision into proximal and distal domains by Homothorax and Distal-less. Development *126*, 109-117.

Wu, J., and Cohen, S.M. (2000). Proximal distal axis formation in the Drosophila leg: distinct functions of teashirt and homothorax in the proximal leg. Mechanisms of development *94*, 47-56.

Wu, J., and Cohen, S.M. (2002). Repression of Teashirt marks the initiation of wing development. Development *129*, 2411-2418.

Wu, S.K., Gomez, G.A., Michael, M., Verma, S., Cox, H.L., Lefevre, J.G., Parton, R.G., Hamilton, N.A., Neufeld, Z., and Yap, A.S. (2014). Cortical F-actin stabilization generates apical-lateral patterns of junctional contractility that integrate cells into epithelia. Nat Cell Biol *16*, 167-178.

Xu, T., and Rubin, G.M. (1993). Analysis of genetic mosaics in developing and adult Drosophila tissues. Development *117*, 1223-1237.

Yurchenco, P.D. (2011). Basement membranes: cell scaffoldings and signaling platforms. Cold Spring Harb Perspect Biol *3*.

Zimmerman, S.G., Thorpe, L.M., Medrano, V.R., Mallozzi, C.A., and McCartney, B.M. (2010). Apical constriction and invagination downstream of the canonical Wnt signaling pathway require Rho1 and Myosin II. Developmental biology *340*, 54-66.

Zirin, J.D., and Mann, R.S. (2004). Differing strategies for the establishment and maintenance of teashirt and homothorax repression in the Drosophila wing. Development *131*, 5683-5693.

Zoranovic, T., Grmai, L., and Bach, E.A. (2013). Regulation of proliferation, cell competition, and cellular growth by the Drosophila JAK-STAT pathway. Jak-Stat *2*, e25408.

Appendix

I. Genotypes

Table 11: Genotypes and experimental conditions; Detailed genotypes and experimental conditions, including time point of dissection (TP), heat-shock length (HS), egg collection/larval staging (EC) and use of spacer between coverslip and slide for microscopy of each figure are listed.

Fig		*Genotype*	*TP*	*HS*	*EC*	*Spacer*
7	b, c	*hsflp ^{122} /+; FRT42D ubi-eGFP / FRT42D iso; +/+*	30 h	60	no	no
	d, e	*hsflp ^{122} /+; FRT42D ubi-eGFP / FRT42D iso; +/+*	54 h	60	no	no
	g, h	*hsflp ^{122} /+; FRT42D ubi-eGFP / FRT42D Psc-Su(z)2^{XL26}; +/+*	30 h	60	no	no
	i, j	*hsflp ^{122} /+; FRT42D ubi-eGFP / FRT42D Psc-Su(z)2^{XL26}; +/+*	54 h	60	no	no
8	a	*hsflp ^{122} /+; FRT42D ubi-mRFP / FRT42D Psc-Su(z)2^{XL26}; +/+*	0 h	45	no	yes
	b, c	*hsflp ^{122} /+; FRT42D ubi-mRFP / FRT42D Psc-Su(z)2^{XL26}; +/+*	30 h	45	no	yes
	d, e	*hsflp ^{122} /+; FRT42D ubi-mRFP / FRT42D Psc-Su(z)2^{XL26}; +/+*	54 h	45	no	yes
	f	*hsflp ^{122} /+; FRT42D ubi-mRFP / FRT42D Psc-Su(z)2^{XL26}; +/+*	54 h	45	no	yes
	g	*hsflp ^{122} /+; FRT42D ubi-mRFP / FRT42D Psc-Su(z)2^{XL26}; +/+*	102 h	45	no	yes
9	a, b	*hsflp ^{122} /+; FRT42D ubi-eGFP / FRT42D Psc-Su(z)2^{1b8recA}; +/+*	27 h	60	no	no
	c	*hsflp ^{122} /+; FRT42D ubi-eGFP / FRT42D Psc-Su(z)2^{1b8recA}; +/+*	72 h	60	no	no
	d, e	*hsflp ^{122} /+; FRT42D ubi-eGFP / FRT42D Psc-Su(z)2^{1b8recA}, yki^{B5}; +/+*	27 h	60	no	no
	f	*hsflp ^{122} /+; FRT42D ubi-eGFP / FRT42D Psc-Su(z)2^{1b8recA}, yki^{B5}; +/+*	72 h	60	no	no
	g, h	*hsflp ^{122} /+; FRT42D ubi-eGFP / FRT42D Psc-Su(z)2^{XL26}; puc$^{A251.1F3}$-lacZ ry^{506}/ +*	54 h	60	no	no
	i	*FM7-GFP/ +; FRT42D ubi-eGFP / FRT42D Psc-Su(z)2^{XL26}; T155 Gal4 UAS-flp/+*	/	/	no	no
	j	*hep^{r75}/Y; FRT42D ubi-eGFP / FRT42D Psc-Su(z)2^{xl26}; T155 Gal4 UAS-flp/+*	/	/	no	no
10	b,c	*hsflp ^{122} / + ; + / +; act > y^{+} > GAL4, UAS-GFP/+*	30 h	10	yes	yes
	d,e	*hsflp ^{122} / + ; + / +; act > y^{+} > GAL4, UAS-GFP/+*	54 h	10	yes	yes
	g, h	*UAS-fkh-3xHA / hsflp ^{122}; + / +; act > y^{+} > GAL4, UAS-GFP/+*	30 h	10	yes	yes
	i, j	*UAS-fkh-3xHA / hsflp ^{122}; + / +; act > y^{+} > GAL4, UAS-GFP/+*	54 h	10	yes	yes
11	a	*hsflp ^{122} / +; UAS-AbdB / + ; act > y^{+} > GAL4, UAS GFP/ +*	54 h	10	no	no
	b, c	*act > CD2 > GAL4, UAS GFP/ UAS-AbdB; MKRS hsflp / +*	54 h	60	no	no
	g, h, i	*hsflp ^{122} / +; UAS-ey / + ; act > y^{+} > GAL4, UAS GFP/ +*	54 h	10	yes	yes
	d, e, f	*hsflp ^{122} / +;+ / +; act > y^{+} > GAL4, UAS GFP / UAS-Lz*	54 h	10	no	no
	j, k, l	*hsflp ^{122} / +; + / +; act > y^{+} > GAL4, UAS GFP/ UAS-Ubx*	54 h	10	no	no
12	b	*UAS-fkh-3xHA / +, act > CD2 > GAL4, UAS GFP/ +; MKRS hsflp / +*	54 h	60	no	no
	c	*act > CD2 > GAL4, UAS GFP/ UAS-AbdB; MKRS hsflp / +*	54 h	60	no	no

	d	*hsflp [122] / +; + / +; act > y[+] > GAL4, UAS GFP / UAS-Lz*	54 h	10	no	no
	e	*act > CD2 > GAL4, UAS GFP/ UAS-ey; MKRS hsflp / +*	54 h	60	no	no
	f	*act > CD2 > GAL4, UAS GFP/ +; MKRS hsflp / UAS-Ubx*	54 h	60	no	no
13	a, b	*hsflp [122] / +; Sp/CyO GFP; act > y[+] > GAL4, UAS GFP/ UAS-dmyc*	54 h	10	no	yes
	c, d	*hsflp [122] / +; Sp or CyO GFP / + ; act > y[+] > GAL4, UAS GFP/ UAS-fln-HA3*	54 h	10	no	no
	e, f	*UAS-fkh-3xHA / hsflp [122]; Sp or CyOGFP / UAS-p35; act > y[+] > GAL4, UAS-GFP/ +*	54 h	10	no	yes
	g, h	*UAS-fkh-3xHA / hsflp [122]; Sp or CyOGFP / +; act > y[+] > GAL4, UAS-GFP/ UAS-DIAP*	54 h	10	no	yes
14	b-f	*hsflp [122] / +; + / +; act > y[+] > GAL4, UAS GFP / UAS-Ci.HA.wt*	54h	10	no	yes
	h-l	*hsflp [122] / +; UAS-hop[TumL]/ +; act > y[+] > GAL4, UAS GFP / +*	54 h	8	no	yes
15	b-f	*hsflp [122] / UAS-armS10; + / +; act > y[+] > GAL4, UAS GFP / +*	54 h	10	no	no
	h-k	*hsflp [122] / +; + / +; act > y[+] > GAL4, UAS GFP / UAS-tkv.CA*	54 h	10	no	no
16	b-d	*hsflp [122] / +; + / +; Act5C.GAL4 (FRT.CD2), UAS-RFP / UAS-Vg*	54 h	10	no	no
	f-h	*hsflp [122] / +; + / +; act > y[+] > GAL4, UAS GFP / UAS-hth*	54 h	10	no	no
17	b-d	*hsflp [122]/ +; + / +; act > y[+] > GAL4, UAS-GFP/+*	30 h	25	yes	yes
	f-h	*UAS-fkh-3xHA / hsflp [122]; + / +; act > y[+] > GAL4, UAS-GFP/+*	30 h	25	yes	yes
	i	*UAS-fkh-3xHA / hsflp [122]; + / +; act > y[+] > GAL4, UAS-GFP/+*	54 h	40	no	no
	k	*hsflp [122] / +; UAS-ey / + ; act > y[+] > GAL4, UAS GFP/ +*	54 h	40	no	no
	j	*hsflp [122] / +; UAS-AbdB / + ; act > y[+] > GAL4, UAS GFP/ +*	54 h	40	no	no
	l	*hsflp [122] / +; + / +; act > y[+] > GAL4, UAS GFP/ UAS-Ubx*	54 h	40	no	no
18	b	*UAS-fkh-3xHA / hsflp [122]; + / +; act > y[+] > GAL4, UAS-GFP/+*	54 h	40	no	no
	d	*hsflp [122] / +; UAS-ey / + ; act > y[+] > GAL4, UAS GFP/ +*	54 h	40	no	no
	c	*hsflp [122] / +; UAS-AbdB / + ; act > y[+] > GAL4, UAS GFP/ +*	54 h	40	no	no
	e	*hsflp [122] / +; + / +; act > y[+] > GAL4, UAS GFP/ UAS-Ubx*	54 h	40	no	no
	g-k	*hsflp [122] / +; + / +; act > y[+] > GAL4, UAS GFP / UAS-Ci.HA.wt*	54 h	30	no	yes
19	a.d	*hsflp [122] / nrgGFP; FRT42D ubi-mRFP / FRT42D Psc-Su(z)2[XL26]; +/+*	54 h	60	no	no
	e, f	*hsflp [122] /+; FRT42D ubi-mRFP / FRT42D Psc-Su(z)2[XL26]; +/+*	54 h	60	no	no
20	a, b	*UAS-fkh-3xHA / hsflp [122]; + / +; act > y[+] > GAL4, UAS-GFP/+*	30 h	10	yes	yes
	c,d	*UAS-fkh-3xHA / hsflp [122]; + / +; act > y[+] > GAL4, UAS-GFP/+*	30 h	25	yes	yes
21	a, c, e	*UAS-fkh-3xHA / hsflp [122]; + / +; act > y[+] > GAL4, UAS-GFP/+*	30 h	10	yes	yes
	b, d	*UAS-fkh-3xHA / hsflp [122]; + / +; act > y[+] > GAL4, UAS-GFP/+*	30 h	15	yes	yes
22	a-c	*hsflp [122] / UAS-fkh-3xHA; + / shq-GFP; Act5C.GAL4 (FRT.CD2), UAS-RFP / +*	30 h	10	no	yes
	d-f	*UAS-fkh-3xHA / hsflp [122]; + / +; act > y[+] > GAL4, UAS-GFP/+*	30 h	10	no	yes
	g-i	*hsflp [122] / UAS-fkh-3xHA; + / zip>GFP; Act5C.GAL4 (FRT.CD2), UAS-RFP /+*	30 h	10	no	yes
	j-l	*UAS-fkh-3xHA / hsflp [122]; + / +; act > y[+] > GAL4, UAS-GFP/+*	30 h	10	no	yes
	m, n	*hsflp [122] / UAS-fkh-3xHA; + / +; Act5C.GAL4 (FRT.CD2), UAS-RFP / sqh>MoeGFP*	30 h	15	no	yes
	n, p	*UAS-fkh-3xHA / hsflp [122]; + / +; act > y[+] > GAL4, UAS-GFP/+*	30 h	10	no	yes
23	a, b	*hsflp [122] / +; FRT42D ubi-mRFP / FRT42D Psc-Su(z)2[XL26], vkg>GFP; +/+*	54 h	40	no	yes
	c-e	*hsflp [122] / +; FRT42D ubi-mRFP / FRT42D Psc-Su(z)2[XL26], vkg>GFP; +/+*	72 h	40	no	yes
	f, h	*hsflp [122]/ +; + / +; act > y[+] > GAL4, UAS-GFP/ +*	54 h	10	yes	yes
	g, i	*UAS-fkh-3xHA / hsflp [122]; + / +; act > y[+] > GAL4, UAS-GFP/+*	54 h	10	yes	yes
25	d, e	*hsflp [122] / +; Sp or CyOubi GFP / UAS-p35; Act5C.GAL4 (FRT.CD2), UAS-RFP /*	54 h	10	no	no

		UAS-RhoV14				
	f	*hsflp [122] / +; Sp or CyOubi GFP / UAS-p35; Act5C.GAL4 (FRT.CD2), UAS-RFP / UAS-RhoV14*	54 h	10	no	yes
	g, h	*hsflp [122] / + ; Sp or CyOGFP / UAS-p35; act > y[+] > GAL4, UAS-GFP / UAS-RhoV14*	54 h	20	no	yes
28	c	*UAS-fkh-3xHA / hsflp [122]; + / +; act > y[+] > GAL4, UAS-GFP/+*	54 h	25	yes	yes
29	a	*hsflp[122]/+; ubi <stop <GFPnls, act5C <stop <lacZnls/+; Act5C <stop <GAL4, UAS-his2A::RFP/+*	30 h	7	24 h	no
	b	*UAS-fkh-3xHA/ hsflp[122]; ubi <stop <GFPnls, act5C <stop <lacZnls/+; Act5C <stop <GAL4, UAS-his2A::RFP/+*	30 h	7	24 h	no
	c	*UAS-fkh-3xHA/ hsflp[122]; ubi <stop <GFPnls, act5C <stop <lacZnls/+; Act5C <stop <GAL4, UAS-his2A::RFP/UAS-DIAP*	30 h	7	24 h	no
	d	*hsflp[122]/ Y; ubi <stop <GFPnls, act5C <stop <lacZnls/+; Act5C <stop <GAL4, UAS-his2A::RFP/UAS-DIAP*	30 h	7	24 h	no
30	a	*UAS-fkh-3xHA / hsflp [122]; + / +; act > y[+] > GAL4, UAS-GFP/+*	30 h	7	no	no
	b	*UAS-fkh-3xHA / hsflp [122]; + / +; act > y[+] > GAL4, UAS-GFP/UAS-DIAP*	30 h	7	no	no
31	a, b, c	*UAS-fkh-3xHA / hsflp [122]; + / +; act > y[+] > GAL4, UAS-GFP/+*	30h	30	no	no
	d, e, f	*UAS-fkh-3xHA / hsflp [122]; + / +; act > y[+] > GAL4, UAS-GFP/UAS-DIAP*	30 h	30	no	no
	g	*hsflp [122] / + or Y; + / UAS-ey; act > y[+] > GAL4, UAS-GFP/ +*	30h	7	no	no
	h	*hsflp [122] / + or Y; + / UAS-ey; act > y[+] > GAL4, UAS-GFP/ +*	30h	30	no	no
32	a	*hsflp [122] / Y or +; Sp / CyO ; act > y[+] > GAL4, UAS-GFP/+*	30 h	10	no	no
	b-d	*hsflp [122] / Y or +; UAS-RasV12 / + ; act > y[+] > GAL4, UAS-GFP/+*	30 h	10	no	no
	e-f	*hsflp [122] / Y or +; UAS-RasV12 / + ; act > y[+] > GAL4, UAS-GFP/+*	30 h	27	no	no
33	a-c	*UAS-fkh-3xHA / hsflp [122]; + / +; act > y[+] > GAL4, UAS-GFP/+*	30 h	15	yes	yes
34	a, b	*hsflp [122] / + ; + / +; act > y[+] > GAL4, UAS-GFP/+*	30 h	10	yes	yes
35	b-d	*ptc Gal4, tubGal80[ts]-20 / UAS-GFP*	EL 4 days at 18°C, TS 24 h 30 °C, back to 18°C for 24 h, dissection			
	e-g	*ptc Gal4, tubGal80[ts]-20 / UAS-ey*	EL 6 days at 18 °C, TS 24 h 30 °C, immediate dissection			
37	b, c	*MS1096 Gal4 / FM7a ; UAS-eGFP/CyO; +/+*	/	/	no	no
	d, e	*MS1096 Gal4 / +; UAS-eGFP/+ ; UAS-hth /+*	/	/	no	no
42	a	*hsflp [122] /+; FRT42D ubi-mRFP / FRT42D shg[R69b]; +/+*	30h	45	no	no
	b, c	*hsflp [122] / +; + / UAS-Ecad-GFP; Act5C.GAL4 (FRT.CD2), UAS-RFP / +*	30h	10	no	no
43	a	*gstD-GFP*	/	/	no	no
	b	*hsflp [122] / UAS-fkh-3xHA; gstD-GFP / CyO; Act5C.GAL4 (FRT.CD2), UAS-RFP /+*	54 h	10	no	no
	C	*hsflp [122] / UAS-fkh-3xHA; gstD-GFP / CyO; Act5C.GAL4 (FRT.CD2), UAS-RFP /+*	54 h	25	no	no
	d	*hsflp [122] / +; gstD-GFP / CyO; Act5C.GAL4 (FRT.CD2), UAS-RFP / UAS-Ci*	54 h	10	no	no
45	a, b	*Vkg-GFP*	/	/	no	no
	c - r	*w118*	/	/	no	no

II. qPCR data

Table 12: qPCR analysis of *fkh*, *Abd-B* and *hth* expression in *Psc-Su(z)2* mutant imaginal discs; **(a)** Mean Ct values of three technical replicates are shown for *GAPDH2*, *CG12703*, *CP1*, *fkh*, *Abd-B* and *hth* in wild-type (wt) and *Psc-Su(z)2* mutant discs and for 3 biological replicates (Rep1, 2 and 3). *GAPDH2*, *CG12703*, *HP1* and *CP-1* values were averaged to obtain one Ct value for control genes. Standard deviation (stdv) is reported. Wt Ct values of *fkh* were set to 40 (red) **(b)** Fold change of *fkh*, *Abd-B* and *hth* expression levels in each replicate (Rep1, 2 and 3) were calculated using the ΔΔCt method. Mean including all 3 replicates and standard deviation (stdv) is reported. Fold change is also reported in Table 1.

a		***wt***	***stdv***	***Psc-Su(z)2$^{-/-}$***	***stdv***
Rep 1	*GAPDH2*	21.10	0.06	22.48	0.13
	CG12703	26.79	0.03	28.34	0.03
	CP1	22.64	0.04	23.09	0.06
	control genes	23.51	2.94	24.64	3.22
	fkh	40		28.43	0.17
	Abd-B	35.76	1.15	27.21	0.36
	hth	21.55	0.20	24.46	0.19
Rep 2	*GAPDH2*	22.53	0.16	21.03	0.11
	HP1	20.29	0.16	20.32	0.04
	CP1	22.88	0.14	22.28	0.05
	control genes	21.90	1.40	21.21	0.99
	fkh	40		27.82	0.08
	Abd-B	38.44	0.23	26.98	0.15
	hth	25.14	0.01	24.78	0.04
Rep 3	*GAPDH2*	20.35	0.08	22.61	0.14
	HP1	19.82	0.16	21.43	0.62
	CP1	22.25	0.10	23.94	0.09
	control genes	20.81	1.28	22.66	1.25
	fkh	40		29.08	0.12
	Abd-B	/		/	
	hth	23.27	0.32	25.31	0.08

b	***Rep 1***	***Rep 2***	***Rep 3***	***Mean***	***stdv***
fkh	6643.73	2879.63	7019.84	5514.40	2289.51
Abd-B	820.93	1742.17		1281.55	651.41
hth	0.29	0.80	0.88	0.66	0.32

III. Actin quantifications

Table 13: Actin intensities measurements; **(a)** Normalized mean intensities and SEM of actin intensity measurements in discs containing Gal4/UAS flip out clones expressing *fkh*. Actin intensities at interfaces between wild-type cells (wt/wt), misspecified *fkh*-expressing cells (mis/mis) and between wild-type and *fkh*-expressing cell (wt/mis) are shown for early stages (30 h) and late stages (54 h) after clone induction. Measurement of *fkh*-expressing clones (10 min heat-shock) and wild-type clones (25 min heat-shock) were pooled to reflect the mirror symmetry of the cyst-forming conditions. Numbers of measured clones are indicated. **(b)** Significance of differences between data sets (table below) was tested by applying a two-tailed WSR-test. Calculated p-values are shown. Red = p-val < 0.01. Lack of statistically significant differences for apical actin intensities at late stages are due to mild cell-autonomous enrichment of actin in *fkh*-expressing cells. Data is visualized in Figure 21 f, g. *Actin quantification done by Anne Classen, Data analysis including statistics by Marco La Fortezza*.

a	**Apical**				**Lateral**			
	Early		Late		Early		Late	
	Mean	SEM	Mean	SEM	Mean	SEM	Mean	SEM
wt/wt	1.000	0.046	1.000	0.055	1.000	0.031	1.000	0.041
wt/mis	1.464	0.077	1.716	0.134	1.525	0.044	1.405	0.045
mis/mis	1.138	0.084	1.463	0.117	1.124	0.030	1.199	0.055
n (10 min HS)	15		7		49		17	
n (25 min HS)	10		3		38		14	
n (total)	25		10		87		31	

b	**Apical**		**Lateral**	
	Early	late	Early	late
wt/mis_wt/wt	0.001	0.002	3.40E-12	2.99E-06
wt/mis_mis/mis	0.001	0.275	7.18E-13	0.006

IV. Shape quantifications

Table 14: Cell dimensions and clone shape analysis – experimental data setup; Gal4/UAS flip out discs expressing *fkh* **(a)**, GFP and Rho^{V14} **(b)** were analyzed at different time points (0 h, 30 h and 54 h after HS) and different heat-shock length (10 min – 25 min) as indicated. NZ= no zoom, HZ= higher zoom, 2.5 or 3. Ticks report which experimental condition underwent which analysis and what image source was used. Number of discs is indicated.

a	***fkh***	30 h						54 h			
		10 min		15 min		25 min		10 min		25 min	
	see	NZ	HZ	NZ	HZ	NZ	HZ	NZ	HZ	NZ	HZ
Actin intensities	4.5.1a	✓	×	✓	×	×	×	✓	×	✓	×
Clone volume	4.5.1b	✓	✓	✓	✓	×	×	✓	✓	×	×
Nuclei counts	4.5.1c	×	✓	×	✓	×	✓	×	✓	×	×
Clone shape	4.51d	✓	✓	✓	×	×	✓	✓	✓	×	×
Circularity	4.5.1e	×	✓	×	✓	×	✓	×	✓	×	×
Wt dimension	4.5.1f	×	✓	×	✓	×	×	×	✓	×	×
# of discs		3		4		6		3		3	

b	**GFP**	0 h	30 h				54 h		54 h		***Rho*^{V14}**	54 h	
			10 min		25 min		10 min		25 min			10 min	
		HZ	NZ	HZ	NZ	HZ	NZ	HZ	NZ	HZ		NZ	HZ
Circularity	4.5.1e	×	×	✓	×	✓	✓	×	×	×		×	✓
Wt dimension	4.5.1f	✓	×	✓	×	✓	×	✓	×	✓		×	×
# of discs		1	3		3		2		3			4	

Table 15: Circularity measurements; **(a)** Gal4/UAS flip out discs expressing GFP (wt), *fkh*, or *Rho*^{V14} were analyzed 30 h and 54 h after HS. Inverse clones (inv) were generated by applying a long HS. Individual circularity measurements are listed. Mean, standard deviation (Stdv), Standard error of the mean (SEM) and number of clones analyzed are listed. **(b)** Significance of differences between data sets was tested by applying a two-tailed WMW test. * = p-val < 0.01, ** = p-val < 0.001. Date is visualized in Figure 23j. *Contributions: Statistical analysis in b: Marco La Fortezza.*

a	30 h				54 h		
	GFP	***fkh***	**GFP inv**	***fkh inv***	**GFP**	***fkh***	***Rho*^{V14}**
	0.39	0.89	0.38	0.89	0.19	0.80	0.37
	0.46	0.78	0.37	0.78	0.24	0.87	0.77
	0.29	0.82	0.70	0.78	0.26	0.87	0.34
	0.24	0.61	0.26	0.72	0.39	0.73	0.40
	0.24	0.83	0.19	0.63	0.23	0.87	0.66
	0.44	0.67	0.52	0.82	0.26	0.87	0.64
	0.34	0.79	0.21	0.67		0.93	0.36
	0.23	0.69	0.48	0.72		0.86	0.41
	0.27		0.26	0.69		0.83	0.53
	0.25					0.98	0.30
						0.91	0.42
Mean	**0.31**	**0.76**	**0.37**	**0.74**	**0.26**	**0.86**	**0.47**
Stdev	0.09	0.09	0.17	0.08	0.07	0.06	0.16
SEM	0.03	0.03	0.06	0.03	0.03	0.02	0.05
# clones	10	8	9	9	6	11	11

b	***wt_fkh***	***wt_Rho*^{V14}**
30h	4.57E-05	
	**	
30 inv	2.90E-04	
	**	
54 h	1.60E-04	1.90E-03
	**	*

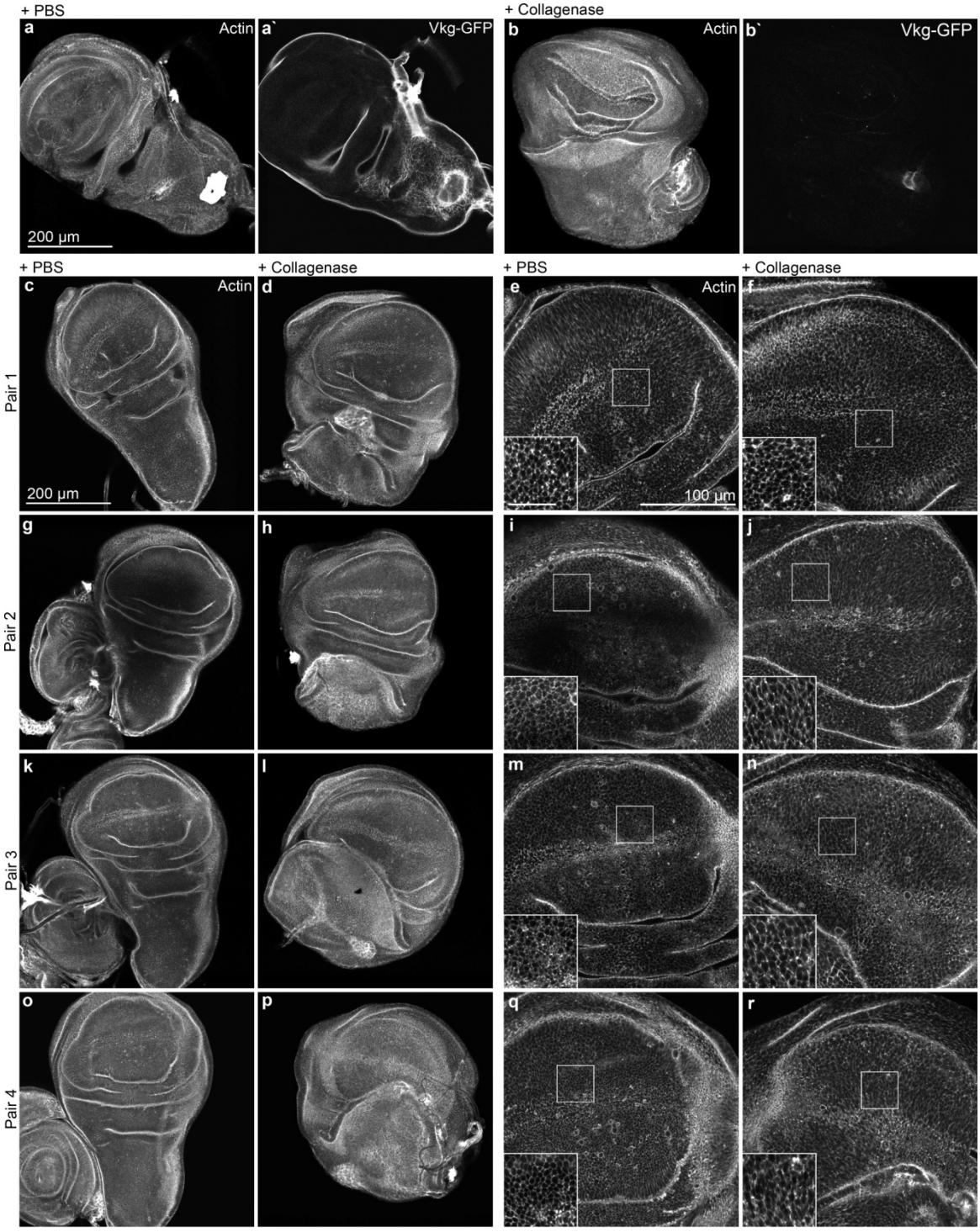

Figure 45: Collagenase treatment of wing imaginal discs; **(a, b)** 3rd instar wing imaginal discs expressing the Collagen IV GFP-fusion protein Vkg-GFP were treated with PBS (a) or Collagenase (b). Imaginal discs originate from same larva to allow better comparison. After Collagenase treatment, Vkg-GFP signal is dramatically reduced (b`) compared to control (a`). Note increase in disc size and folding. **(c-o)** Xy sections of 4 wing imaginal discs pairs where one disc was treated with PBS (left column) and the sibling with collagenase (second row from left). The two right columns show the same discs imaged closer. Lower left insets are higher magnifications of white framed regions. Scale bar as indicated, scale bars in insets represent 25 µm. Note the increase in cell area. Refer for measurements to Table 16.

Table 16: Cell dimensions; Mean of cell height, apical area, volume, aspect ratios and numbers of analyzed discs are reported. Tot=mean of ROI1 and 2. ROI1=means of measurements in periphery of the wing pouch. Roi2=means of measurements in the pouch center. Stdv = standard deviation. Measurements include **(a)** Gal4/UAS flip out clones expressing GFP at 0 h, 30 h and 54 h after heat-shock; **(b)** 3rd instar wing imaginal disc treated with collagenase and sibling imaginal discs treated with PBS as control. **(c)** Surrounding wild-type (wt) cells (GFP^-) and **(d)** *fkh*-expressing cells itself (GFP^+) of Gal4/UAS flip out discs 30 h and 54 h after heat-shock.

	Tot	***Stdv***	***ROI1***	***Stdv***	***ROI2***	***Stdv***	***Nr. of discs***
a *GFP-expressing cells*							
0 h							
cell height	**28.41**	1.01	**29.12**		**27.70**		n=1 disc
apical area	**11.97**	1.72	**10.75**		**13.19**		
cell volume	**339.11**	36.85	**313.06**		**365.17**		
aspect ratio	**8.25**	0.89	**8.88**		**7.63**		
30 h							
cell height	**41.26**	6.34	**39.33**	6.82	**43.19**	5.89	n=5 discs
apical area	**6.75**	2.06	**8.61**	0.71	**4.88**	0.58	
cell volume	**275.01**	81.71	**337.52**	54.22	**212.50**	48.12	
aspect ratio	**16.50**	3.91	**13.45**	2.59	**19.55**	2.10	
54 h							
cell height	**43.95**	3.84	**44.33**	3.90	**43.56**	4.34	n=4 discs
apical area	**6.39**	1.69	**7.85**	0.92	**4.94**	0.40	
cell volume	**281.35**	80.18	**347.86**	51.43	**214.85**	23.72	
aspect ratio	**17.77**	2.76	**15.89**	1.69	**19.65**	2.33	
b *Collagenase*	PBS		Collagenase				
cell height	**37.23**	7.31	**25.76**	5.39			n=4 discs
apical area	**3.81**	0.61	**4.90**	0.65			
cell volume	**143.82**	42.88	**127.64**	39.01			
aspect ratio	**19.07**	3.21	**11.63**	2.05			
c *wt cells surrouning fkh$^+$ clones*							
30 h							
cell height	**39.48**	2.58	**38.64**	2.50	**40.33**	2.88	n=3 discs
apical area	**8.44**	2.24	**10.22**	1.67	**6.65**	0.35	
cell volume	**329.99**	73.28	**392.41**	39.29	**267.58**	13.95	
aspect ratio	**13.93**	2.35	**12.20**	1.67	**15.67**	1.42	
54 h							
cell height	**53.24**	1.94	**53.64**	2.02	**52.83**	2.20	n=3 discs
apical area	**6.64**	1.65	**8.07**	0.72	**5.21**	0.37	
cell volume	**353.54**	89.51	**432.14**	31.84	**274.93**	21.88	
aspect ratio	**21.06**	2.65	**18.94**	1.44	**23.19**	1.38	
d *fkh$^+$ cells*							
30 h							
cell volume	**266.05**	33.73					n=8 clones, 3 discs
54 h							
cell volume	**192.86**	2.23					n=13 clones, 3 discs

Table 17: Parameter set for 3-D vertex modeling; List of parameters obtained from comparison of the vertex model to clone shape measurements as a function of clone size; 60 simulations with 10 cyst sizes and 6 different initial tissue configurations were run, from which averages and standard deviations were calculated. These curves were generated for 200 different parameter sets. The set of parameters shown here was found to give rise to equilibrium shapes that closely resemble the experimental data. * marks changes to initial parameters during cyst simulations. *Parameter definition by Silvanus Alt.*

Description	***Parameter***	***Value***
cell volume	V_0/l_0^3	1.0
lateral surface tension	T_l/T_l	1.0
*lateral surface tension MWI	T_l^c/T_l	3.0
apical surface tension	T_a/T_l	3.1
basal surface tension	T_b/T_l	6.95
external compression	T_{ext}/T_l	-4.2
apical line tension	$\Lambda_a/(l_0T_l)$	0.18
*apial line tension MWI	$\Lambda_a^c/(l_0T_l)$	0.53
basal line tension	$\Lambda_b/(l_0T_l)$	0.18
stiffness ECM attachment	k_v/T_l	5.0

V. Tie-Dye analysis

Table 18: Total clone counts; The amount of GFP control clones and RFP clones expressing RFP alone (wt); *fkh*; *dIAP;* or *fkh, dIAP* of a given size (from 1 to 20 cells) was determined in all discs (10 disc for *wt*, *fkh*, and *fkh, dIAP* and 8 discs for *dIAP*). Numbers represent the sum of all analyzed discs. The total clone counts for all clone sizes up to 20 cells (# clones ≤ 20 cells) and all sizes (# total clones) is shown. *Analysis by Marco La Fortezza.*

	wt		***fkh***		***dIAP***		***fkh, dIAP***	
# cells	GFP	RFP	GFP	RFP	GFP	RFP	GFP	RFP
1	470	493	352	211	378	373	352	239
2	305	359	249	207	269	281	244	210
3	179	253	172	135	159	195	167	164
4	158	174	168	104	138	120	134	118
5	106	141	120	74	82	100	105	114
6	75	87	110	45	82	68	106	86
7	77	77	89	32	56	44	69	52
8	63	51	81	42	36	38	67	60
9	53	45	64	24	26	32	60	33
10	40	40	49	23	47	34	41	28
11	40	31	50	19	24	25	30	23
12	32	24	29	12	15	11	37	19
13	17	23	31	17	14	20	29	13
14	24	18	34	12	18	11	22	13
15	19	11	29	9	14	9	26	7
16	19	9	20	5	29	2	23	15
17	12	8	22	7	21	5	16	7

18	16	6	16	12	9	7	22	9
19	13	7	17	4	6	4	14	4
20	20	4	12	3	8	2	8	7
# clones ≤ 20 cells	1738	1861	1714	997	1431	1381	1572	1221
# total clones	1942	1917	1927	1031	1546	1416	1755	1259
n (discs)	10		10		8		10	

Table 19: Single nuclei volumes measured in Tie-Dye experiments; Nuclei volumes determined in GFP control clones and RFP clones expressing RFP alone (wt), *fkh*, *dIAP* or *fkh, dIAP*. Number of measured clones is indicated (n (clones)) as well as number of discs (n (discs)) that were analyzed. Mean and standard deviation (stdv) is shown. For following quantifications, the average of GFP and RFP measurements for each individual genotype was used (final).

	GFP			***RFP***				
	Mean	stdv	n (clones)	Mean	stdv	n (clones)	n (discs)	**final**
wt	158.88	51.25	28	140.89	38.05	34	10	**149.88**
fkh	135.51	46.07	28	148.32	50.27	30	10	**141.91**
dIAP	131.68	41.63	24	152.23	47.83	26	8	**141.95**
fkh, dIAP	138.45	34.02	30	156.84	48.27	33	10	**147.65**

Table 20: GFP clone frequencies for given clone sizes; The amount of GFP control clones of the genotypes RFP alone (wt); *fkh*; *dIAP* or *fkh, dIAP* of a given size (from 1 to 20 cells) was determined in all discs. The mean of 10 (*wt, fkh,* and *fkh, dIAP*) and 8 (*dIAP*) discs is shown as well as the standard error of the mean (SEM). Data is visualized in Figure 29 e. *Analysis by Marco La Fortezza.*

	Wt		***fkh***		***dIAP***		***fkh, dIAP***	
# cells	Mean	SEM	Mean	SEM	Mean	SEM	Mean	SEM
1	47.00	8.68	35.20	4.35	47.25	9.76	35.20	3.11
2	30.50	4.99	24.90	4.18	33.63	7.71	24.40	3.50
3	17.90	3.09	17.20	2.19	19.88	3.69	16.70	2.65
4	15.80	1.87	16.80	2.28	17.25	2.74	13.40	1.27
5	10.60	0.91	12.00	1.28	10.25	1.68	10.50	1.11
6	7.50	0.65	11.00	1.17	10.25	2.06	10.60	1.54
7	7.70	1.51	8.90	1.59	7.00	1.24	6.90	0.74
8	6.30	0.78	8.10	0.77	4.50	0.87	6.70	0.99
9	5.30	0.79	6.40	0.69	3.25	1.00	6.00	0.67
10	4.00	0.42	4.90	0.85	5.88	0.88	4.10	0.48
11	4.00	0.67	5.00	0.52	3.00	0.65	3.00	0.61
12	3.20	0.57	2.90	0.55	1.88	0.35	3.70	0.65
13	1.70	0.40	3.10	0.84	1.75	0.37	2.90	0.55
14	2.40	0.48	3.40	0.73	2.25	0.41	2.20	0.36
15	1.90	0.35	2.90	0.72	1.75	0.31	2.60	0.34
16	1.90	0.38	2.00	0.33	3.63	0.65	2.30	0.40
17	1.20	0.33	2.20	0.36	2.63	0.26	1.60	0.37
18	1.60	0.58	1.60	0.45	1.13	0.35	2.20	0.47
19	1.30	0.30	1.70	0.40	0.75	0.41	1.40	0.43
20	2.00	0.42	1.20	0.13	1.00	0.38	0.80	0.25
n	10		10		8		10	

Table 21: RFP clone frequencies for given clone sizes; The amount of RFP clones of the genotypes RFP alone (wt); *fkh*; *dIAP* or *fkh, dIAP* of a given size (from 1 to 20 cells) was determined in all discs. The mean of 10 (*wt, fkh,* and *fkh, dIAP*) and 8 (*dIAP*) discs is shown as well as the standard error of the mean (SEM). Data is visualized in Figure 29 e`. *Analysis by Marco La Fortezza.*

	Wt		***fkh***		***dIAP***		***fkh, dIAP***	
# cells	Mean	SEM	Mean	SEM	Mean	SEM	Mean	SEM
1	49.30	8.60	21.10	3.51	46.63	11.37	23.90	4.55
2	35.90	6.45	20.70	4.19	35.13	8.36	21.00	3.31
3	25.30	4.12	13.50	1.35	24.38	4.77	16.40	1.77
4	17.40	2.40	10.40	1.32	15.00	2.24	11.80	0.95
5	14.10	1.40	7.40	0.97	12.50	1.48	11.40	1.05
6	8.70	1.29	4.50	0.91	8.50	1.07	8.60	0.88
7	7.70	1.33	3.20	0.71	5.50	0.89	5.20	0.65
8	5.10	0.77	4.20	0.84	4.75	0.84	6.00	0.87
9	4.50	0.62	2.40	0.45	4.00	0.89	3.30	0.82
10	4.00	0.68	2.30	0.52	4.25	0.75	2.80	0.51
11	3.10	0.60	1.90	0.35	3.13	0.79	2.30	0.47
12	2.40	0.67	1.20	0.36	1.38	0.38	1.90	0.31
13	2.30	0.60	1.70	0.37	2.50	0.50	1.30	0.33
14	1.80	0.61	1.20	0.39	1.38	0.46	1.30	0.26
15	1.10	0.41	0.90	0.41	1.13	0.35	0.70	0.21
16	0.90	0.46	0.50	0.17	0.25	0.16	1.50	0.31
17	0.80	0.29	0.70	0.26	0.63	0.26	0.70	0.26
18	0.60	0.27	1.20	0.53	0.88	0.30	0.90	0.31
19	0.70	0.26	0.40	0.22	0.50	0.27	0.40	0.22
20	0.40	0.22	0.30	0.15	0.25	0.16	0.70	0.30
n	10		10		8		10	

Table 22: Relative RFP clone frequencies; For each disc, the number of GFP control clones was subtracted from the number of RFP clones expressing RFP alone (wt); *fkh*; *dIAP;* or *fkh, dIAP* and normalized to the number of GFP control clones of the respective bin. The average of 10 disc for *wt*, *fkh*, and *fkh, dIAP* and 8 discs for *dIAP* is shown as well as the standard error of the mean (SEM). Data is visualized in Figure 29 f. *Analysis by Marco La Fortezza.*

	wt		***fkh***		***dIAP***		***fkh, dIAP***	
# cells	Mean	SEM	Mean	SEM	Mean	SEM	Mean	SEM
1	0.12	0.10	-0.42	0.05	-0.06	0.06	-0.35	0.09
2	0.23	0.15	-0.15	0.15	0.14	0.18	-0.13	0.08
3	0.56	0.25	-0.14	0.09	0.30	0.20	0.12	0.12
4	0.11	0.10	-0.36	0.07	-0.07	0.10	-0.05	0.11
5	0.38	0.17	-0.30	0.11	0.44	0.25	0.21	0.17
6	0.22	0.20	-0.59	0.07	0.10	0.20	0.21	0.43
7	0.47	0.36	-0.49	0.16	0.00	0.23	0.09	0.44
8	0.48	0.74	-0.44	0.13	0.29	0.28	0.23	0.40
9	0.03	0.25	-0.59	0.09	1.20	0.59	-0.48	0.12
10	0.19	0.27	-0.46	0.10	-0.03	0.24	-0.27	0.15
11	-0.01	0.23	-0.56	0.11	0.26	0.33	-0.44	0.10
12	-0.01	0.26	-0.53	0.13	-0.08	0.25	-0.30	0.20
13	-0.09	0.24	-0.11	0.22	0.57	0.25	-0.44	0.14
14	-0.03	0.28	-0.37	0.25	-0.29	0.31	-0.50	0.11
15	-0.26	0.34	-0.68	0.11	-0.21	0.23	-0.75	0.08
16	-0.53	0.24	-0.73	0.11	-0.92	0.06	-0.14	0.27
17	-0.24	0.16	-0.61	0.13	-0.77	0.08	-0.44	0.22

18	-0.67	0.15	-0.19	0.31	-0.50	0.17	-0.61	0.12
19	-0.33	0.23	-0.74	0.21	-0.67	0.18	-0.83	0.09
20	-0.80	0.11	-0.70	0.15	-0.90	0.07	-0.33	0.33
n	10		10		8		10	

Table 23: p-values of statistical analysis of TIE-DYE experiments; **(a)** p-values calculated to test for statistical differences of relative clone frequencies (*fkh* compared to wt and *fkh, dIAP* to *dIAP)* (Figure 29 f and Table 22) per clone size utilizing a one-tailed WMW test. p-values < 0.0.1 are red. The analysis suggests that *fkh*-expressing clones of less than 6 cells and *fkh, dIAP*-expressing clones of 1 cell are significantly underrepresented in the data set (red lines). We thus chose these thresholds for further analysis. **(b)** p-values calculated to test for statistical differences of relative clone frequencies (*fkh* compared to wt and *fkh, dIAP)* binned into two statistically significant clone size categories (Figure 29 g: 1 cell clone and 2 to 6 cell clones for both *fkh* and *fkh, dIAP*; Figure 29 h: *fkh* 1-6 cells and above 6 cells, *fkh, dIAP* 1 cell clones and above 1 cell clones. Significant differences between non-parametrically distributed data sets were tested by applying a one-tailed WMW test. A one-tailed Welch's t test was applied to normally distributed data sets with unequal variances. * = *p-val* < 0.01, ** = *p-val* < 0.001, *ns*= not significant. *Analysis by Marco La Fortezza.*

a	**# cells**	***wt _fkh***	***dIAP _fkh, dIAP***	**b**	**# cells**	***wt _fkh***	***dIAP _fkh, dIAP***	***Fkh _fkh, dIAP***
	1	0.0003	0.0075		1	2.89E-04	0.0075	/
	2	0.0481	0.1305		1 to 6	1.42E-04	/	/
	3	0.0014	0.3519		2 to 6	5.41E-06	0.3283	0.0059
	4	0.0023	0.4396		2 to 20	/	0.0864	/
	5	0.0026	0.3804		7 to 20	1.16E-02	0.0092	0.0273
	6	0.0004	0.2591					
	7	0.0205	0.3240					
	8	0.0698	0.1805					
	9	0.0055	0.0213					
	10	0.0315	0.1700					
	11	0.0221	0.0385					
	12	0.1042	0.2336					
	13	0.5000	0.0071					
	14	0.2138	0.5000					
	15	0.4595	0.0404					
	16	0.5330	0.9969					
	17	0.0777	0.8200					
	18	0.8208	0.2214					
	19	0.0649	0.1970					
	20	0.5790	0.7686					

VI. Apoptotic volume analysis

Table 24: Nuclei volumes and statistical analysis; **(a)** Nuclei volumes determined in *fkh* and *fkh, dIAP* expressing flip out clones. Number of measured clones is indicated (n (clones)) as well as number of discs (n (discs)) that were analyzed. Mean and standard deviation (stdv) is shown.**(b)** p-values calculated to test for statistical significance in relative apoptotic volume ratios between *fkh* and *fkh, dIAP*-expressing clones per clone size bin applying two-tailed WMW test. Red = p-val < 0.01. Data is visualized in Figure 30 c. *Contributions: Statistics in b: Marco La Fortezza.*

a		Mean	stdv	n (clones)	n (discs)
	fkh	146.49	30.00	12	3
	fkh, dIAP	206.69	44.35	12	3

b	# cells	*fkh_fkh, dIAP*
	1	0.0277
	2 to 6	0.0021
	> 6	0.0026